

8-2016

Response of high-strength steel reinforced concrete structures to simulated earthquakes

Lucas Laughery
Purdue University

Follow this and additional works at: https://docs.lib.purdue.edu/open_access_dissertations



Part of the [Civil Engineering Commons](#)

Recommended Citation

Laughery, Lucas, "Response of high-strength steel reinforced concrete structures to simulated earthquakes" (2016). *Open Access Dissertations*. 792.

https://docs.lib.purdue.edu/open_access_dissertations/792

This document has been made available through Purdue e-Pubs, a service of the Purdue University Libraries. Please contact epubs@purdue.edu for additional information.

**PURDUE UNIVERSITY
GRADUATE SCHOOL
Thesis/Dissertation Acceptance**

This is to certify that the thesis/dissertation prepared

By Lucas A Laughery

Entitled

Response of High-Strength Steel Reinforced Concrete Structures to Simulated Earthquakes

For the degree of Doctor of Philosophy

Is approved by the final examining committee:

Santiago Pujol

Chair

Mete A. Sozen

Co-chair

Michael E. Kreger

Co-chair

Robert L. Nowack

To the best of my knowledge and as understood by the student in the Thesis/Dissertation Agreement, Publication Delay, and Certification Disclaimer (Graduate School Form 32), this thesis/dissertation adheres to the provisions of Purdue University's "Policy of Integrity in Research" and the use of copyright material.

Approved by Major Professor(s): Santiago Pujol

Approved by: Dulcy M. Abraham

Head of the Departmental Graduate Program

7/21/2016

Date

RESPONSE OF HIGH-STRENGTH STEEL REINFORCED
CONCRETE STRUCTURES TO SIMULATED EARTHQUAKES

A Dissertation

Submitted to the Faculty

of

Purdue University

by

Lucas Laughery

In Partial Fulfillment of the

Requirements for the Degree

of

Doctor of Philosophy

August 2016

Purdue University

West Lafayette, Indiana

To my parents Tim and Lisa.

ACKNOWLEDGEMENTS

I would like to express my gratitude to the people who helped me get to where I am today, starting with my family – Tim, Lisa, and Kayla – for their boundless support. I would also like to thank my fiancée, Yunlan Zhang, for her patience and support during my years in graduate school.

Santiago Pujol has been a great friend and mentor throughout my time at Purdue. Discussions with him have been of enormous benefit to my understanding of the behavior of reinforced concrete. His critique of my prose and the opportunities he made available to me are both greatly appreciated. For these and more, I thank you.

Thank you to Professor Mete Sozen, for always having an open door and taking the time to discuss anything at a moment's notice. Thank you also to my committee members Professors Michael Kreger and Robert Nowack. Your advice and suggestions throughout the process have been invaluable.

Finally, I would like to thank the staff at Bowen Laboratory who have assisted me: Harry Tidrick, Kevin Brower, and Molly Stetler. I would also like to thank my fellow graduate students: Ying Wang and Enrique Villalobos for their mentorship; and Aishwarya Puranam, Derek Daluga, Ryan Jenkins, Will Pollalis, Prateek Shah, and Tomomi Suzuki for their help.

My graduate education would not have been possible without a fellowship from Purdue University and support from the Network for Earthquake Engineering Simulation. Similarly, the experimental work would not have been possible without support from MMFX Technologies, Precision-Hayes International, and Voss Engineering, LLC.

TABLE OF CONTENTS

	Page
LIST OF TABLES	viii
LIST OF FIGURES	xi
NOMENCLATURE	xix
ABSTRACT.....	xxii
CHAPTER 1. INTRODUCTION	1
CHAPTER 2. LITERATURE REVIEW	4
2.1. Static Tests.....	4
2.2. Dynamic Tests	5
2.2.1. Otani and Sozen (1972).....	5
2.2.2. Cecen (1979).....	6
2.2.3. Application to HSSRC Frames	7
2.3. Numerical Investigations	8
CHAPTER 3. EXPERIMENTAL DESIGN AND PROGRAM.....	11
3.1. Scope of Work	11
3.2. Test Specimens	12
3.2.1. Moment-Curvature Relationships of the Columns.....	15
3.2.2. Trilinear Approximations	17
3.2.3. Expected Behavior of Frames	18
3.2.4. Dynamic Properties of the Frames	19
3.2.5. Numerical Models	21
3.3. Test Setup	22
3.3.1. Specimen and Mass	23
3.3.2. Out-of-plane Bracing.....	23
3.3.3. Instrumentation	24
3.4. Ground Motion Profiles.....	25
3.5. Control of Earthquake Simulator.....	26
3.6. Test Procedure	26

	Page
CHAPTER 4. OBSERVED RESPONSE	28
4.1. Data Processing	28
4.1.1. Main Data Acquisition System	28
4.1.2. Optotrak.....	29
4.2. Ground Motions.....	31
4.2.1. Ground Motion Histories and Summary Properties	31
4.2.2. Linear Response Spectra	32
4.3. Free Vibration Tests	34
4.4. Specimen Response Histories.....	34
4.4.1. In-Plane Motion	34
4.4.2. Curvature Distributions	35
4.4.3. Out-of-Plane Motion	36
4.4.4. Vertical Motion	36
4.5. Inertial Force versus Drift Envelopes	37
4.6. Damage.....	38
4.6.1. Frame C1 (Figure 4-48).....	38
4.6.2. Frame C2 (Figure 4-49).....	38
4.6.3. Frame H1 (Figure 4-50)	39
4.6.4. Frame H2 (Figure 4-51)	39
CHAPTER 5. DISCUSSION OF OBSERVED RESPONSE.....	41
5.1. Initial Stiffness.....	41
5.2. Post-Cracking Stiffness	43
5.3. Strength.....	45
5.4. Lateral Resistance.....	45
5.4.1. Type C.....	45
5.4.2. Type H.....	46
5.5. Drift Response	49
5.5.1. Type C vs. Type H	51
5.5.2. Series 1 vs. Series 2.....	51
5.5.3. First vs. Second 100% Motion	55
5.6. Summary.....	56

	Page
CHAPTER 6. EVALUATION OF ESTIMATES OF PEAK DRIFT	59
6.1. History of Simple Expressions for Peak Inelastic Response	59
6.2. Dataset	63
6.2.1. Parameters	63
6.2.2. SDOF Tests	67
6.2.3. MDOF Tests	69
6.2.4. Instrumented Buildings	74
6.3. Evaluation	77
6.4. Ground Motions with Low PGV/PGA Ratios	79
6.5. Summary	81
CHAPTER 7. SUMMARY AND CONCLUSIONS	82
7.1. Summary of Experimental Work	82
7.2. Summary of Dataset	83
7.3. Conclusions	84
TABLES	85
FIGURES	119
REFERENCES	214
APPENDICES	
A1. MATERIALS	221
A1.1. Grout Mix	221
A1.2. Longitudinal Reinforcement	222
A1.3. Transverse Reinforcement	223
A1.4. Corrosion of Reinforcement to Improve Bond	224
A2. PULLOUT TESTS	225
A2.1. Hook Specimen	226
A2.2. Plate Specimen	227
A2.3. Anchor Specimens	227
A3. TEST STRUCTURES	229
A3.1. Overall Dimensions	229
A3.2. Reinforcing Details	229
A3.3. Anchorage of High-Strength Steel	230

	Page
A4. TEST SETUP COMPONENTS.....	231
A4.1. Reusable Concrete Mass.....	231
A4.2. Specimen Base Connection Components.....	232
A4.3. Out-of-plane Bracing.....	233
A4.4. Instrumentation Truss.....	233
A4.5. Friction Tests.....	234
A5. CONTROL AND INSTRUMENTATION.....	236
A5.1. Control.....	236
A5.2. Instrumentation.....	237
A5.2.1. Primary Data Acquisition System.....	237
A5.2.2. Optical Tracking System.....	239
A5.2.3. Cameras.....	239
A6. GROUND MOTION SELECTION AND MODIFICATION.....	240
A6.1. Details of Selected Record.....	241
A6.2. Modification of Selected Record.....	242
A7. TEST NOTES.....	243
A7.1. Frames C1 and H1: Initial Period.....	243
A7.2. Videos.....	244
A7.2.1. Dial Gauge.....	244
A7.2.2. GoPro.....	244
A7.2.3. Drone.....	245
A7.3. Sensor Malfunctions.....	245
A8. DATASET DETAILS.....	246
A8.1. Rayleigh’s Method.....	246
A8.2. SAP2000 Model of 20-Story Structure.....	247
A9. SUGGESTIONS FOR FUTURE TESTS.....	249
A9.1. Anchorage of High-strength Steel.....	249
A9.2. Reusable Mass.....	249
VITA.....	291

LIST OF TABLES

Table	Page
Table 2-1: Summary of previous quasi-static investigations of high-strength steel reinforced concrete members.....	85
Table 2-2: Summary of previous dynamic investigations of conventionally reinforced concrete.....	88
Table 3-1: Selected properties of four test specimens.	90
Table 3-2: Breakdown of components adding up to effective mass of system.....	91
Table 3-3: Selected calculated properties of test specimens (used in LARZ models).	91
Table 3-4: Summary of target ground motion characteristics for each base motion.	92
Table 3-5: Typical sequence of test procedure.	93
Table 4-1: Measured properties of ground motions during each test.....	94
Table 4-2: Effect of reducing lowpass filter frequency on PGA and PGV. Values generated from acceleration data using Butterworth bandpass filter with highpass frequency 0.5 Hz and lowpass frequency as specified below.....	95
Table 4-3: Coefficients of variation for linear displacement response spectra (across all tests).....	96
Table 4-4: Calculated and measured initial periods.....	96
Table 4-5: Measured in-plane response, specimen C1 (Figure 4-11 through Figure 4-15).....	97
Table 4-6: Measured in-plane response, specimen C2 (Figure 4-16 through Figure 4-20).....	98
Table 4-7: Measured in-plane response, specimen H1 (Figure 4-21 through Figure 4-25).....	99
Table 4-8: Measured in-plane response, specimen H2 (Figure 4-26 through Figure 4-30).....	100
Table 4-9: Summary of peak displacement response for each test.	101

Table	Page
Table 5-1: Calculated versus measured initial periods (from free vibration tests) for past dynamic tests of SDOF reinforced concrete structures.	102
Table 5-2: Calculated versus measured initial first mode periods (from free vibration tests) for past dynamic tests of MDOF reinforced concrete structures with walls [adapted from Lepage (1997)].....	103
Table 5-3: Calculated versus measured initial first mode periods for past dynamic tests of MDOF reinforced concrete structures without walls [adapted from Lepage (1997)].	104
Table 5-4: Mean effective periods calculated using zero crossing rate from $t = 1.5 - 11$ sec.	105
Table 5-5: Percent difference* in peak drift for frame type C versus frame type H.	105
Table 5-6: Percent difference** in peak drift for frames in Series 1 versus Series 2.....	105
Table 5-7: Percent change*** in peak drift for a given frame type from first 100% motion to second 100% motion.	106
Table 6-1: Summary of single-degree-of-freedom experiments.	107
Table 6-2: Summary of multiple-degree-of-freedom experiments.	110
Table 6-3: Summary of instrumented buildings that experienced earthquakes.	116
Table 6-4: Amplification factors for selected damping coefficients [reproduced from Newmark and Hall (1982)]......	117
Table 6-5: Summary of D_{max}/S_{dv} ratios for different PGV/PGA ranges.	117
Table 6-6: Summary of D_{max}/S_{dv} ratios for different PGV/PGA ranges if $\Gamma=2$ is assumed for MDOF systems.	117
Table 6-7: Ground motion records used for analyses of bilinear SDOF systems.	118
Table 6-8: Summary of peak drifts from analyses of bilinear SDOF systems with specified initial periods and base shear coefficients.	118
Appendix Table	
Table A1-1: Grout mix proportions (as-delivered, per cubic yard).	250
Table A1-2: Gradation of INDOT #23 sand (from INDOT Standard Specification §904.02h).....	250
Table A1-3: Concrete compressive strength progression through end of curing.....	251
Table A1-4: Summary of concrete material properties established on test days.	251
Table A1-5: Longitudinal reinforcing steel sample test results.	252

Appendix Table	Page
Table A1-6: Values of parameters used in ideal Menegotto-Pinto (1973) relationship.....	252
Table A1-7: Transverse reinforcing steel sample test results.	252
Table A3-1: As-built measurements of frame dimensions (see Figure A3-3 for key). All measurements are in inches.	253
Table A3-2: Specimen reinforcement summary.	254
Table A3-3: As-built measurements of column hoop spacing.....	255
Table A4-1: Summary of drag tests (conducted on 2015-July-13).....	257
Table A5-1: Channels assignments on main DAQ system. All sensors are connected parallel to the axis of excitation and sample at 1000 Hz.	258
Table A5-2: Overview of main data acquisition system.	259
Table A5-3: Model and serial numbers of instrumentation used.	259
Table A6-1: Ranges and factors used to modify Fourier amplitudes of acceleration record.	260
Table A7-1: List of videos recorded during test program.	261
Table A8-1: Summary of concrete material properties used in SAP2000 model.	262

LIST OF FIGURES

Figure	Page
Figure 1-1: Reinforcement congestion at a beam-column joint (Risser & Hoffman, 2011).	119
Figure 1-2: Honeycombing as a result of reinforcement congestion (Kenai & Bahar, 2003).	119
Figure 2-1: Comparison of hysteresis loops for HSSRC (gray) and CRC (black) columns, with HSSRC exhibiting a lower unloading stiffness [from Rautenberg (2011)].	120
Figure 2-2: Qualitative moment-curvature diagrams for Rautenberg's two column types.	122
Figure 2-3: Comparison of computed mean roof drift ratios in multi-degree-of-freedom models using Gr.-60 steel and models using Gr.-120 steel in the columns [from Rautenberg (2011)].	122
Figure 3-1: Test structure elevation view.	123
Figure 3-2: Typical column cross-section.	123
Figure 3-3: Measured stress-strain curves for conventional steel alongside model curve.	124
Figure 3-4: Measured stress-strain curves for high-strength steel alongside model curve. (Note: Extensometer was removed at 0.03 in./in. for samples 2, 3, and 4).	124
Figure 3-5: Column longitudinal reinforcement development lengths.	125
Figure 3-6: Column reinforcement plans showing anchorage assemblies in type H columns.	125
Figure 3-7: Concrete stress-strain model used in FLECHA (based on Hognestad, 1951).	127
Figure 3-8: Model stress-strain curves for column longitudinal reinforcing steel.	127
Figure 3-9: Idealized trilinear moment curvature relationships for columns ($P = 0.025A_g f_c$).	128
Figure 3-10: Elastic bending moment diagram for a portal frame subject to lateral load at the top.	129
Figure 3-11: Renderings of specimen, mass, and connection components.	129

Figure	Page
Figure 3-12: Assumed geometry for LARZ models.	130
Figure 3-13: Lateral force versus displacement curves for C and H frames (from LARZ).	130
Figure 3-14: Rendering of west elevation of test setup highlighting primary components.	131
Figure 3-15: Instrumentation layout.	131
Figure 3-16: Plan view of setup showing camera and Optotrak positions.	132
Figure 3-17: Fourier spectrum modification process used to smoothen displacement spectrum.	132
Figure 3-18: Comparison of linear displacement spectra of modified and original ground motions.	133
Figure 3-19: Comparison of original and modified acceleration histories.	133
Figure 3-20: Ground motion histories for target 100% motion.	134
Figure 3-21: Linear acceleration response spectra for scaled ground motion records (2% damped).	135
Figure 3-22: Linear velocity response spectra for scaled ground motion records (2% damped).	135
Figure 3-23: Linear displacement (drift) response spectra for scaled ground motion records (2% damped).	136
Figure 4-1: Illustration of experiment coordinate system vectors.	137
Figure 4-2: Method for obtaining in-plane transformation vector for Optotrak targets.	137
Figure 4-3: Comparison of target platform displacement with Optotrak and MTS feedback.	138
Figure 4-4: Comparison of linear displacement response spectra obtained from 25% runs with target spectrum (2% damped).	140
Figure 4-5: Comparison of linear displacement response spectra obtained from 50% runs with target spectrum (2% damped).	140
Figure 4-6: Comparison of linear displacement response spectra obtained from 75% runs with target spectrum (2% damped).	141
Figure 4-7: Comparison of linear displacement response spectra obtained from first 100% runs with target spectrum (2% damped).	141
Figure 4-8: Comparison of linear displacement response spectra obtained from second 100% runs with target spectrum (2% damped).	142
Figure 4-9: Response histories for specimen C1, 25% run (first of five runs).	143

Figure	Page
Figure 4-10: Response histories for specimen C1, 50% run (second of five runs).....	144
Figure 4-11: Response histories for specimen C1, 75% run (third of five runs).	145
Figure 4-12: Response histories for specimen C1, 100% run (fourth of five runs).	146
Figure 4-13: Response histories for specimen C1, second 100% run (fifth of five runs).	147
Figure 4-14: Response histories for specimen C2, 25% run (fourth of five runs).	148
Figure 4-15: Response histories for specimen C2, 50% run (third of five runs).	149
Figure 4-16: Response histories for specimen C2, 75% run (second of five runs).....	150
Figure 4-17: Response histories for specimen C2, 100% run (first of five runs).	151
Figure 4-18: Response histories for specimen C2, second 100% run (fifth of five runs).	152
Figure 4-19: Response histories for specimen H1, 25% run (first of five runs).	153
Figure 4-20: Response histories for specimen H1, 50% run (second of five runs).....	154
Figure 4-21: Response histories for specimen H1, 75% run (third of five runs).	155
Figure 4-22: Response histories for specimen H1, 100% run (fourth of five runs).	156
Figure 4-23: Response histories for specimen H1, second 100% run (fifth of five runs).	157
Figure 4-24: Response histories for specimen H2, 25% run (fourth of five runs).	158
Figure 4-25: Response histories for specimen H2, 50% run (third of five runs).	159
Figure 4-26: Response histories for specimen H2, 75% run (second of five runs).....	160
Figure 4-27: Response histories for specimen H2, 100% run (first of five runs).	161
Figure 4-28: Response histories for specimen H2, second 100% run (fifth of five runs).	162
Figure 4-29: Comparison of velocity history derived from accelerometers to velocity history derived from LVDT (C2-75).....	163
Figure 4-30: Curvature distributions at selected times for test C1-100. [Note: Top curvatures could not be measured.]	164
Figure 4-31: Curvature distributions at selected times for test C2-100. [Note: Top curvatures could not be measured.]	165
Figure 4-32: Curvature distributions at selected times for test H1-100. [Note: Top curvatures could not be measured.]	166
Figure 4-33: Curvature distributions at selected times for test H2-100. [Note: Top curvatures could not be measured.]	167
Figure 4-34: Diagram showing method of calculating curvatures using optical targets.	168

Figure	Page
Figure 4-35: Out-of-plane movement measured during test C1-100.	169
Figure 4-36: Out-of-plane movement measured during test C2-100.	169
Figure 4-37: Out-of-plane movement measured during test H1-100.	170
Figure 4-38: Out-of-plane movement measured during test H2-100.	170
Figure 4-39: Vertical movement measured during test C1-100.	171
Figure 4-40: Vertical movement measured during test C2-100.	171
Figure 4-41: Vertical movement measured during test H1-100.	172
Figure 4-42: Vertical movement measured during test H2-100.	172
Figure 4-43: Envelopes derived from response histories.	173
Figure 4-44: LARZ predicted envelope alongside measured envelopes for specimens C1 and C2 (measured are uppermost points from positive and negative directions).	174
Figure 4-45: LARZ predicted envelope alongside measured envelopes for specimens H1 and H2 (measured are uppermost points from positive and negative directions).	174
Figure 4-46: Crack map for specimen C1, west face.	175
Figure 4-47: Crack map for specimen C2, west face.	176
Figure 4-48: Crack map for specimen H1, west face.	177
Figure 4-49: Crack map for specimen H2, west face.	178
Figure 5-1: Illustration of expected limit state for portal frames (based on flexural behavior).	179
Figure 5-2: Illustration of possible limit state for type H frames (assuming slip).	179
Figure 5-3: Comparison of top drift responses of tests C1-25 and H1-25.	180
Figure 5-4: Comparison of top drift responses of tests C1-50 and H1-50.	180
Figure 5-5: Comparison of top drift responses of tests C1-75 and H1-75.	181
Figure 5-6: Comparison of top drift responses of tests C1-100 and H1-100.	181
Figure 5-7: Comparison of top drift responses of tests C1-100(2) and H1-100(2).	182
Figure 5-8: Comparison of top drift responses of tests C2-25 and H2-25.	182
Figure 5-9: Comparison of top drift responses of tests C2-50 and H2-50.	183
Figure 5-10: Comparison of top drift responses of tests C2-75 and H2-75.	183
Figure 5-11: Comparison of top drift responses of tests C2-100 and H2-100.	184
Figure 5-12: Comparison of top drift responses of tests C2-100(2) and H2-100(2).	184

Figure	Page
Figure 5-13: Comparison of top drift responses of tests C1-25 and C2-25.	185
Figure 5-14: Comparison of top drift responses of tests C1-50 and C2-50.	185
Figure 5-15: Comparison of top drift responses of tests C1-75 and C2-75.	186
Figure 5-16: Comparison of top drift responses of tests C1-100 and C2-100.	186
Figure 5-17: Comparison of top drift responses of tests C1-100(2) and C2-100(2).	187
Figure 5-18: Comparison of top drift responses of tests H1-25 and H2-25.	187
Figure 5-19: Comparison of top drift responses of tests H1-50 and H2-50.	188
Figure 5-20: Comparison of top drift responses of tests H1-75 and H2-75.	188
Figure 5-21: Comparison of top drift responses of tests H1-100 and H2-100.	189
Figure 5-22: Comparison of top drift responses of tests H1-100(2) and H2-100(2).	189
Figure 5-23: Comparison of top drift responses of tests C1-100(1) and C1-100(2).	190
Figure 5-24: Comparison of top drift responses of tests C2-100(1) and C2-100(2).	190
Figure 5-25: Comparison of top drift responses of tests H1-100(1) and H1-100(2).	191
Figure 5-26: Comparison of top drift responses of tests H2-100(1) and H2-100(2).	191
Figure 5-27: Measured peak in-run drift of H frames vs. C frames.	192
Figure 5-28: Measured peak cumulative drift of H frames vs. C frames.	192
Figure 5-29: Measured peak in-run drift of Series 2 frames vs. Series 1 frames.	193
Figure 5-30: Measured peak cumulative drift of Series 2 frames vs. Series 1 frames.	193
Figure 5-31: Comparison of mean effective periods for each test.	194
Figure 5-32: Excursions beyond drift versus drift for tests at 25%.	194
Figure 5-33: Excursions beyond drift versus drift for tests at 50%.	195
Figure 5-34: Excursions beyond drift versus drift for tests at 75%.	195
Figure 5-35: Excursions beyond drift versus drift for tests at 100%.	196
Figure 5-36: Excursions beyond drift versus drift for second tests at 100%(2).	196
Figure 6-1: Reproduction of Sozen's (1980) plot of peak drift ratio versus spectrum intensity.	197
Figure 6-2: Illustration of idealized constant acceleration, velocity, and displacement regions of response (based on 1940 El Centro 180 component).	197

Figure	Page
Figure 6-3: Frames tested by Gulkan and Sozen (1971).....	198
Figure 6-4: Schematic showing idealized response of specimens tested by Bonacci [from Bonacci (1989), Fig. 2.2].....	198
Figure 6-5: Frames tested by Elwood and Moehle (2003). Outer columns are circular, inner column is square [from Elwood and Moehle (2003), Fig. B-1].	199
Figure 6-6: Schematics of building tested by Shahrooz and Moehle [from Shahrooz and Moehle (1987), Fig. 2.1].....	200
Figure 6-7: Elevation and plan view of building slice tested by Panagiotou et al. [from Panagiotou et al. (2007), Fig. 2.1].	201
Figure 6-8: Building tested at E-DEFENSE [from Sugimoto et al. (2016), Fig. 2].....	202
Figure 6-9: Plan and elevation views of Van Nuys Holiday Inn [from Lepage (1997), Fig. 5.1].....	203
Figure 6-10: Floor plan of Millikan Library [from Kuroiwa (1967), Fig. 1.1].....	204
Figure 6-11: Floor plan of the Building of the Department of Civil Engineering (dimensions in mm) [from Wang et al. (2012), Fig. 2].	205
Figure 6-12: Measured versus estimated peak drift (D_{max} = measured peak roof drift, S_{dv} = estimated peak roof drift, H = height of structure).	206
Figure 6-13: Ratio of measured-to-estimated peak drift versus PGA.....	206
Figure 6-14: Ratio of measured-to-estimated peak drift versus PGV.....	207
Figure 6-15: Ratio of measured-to-estimated peak drift versus ratio of measured-to- estimated period.....	207
Figure 6-16: Ratio of measured-to-estimated peak drift versus measured peak drift ratio.	208
Figure 6-17: Ratio of measured-to-estimated peak drift versus PGV/PGA.....	208
Figure 6-18: Close-up: ratio of measured-to-estimated peak drift versus PGV/PGA.....	209
Figure 6-19: Measured versus estimated peak drift ratio for ground motions with PGV/PGA > 0.03 sec (D_{max} = measured peak roof drift, S_{dv} = estimated peak roof drift, H = height of structure).	210
Figure 6-20: Ratio of measured-to-estimated peak drift versus PGV/PGA if $\Gamma=2$ is assumed for MDOF systems.....	211
Figure 6-21: Displacement response spectra for records with low PGV/PGA compared with El Centro 1940.....	212
Figure 6-22: Peak drift response of bilinear oscillators with base shear coefficients of 0.2.....	213
Figure 6-23: Peak drift response of bilinear oscillators with base shear coefficients of 0.3.....	213

Appendix Figure	Page
Figure A1-1: Development of concrete strength during and after curing process.	263
Figure A1-2: Photograph of Baldwin 120-kip universal testing machine used to test reinforcing bars.	264
Figure A1-3: Expected stress-strain relationship of 12L14 steel wire used as specimen transverse reinforcement.	265
Figure A1-4: Comparison of (a) non-corroded, and (b) corroded transverse reinforcement.	266
Figure A1-5: Comparison of (a) non-corroded, and (b) corroded high-strength steel.	266
Figure A2-1: Pullout test specimen types.	267
Figure A2-2: Anchor specimen details.	268
Figure A2-3: Schematic of pullout test setup.	269
Figure A2-4: Photograph of pullout test setup (plate specimen).	270
Figure A2-5: Stress-extension curve for hook pullout specimen.	271
Figure A2-6: Stress-extension curve for plate pullout specimen.	271
Figure A2-7: Stress-extension curve for anchor pullout specimens.	272
Figure A3-1: Overall dimensions of frames.	272
Figure A3-2: Isometric of frames.	273
Figure A3-3: Schematic for as-built dimensions.	274
Figure A3-4: Comparison of specimen reinforcement details.	275
Figure A4-1: Isometric of test setup (for clarity, threaded rods, nuts, and plates are not shown).	276
Figure A4-2: Test component details.	277
Figure A4-3: Mass reinforcement details.	278
Figure A4-4: Out-of-plane bracing system.	279
Figure A4-5: Annotated photograph of instrumentation truss.	280
Figure A4-6: Schematic of LVDT mount.	281
Figure A5-1: Master instrumentation plan (west face of test setup).	282
Figure A5-2: Overhead view of instrumentation plan.	283
Figure A5-3: Photograph showing location where dial gauges were installed.	284

Appendix Figure	Page
Figure A6-1: Idealized displacement response spectrum.	285
Figure A6-2: Displacement response spectra of original and compressed/scaled record.	285
Figure A6-3: Close-up of displacement response spectra of original and compressed/scaled record.	286
Figure A8-1: SAP2000 models of 20-story frames tested in Japan, X-direction.....	287
Figure A8-2: SAP2000 models of 20-story frames tested in Japan, Y-direction.....	288
Figure A8-3: Gross dimensions of members in SAP2000 models.	289

NOMENCLATURE

Symbol or Abbreviation	First page	Description
A_b	48	Cross-sectional area of reinforcing bar ($= \pi d_b^2/4$)
A_F	25	Factor used to adjust amplitude of frequencies in Fourier domain
b	17	Width of column
c	37	Damping constant of system
CoV	33	Coefficient of variation (= standard deviation / mean)
CRC	4	Conventional reinforced concrete
d'	13	Depth to closest layer of reinforcing steel
d	2	Effective depth; depth to farthest layer of reinforcing steel
d_b	13	Diameter of reinforcing bar
D_{max}	63	Peak drift reached by system
$D_{rel,i}$	29	Relative displacement of Optotrak target at time i
e	47	Elongation of bar
E_c	2	Modulus of elasticity of concrete (measured to 40% f'_c)
E_s	16	Initial modulus of elasticity of steel
$E_{s\infty}$	16	Tangent modulus of elasticity of steel at ultimate
f	65	Frequency
F_a	9	Acceleration amplification factor in Newmark's region of nearly constant acceleration
F_p	19	Base shear strength
f'_c	14	Compressive strength of concrete
f_r	17	Modulus of rupture of concrete
f_t	16	Tensile strength of concrete
F_v	66	Velocity amplification factor in Newmark's region of nearly constant velocity
f_y	1	Yield stress of steel
g	9	Gravitational acceleration
h	77	Depth of column
H	77	Total height of structure
HSSRC	1	High-strength steel reinforced concrete
I_g	2	Gross moment of inertia ($= bh^3/12$)

Symbol or Abbreviation	First page	Description
IP_i, IP_k, I_k	30	Unit vector in in-plane direction (for transforming Optotrak coordinates)
k	20	Lateral stiffness
k_1	2	Initial stiffness
k_2	2	Post-cracking stiffness
k_s	16	Parameter used in Menegotto-Pinto (1973) steel model to define slope of stress-strain curve ($= E_{sc}/E_s$)
L	13	Length (height) of columns
LVDT	24	Linear variable differential transformer
m	37	Mass
M_{cr}	17	Cracking moment ($= f_r bh^2/6$)
MDOF	9	Multiple-degree-of-freedom
M_p	18	Plastic moment of cross-section
N	67	Number of stories of structure
OOP_i, OOP_k, OOP_k	30	Unit vector in out-of-plane direction (for transforming Optotrak coordinates)
PGA	9	Peak ground acceleration
PGD	31	Peak ground displacement
PGV	9	Peak ground velocity
R	16	Parameter used to define the shape of steel stress-strain curve using Menegotto-Pinto (1973) relationship
s	14	Spacing of transverse reinforcement
S_a	9	Spectral acceleration
S_d	27	Spectral displacement
S_{da}	8	Peak drift estimated using PGA and from Lepage's expression (1997)
SDOF	11	Single-degree-of-freedom
S_{dv}	9	Peak drift estimated using PGV and from Sozen's expression (2003)
SI_{20}	5	Spectrum intensity at 20% critical damping
S_v	6	Spectral velocity
$S_{v,avg}$	66	Average spectral velocity in region of nearly constant velocity
T	6	Period
T_{calc}	63	Calculated initial first-mode period from gross cross-sectional properties
T_{cr}	19	Period based on cracked section
T_{eff}	9	Effective period
T_g	9	Characteristic period of ground motion
T_i	9	Initial period from gross cross-sectional properties (see I_g)

Symbol or Abbreviation	First page	Description
T_{meas}	63	Measured initial first-mode period
T_s	19	Secant period calculated based on stiffness from origin to yield point
U	48	Elastic potential energy
$Vert_i, Vert_k, Vert_k$	30	Unit vector in vertical direction (for transforming Optotrak coordinates)
V_{s30}	241	Shear wave velocity in the top 30 m of the subsurface
W_c	19	Weight of columns
W_{ext}	47	External work
W_{int}	47	Internal work
$W_{int,slip}$	48	Internal work assuming slip of reinforcing steel
W_{me}	19	Weight of effective mass
W_{ml}	19	Lumped weight at top of specimens
x	37	Relative displacement of oscillator
\dot{x}	37	Relative velocity of oscillator
\ddot{x}	37	Relative acceleration of oscillator
x_i	28	Measurement at time i
x_{u0}, y_{u0}, z_{u0}	29	Untransformed Optotrak coordinates at start of test
x_{ui}, y_{ui}, z_{ui}	29	Untransformed Optotrak coordinates at time i
y_i	28	Smoothed value of measurement x_i
Z	16	Parameter used to define slope of concrete stress-strain curve after peak stress is reached
\ddot{z}	37	Base acceleration
β	6	Damping coefficient, as a percent of critical damping
Γ	9	First-mode participation factor
Δ	47	In-plane displacement
ϵ_{c0}	15	Concrete strain at peak stress
ϵ_{cu}	15	Concrete strain at failure
ϵ_c	15	Concrete strain
ϵ_s	16	Steel strain
ϵ_{s0}	16	Steel strain at intersection of initial modulus line and tangent modulus at ultimate
ϵ_s^*	16	Normalized steel strain
θ	47	Average rotation of columns, also known as drift ratio ($=\Delta/L$)
ρ_l	1	Longitudinal reinforcement ratio ($=4A_b/bh$)
σ_c	15	Concrete stress
σ_{s0}	15	Steel stress at intersection of initial modulus line and tangent modulus at ultimate

ABSTRACT

Laughery, Lucas Alan. Ph.D., Purdue University, August 2016. Response of High-Strength Steel Reinforced Concrete Structures to Simulated Earthquakes. Major Professor: Santiago Pujol.

In reinforced concrete (RC) structures expected to resist earthquake demands, substituting smaller amounts of high-strength steel for conventional steel reinforcement can help reduce reinforcement congestion and placement costs while keeping strength unchanged.

Provided cross-sectional dimensions remain unchanged, reducing the amount of longitudinal steel in a member will result in a member with similar initial stiffness but lower post-cracking stiffness. Nominal strength can be kept nearly the same if this reduction in the amount of steel is accompanied by a corresponding increase in the strength of the steel. The topic of this investigation is whether two frames with the same initial stiffness and nominal strength, but different post-cracking stiffnesses, reach comparable peak drift during a given ground motion. This is a question about drift demand, not drift capacity. The impact of changes in steel strength on drift capacity has been examined by others and is not the subject of this study.

Four nominally identical reinforced concrete frames were tested on a unidirectional earthquake simulator. In two frames, conventional reinforcing steel was used in the columns at a reinforcement ratio of 1.8%. In the other two frames, high-strength reinforcing steel was used in the columns at a reinforcement ratio of 0.8%. Each frame was subjected to one of two series (or sequences) of five ground motions. The first four motions were of either increasing intensity (series 1) or decreasing intensity (series 2). The last motion was the strongest used in this study, and had a peak ground acceleration of 1 g, a peak ground velocity of 11 in./sec, and a peak ground displacement of 1.3 in.

Comparisons of frames with different post-cracking stiffness, and comparisons of similar frames subjected to different ground motion sequences supported the hypothesis that the dominant factor driving peak drift is initial period calculated using gross cross-sectional properties. To examine further the idea that initial period drives peak drift in RC structures subjected to earthquake demands, a dataset was compiled using results from more than 160 dynamic tests of RC structures and the measured responses of 3 instrumented RC buildings. This dataset was used to evaluate an expression proposed by Sozen (2003) indicating that peak drift is directly proportional to the product of peak ground velocity and initial period (calculated from gross cross-sectional properties). Comparisons of measured-to-estimated peak drift revealed that, for ground motions with $PGV/PGA > 0.03$ sec, the studied expression produced reasonable and safe estimates of peak drift. Ground motions outside this range have been used in laboratory tests but are unlikely to occur frequently in the field.

All the evidence examined suggest that peak drift caused by earthquake demands is proportional to initial period. It follows that replacing conventional steel reinforcing bars with fewer or smaller bars of higher strength is unlikely to result in consistent increases in drift demand, provided the cross-sectional dimensions remain unchanged.

CHAPTER 1. INTRODUCTION

Seismic design provisions for structural concrete in the United States limit the nominal yield stress (f_y) of longitudinal reinforcement to 60,000 psi [ACI 318 (2014)]. This limitation can lead to steel congestion in members where high longitudinal reinforcement ratios are required to resist earthquake demands (Figure 1-1). Congestion complicates construction, increases labor, and can lead to poor concrete consolidation and honeycombing (Figure 1-2). There are two apparent solutions to the problem of steel congestion in a structural concrete member: (1) increase the member dimensions to accommodate the steel, or (2) decrease the longitudinal reinforcement ratio (ρ_l) of the member. The former solution has the added advantage of increasing the gross stiffness of the member, but is often disagreeable to building owners and architects, who seek to maximize floor area. To achieve the same nominal member strength, the latter solution can only be accomplished within the same cross section with a corresponding increase in steel yield stress (f_y). Because of the limitation on f_y set by ACI 318 (2014), this is not currently permitted in the United States. Before high-strength longitudinal steel ($f_y \geq 80,000$ psi) can be used safely in seismic regions, the behavior of members reinforced using it must be studied and understood. Note that the term high-strength steel reinforced concrete (HSSRC) as it is used here refers to reinforced concrete in which the longitudinal steel is high-strength. The use of high-strength steel as transverse reinforcement is already permitted in seismic regions (up to $f_y = 100,000$ psi) and is not the focus of the present investigation.

When designing a structure, there are two aspects to consider: capacity and demand. Much work has been done to understand the capacity of HSSRC members. This work is described in Chapter 2. By comparison, relatively little research has been conducted to understand demand on HSSRC

structures during strong ground motions. The work that has been done to understand demand on HSSRC structures has been limited to numerical investigations such as Rautenberg (2011). To date (and the author's knowledge), no dynamic test has been conducted on a HSSRC structure. The purpose of this investigation is to make up for the lack of data from dynamic tests.

When a reinforced concrete member is subjected to a lateral demand, its response can be separated into three regions: (1) pre-cracking, (2) post-cracking / pre-yielding, and (3) post-yielding. In region 1, the flexural stiffness of a member is governed by two properties: the modulus of elasticity of the concrete (E_c) and the gross moment of inertia of the cross section (I_g).¹ In region 2, the flexural stiffness of a member is driven by the cracked moment of inertia, which is dominated by the longitudinal reinforcement ratio (ρ_l), and the depths to layers of reinforcement (d). That is:

$$k_1 \propto E_c I_g \quad \text{Equation 1-1}$$

$$k_2 \propto d \rho_l \quad \text{Equation 1-2}$$

where k_1 is flexural stiffness in the pre-cracking range of response (i.e. initial flexural stiffness), and k_2 is the flexural stiffness in the post-cracking/pre-yielding range of response. From Equation 1-1, it is clear that two members with the same concrete and cross-sectional dimensions will have the same initial flexural stiffness. From Equation 1-2, it is clear that if one of the cross sections has less reinforcing steel, it will have less post-cracking flexural stiffness. This would be the case if high-strength steel was substituted in reduced amounts for conventional steel. There are concerns that, during an earthquake, such a reduction in post-cracking flexural stiffness could lead to more drift demand in HSSRC frames when compared with equivalent conventionally-reinforced frames. Dynamic tests of HSSRC frames are needed to examine this possibility.

¹ Transformed moment of inertia (I_t) may be used, but I_g provides comparable values for lightly-reinforced sections without requiring knowledge of reinforcing details.

The objective of this investigation was to test whether two nominally-identical reinforced concrete frames with comparable design strengths and comparable initial stiffnesses, but different post-cracking stiffnesses will reach similar peak drift during a given ground motion. This was accomplished by testing four reinforced concrete frames with equal dimensions but different column longitudinal reinforcement – two containing Grade 60 reinforcing bars, and two containing smaller bars with higher strength – on an earthquake simulator.

In Chapter 2, findings are presented from past dynamic tests of conventional reinforced concrete, static tests of HSSRC, and numerical investigations of HSSRC. In Chapter 3, the hypothesis underlying this investigation is presented and the experimental program is described. This includes details of the test specimens, test setup, ground motions, and test procedure. In Chapter 4, observations from the experiments are presented. These include consistency of the ground motions, response of the specimens, and derived force-drift envelopes. In Chapter 5, differences in the response of the specimens are discussed. In Chapter 6, an expression for estimating peak drift is evaluated using a dataset of laboratory experiments and the response of buildings to earthquakes. In Chapter 7, conclusions are presented.

CHAPTER 2. LITERATURE REVIEW

This chapter is divided into three parts: (1) static tests of high-strength steel reinforced concrete (HSSRC) structural members, (2) dynamic tests of conventional reinforced concrete (CRC) structures, and (3) numerical investigations. Research presented in the first section examines the capacity of HSSRC members and their behavior under static demands. The dynamic tests of CRC presented in the second section provide a frame of reference for the possible behavior of HSSRC in a dynamic environment. The numerical investigations presented in the third section supplement these dynamic tests and provide a basis for the hypothesis presented in Chapter 3.

2.1. Static Tests

For more than 50 years, lateral monotonic and cyclic experiments have been conducted on HSSRC members. An overview of investigations and major findings is presented in Table 2-1. The focuses of these investigations have varied. Some were: (1) flexural crack control, (2) flexural behavior, (3) shear behavior, (4) response to displacement reversals, (5) the effect of variable axial load, and so forth. Overall, the tests show that, given proper detailing, members reinforced with high-strength steel possess adequate toughness to maintain their strengths during cycles at drift ratios up to 4%. For non-masonry structures four stories or lower, the American Society of Civil Engineers' "Minimum Design Loads for Buildings and Other Structures" [ASCE 7 (2010)] limits story drift ratio to 2.5% or less for the lowest risk category, and to 2% or less for higher risk categories. For structures more than four stories tall, these limits are reduced to 2% and 1.5% [ASCE 7 (2010)]. Based on these limits, the ability of well-detailed HSSRC members to maintain their strengths at drift ratios up to 4% is sufficient from a design standpoint.

Another observation from past cyclic tests of HSSRC members pertains to the shape of their hysteresis loops. The unloading slope of HSSRC members is consistently lower than that of equivalent CRC members. This is illustrated in Figure 2-1, which was generated using test data from Rautenberg (2011). The black line is from a test of a CRC column; the gray line is from a test of a HSSRC column. When the two columns were unloaded from comparable drifts, the HSSRC column unloading curve was less steep, leading to a “pinched” appearance and less area within the hysteresis loops.

2.2. Dynamic Tests

To date, there are no publications describing dynamic tests of HSSRC structures. Nevertheless, for more than 40 years dynamic tests have been conducted on CRC specimens. A summary of these tests and major findings is presented in Table 2-2. Two of particular interest to the current investigation are discussed in detail in the following sections.

2.2.1. Otani and Sozen (1972)

In 1972, Otani and Sozen published findings from dynamic tests of three pairs of 3-story 1-bay frames. A typical frame is illustrated in Figure 2-2. All frames had the same nominal dimensions and the same longitudinal steel reinforcement. In each test series, two identical frames were oriented parallel to one another and connected by a mass at each level. Each pair of frames was then subjected to a series of ground motions of increasing demand. The demand of each ground motion was measured using spectrum intensity at 20% critical damping (SI_{20}).

Spectrum intensity was calculated as the area under the velocity response spectrum for periods ranging from 0.1 sec to 2.5 sec:

$$SI_{\beta} = \int_{0.1}^{2.5} S_v(\beta, T) dT \quad \text{Equation 2-1}$$

where S_v is the velocity response spectrum, β is the damping ratio as a percent of critical damping (20% in this case), and T is the period of a linear elastic oscillator. This velocity response spectrum was calculated using the measured acceleration of the simulator platform for each test. The ground motions were adapted from records obtained during the El Centro (1940) and Taft (1952) earthquakes.

In Series 1, a pair of frames was subjected to six ground motions of increasing demand. In Series 2, a different pair of identical frames was subjected to four ground motions of increasing demand. The ground motion used in the fourth test in Series 1 was identical to that of the first test in Series 2. The two ground motions registered nearly the same peak accelerations (0.88 g and 0.86 g, respectively) and had comparable spectrum intensities ($SI_{20} = 15.7$ and 15.8, respectively). Before this “common ground motion” (i.e. ground motion of equal spectrum intensity), Series 1 frames had sustained damage from three ground motions. In contrast, Series 2 frames were expected to be pristine. Having sustained damage during previous tests, Series 1 frames were softer than Series 2 frames before the “common ground motion.” In spite of this softening, frames in Series 1 and 2 reached nearly the same average peak roof drifts (1.06 in. for Series 1 compared with 1.08 in. for Series 2, corresponding to a drift ratio of approximately 2%). This suggests that softening of the frames in Series 1 as a result of damage from previous motions did not impact peak drift response. Stated differently, provided that the ground motion was the strongest the frames had experienced, softening as a result of damage from previous events did not affect peak drift response.

2.2.2. Cecen (1979)

In 1979 Cecen tested scaled, 10-story 3-bay reinforced concrete frames on an earthquake simulator. A typical frame is illustrated in Figure 2-3. Similar to what Otani had done, two identical frames were tested in parallel, connected at each story by a mass. Each pair of frames was subjected to a

series of scaled strong ground motions adapted from records obtained during the El Centro (1940) earthquake.

Frames in Series 1 were subjected to three ground motions of increasing demand. Frames in Series 2 were subjected to seven ground motions of increasing demand. The final ground motion in each test series was the same. Normalized by the spectrum intensity of this shared final ground motion, the relative intensities of ground motions in Series 1 were 32%, 70% and 100%. In Series 2, these relative intensities were 13%, 26%, 40%, 40%, 60%, 80%, and 100%. This means that, before the final ground motion, Series 2 frames had experienced three times as many ground motions as Series 1 frames. Series 2 frames had also experienced stronger ground motions, and more displacement cycles at larger drift ratios. Nevertheless, the two systems reached comparable peak roof drifts (3.39 in. for Series 1 versus 3.43 in. for Series 2, corresponding to a drift ratio of approximately 3.8%). This was consistent with previous observations by Otani and Sozen (1972).

2.2.3. Application to HSSRC Frames

The findings from dynamic tests of CRC can be extended to HSSRC. In both Otani's and Cecen's tests, the damaged frames had the same gross stiffness and design strength as the "pristine" frames (in the case of Cecen, the less damaged frames). This would also be the case if high-strength steel was substituted in reduced amounts for conventional steel, provided that the cross-sectional dimensions and reinforcement depths were maintained. In both Otani's and Cecen's tests, the damaged frames had lower stiffness than the "pristine" (less damaged) frames. That is, one pair of frames was softer than the other pair of frames before the common ground motion. This would also be the case if high-strength steel was substituted in reduced portions for conventional steel: the HSSRC structure would be expected to be softer after cracking, as ρ_l dominates post-cracking flexural stiffness. Stated differently, the reduction in stiffness associated with using less reinforcing steel can be thought of as similar to the reduction in stiffness associated with damage.

In Otani's and Cecen's tests, the two pairs of frames (damaged and pristine / less damaged) reached comparable peak drift during the same ground motion. Following the same line of thinking, CRC and HSSRC frames could be expected to reach comparable peak drifts, provided the same conditions are met:

- (1) The ground motion to which the frames are subjected is the strongest the frames have experienced
- (2) The frames have the same masses and member dimensions [i.e. gross stiffnesses are equal]
- (3) The frames have the same nominal strengths [i.e. $(\rho f_y d)_{CRC} = (\rho f_y d)_{HSSRC}$]

Condition 1 is simply a restriction based on what has been observed: no experiments have been conducted in which a pristine frame is subjected to progressively weaker ground motions. Condition 2 is also a restriction based on what has been observed. It ensures that the frames will have the same initial period. Condition 3 ensures that both frames will have adequate strength to endure the ground motions without failure.

The tests described above point to initial period as the dominant factor driving the peak drift response of RC frames. This idea is examined in the next section.

2.3. Numerical Investigations

In 1997, Lepage compiled results from tests of 33 small-scale, multistory RC structures subjected to simulated earthquakes. Using these results, he proposed the following expression for estimating peak roof drift in a reinforced concrete structure:

$$S_{da} = \frac{F_a * PGA * g * T_g}{(2\pi)^2} * T_{eff} * \Gamma \quad \text{Equation 2-2}$$

where S_{da} = peak roof drift estimated using ground acceleration (D_{max} in original formulation)

F_a = acceleration amplification factor (S_a/PGA , where S_a is spectral acceleration)

PGA = peak ground acceleration (α in original formulation)

g = gravitational acceleration

T_g = characteristic period of ground motion

T_{eff} = effective initial period of vibration of the system (T in original formulation), taken as $\sqrt{2}$ times the first mode period based on uncracked sections, T_i

Γ = participation factor for the first mode shape

[may be taken as 5/4 for multi-degree-of freedom (MDOF) structures with uniform story heights and stiffnesses]

This expression was reported to provide a reasonable upper bound estimate of peak roof drift for structures with base shear coefficients meeting a minimum threshold.

Later, the following expression was proposed by Sozen (2003) as an estimate of peak roof drift:

$$S_{dv} = \frac{PGV}{\sqrt{2}} * T_i * \Gamma \quad \text{Equation 2-3}$$

where S_{dv} is peak roof drift estimated using ground velocity, PGV is peak ground velocity, T_i is first mode period based on uncracked sections, and Γ is first mode participation factor. Both equations share one common feature: initial period as the characteristic describing the structure. Because HSSRC frames have comparable initial stiffness to CRC frames with the same nominal dimensions, this implies that the two frames should experience comparable peak drift during a given ground motion. This idea has since been investigated via numerical simulations.

In 2011, Rautenberg conducted simulations of CRC and HSSRC frames. He modeled the frames using LARZ, a nonlinear reinforced concrete analysis program developed by Saiidi and Sozen (1979). Two types of 3-, 6-, 12-, and 20-story buildings were modeled. In one type, columns were

reinforced using conventional (Grade 60) steel. In the other type, columns were reinforced using a reduced amount of high-strength (Grade 120) steel. The nominal dimensions and masses of the models were otherwise the same. Differences in the flexural behavior of the two column types were captured by altering moment-curvature diagrams and unloading stiffness coefficients. The reduced post-cracking stiffness of HSSRC columns was captured by increasing yield curvature (Figure 2-4). The “pinched” appearance of HSSRC column hysteresis loops was captured by using a larger unloading stiffness coefficient (0.5 for Grade 120 models versus 0.4 for Grade 60 models).

Each building model was subjected to a suite of ground motions, with its peak roof drift recorded for each. In Figure 2-5, the peak roof drift of HSSRC frames is plotted against that of CRC frames. For all simulations, the average ratio of peak roof drift in HSSRC frames to peak roof drift in CRC frames was 1.03. Because the common characteristic of the frames was their initial stiffness, this finding supports the idea that initial stiffness (and initial period) – not post-cracking stiffness – drives the peak drift response of RC frames.

The purpose of the present investigation was to test experimentally this idea: that initial stiffness drives the peak drift response of RC frames.

CHAPTER 3. EXPERIMENTAL DESIGN AND PROGRAM

3.1. Scope of Work

The experimental program described in this chapter was conducted to test the following hypothesis:

Two reinforced concrete frames with columns having similar nominal design strengths and initial stiffnesses, but different post-cracking stiffnesses, reach the same peak drift response during the same strong ground motion, provided this motion is the strongest each frame has experienced.

A single-degree-of-freedom (SDOF) system subject to unidirectional motion at its base was used to test this hypothesis. The system was not a prototype of any full-scale structure. Instead, it was designed and proportioned to test an idea.

The system comprised a reinforced concrete portal frame with a lumped mass at the top. Two different types of frames were built, the only difference being column longitudinal reinforcement. In type C frames, columns contained conventional steel. In type H frames, columns contained a reduced amount of high-strength steel. High-strength steel provided a convenient method for testing the stated hypothesis because two frames having nearly equal nominal strengths and initial stiffnesses but different post-cracking stiffnesses could be built by keeping member dimensions identical while varying the grade and size of reinforcing bars.

The specimens were tested one at a time on the earthquake simulator. Each frame was subjected to five simulated earthquakes, the strongest of which had a peak ground acceleration of 1 g, a peak ground velocity of 11 in./sec, and a peak ground displacement of 1.3 in. In Series 1, frames C1 and

H1 were subjected to four ground motions of increasing demand (25%, 50%, 75%, and 100% of the strongest ground motion considered in this study), followed by a repeat of the strongest ground motion (100%). In Series 2, frames C2 and H2 were subjected to four ground motions of decreasing demand (100%, 75%, 50%, and 25%), followed by a repeat of the strongest ground motion (100%). Varying the order of testing ensured that frames in one series had always experienced more or stronger ground motions than the frames in the other series. For example, Series 1 frames were undamaged before the 25% motion, having experienced no earthquakes. In contrast, Series 2 frames had experienced 3 stronger motions and were damaged as a result. For another example, before the first 100% motion, Series 1 frames were damaged (having experienced 3 weaker motions previously), whereas Series 2 frames were undamaged.

Having experienced more demanding ground motions, the frames in one series were expected to be more damaged (and softer) than frames in the other series before the same ground motion. This allowed the hypothesis that initial stiffness drives peak drift to be evaluated not just by comparing the response of type H frames with that of type C frames, but also by comparing the response of Series 2 frames with that of Series 1 frames of the same type. The response of the same frame to subsequent 100% ground motions provided a third point of comparison. These comparisons are similar to those described in Section 2.2.

Details of the specimens, setup, ground motions, and test procedure are described in the following sections. Additional details can be found in the Appendices.

3.2. Test Specimens

Four specimens were built and tested. The specimens were portal frames with an out-of-plane thickness of 5-in. The lower and upper beams of the frames had depths of 12 in. and 10 in. Each

frame had two square columns with clear heights of $L = 42$ in. and cross sections measuring 5 in. by 5 in. (Figure 3-1). Attributes of the frames and test program are summarized in Table 3-1.

The frames were nominally identical except for column longitudinal reinforcement, of which there were two configurations (illustrated in Figure 3-2). In both configurations, the depths to longitudinal reinforcement layers were approximately $d' = 1$ in. and $d = 4$ in. In type C frames, column longitudinal reinforcement consisted of four 3/8-in. diameter, conventional deformed steel bars ($\rho_t = 1.8\%$). Stress-strain curves for these bars are presented in Figure 3-3 alongside a model curve (discussed in Section 3.2.1). These conventional bars had a 0.2% offset yield stress of approximately 65 ksi and a strength of approximately 100 ksi. In type H frames, column longitudinal reinforcement consisted of four approximately 1/4-in. diameter (6.5-mm actual), high-strength undeformed steel rods ($\rho_t = 0.8\%$). Stress versus strain curves for these bars are presented in Figure 3-4 alongside a model curve. This steel had a 0.2% offset yield stress of approximately 160 ksi and a strength of nearly 190 ksi.

For the columns to reach their strengths, longitudinal reinforcement needed to develop its strength along two lengths: [1] in the beams, from the end of the hooked bar to the beam-column interface (22 in.), and [2] in the columns, from the point of inflection near mid-height to the beam-column interface (21 in.). These lengths are illustrated in Figure 3-5. In Type C frames, these lengths corresponded to $58d_b$ and $56d_b$ ($d_b =$ diameter of the longitudinal bar). In type H frames, these lengths corresponded to $88d_b$ and $84d_b$ (because high-strength steel bars had smaller diameter).

In spite of the higher ratio of embedment length to bar diameter in type H frames, there was concern that the smooth high-strength steel rod would slip before reaching its yield stress. For this reason, the high-strength steel rods were corroded to improve bond with the surrounding concrete. This was done by spraying a 10% solution of hydrochloric acid (HCl) on the bars and then storing them

in a moist curing room (i.e. a humidity chamber). After 72 hours, the bars were removed from the room and their surfaces were cleaned to remove excess rust. The resulting bars had a roughened surface.

In addition to corroding their surfaces, the rods were anchored in the beams using assemblies consisting of prestressing anchors and plates. Schematics of these assemblies are shown in Figure 3-6, and a photograph is provided in Figure 3-7. These assemblies were devised after conducting pullout tests on specimens with different bar anchorage details (described in the Appendices). The anchor chucks used in these assemblies were engaged by adjusting nuts on the threaded rods that were placed between the steel plates. These nuts pushed the two plates apart, engaging the anchor chucks.

Transverse reinforcement was the same in all specimens (Figure 3-6). All hoops were built using 3/16-in. diameter smooth steel wire with a yield and ultimate stresses of approximately 74 ksi and 82 ksi, respectively. Beam hoops were rectangular with 135 degree hooks at each end. Column hoops were square with 135 degree hooks at each end. Column hoops were spaced at 1 in. on center over the first 12 in. from the face of each beam ($s = d/4$ for $3d$). In the center 18 in. of the columns, the hoops were spaced at approximately 1-13/16 in. on center (1-5/8 in. clear). Spirals were placed in the beam-column joints to improve confinement.

All specimens were cast on their sides on the same day using a grout mix with a maximum aggregate size of 3/8 in. The mix had an average compressive strength on test days of $f'_c = 3,800$ psi. A grout mix was used instead of concrete with large aggregate for two reasons. The first was to reduce problems with consolidation and honeycombing due to the tight spacing of transverse reinforcement. Second, the elimination of large aggregate was expected to reduce the modulus of elasticity of the concrete. This would in turn reduce the stiffness of the frames, allowing them to be

pushed further into their nonlinear range of response using ground motions that were within the capacity of the earthquake simulator. A summary of material properties measured on test days is presented in Table 3-1. Additional details about the mix and development of compressive strength during curing are available in the Appendices.

3.2.1. Moment-Curvature Relationships of the Columns

Moment-curvature relationships² were generated for each column type using FLECHA, a spreadsheet developed by Pujol (2001). FLECHA idealizes the stress-strain behavior of concrete using Hognestad's formulation (1951). In Hognestad's formulation, the strain at peak compressive stress is defined as:

$$\varepsilon_{c0} = \frac{2f'_c}{E_c} \quad \text{Equation 3-1}$$

where f'_c is the compressive strength of the concrete and E_c is the modulus of elasticity of the concrete. Concrete stress is defined in three regions: (1) tension less than the tensile strength, (2) compression at strains less than ε_{c0} , and (3) compression at strains between ε_{c0} and the ultimate strain, ε_{cu} . For tension defined as negative, the stresses in each of these regions are given as:

$$\sigma_c = \varepsilon_c E_c \quad \text{for} \quad f_t/E_c < \varepsilon_c < 0 \quad \text{Equation 3-2}$$

$$= f'_c \left(\frac{2\varepsilon_c}{\varepsilon_{c0}} - \left(\frac{\varepsilon_c}{\varepsilon_{c0}} \right)^2 \right) \quad \text{for} \quad 0 < \varepsilon_c < \varepsilon_{c0} \quad \text{Equation 3-3}$$

$$= f'_c \left(1 - Z * \left(\frac{\varepsilon_c}{\varepsilon_{c0}} \right) \right) \quad \text{for} \quad \varepsilon_{c0} < \varepsilon_c < \varepsilon_{cu} \quad \text{Equation 3-4}$$

where ε_c = concrete strain

σ_c = concrete stress

f'_c = concrete compressive strength (3,800 psi from measurements)

² Moment-curvature relationship refers to the variation of bending moment with unit curvature.

E_c = concrete modulus of elasticity (2,700 ksi from measurements)

f_t = concrete tensile strength (420 psi from measurements)

$Z = 0.15*(\epsilon_{cu} - \epsilon_{c0})$, where ϵ_{cu} is assumed to be 0.0038 [from Hognestad (1951)]

Using these equations, the stress-strain relationship for the concrete is plotted in Figure 3-8.

Neither type of longitudinal steel exhibited a well-defined yield plateau during coupon tests, so the Menegotto-Pinto (1973) steel model was used for each. The original formulation by Menegotto and Pinto simplifies to the following two expressions:

$$\epsilon_s^* = \left| \frac{\epsilon_s}{\epsilon_{s0}} \right| \quad \text{Equation 3-5}$$

$$\sigma_s = \left(k_s \epsilon_s^* + \frac{(1 - k_s) \epsilon_s^*}{(1 + \epsilon_s^{*R})^{1/R}} \right) \sigma_{s0} \quad \text{Equation 3-6}$$

where ϵ_s = steel strain

σ_s = steel stress

ϵ_s^* = normalized steel strain

ϵ_{s0} = steel strain at intersection of initial modulus line and tangent modulus at ultimate

σ_{s0} = steel stress at intersection of initial modulus line and tangent modulus at ultimate

$k_s = E_{s\infty} / E_s$, ratio of tangent modulus at ultimate to initial modulus

R = parameter defining the shape of the curve

The variables ϵ_{s0} , σ_{s0} , k_s , and R were adjusted until agreement was reached with measured stress-strain curves from coupon tests. Representative stress-strain relationships obtained from this process are shown in Figure 3-9.

Using these material formulations, moment-curvature diagrams were generated using FLECHA. These moment-curvature diagrams are shown in Figure 3-10. There are three features worth noting about these idealized relationships. First, the initial slopes – representing the uncracked flexural

stiffnesses of the cross sections – are approximately equal. This is expected because both sections have nearly the same gross moment of inertia (I_g) and modulus of elasticity of concrete (E_c). The second notable feature is that, after cracking at approximately 11 kip-in., the tangential slope of type H columns is smaller than that of type C columns. That is, type H columns have lower post-cracking flexural stiffness. This is also expected because type H columns have a lower longitudinal reinforcement ratio than type C columns. The third notable feature in Figure 3-10 is that the two column types have comparable nominal strengths (within 10% of each other), because the product $\rho_f f_y d$ is comparable.

3.2.2. Trilinear Approximations

Trilinear approximations were made for the moment-curvature diagram for use later in numerical models. These approximations required three bending moments to be estimated: (1) at cracking, (2) at yielding (along with the corresponding curvature), and (3) at ultimate (along with the corresponding curvature). The cracking moment of each column M_{cr} can be estimated as:

$$M_{cr} = \frac{f_r b h^2}{6} \quad \text{Equation 3-7}$$

where f_r is the modulus of rupture of the concrete, b is the width of the column, and h is the total depth of the column. The concrete had a very high modulus of rupture ($850 \text{ psi} \approx 14\sqrt{f'_c}$). As a result the estimated cracking moment was high (17.7 kip-in.) relative to the point at which cracking occurred in the FLECHA idealization (11 kip-in.). This is because cracking in FLECHA is based on the tensile strength of the concrete ($f_t = 420 \text{ psi}$). For consistency with FLECHA, a cracking moment of 11 kip-in. was assumed instead of the moment calculated from f_r .

The ultimate curvature was taken as the curvature corresponding to the maximum bending moment (which occurred at a concrete strain of 0.004). The bending moment at yield was taken as 95% of this maximum bending moment. The curvature at yield was more difficult to define because neither

steel exhibited a well-defined yield plateau. Values of yield curvature were adjusted until visual agreement was reached with the moment-curvature diagram from FLECHA. The curvatures and bending moments for this idealized trilinear approximation are summarized in Table 3-2.

3.2.3. Expected Behavior of Frames

Frames resist lateral demand through flexure in their columns and beams. In the case of a portal frame in its elastic range of response, an idealized bending moment diagram for this is shown in Figure 3-11(a). In this idealization, moment (and curvature) in the columns varies with height from maxima at column-beam interfaces to zero near mid-height. Similarly, moment (and curvature) in the beam varies from maxima at the column-beam interface to zero near midspan. As the frame displaces sideways, moments at critical sections increase until the plastic moment of each section is reached, M_p (i.e. the point at which an increase in curvature produces no corresponding increase in resistance). Curvature concentrates near the ends of members in regions called “plastic hinges” [Figure 3-11(b)]. It is desirable for these hinges to form in beams rather than columns to prevent the formation of story mechanisms that can lead to collapse in buildings. To accomplish this, in modern reinforced concrete frames engineers design columns framing into a joint to have more nominal flexural strength than beams. This is commonly referred to as “strong column weak beam” design.

The frames tested in this investigation did not follow the “strong column weak beam” design. Instead, the columns were weaker than the beams so that the dynamic behavior of the system would be driven by the columns. Consequently, this “weak column strong beam” design meant that hinges were expected to form at the tops and bottoms of the columns.

Assuming hinges formed at the top and bottom of both columns, the lateral strength of the frames can be estimated as:

$$F_p = \frac{4M_p}{L} \quad \text{Equation 3-8}$$

where F_p is lateral strength (i.e. base shear strength), M_p is the plastic moment of the columns, and L is the length (clear height) of the columns (42 in.). For the frames in this investigation, M_p was approximately 65 kip-in. This resulted in an expected base shear strength of approximately 6.2 kip.

3.2.4. Dynamic Properties of the Frames

Each specimen had a lumped mass fastened to its upper beam before testing. The weight of this mass, the hardware needed to secure it to the specimen (shown in Figure 3-12), and the upper beam of the specimen was approximately 4,860 lb. According to Biggs (1964), to idealize this system as a single-degree-of-freedom, two-thirds of the self-weight of the columns ($2/3W_c$) should also be added to this lumped mass (W_{ml}) to determine an effective mass (W_{me}):

$$W_{me} = W_{ml} + 2/3W_c \quad \text{Equation 3-9}$$

This results in an effective mass with a weight of approximately 5,000 lb. A detailed account of components contributing to this mass is shown in Table 3-3. Several estimates of the period of the test frames can be obtained using this effective mass and different estimates of flexural stiffness (EI) calculated using different line segments on the moment-curvature diagram. Three of particular interest in this investigation are:

- (1) Initial period, T_i : defined using the gross cross-sectional moment of inertia ($E_c I_g$)
- (2) Secant period, T_s : defined using EI as the slope from the origin to the point at yield [$(EI)_s$]
- (3) Post-cracking period, T_{cr} : defined using EI as the slope from the point at cracking to the point at yield [$(EI)_{cr}$]

These stiffnesses are illustrated in Figure 3-10 and are listed in Table 3-2. Lateral flexural stiffness, k , was estimated using the following expression for a frame with 2 columns fixed at each end:

$$k = 2 * \frac{12EI}{L^3} \quad \text{Equation 3-10}$$

where k = lateral flexural stiffness

EI = flexural stiffness defined using one of three segments described before

L = clear length of the columns (i.e. height, 42 in.)

This estimate of lateral stiffness assumes fixed end conditions and double curvature in the columns. In reality, perfect fixed end conditions are not possible and the actual stiffness can be expected lower than the stiffness estimated from Equation 3-10. Reasons for the lower actual stiffness are discussed in more detail in Section 5.1. Because quantifying this reduction in stiffness is difficult, from the design viewpoint it is simpler to assume fixed-end conditions.

The periods of the frames were estimated as:

$$T = 2\pi \sqrt{\frac{W_{me}}{gk}} \quad \text{Equation 3-11}$$

where g = gravitational acceleration (386 in./sec²), W_{me} is effective mass, and k is stiffness defined using one of the aforementioned methods. The initial period obtained from Equation 3-10 and Equation 3-11 is approximately 0.1 sec. The secant periods of the frames were estimated to be approximately 0.19 sec (type C) and 0.23 sec (type H). The estimated post-cracking periods of the frames were comparable to secant periods. These and other properties of each specimen type are summarized in Table 3-2.

In Section 3.2.3, the base shear strength of the frames was estimated to be approximately $F_p = 6.2$ kips. For an effective mass of 5 kips, the base shear strength coefficient was 1.2 (6.2 kips / 5 kips).

This value is much larger than typical base shear coefficients for reinforced concrete special moment frame buildings, which are permitted to be designed for base shears of $1/8$ (special moment frame) and $1/5$ (intermediate moment frame) of the shear force from a linear analysis [ASCE 7 (2010)]. Because the goal of the experiments was to test an idea – not to represent a prototype of an actual structure – this large base shear coefficient was deemed acceptable.

3.2.5. Numerical Models

Models of both frame types were created using LARZ, a nonlinear analysis program for reinforced concrete structures. LARZ was developed by Saiidi and Sozen (1979), and has since been updated [Lopez and Sozen (1988)]. In past investigations, it has been found to have good agreement with experimental results [Saiidi and Sozen (1979); Lepage (1997)]. A concise list of simplifying assumptions used in LARZ was compiled by Rautenberg (2011).

Each frame was modeled using the simplified trilinear moment curvature relationship shown in Figure 3-10. Zero slip was assumed. If slip had been assumed, the effect would have been to shift the moment-curvature relationship to the right (i.e. larger curvature for a given moment), resulting in lower flexural stiffnesses for both systems. Leaving slip out of the LARZ models allowed the force-drift relationships of frames to be compared against an “ideal” force-drift relationship.

The frames were modeled as single-degree-of-freedom systems, with massless columns and a concentrated 5-kip mass at the top of the top beam. The modulus of elasticity of the concrete was assumed to be 2,700 ksi based on measurements obtained during the test program (summarized in Table 3-1).

The model geometry is shown in Figure 3-13. For simplicity, the bottom beam was not modeled. Instead, it was assumed that the columns were fixed at their bases. The columns were modeled as 47 in. tall, with a rigid length of 5 in. at the top (clear height = 47 in. – 5 in. = 42 in.), where they

intersected with the lower half of the top beam (depth = 10 in.). The top beam was modeled as 37 in. long, with rigid lengths of 2.5 in. at each end where it intersected with half of each column (5 in. /2).

LARZ was used to create reference force-drift curves. Lateral force versus displacement curves for both frame types are shown in Figure 3-14. Like moment-curvature diagrams, these show the test specimens with similar initial stiffnesses and similar nominal strengths, but type H frames having lower post-cracking stiffness.

3.3. Test Setup

The frames were tested on the unidirectional earthquake simulator at Bowen Laboratory for Large-Scale Civil Engineering Research. The simulator has operating limits of ± 2 in. stroke, 2 g acceleration, and 12 in./sec velocity. Its platform measures 12 ft by 12 ft and has a grid of 1/2 in. threaded holes at 12 in. on center in both directions for fastening components. Additional details of the simulator as it was constructed are available in Sozen et al. (1969).

A schematic of the test setup is shown in Figure 3-15. The earthquake simulator is oriented in Bowen Laboratory such that motion is in the north-south direction (left-to-right in this figure). Each specimen was placed at the center of the platform in the east-west direction, and 6 in. north of center in the north-south direction. South of each specimen, an instrumentation truss was installed. On the east and west sides, steel posts were installed with arms and slide bearings to limit out-of-plane movement during testing. The following sections describe these components of the test setup. More details can be found in the Appendices.

3.3.1. Specimen and Mass

The specimens were tested one at a time. Each specimen was positioned such that its plane was concentric with the axis of the hydraulic actuator driving the table. A thin layer of Hydrostone® gypsum cement was placed between the simulator platform and the lower beam of the frame to level the specimen and provide a uniform contact surface. Likewise, thin layers of Hydrostone® were used elsewhere on the setup on contact surfaces where components were fastened to the specimen.

Each specimen was fastened to the platform using 21 steel threaded rods (Figure 3-12). Seven threaded rods went through the lower beam of the specimen and into threaded openings in the platform. These rods passed through steel angles that reacted against the top of the lower beam, transverse to the direction of motion (Figure 3-12 south elevation). These angles allowed two outer rows of threaded openings to be used to fasten the specimen to the platform. Steel pipes were placed beneath the angles on these outer rows. Each threaded rod on these outer rows passed through the angle and pipe. Nuts were tightened on each rod until contact was made between the angles and pipes (typically 5/6 of a turn). This created an outrigger system that provided resistance against out-of-plane movement. Two steel L8x8x7/8 angles were used to provide additional resistance to out-of-plane movement. These angles were positioned parallel to the direction of motion on the east and west sides of the lower beam (Figure 3-12). The angles were clamped to the sides of the lower beam using threaded rods. A reusable reinforced concrete mass was used in all tests. This mass straddled the top beam of the specimen (Figure 3-12). The mass was fastened to this beam using steel threaded rods and plates.

3.3.2. Out-of-plane Bracing

A system was devised to limit out-of-plane movement of each specimen during testing. This system comprised two W14x99 posts fastened to the simulator platform, one on each side of the specimen.

These posts were oriented with their strong axis in the direction of motion. Each post had two steel channels extending towards the added mass at the level of its center of gravity. At the end of these channels, steel angles with PTFE (Polytetrafluoroethylene, similar to Teflon®) slide bearings were installed. These slide bearings bore against stainless steel plates attached to the sides of the added mass. Before testing, the assembly was adjusted to provide a 1/8-in. gap between the bearings and the stainless steel plates.

3.3.3. Instrumentation

An instrumentation plan is shown in Figure 3-16. The specimens were instrumented with linear variable differential transformers (LVDTs), accelerometers, and optical tracking targets. Accelerometers and LVDTs were sampled at a rate of 1,000 Hz. Optical targets were sampled at a rate of 50 Hz by a separate system from accelerometers and LVDTs.

Four accelerometers were installed: two on the simulator platform (northwest and south of the specimen), one on top of the lower beam of the specimen, and one on top of the mass above the north column. Ten LVDTs were installed. One LVDT was connected to the north face of the lower beam of the specimen to measure whether there was slip of the base of the specimen. The remaining nine were installed along the height of the specimen on its south side. Seven of these nine LVDTs were connected along the height of the south column, starting at a height of 3 in. above the top surface of the base beam and spaced at 6 in. thereafter. The remaining two LVDTs were used to measure the top displacement of the specimen. One was connected to the south face of the top beam; the other was connected to the south face of the mass.

Sixty-four Optotrak optical tracking targets were placed on the west face of the test setup [Northern Digital (2011)]. Fifty-six of these were installed on the column faces as shown in Figure 3-16. Two were installed on the mass to measure the top displacement of the specimen, as well as out-of-plane

and vertical movement. The remaining six were installed on the simulator platform, instrumentation truss, and one bracing post. The main optical tracker unit was positioned approximately 13 ft west of the simulator platform.

Videos were recorded by cameras positioned at two different positions (Figure 3-17). One camera was setup above the optical tracker to the west of the earthquake simulator. Another camera was setup northwest of the simulator platform. The second camera had in its field of view a LED that was strobed by the main data acquisition system during the test.

3.4. Ground Motion Profiles

All motions were adapted from the east-west component of the ground motion measured at the Sun Valley – Roscoe Boulevard station during the 1994 Northridge earthquake. The record was selected after running dozens of different scaled ground motions on the earthquake simulator with different added masses. Criteria for choosing this record are described in the Appendices.

The record was scaled by dividing the original time step (0.01 sec) by 3 and by multiplying the accelerations by 3.9. Adjustments were then made to the frequency content of the record to smoothen the displacement response spectrum in the constant velocity region of Newmark's idealized trilinear spectrum [Newmark (1973)]. This was to reduce peaks and valleys and make the linear response spectrum fit an idealized spectrum more closely [Figure 3-18(a)].

The modification process consisted of transforming the record into the Fourier domain and adjusting the amplitudes at periods where peaks and valleys were observed. At periods around peaks, Fourier amplitudes were reduced by multiplying by a factor $A_F < 1$ [Figure 3-18(b)]. Around valleys, Fourier amplitudes were multiplied by a factor $A_F > 1$. Everywhere else, Fourier amplitudes were multiplied by a factor $A_F = 1$. This process is described in detail in the Appendices. The

resulting linear displacement response spectrum from this modified acceleration record had peaks and valleys that were less prominent, lower response in the high frequency range (Figure 3-19), and an acceleration history that was similar to the unmodified history (Figure 3-20).

The modified ground acceleration record was numerically integrated twice (using trapezoidal rule) to obtain a displacement profile with which to control the earthquake simulator. This displacement profile, representing the strongest motion that could be reproduced within the limits of the simulator, is referred to as the “100%” ground motion. It had a peak acceleration of 1 g, a peak velocity of 11 in./sec, and a peak displacement of 1.3 in. Plots showing the acceleration, velocity, and displacement histories for this “100%” motion are shown in Figure 3-21. Weaker motions were obtained by multiplying the amplitude of this “100%” displacement profile by a factor less than one (i.e. the 25% motion was obtained by multiplying by 0.25, etc.). These displacement profiles, which were used to define a program to control the simulator, are referred to hereafter as the “ideal” profiles.

3.5. Control of Earthquake Simulator

The earthquake simulator was operated using a MTS FlexTest™ FT60 digital controller. This controller provided two channels of data. One channel reported the command displacement to the actuator; the other channel reported the feedback displacement. Both channels were sampled by the main data acquisition system at a rate of 1,000 Hz.

3.6. Test Procedure

Specimens were subjected to horizontal base motion parallel to their planes. Two series of tests were conducted (summarized at the bottom of Table 3-1). In Series 1, specimens were each subjected to four ground motions of increasing relative amplitude (i.e. 25%, 50%, 75%, 100%),

followed by a final motion at 100%. In Series 2, specimens were subjected to four ground motions of decreasing relative amplitude (100%, 75%, 50%, 25%), followed by a final motion at 100%. These sequences were selected to measure the effect of softening on the peak drift response of the frames. Table 3-4 summarizes the ideal motion characteristics of these four scaled ground motions (i.e. peak acceleration, peak velocity, and peak displacement). Linear response spectra for the motions are presented in Figure 3-22 through Figure 3-24 (for 2% critical damping). In Figure 3-24, the y-axis shows both spectral drift (S_d) in inches and spectral drift ratio (S_d/L , where $L = 42$ in.) in percent. For the strongest ground motion, the expected drift ratio of a linear oscillator with a period between 0.1 and 0.2 sec was between 0.7% and 3%.

The test protocol is summarized in Table 3-5. Before the first test, free vibration tests were conducted to determine the initial period of each frame. During these tests, the frame was struck multiple times by a 4-lb dead-blow hammer at the top beam parallel to the axis of motion of the ground motion tests. This process was repeated five times. The actuator driving the earthquake simulator was then pressurized, first to low pressure and then to high pressure. This pressurization caused the platform to jolt. This jolt provided another free vibration test with which to measure period. The frame was then subjected to a single ground motion. After this, the simulator was depressurized and another hammer test was conducted to determine the final period of the frame. This hammer test was taken as the measure of the starting period for the following test. The results from these free vibration tests are presented in Section 4.3. After each test, the frame was inspected for cracks. Cracks were marked, mapped, photographed, and measured using a crack-width gauge. These damage maps are presented in Section 4.6.

CHAPTER 4. OBSERVED RESPONSE

Each test was designated using a combination of letters and numbers. The first letter and number indicate the frame type (either C or H) and Series (either 1 or 2). The second number, separated by a hyphen from the first, denotes the relative amplitude of the ground motion. For example, C1-50 was the test of frame C1 at 50% of the maximum ground motion, and H2-100 was the test of frame H2 at 100% of the maximum ground motion. For the second test in a series at 100% of the maximum motion, the number 2 was appended to the end in parenthesis. For example, H2-100(2) denotes the second time frame H2 was subjected to the motion at 100%.

4.1. Data Processing

Different methods were used to process measurements from the main data acquisition system and Optotrak. These processing methods are described in the following sections.

4.1.1. Main Data Acquisition System

After applying zero offsets and calibration constants to the raw data, all records were smoothed using an unweighted 5-point moving average. That is, for a given measurement x recorded at time i , the smoothed value of this measurement y was taken as:

$$y_i = \frac{1}{5}(x_{i-2} + x_{i-1} + x_i + x_{i+1} + x_{i+2}) \quad \text{Equation 4-1}$$

This was similar to applying to a simple lowpass filter. A similar method was used by Otani and Sozen (1972), who used a combination of weighted 3-point and 11-point moving averages when processing data.

After smoothing, records from the accelerometers were filtered using a fourth-order Butterworth bandpass filter with highpass and lowpass frequencies of 0.5 Hz and 60 Hz, respectively. The highpass frequency (0.5 Hz) was selected because the minimum frequency measurable by the accelerometers was 0.5 Hz. The lowpass frequency (60 Hz) was selected based on previous experience operating the earthquake simulator (described in the Appendices). During trial runs a lowpass filter of 60 Hz was observed to reduce noise caused by rattling of the components of the simulator platform, and a highpass filter of 0.5 Hz was found to reduce signal drift.

4.1.2. Optotrak

Optotrak output consists of arrays of x, y, and z coordinates for each target at each point in time. The measured coordinates were transformed to the experiment coordinate system illustrated in Figure 4-1. This transformation required three transformation vectors: one in-plane, one out-of-plane, and one vertical.

The out-of-plane vector shown in Figure 4-1 was perpendicular to a plane fitted (using least squares) to include all targets on the columns. This vector was normalized to a unit length.

The in-plane vector was derived using the targets attached to the simulator platform (Figure 3-15). This vector was defined using the position of each target on the platform relative to its starting position. First, the magnitudes of relative displacements were calculated for each target at every point in time:

$$D_{rel,i} = \sqrt{(x_{Ui} - x_{U0})^2 + (y_{Ui} - y_{U0})^2 + (z_{Ui} - z_{U0})^2} * \text{sign}(y_{Ui} - y_{U0}) \quad \text{Equation 4-2}$$

where $\{x_{Ui}, y_{Ui}, z_{Ui}\}$ are untransformed coordinates (i.e. Optotrak coordinate system) of a target at the i^{th} time step. The sign was based on y-axis relative displacement because the Optotrak y-axis was nearly parallel to the experiment in-plane axis. These signed relative displacements were

processed to find the two points with (a) opposite sign, and (b) the smallest difference in absolute value (as a percent of the relative displacement). That is, these two points satisfied the following criteria:

$$\frac{D_{rel,n}}{D_{rel,m}} < 0 \quad \text{Equation 4-3}$$

$$\frac{|D_{rel,n}| - |D_{rel,m}|}{(|D_{rel,n}| + |D_{rel,m}|)/2} \text{ is minimized} \quad \text{Equation 4-4}$$

The vector between these two points was normalized to a unit length. This process was repeated for the three targets connected to the simulator platform to obtain three in-plane unit vectors. The average of these unit vectors was used as the in-plane vector. The vertical vector was defined as the cross product of the in-plane and out-of-plane unit vectors. With all three vectors obtained, Optotrak measurements were transformed to the experiment coordinate system using a transformation matrix:

$$Trans = \begin{bmatrix} Vert_i & Vert_j & Vert_k & 0 \\ IP_i & IP_j & IP_k & 0 \\ OOP_i & OOP_j & OOP_k & 0 \\ 0 & 0 & 0 & 1 \end{bmatrix} \quad \text{Equation 4-5}$$

where $\langle Vert_i, Vert_j, Vert_k \rangle$ is the vertical unit vector, $\langle IP_i, IP_j, IP_k \rangle$ is the in-plane unit vector, and $\langle OOP_i, OOP_j, OOP_k \rangle$ is the out-of-plane unit vector. Relative positions and movements of each target in the experiment coordinate system were then calculated by subtraction.

In Figure 4-3, the ideal platform displacement is compared with in-plane displacement measured by Optotrak and feedback from the MTS controller for test C2-100. The MTS feedback was from an internal LVDT in the hydraulic ram that drove the simulator platform. This figure shows that measurements obtained using Optotrak were consistent with those recorded by the main data acquisition system and with the ideal profile.

4.2. Ground Motions

It was critical that the ground motions in the test program be reproducible. That is, the ground motion at 25% for frame C1 needed to be the same as the ground motion at 25% for the other frames (and likewise for other motions). In this section, the reproducibility of the motions is discussed.

4.2.1. Ground Motion Histories and Summary Properties

Peak ground acceleration (PGA) was computed as the average of the maximum absolute accelerations recorded by the three accelerometers on the base of the test setup. In two test runs (C1-25, C1-50), the accelerometer attached to the lower beam of the specimen malfunctioned and was excluded from this averaging process. Velocity histories were obtained for each accelerometer by integrating the acceleration histories with respect to time. The average of the peak velocities from these velocity histories was taken as the peak ground velocity (PGV) for that test run. Peak ground displacement (PGD) was taken as the peak displacement from the MTS feedback channel.

Values of measured PGD, PGV, and PGA are presented in Table 4-1 for all tests alongside target values (i.e. expected based on the input motion). Measured PGDs were comparable to target PGDs, and were consistent for tests of the same ground motion amplitude (i.e. tests at 25% were similar, tests at 50% were similar, and so forth). Similarly, PGVs computed from acceleration histories were comparable to target PGVs and were consistent for tests of the same ground motion amplitude. Measured PGAs were consistent for tests of the same ground motion amplitude, but were much larger than target PGAs (as much as 3.7 times larger). The large measured PGAs were the result of high frequency components in the measured acceleration response, particularly with frequencies from 15 and 50 Hz.

These high frequency components can be attributed to several causes: dynamic modes of the earthquake simulator, mechanical vibrations (i.e. “rattle”) caused by interaction of simulator components, and so forth. By reducing the lowpass frequency of the bandpass filter, these high frequency components can be filtered out. Examples of the effect on PGA and PGV of reducing the lowpass cutoff frequency are summarized in Table 4-2. Statistics for these data are presented in Figure 4-4 (for PGA) and Figure 4-5 (for PGV). These figures show that PGA decreased when using lower lowpass cutoff frequencies, but PGV was relatively insensitive to changes in lowpass cutoff frequencies (within the range considered). This is because sharp (i.e. short duration, high amplitude) pulses in an acceleration history have little effect on the corresponding velocity history obtained from integration. Table 4-2 also shows that PGAs were consistent for tests of the same ground motion amplitude, regardless of the lowpass frequency chosen. Because they required less alteration to the measured data (i.e. less filtering), the values of PGA and PGV obtained after applying a bandpass filter from 0.5 to 60 Hz are used throughout the remainder of this document (as reported in Table 4-1).

Overall, comparisons of PGD, PGV, and PGA indicate that the ground motions to which the frames were subjected were consistent throughout the test program.

4.2.2. Linear Response Spectra

The acceleration histories recorded at the base of the test setup were used to compute linear response spectra for each test (for 2% damping). The average displacement response spectrum for each test is presented in Figure 4-6 through Figure 4-10 alongside the target spectra. Only displacement response spectra are shown because the focus of this investigation is drift response.

One consistent feature of all spectra is amplification of response compared with the target response spectra. In the range of periods of interest (0.1 sec to 0.4 sec), this amplification ranged from 10%

to 23% for ground motion amplitudes ranging from 25% to 100%. The amplification is higher in the low period (< 0.1 sec) range. Similar amplification at low periods (high frequencies) has been observed in previous tests on this earthquake simulator and can be attributed to the displacement control method used [Otani and Sozen (1972)]. Suppose the displacement control signal was expanded into a Fourier series. The corresponding acceleration signal would be the Fourier series of the displacement signal multiplied by circular frequency squared. As a result, if there is noise in the displacement signal, the corresponding noise in the acceleration signal is proportional to the noise in the displacement signal multiplied by the circular frequency squared. This means that high-frequency noise is amplified by larger factors than low frequency noise. This accounts for the high-frequency noise observed during both trial runs of the earthquake simulator and tests of the specimens.

The coefficients of variation (CoVs) of the displacement response spectra were taken as a measure of repeatability of the tests. Using the motion at 25% as an example, this process was as follows: for each test (C1-25, H1-25, C1-25, and C2-25), calculate an average displacement response spectrum by averaging the spectra obtained from the three platform accelerometers at each period. For the resulting four average displacement response spectra, calculate the mean and standard deviations at each period. Next, calculate the coefficient of variation of the spectra at each period as the standard deviation divided by the mean. Table 4-3 presents a summary of average CoVs for each motion. The CoV is larger for low periods. This can be attributed to the lower denominator (spectral displacement) for weaker ground motions and amplification of high frequency noise. For periods ranging from 0.1 sec to 0.4 sec (the range of interest in this investigation), the CoV ranged from 7% for the weakest ground motion to 4% for the strongest ground motion. This indicates that the motions to which the frames were subjected were consistent.

4.3. Free Vibration Tests

Hammer tests and platform jolts were both used to measure the period of the frames, as described in Section 3.6. Period was measured by counting the zero crossing rate of the displacement response measured at the top of the frame. Initial periods are summarized in Table 4-4 alongside the peak displacement in the interval over which period was calculated. Other periods (pre- and post-test) are listed in the respective summary tables for each frame (Table 4-5 through Table 4-8).

4.4. Specimen Response Histories

Summaries of peak input motion characteristics and test specimen responses are presented in Table 4-5 through Table 4-8. These summaries include PGA, PGV, and PGD, as well as peak in-plane response at the top of the frame (acceleration, velocity, and drift). Peak in-plane drift, out-of-plane displacement, and vertical displacement for all tests are summarized in Table 4-9.

4.4.1. In-Plane Motion

The in-plane responses of the frames were measured using Optotrak targets attached to the mass, two LVDTs (one attached to the top girder and the other attached to the mass), and an accelerometer atop the mass. Response histories for each frame obtained from these sensors are presented in Figure 4-11 through Figure 4-30.

These figures are organized by frame and from weakest to strongest ground motion. The following ranges correspond to each frame:

- Specimen C1: Figure 4-11 – Figure 4-15
- Specimen C2: Figure 4-16 – Figure 4-20
- Specimen H1: Figure 4-21 – Figure 4-25
- Specimen H2: Figure 4-26 – Figure 4-30

The acceleration histories shown in these figures were obtained from the top accelerometer, and are absolute accelerations. Some of these acceleration histories have high frequency components and sharp peaks. The high frequency components can be attributed to high frequency components in the motion produced by the simulator, as discussed in Section 4.2.1. The sharp peaks can be attributed to collisions between the mass and out-of-plane bracing during testing. Both had little effect on the velocity histories, which were obtained by integrating relative accelerations (absolute acceleration minus base acceleration). The displacement histories were obtained from the 3-in. LVDT connected at the top of the test structure.

As a check, the displacement histories obtained from the LVDTs were differentiated to generate velocity histories to compare with the velocity histories obtained by integrating relative acceleration. One example of this is shown in Figure 4-31. Overall, the velocity histories obtained using these two methods showed good agreement, lending credibility to the measurements obtained using both sensor types.

4.4.2. Curvature Distributions

Column curvature distributions were calculated for selected relative peak displacements throughout the response of each frame. This was done to aid in understanding how the frames deformed as a result of lateral demand from the ground motions. Plots showing column curvature distributions at selected relative peak displacements are presented alongside displacement response histories in Figure 4-32 through Figure 4-35 for the first motion at 100%. Because the mass overhang covered the top beam, it was not possible to place Optotrak targets on this beam with which to measure strains at the tops of the columns. It is expected that unit curvature at this location was opposite in sign but similar magnitude to the corresponding unit curvature at the bottom.

Unit curvatures were calculated using the relative movement of the Optotrak targets attached to each column face. Figure 4-36 illustrates Optotrak targets on a column in the undeformed and deformed states. In the undeformed state, lines AB and CD lie parallel to each other and perpendicular to lines AD and BC. As the top of the frame displaces laterally, line BC contracts and line AD extends. Unit curvature was calculated by summing the mean compressive strain on line BC with the mean tensile strain on line AD and dividing by the initial perpendicular distance between these two lines.

4.4.3. Out-of-Plane Motion

Out-of-plane motion was observed during all tests. For the first test at 100% of each frame, out-of-plane displacement of the mass (measured by two Optotrak targets attached to the mass) is plotted alongside in-plane displacement in Figure 4-37 through Figure 4-40. The maximum measured was approximately 1/4 in.

4.4.4. Vertical Motion

As the mass displaced laterally in-plane it also experienced vertical displacement. This was the result of crack opening in the columns. The two Optotrak targets attached to the mass provided information about the magnitude of this vertical displacement. For the first test at 100% of each frame, Figure 4-41 through Figure 4-44 show the average vertical movement of the two targets connected to the mass alongside the top in-plane displacement. It should be noted that the earthquake simulator platform experiences vertical movement during testing (up to approximately 1/32 in. for the strongest motions in the test program). This motion has been removed from these vertical displacements (i.e. they are relative displacements). For the strongest motions in the test program, the peak vertical displacement of the mass was on the order of 1/8 in.

4.5. Inertial Force versus Drift Envelopes

The development of force-drift envelopes is described below. Starting with the equation of motion for a single-degree-of-freedom (SDOF) system subject to base acceleration:

$$m\ddot{x} + c\dot{x} + kx = -\ddot{z} \quad \text{Equation 4-6}$$

where m = effective mass of the system (W_{me} divided by gravitational acceleration, g)

c = damping constant of the system

k = stiffness of the system

x = relative displacement of oscillator (dots indicate differentiation with respect to time t)

\ddot{z} = base acceleration

This equation was rearranged to obtain:

$$m(\ddot{x} + \ddot{z}) + c\dot{x} + kx = 0 \quad \text{Equation 4-7}$$

where $(\ddot{x} + \ddot{z})$ is absolute acceleration. At points of zero velocity ($\dot{x}=0$), displacement is maximized and this equation simplifies to:

$$m(\ddot{x} + \ddot{z}) + kx = 0 \Big|_{\dot{x}=0} \quad \text{Equation 4-8}$$

The first term is inertial force in the system. The second term contains relative in-plane displacement (x , or drift). This equation can be restated as:

$$\underbrace{W_{me}(\ddot{x} + \ddot{z})}_{\overset{F}{\text{}}} + kx = 0 \Big|_{\dot{x}=0} \rightarrow F + kx = 0 \Big|_{\dot{x}=0} \quad \text{Equation 4-9}$$

Using Equation 4-9, inertial force versus drift plots were created for each test. The y-axis on these plots was calculated as the product of effective mass and absolute acceleration. The x-axis was drift measured by the top 3-in. LVDT.

For each frame, an inertial force versus drift envelope was obtained by overlaying the force-drift curves from each of the five tests and connecting the uppermost points. These envelopes are presented in Figure 4-45. They are also presented beside force-drift curves obtained using LARZ in Figure 4-46 (C1 and C2) and Figure 4-47 (H1 and H2). Overall, type C frames showed good

agreement with estimates, whereas type H frames had lower lateral stiffness and resistance than expected. These observations are discussed in more detail in Chapter 5.

4.6. Damage

After each test, cracks were marked and mapped. Crack maps of the specimens are presented in Figure 4-48 through Figure 4-51. These figures also show the maximum crack width measured on both columns following each ground motion. An account of damage propagation in each frame follows.

4.6.1. Frame C1 (Figure 4-48)

After the initial motion at 25%, flexural cracks were visible along both columns, with closer spacing near column ends. All cracks were less than 0.005 in. wide. After the subsequent motion at 50%, additional cracks were observed. These new cracks were located primarily near the ends of the columns. The maximum crack width measured after this test was 0.005 in. During the motion at 75%, fewer new cracks formed. Cracks that formed were typically extensions of cracks from the previous two motions. Existing cracks at the column ends were as wide as 0.015 in. after this test, and some spalling was visible. After the first motion at 100%, almost no new cracks appeared, but existing cracks at the column ends were as wide as 0.035 in. and some cracks along the length of the column were as wide as 0.020 in. Again after the second motion at 100%, almost no new cracks appeared. The cracks that appeared connected existing cracks from previous motions. Additional spalling was visible at the column-beam interface. The largest crack width was 0.035 in.

4.6.2. Frame C2 (Figure 4-49)

After the initial motion at 100%, nearly all the cracks that would form for the remainder of the test series were visible. Like frame C1, flexural cracks were distributed along the length of both columns, with closer spacing near the ends. The maximum crack width was 0.025 in. (at the column

ends). During the subsequent motion at 75%, some new cracks formed, most of which were extensions of cracks from the previous run. Spalling was also observed at the column ends. The widest crack remained 0.025 in. at the same location where the widest crack was observed after the previous test. Elsewhere, crack widths were observed to be wider. After the test at 50%, few new cracks formed. Most new cracks were extensions of existing cracks. The maximum crack width increased to 0.030 in. and some other cracks on the columns widened to as much as 0.025 in. After the motion at 25%, only a single new crack was visible. The maximum crack width narrowed to 0.025 in. After the second and final motion at 100%, the maximum crack width increased again to 0.030 in.

4.6.3. Frame H1 (Figure 4-50)

After initial motion at 25%, horizontal cracks were observed at the top and bottom of each column (at the column ends). A horizontal crack also was observed on the south side of the south column. The maximum crack width was 0.005 in. During the subsequent motion at 50%, existing cracks at the top and bottom of each column widened and extended, and some spalling was observed. The maximum crack width increased to 0.010 in. No new cracks were observed along the length of the columns. After the motion at 75%, a few new cracks were observed, once again only at the ends of the columns. The maximum crack width increased again to 0.015 in. After the first motion at 100%, spalling was observed at the column ends. The maximum crack width remained 0.015 in. After the second and final test at 100% no new cracks were observed, although some spalling was visible. The maximum crack width increased to 0.020 in.

4.6.4. Frame H2 (Figure 4-51)

After the initial motion at 100%, cracks were observed only at the top and bottom of each column, with a maximum width of 0.015 in. Spalling was also visible in these regions. Following the subsequent test at 75%, two new cracks were observed in the same regions. The maximum crack

width increased to 0.020 in. After the next test at 50%, additional spalling at the column-beam intersection was observed and the maximum crack width narrowed to 0.010 in. After the next motion (25%), additional spalling was observed (in fact, one Optotrak target on the north column was found to be on a dislodged piece of concrete). The maximum crack width was found to be wider at one location (0.015 in.) although elsewhere the crack widths remained nearly the same. After the second and final ground motion at 100%, additional spalling was observed and the maximum crack width increased to 0.020 in.

CHAPTER 5. DISCUSSION OF OBSERVED RESPONSE

The objective of this investigation was to test the hypothesis that two frames with (1) similar initial stiffness, (2) similar strength, and (3) different post-cracking stiffnesses, would reach comparable peak drift during the same ground motion. In Sections 5.1 through 5.3, the stiffnesses and strengths of the test frames are compared. In Section 5.4, the resistance mechanisms of the frames are examined. In Section 5.5, the hypothesis that initial stiffness drives peak drift is evaluated by comparing the drift responses of: (1) type C frames with type H frames, (2) Series 1 frames with Series 2 frames, and (3) the first motion at 100% with the second motion at 100% for each frame.

5.1. Initial Stiffness

Because the frames had the same mass, initial period was used as a measure of initial stiffness. Initial period was calculated from the displacement response at the top of each frame for three different cases: (1) hammer tests, (2) testing platform jolts, and (3) the initial response of each frame to its first ground motion. The first two cases are referred to as “small-displacement” periods because the maximum drift reached during these cases was 0.004 in. (0.01% drift ratio). The last case is referred to as a “large-displacement” period because the maximum drift reached during this case was 0.035 in. (0.08% drift ratio). Peak drifts and calculated initial periods for these three cases for each frame are summarized in Table 4-4.

On average, small-displacement periods were 0.15 sec for type C frames and 0.12 sec for type H frames. Average large-displacement periods were 0.19 sec for type C frames and 0.18 sec for type H frames. The initial period of the frames was calculated to be 0.1 sec based on gross cross-

sectional properties and fixed-end conditions (Section 3.2.4). For all frames, calculated initial period underestimated measured initial period (using both small- and large-displacements).

Similar underestimates of initial period have occurred for past dynamic tests of reinforced concrete structures. Calculated and measured initial periods for past tests of SDOF reinforced concrete structures are summarized in Table 5-1. Calculated initial periods in this table are based on gross cross-sectional properties. Measured initial periods in this table are from free vibration tests, which would be comparable to the small-displacement methods in this investigation (which included free vibration after either a hammer impact or platform jolt). For all tests in this table, the average ratio of measured-to-calculated initial period was 1.23. For the tests most similar to the tests conducted in this investigation (Gulkan's portal frames), this ratio was as high as 1.9, with an average of 1.64.

Underestimates of initial period have also been observed for multi-degree-of-freedom systems. In Table 5-2 and Table 5-3, calculated and measured initial periods are listed for past studies of reinforced concrete systems with and without walls. In these tables, calculated period was based on gross cross-sectional properties (i.e. uncracked sections). Details of the procedures used to calculate period are discussed in Lepage (1997). For structures with walls, the average ratio of measured-to-calculated initial period was 1.26 and the maximum was 1.76. For structures without walls, these ratios were 1.17 and 1.63. Overall, the underestimates in this investigation fell within ranges observed in past investigations of both SDOF and MDOF systems.

The mentioned systematic underestimation of initial period can be attributed to two causes: underestimating effective mass, or overestimating lateral stiffness (in Equation 3-10). Because the mass was known from weighing components before testing, overestimating the stiffness of the system is a more likely cause. The as-built frames and test setup may have been less stiff than expected because of: (a) flexibility of connections and the testing platform, (b) indentation of the

column into the beam at small deformations, and (c) fine cracks that may not have been visible to the eye. Regarding item (a), it is impossible to achieve perfect fixed end conditions. The components used to fasten the frames to the platform and the added mass were not rigid. Flexibility of these fastening components would have permitted deformation of the top and bottom beams which would have reduced the lateral stiffness of the system. This has been observed in past investigations of RC columns [Matamoros (1999)]. Because the same setup was used for all tests, any contributions of the flexibility of the setup to the flexibility of the system would have been similar for all tests. Regarding item (b), as the columns deformed, the compressed regions at their ends bore against the concrete in the beams. Being a compressible material, the concrete at these sections would have deformed as a result, permitting more drift and reducing the lateral stiffness of the system. Regarding item (c), it is possible that volumetric shrinkage of the concrete could have induced fine cracks that were invisible to the eye. Although care was exercised when moving the frames, it is also possible that fine cracks could have formed when the frames were tilted up to vertical from their sides (the frames were cast on their sides), or when the frames were moved around the laboratory. Any of these causes could have reduced the initial stiffnesses of the systems. Overall, although calculated initial periods differed from measured initial periods, when using the same measurement method (i.e. small- or large-displacement) the measured initial periods of the two frame types were comparable. For small-displacement methods (<0.004 in.), the periods of type C and H frames were within 25% of one another. For large-displacement methods (<0.035 in.), the periods were within 5% of one another.

5.2. Post-Cracking Stiffness

At a lateral inertial force of approximately 1 kip, the force-drift envelopes for three out of four frames (C1, H1, and H2) showed a sudden reduction in tangential stiffness (Figure 4-46 and Figure 4-47). Based on this sudden reduction in stiffness, this point is thought to mark the onset of cracking

in the columns and is referred to as the “apparent” cracking point. The force at apparent cracking was 1.7 times lower than the force that would have been calculated based on a modulus of rupture of $f_r = 850$ psi (Section 3.2.1), but was consistent with estimates from FLECHA. One plausible explanation for the lower apparent cracking force is that there were too few points with low drifts in the force-drift envelope to capture the cracking moment. For example, in the envelope for type C frames, points jump from approximately 0.02 in. or less to nearly 0.1 in. Another plausible explanation is that fine cracks at a cross-section may have reduced the magnitude of bending moment required to crack the section (i.e. b or h in the estimate of M_{cr} may have been less than gross dimensions as a result of fine cracks). Regardless of the source of the difference between calculated and apparent force at cracking, the test specimens generally showed a reduction of stiffness at the same point (1 kip).

The post-cracking stiffnesses of the frames can be estimated by drawing a secant line from the point at cracking (approximately 0.02 in.) to a second point before yielding was expected. Based on the LARZ models (Figure 3-14), yielding was expected to start in type C frames at 0.5 in. and in type H frames at 0.6 to 0.7 in. If the second point is set to 0.4 in. (below both of these), then the average post-cracking stiffness of type C frames was approximately 10.7 kip/in. and the average post-cracking stiffness of type H frames was 4.4 kip/in. (nearly 60% lower than type C). Based on moment-curvature diagrams created using FLECHA, the post-cracking stiffness of type H frames was expected to be no more than 40% less than type C frames. This means that the as-tested type H frames had lower post-cracking stiffness than was estimated assuming perfect bond. One possible reason for the added flexibility in type H frames is slip of longitudinal reinforcement. This is discussed in Section 5.4.2.

5.3. Strength

The two frame types were designed to have equal flexural strengths, but because no frames were tested to failure, it is impossible to know the strengths of the frames. On average, type C frames reached a peak resisting force of 7.9 kips, whereas type H frames reached an average peak resisting force of only 3.8 kips (Figure 4-45). It is possible that type H frames could have reached higher resisting force at higher drifts, but within the range of drifts reached, type H frames reached just half the force of type C frames.

5.4. Lateral Resistance

5.4.1. Type C

The LARZ estimates represent what would be computed assuming perfect bond of reinforcing steel with surrounding concrete. In the range of drifts reached, the resisting forces of type C frames were similar to the estimated force from LARZ (Figure 4-46). Initial and post-cracking stiffnesses of the two were comparable to a drift of 0.3 in., after which measured resisting forces were 10–20% lower than estimated resisting forces. Although the comparison is not perfect, these similarities suggest that the assumption of perfect bond in LARZ models was a reasonable representation of the behavior of type C frames. This is supported by curvature distributions and crack patterns in type C frames. Curvature distributions derived from measurements for the first tests at 100% of type C frames are presented alongside displacement response histories in Figure 4-32 and Figure 4-33. These curvature distributions are similar in shape to the expected curvature distributions shown in Figure 3-11(b). Differences between derived and expected curvature distributions can be attributed to the formation of cracks at discrete locations that were not always between Optotrak targets. The fact that the derived curvature distributions were similar in shape to expected distributions indicates that type C columns experienced deformations along their length during testing. The crack maps in

Figure 4-48 and Figure 4-49 support this idea, with transverse cracks along the length of the columns.

5.4.2. Type H

Force-drift envelopes for type H frames are presented alongside LARZ estimates in Figure 4-47. Until cracking (marked by a sudden reduction in stiffness at approximately 1 kip), measurements and estimates from LARZ showed good agreement. But after cracking, the measured force in type H frames was 50% or less of the force estimated by LARZ, which assumes perfect bond. One plausible explanation is that the undeformed, high-strength steel bars slipped along the length of the column. Slip of the high-strength bars would have reduced the stiffness of type H frames to less than what was expected based on perfect bond. This idea is examined in detail in this section.

Bars in type H frames were corroded to roughen their surfaces in order to improve bond. They were also anchored into the beams using mechanical assemblies. Along the 21 in. length from the expected point of inflection at column mid-height to the joint face, to reach yield a 1/4 in. diameter bar with a yield stress of approximately 160 ksi would be required to develop a uniform bond stress on the order of 500 psi. At fracture, a uniform bond stress of nearly 600 psi along the same length would have been required. In past tests, undeformed reinforcing bars have been observed to reach maximum bond stresses of 450 psi, with slip initiating at approximately 270 psi [Abrams (1913)]. The estimated uniform bond stresses at yield and at ultimate (500 psi, 600 psi) were 10% and 33% more than this maximum value (450 psi), and 80% and 120% more than the value at which slip can be expected to initiate (270 psi). Slip would have resulted in the additional flexibility observed during the tests.

Curvature distributions and damage patterns support the idea that high-strength bars slipped and subsequently reduced the post-cracking stiffness of type H frames below what would be calculated

assuming perfect bond. Unlike type C frames – in which curvature varied along the height of the columns – in type H frames there was almost no curvature along the columns except at the ends (Figure 4-34 and Figure 4-35). Similarly, cracks were observed only at the ends of the columns (Figure 4-50 and Figure 4-51). This suggests that type H frames worked similar to concrete elements with unbonded reinforcement, except that friction along the reinforcement in type H frames is likely to have been relatively high. As a check, virtual work was used to estimate the peak force reached by type H frames within the displacement range reached.

If a portal frame is subjected to a lateral force at the top F causing an in-plane displacement Δ , then the work done by this force is:

$$W_{\text{ext}} = F\Delta \quad \text{Equation 5-1}$$

If yielding is reached at the column ends (Figure 5-1), then the internal work is:

$$W_{\text{int}} = 4M_p\theta \quad \text{Equation 5-2}$$

where 4 is the number of plastic hinges (2 columns x 2 hinges each), M_p is the plastic moment of the columns, and θ is rotation of each hinge. Equating internal work to external work ($W_{\text{ext}} = W_{\text{int}}$) results in the following relationship:

$$F\Delta = 4M_p\theta \quad \text{Equation 5-3}$$

The term θ can be expressed as a function of in-plane displacement as $\theta = \Delta/L$, where L is the length (height) of the columns. Substituting this into Equation 5-3, and solving for F results in:

$$F = \frac{4M_p}{L} \quad \text{Equation 5-4}$$

This equation overestimates the peak resisting force reached by type H frames by 50% within the range of displacements reached. If the steel is assumed to slip along the height of the column (Figure 5-2), then the total elongation of each bar is nearly:

$$e = \theta(d + d') \quad \text{Equation 5-5}$$

where d is the depth to the farthest layer of longitudinal reinforcement and d' is the depth to the closest layer of longitudinal reinforcement.

Assuming the bars remain elastic, the potential energy associated with this elongation can be expressed as:

$$U = 1/2 * \frac{E_s A_b}{L} * e^2 \quad \text{Equation 5-6}$$

where U = elastic potential energy

E_s = modulus of elasticity of steel

A_b = area of a bar

L = height of the column

e = elongation of the steel bars

Substituting elongation (Equation 5-5) into Equation 5-6 yields:

$$U = 1/2 * \frac{E_s A_b}{L} * [\theta(d + d')]^2 \quad \text{Equation 5-7}$$

This is the potential energy in each bar as a function of rotation angle. There are 2 bars per layer of reinforcing steel, 2 layers of steel per column, and 2 columns per frame, so this equation must be multiplied by 8 to obtain the total internal work of the frame. Again, $\theta = \Delta/L$ can be substituted to express internal work as a function of drift instead of rotation:

$$W_{\text{int,slip}} = 4 * \frac{E_s A_b}{L} * \left[\frac{\Delta}{L} (d + d') \right]^2 \quad \text{Equation 5-8}$$

Equating internal work with external work ($W_{\text{int,slip}} = W_{\text{ext}} = F\Delta$), and solving for F results in:

$$\begin{aligned} F &= 4 * \frac{E_s A_b}{L\Delta} * \left[\frac{\Delta}{L} (d + d') \right]^2 \\ &= 4 * \frac{E_s A_b \Delta}{L^3} * (d + d')^2 \end{aligned} \quad \text{Equation 5-9}$$

Assuming:

- $E_s = 30,000$ ksi (based on coupon tests)
- $A_b = 0.051 \text{ in.}^2 = \pi/4*(0.255 \text{ in.})^2$ (area of each bar)
- $L = 42$ in. (height of columns)
- $d = 4$ in., $d' = 1$ in. (depths to each layer of steel)
- $\Delta = 1.6$ in. (the peak drift reached by type H frames)

yields an estimated lateral resistance of 3.3 kips. This is just 10% less than the measured resistance at this drift (3.65 kips). Although this estimate is simplistic, it supports the plausibility that high-strength longitudinal steel in type H columns slipped.

The purpose of these experiments was to compare two frames with similar initial stiffnesses, but where one frame (type H) had approximately half the post-cracking stiffness of the other (type C). Bar slip caused the post-cracking stiffness of type H frames to be less than what was calculated assuming perfect bond. As a result, the hypothesis was tested in a more demanding scenario than it would have had slip not occurred.

5.5. Drift Response

In the following sections, dynamic responses of the frames are compared using the following metrics: (a) peak drifts, (b) mean effective periods, and (c) counts of the number of excursions past a given drift ratio. Side-by-side comparisons of drift histories are illustrated in the following figures:

(1) Type C vs. Type H:

- C1 vs. H1: Figure 5-3 – Figure 5-7
- C2 vs. H2: Figure 5-8 – Figure 5-12

(2) Series 1 vs. Series 2:

- C1 vs. C2: Figure 5-13 – Figure 5-17
- H1 vs. H2: Figure 5-18 – Figure 5-22

(3) First vs. Second motion at 100%

- C1, C2, H1, H1: Figure 5-23 – Figure 5-26

Peak drifts reached during each test are compared in Figure 5-27 through Figure 5-30. Two types of drift are presented in these figures: in-run and cumulative. In-run drift is measured relative to the position of the frame at the start of each test. It does not include permanent drift from previous motions. Cumulative drift is measured relative to the initial position of each frame before the first test of that frame. It includes permanent drift from previous motions. Percent differences in peak drifts for each comparison (C vs. H, Series 1 vs. 2, first vs. second motion at 100%) are summarized in Table 5-5 through Table 5-7.

Mean effective periods were estimated as two times the duration of motion divided by the number of zero crossings (from the 3-in. LVDT). For all tests, the duration of motion was defined from $t = 1.5$ sec to 11 sec. This corresponds to 0.5 sec after the ground motion began to when the ground motion ended (Figure 3-21). The values of mean effective period obtained are listed in Table 5-4 and are plotted in Figure 5-31.

Plots of the number of excursions beyond a given drift ratio provide information about how many cycles each frame experienced beyond different drifts. These “excursion plots” can be used to see whether two frames that reached similar peak drifts also reached a similar number of cycles at other drift ratios, or if one consistently reached smaller (or larger) drifts than the other throughout the rest of its response. Excursion plots are presented for each ground motion in Figure 5-32 through Figure 5-36. The x-axis in these plots is in-run drift ratio, and the y-axis is the number of excursions a frame experienced past that drift ratio.

5.5.1. Type C vs. Type H

On average, mean effective periods of type H frames were approximately 30% longer than type C frames in the same test series. The longer effective period of type H frames may be attributed to their lower post-cracking stiffness caused by: (a) the reduced longitudinal reinforcement ratio, and (b) bar slip. This increase in effective period did not lead consistently to increases in peak drift (as shown in Figure 5-27 and Figure 5-28), but did lead to fewer displacement cycles as shown in the excursion plots. Based on these findings, the hypothesis that a reduction in post-cracking stiffness would not lead to consistently larger drifts was supported.

5.5.2. Series 1 vs. Series 2

In the previous section, the effect on drift response of reduced post-cracking stiffness caused by lower longitudinal reinforcement ratio and bar slip was discussed. In this section, the effect of damage from previous ground motions on drift response is examined. This is done by comparing the response of frames of the same type, but from different series. These comparisons are organized by the relative amplitude of the ground motions, from 25% to 100%. A summary of the load histories of Series 1 frames and Series 2 frames before each ground motion is presented below:

- 25%: Series 1 frames were uncracked, Series 2 frames had experienced three stronger motions (100%, 75%, 50%)
- 50%: Series 1 frames had experienced one weaker motion (25%), Series 2 frames had experienced two stronger motions (100%, 75%)
- 75%: Series 1 frames had experienced two weaker motions (25%, 50%), Series 2 frames had experienced one stronger motion (100%)
- 100% (1): Series 1 frames had experienced three weaker motions (25%, 50%, 75%), Series 2 frames were uncracked
- 100% (2): both series had experienced the same ground motions, but in different order

5.5.2.1. 25% Motion

Series 1 frames experienced no ground motions before this test. In contrast, Series 2 frames had experienced three stronger ground motions (100%, 75%, and 50%) and sustained damage as a result of these motions. This damage included cracking, and sometimes also included spalling and permanent drift.

Drift histories from tests C1-25 and C2-25 are compared in Figure 5-13. On average, frame C2 responded with a longer period than frame C1 (0.42 sec vs. 0.28 sec). This can be attributed to damage from the previous test runs, which led to softening of frame C2. Drift histories from tests H1-25 and H2-25 are compared in Figure 5-18. Similar to what was observed for type C frames, frame H2 responded with a longer period than frame H1 as a result of softening caused by damage (0.61 sec vs. 0.28 sec).

Comparing peak drifts, frame C2 reached a peak in-run drift nearly 40% larger than frame C1, and a peak cumulative drift nearly 170% larger than frame C1 (Table 5-6). This large difference in peak cumulative drift is the result of permanent drift from the first test of frame C2 (test C2-100), which had a permanent drift of 0.3 in. Frames H1 and H2 reached comparable peak in-run drifts (within 15% of one another, Figure 5-29), and comparable peak cumulative drifts (within 18% of one another, Figure 5-30).

5.5.2.2. 50% Motion

Before the test at 50%, Series 1 frames experienced one weaker ground motion (25%). These frames were cracked as a result of this motion, but had negligible permanent drift (<0.01 in.) and no spalling. On the other hand, Series 2 frames had experienced two stronger ground motions (100%, 75%), the strongest of which was four times stronger than what Series 1 frames had

experienced. Frame C2 had over 0.3 in. of permanent drift going into the test at 50%, whereas frame H2 had only 0.03 in.

Drift histories from tests C1-50 and C2-50 are compared in Figure 5-14. The frames had similar response for $t < 2$ sec, but after this point the responses of the frames diverged. On average over the entire test, frame C1 responded with a period within 15% of that of frame C2. Drift histories from tests H1-50 and H2-50 are compared in Figure 5-19. Like type C frames, type H frames had similar response for $t < 2$ sec. Unlike the test at 25%, frame H2 responded with the same effective period as frame H1.

Comparing peak drifts, frame C2 reached a peak in-run drift within 16% of frame C1 (0.78 in. for C1 vs. 0.90 for C2). Type H frames also reached similar in-run drifts (within 14% of one another). Comparing cumulative drifts, frame C2 reached a peak over 50% larger than frame C1. Like the 25% motion, this difference was the result of permanent drift from the first test of frame C2 (C2-100). Frames H1 and H2 reached similar peak cumulative drifts during this test (within 6% of one another).

5.5.2.3. 75% Motion

Before the test at 75%, Series 1 frames had experienced two weaker ground motions (25%, 50%), whereas Series 2 frames had experienced one stronger ground motion (100%). Frames from both series were damaged, but to different extents. Both type C frames had cracking along the height of the columns, but the maximum crack width was four times wider in frame C2 than frame C1 (0.020 in. versus 0.005 in.). Concrete spalling also was observed in one column of frame C2. Type H frames had cracks only at the ends of the columns. In frame H2, the maximum crack width was three times wider than in frame H1 (0.015 in. versus 0.005 in.).

Drift histories from tests C1-75 and C2-75 are compared in Figure 5-15. The two frames responded with similar effective (within 11%). Although frame C2 was more damaged – evidenced by larger cracks and spalling – its peak in-run drift was within 18% of the peak in-run drift of frame C1 and its peak cumulative drift was within 15%.

Drift histories from tests H1-75 and H2-75 are compared in Figure 5-20. As was observed for type C frames, type H frames had drift histories that were similar in shape, and had the same average period. Given these similarities, it is not surprising that the two type H frames reached comparable peak drifts (both in-run and cumulative were within 3% of one another).

5.5.2.4. First 100% Motion

Before the first test at 100%, Series 1 frames had experienced three weaker ground motions (25%, 50%, and 75%) and sustained damage as a result. Series 2 frames, on the other hand, had experienced no previous motions. This is opposite to the comparison for the ground motion at 25%, where frames in Series 1 were undamaged and frames in Series 2 were damaged.

Drift histories from tests C1-100 and C2-100 are compared in Figure 5-16. The two frames responded with similar effective periods. They also reached the same peak in-run drifts (1.7 in.) and comparable peak cumulative drifts (frame C1 reached a peak just 7% larger than frame C2).

Drift histories from tests H1-100 and H2-100 are compared in Figure 5-21. The two profiles illustrated in this figure are different in shape for $t < 4$ sec. After the pulse at approximately $t = 4$ sec (where the two frames reached their peak drifts), the responses of the two frames “synchronized” and became nearly the same for the remainder of the tests. The effective period of frame H1 was 25% longer than H2 (owing to its longer period at the beginning of the test). In spite of this difference, type H frames reached similar peak in-run and peak cumulative drifts (within 3% of one another).

5.5.2.5. *Second 100% Motion*

Before the final test at 100%, Series 1 and Series 2 frames had both experienced the same four ground motions, but in different order. Frames C1 and C2 had cracks along the height of the columns and spalling near the ends of the columns, the extent of which was more severe in C2 (see Figure 4-48 and Figure 4-49). The maximum crack width in frame C1 was 0.035 in., compared with 0.020 in. for frame C2. Frames H1 and H2 had cracks and spalling only at the ends of the columns. In both type H frames, the maximum crack width was 0.015 in.

Drift histories from frames C1 and C2 for this ground motion were nearly identical in shape (Figure 5-17). The two frames also had comparable average periods and reached comparable excursions past each drift ratio (Figure 5-36). Despite these similarities, frame C2 reached a peak in-run drift 22% larger than frame C1, and a peak cumulative drift 28% larger. This shows that even two systems that are nominally identical and that have experienced the same load history (albeit in different order), can have peak drifts that differ by as much as 28%.

Drift histories from tests H1-100(2) and H2-100(2) were also nearly identical in shape (Figure 5-22), differing only by an offset of approximately -0.15 in. The two frames also reached peak in-run drifts within 10% of one another and peak cumulative drifts within 4% of one another during this test.

5.5.3. *First vs. Second 100% Motion*

In the previous section, the drift responses of two nominally identical frames subjected to the same ground motions (but different order) were compared. In this section, the drift responses of the same frame subjected to a repetition of the same ground motion at 10% are compared. This is similar to the comparison of Series 1 and 2 frames, because if peak drift response is insensitive to softening

from previous ground motions, then repetitions of the same ground motion should not lead to more drift for a given frame.

Table 5-7 summarizes the percent change in peak drift response of each frame from the first to the second motion at 100%. This table shows that repetitions of the same strong ground motion did not lead to larger peak drifts. Peak in-run drifts reached during the second motion at 100% were within 20% of peak-in run drifts reached during the first motion at 100%. The same was observed for peak cumulative drifts. This suggests that the reduction in secant stiffness as a result of damage from prior ground motions did not lead to larger drifts.

5.6. Summary

The hypothesis underlying the experimental work in this investigation was:

Two reinforced concrete frames with columns having similar nominal design strengths and initial stiffnesses, but different post-cracking stiffnesses, reach the same peak drift response during the same strong ground motion, provided this motion is the strongest each frame has experienced.

The frames tested had initial periods within 5% to 25% of one another (depending on whether large-displacement or small-displacement periods are compared). Nominal strengths were within 10% of each other, but type H frames did not reach their strength within the range of drifts reached. The post-cracking stiffness of type H frames was approximately 40% of the post-cracking stiffness of type C frames because of reduced longitudinal reinforcement ratio and bar slip. This was lower than would have been obtained based on assumptions of perfect bond. As a result, the experiments were more demanding tests of the hypothesis.

The idea that initial stiffness – not post-cracking or secant stiffness – drives peak drift response was evaluated from three perspectives. First, type C frames were compared with type H frames (Table 5-5). This comparison examined whether the reduction in post-cracking stiffness associated with reduced reinforcement ratio and bar slip would lead to more drift in type H frames. For all but the weakest ground motion, peak in-run drifts ranged from 18% smaller to 18% larger for type H frames compared with type C frames (mean difference: 0%). Similarly, for all but the weakest ground motion, peak cumulative drifts ranged from 25% smaller to 12% larger for type H frames compared with type C frames, with a mean difference of -12% (type H lower). Only for the weakest ground motion did type H frames reach larger cumulative drifts than type C frames. These comparisons suggest that the lower reinforcement ratios – and post-cracking stiffnesses – of type H frames did not consistently lead to larger peak drift.

Second, frames tested in Series 1 were compared with frames tested in Series 2 (Table 5-6). This examined whether softening (and a reduction in secant stiffness) caused by previous motions would lead to more drift. In past investigations, softening caused by damage from previous motions has not been observed to lead to a consistent increase in peak drift [Otani and Sozen (1972), Cecen (1979)]. Comparisons of frames tested in Series 1 with frames tested in Series 2 in this investigation showed similar results. In 8 out of 10 comparisons, peak in-run drifts of frames tested in Series 2 were within 15% of peak in-run drifts of frames tested in Series 1. Similar results were obtained when comparing peak cumulative drifts. In 7 out of 10 comparisons, peak cumulative drifts in Series 2 were within 20% of Series 1 peaks. Of the remaining 3 cases, peak cumulative drifts in Series 2 exceeded peak cumulative drifts in Series 1 by 167% [C2-25], 55% [C2-50], and 28% [C2-100(2)]. These results suggest that softening caused by damage from preceding motions did not have a consistent impact on peak cumulative drift.

Last, the responses of the frames to their first and second motions at 100% were compared (Table 5-7). In this comparison, no systematic increase in peak drift was observed for frames subjected to repetitions of the same strong ground motion. This was consistent with observations from the comparisons of Series 1 and 2 frames.

These test results suggest that a common property of the frames drove their peak drift responses. The one property that the frames had in common was initial stiffness (and period), calculated based on gross cross-sectional properties. This is not the first time calculated initial period has been identified as the dominant factor driving peak drift response of RC structures subjected to strong ground motions. Since the 1990s, expressions have been proposed that state peak drift in terms of calculated initial period and parameters that describe the intensity of the ground motion [Lepage (1997), Sozen (2003)]. These expressions are the result of decades of research on the response of RC structures to earthquakes. In the next chapter, the most recent expression [Sozen (2003)] is evaluated against results from the tests conducted in this investigation, more than 140 tests reported by others, and measurements from three instrumented buildings that experienced earthquakes.

CHAPTER 6. EVALUATION OF ESTIMATES OF PEAK DRIFT

In this chapter, an expression proposed by Sozen (2003) as an upper bound estimate of peak drift is evaluated using results from more than 160 tests. This expression is the product of more than 40 years of research on the response of RC structures to earthquakes [Sozen (2003)]. It states that peak drift reached by a RC structure during an earthquake is proportional to the product of PGV and the calculated initial period of the structure. That peak drift is linearly proportional to calculated initial period is consistent with both the hypothesis and with the test results obtained in this investigation.

The history of thinking that led to the development of Sozen's expression is presented in Section 6.1. In Section 6.2, the dataset used to evaluate the expression is presented. In Section 6.3, the expression is evaluated and findings are discussed.

6.1. History of Simple Expressions for Peak Inelastic Response

In 1974, Shibata and Sozen proposed a procedure for estimating design forces in RC structures subjected to earthquake demands. This procedure revolved around a simple idea: that the inelastic response of a RC structure subjected to earthquake demands could be approximated from the linear response of a "substitute" structure having lower stiffness and higher damping. The flexural stiffness of each member in this "substitute" structure was defined as the product of the stiffness of the corresponding member in the actual structure and a coefficient less than one. This coefficient was a function of "damage ratio," which is similar (but not identical) to ductility ratio, μ (the ratio of maximum-to-yield rotation). Larger damage ratios resulted in larger reductions in stiffness. Similarly, the damping ratio of each member in the substitute structure was related to the ductility

ratio of the member, with higher ductility ratios resulting in more damping. Both ideas went on to influence future thinking on the topic of inelastic response.

After a series of experiments on RC portal frames in the early 1970s, Gulkan and Sozen (1974) proposed a method for estimating design base shear for RC structures. This method was based on a similar idea to that of Shibata and Sozen (1974): that inelastic response of a RC structure could be estimated from elastic response of a “substitute” RC structure. Gulkan defined the period of this “substitute” structure as $T_i\sqrt{\mu}$, where T_i was the calculated initial period of the structure and μ was ductility ratio. The damping coefficient was defined using a similar procedure to Shibata. For example, for $\mu=2$, the period was $T_i\sqrt{2}$ and the damping coefficient was 8% of critical. Using these values, the design base shear of the structure – which was at the center of the design procedure at the time – could be read from a linear response acceleration spectrum.

Later, the focus shifted from force to drift. In 1980, Sozen stated “drift control should be centerpiece of design methods for multi-story buildings rather than presented as simply another check on the completed designs.” He also presented results from tests of 16 small-scale, multi-story RC structures subjected to simulated earthquakes at the University of Illinois Urbana-Champaign (these tests are included in the dataset described in Section 6.2). The peak drift ratios reached by these structures were plotted against spectrum spectrum for each test. This plot – reproduced in Figure 6-1 – shows peak drift ratio increasing almost linearly with increasing spectrum intensity. Spectrum intensity was defined as the area under the spectral velocity curve for a damping factor of 20% over periods from $T = 0.04$ to 1.0 sec (the assumed region of nearly constant velocity for the scaled ground motions used). The work of Newmark (1973) implies this area is proportional to PGV. The basis was there for estimating peak drift in terms of PGV and period, but it would be another 23 years before an expression was proposed in terms of PGV.

In 1984, Shimazaki and Sozen proposed a procedure for estimating peak drift in RC buildings subjected to strong ground motions causing deformations in the nonlinear range of response. In this method, they defined three dimensionless ratios: strength ratio (SR), displacement ratio (DR), and period ratio (TR). Strength ratio was defined as the ratio of base shear coefficient to PGA. Displacement ratio was defined as the ratio of peak displacement of a nonlinear oscillator with an initial period T_i to the peak displacement of a linear oscillator with the same period (note that T_i was T_0 in the original formulation). Period ratio was defined as the ratio of the period of the structure to the “characteristic period” of the ground motion. This characteristic period corresponded approximately to the period separating the constant acceleration region from the constant velocity region in the trilinear spectrum defined by Newmark (1973), as shown in Figure 6-2. Shimazaki and Sozen concluded that, for systems with $TR+SR \geq 1$, DR was nearly equal to 1 regardless of the hysteresis model assumed. This suggested that the peak drift of a structure, (a) expected to enter its nonlinear range of response during a ground motion, and (b) with a period in the constant velocity region, could be estimated using a linear response spectrum. For structures with $TR+SR < 1$, DR was not nearly equal to one and Shimazaki and Sozen suggested the use of detailed dynamic analysis to determine peak drift.

Building on the work of Shimazaki and Sozen and in search for a simple method for estimating peak drift for systems with $TR+SR < 1$, in 1997 Lepage proposed a new expression for estimating peak drift. This expression was presented in Section 2.3 (Equation 2-2), and states peak drift in terms of the initial period of the structure (T_i), the characteristic period of the ground motion (T_g), and peak ground acceleration (PGA). Lepage evaluated his procedure against results from tests of RC structures and the measured response of the Van Nuys Holiday Inn building during the 1971 San Fernando earthquake. For the cases considered, Equation 2-2 was found to provide a reasonable upper bound estimate of peak drift. Lepage also stated that the expression could be simplified for

a ground motion with the following properties: acceleration amplification factor for 2% damping $F_a = 3.7$, $PGA = 0.5$ g, and characteristic period $T_g = 0.55$ sec (representative of El Centro 1940 NS normalized to 0.5 g). For ground motions meeting these criteria, peak drift (in mm) could be estimated as $250T$, where 250 is in mm/sec and T_i is in sec.

Later, Sozen (2003) proposed the following expression as a simpler alternative:

$$S_{dv} = \frac{PGV}{\sqrt{2}} * T_i * \Gamma \quad \text{Equation 6-1}$$

where S_{dv} is peak roof drift estimated using ground velocity, PGV is peak ground velocity, T_i is calculated initial period, and Γ is first-mode participation factor. This expression builds on the idea that peak drift in a RC structure that enters its nonlinear range of response can be estimated as the peak drift of a linear system with a longer period. It also builds on three other ideas: (1) that the demand from a given ground motion can be expressed in terms of PGV, (2) that spectral velocity can be related to PGV using a constant amplification factor, and (3) that pseudo spectral velocity can be related to spectral displacement through circular frequency. The first idea can be traced to Westergaard, who suggested in 1933 that earthquake demand be expressed in terms of PGV instead of PGA. The second can be traced to Newmark (1973), who sought to construct idealized linear response spectra from PGA, PGV, and PGD by applying amplification factors to these parameters in each range of assumed nearly constant response. The third comes from what is known about periodic functions (i.e. the relationship between pseudo spectral velocity and spectral displacement).

This chapter focuses on the evaluation of Equation 6-1 using a dataset comprising: (1) results from the 20 tests in this investigation, (2) results from more than 140 previous tests by others, and (3) the measured responses of 3 instrumented RC buildings to 4 earthquakes.

6.2. Dataset

The dataset is presented in the following tables:

- Table 6-1: SDOF tests in laboratories
- Table 6-2: MDOF tests in laboratories
- Table 6-3: MDOF buildings in the field subjected to earthquakes

Each case in the dataset corresponds to a single test of a single structure. Like the tests conducted in this investigation, each test was often one of many conducted on a structure. For that reason, although the dataset contains more than 160 tests, it contains only five dozen structures. Lepage (1997) created a similar dataset when he proposed Equation 2-2. His dataset included tests conducted at the University of Illinois Urbana-Champaign between 1971 and 1989 as well as the Van Nuys Holiday Inn building, which experienced three earthquakes. Lepage's dataset is a subset of the dataset presented in this chapter, with intersecting cases noted.

6.2.1. Parameters

To use Equation 6-1, the following parameters were needed for each case:

- Initial first-mode period calculated using gross cross-sectional properties (T_i), also referred to as T_{calc} to distinguish it from measured initial first mode period (T_{meas})
- First-mode participation factor calculated for gross cross-sectional properties (Γ)
- Peak ground velocity (PGV)

To evaluate the equation, the peak drift reached by the uppermost floor of each structure, D_{max} , to also was needed. Other parameters were also recorded for the purpose of organizing and plotting the data, including degrees of freedom, height of the structure, ground motion time compression, and peak ground acceleration (PGA).

The parameters were obtained from one of the following sources. The sources are ordered by precedence, and the parameter obtained from the source is noted afterwards in brackets.

1. Test data [PGA, PGV, D_{\max}]
2. Lepage's (1997) dataset [T_i , Γ , PGA, T_g , D_{\max}]
3. Corresponding literature (i.e. publications and theses) [T_i , Γ , PGA, PGV, D_{\max}]
4. Figures (extracted, as discussed in Sections 6.2.1.1 and 6.2.1.2) [D_{\max} , PGV]
5. Calculated (discussed in Section 6.2.1.3) [T_i , Γ]

If test data were available for a case, parameters were obtained from these data. The most frequently available data were base acceleration records, from which PGA and PGV were obtained. The ground acceleration history was first baseline-corrected in Seismosignal v5.1.2 [Seismosoft (2016)] to remove initial offset that can cause the signal to drift. Peak ground acceleration (PGA) was taken as the maximum absolute value of this baseline-corrected ground acceleration record. Peak ground velocity (PGV) was taken as the maximum absolute value of the velocity history, which was obtained after integrating the baseline-corrected acceleration history. In some cases, roof drift histories were also available and were used to obtain D_{\max} (the maximum absolute value of the drift history).

If test data were unavailable but the cases were included in Lepage's dataset, parameters were obtained from Lepage (1997) and checked against the literature. If test data were unavailable and the cases were not included in Lepage's dataset, parameters were obtained from the corresponding literature. Most often, parameters were summarized in tables or the body of corresponding literature. When parameters were not reported explicitly, they had to be either extracted from figures or calculated. These procedures and the parameters obtained with them are described in the following subsections.

6.2.1.1. Figure Extraction: Reading PGA and D_{max} from Histories

In this procedure, a figure was clipped and pasted into Inkscape [Bah et al. (2016)], an open-source vector graphics software. There, the clipped figure was scaled and the peak value of the parameter was read from the scaled figure.

6.2.1.2. Figure Extraction: PGV from Linear Response Spectra

This procedure stems from work done by Newmark. In 1973, Newmark examined 14 sets of ground motion records from earthquakes that occurred on the west coast of the United States between 1940 and 1971. Linear response spectra were developed for the 28 horizontal components of these ground motion recordings (each recording had 2 horizontal components and 1 vertical). These linear response spectra were organized into regions of nearly constant acceleration, nearly constant velocity, and nearly constant displacement response (Figure 6-2). In each range of nearly constant response, an amplification factor was calculated. For example, the velocity amplification factor, F_v was calculated as the ratio of average spectral velocity in the constant velocity region to PGV. These amplification factors were tabulated for different damping ratios and percentiles. This allowed linear response spectra to be generated for different combinations of ground motion properties (PGA, PGV, PGD), damping ratios (from 0.5% to 10% critical damping), and percentiles (from 50% to 95%). This work was expanded later to include more ground motion records [Hall et al. (1976), Newmark and Hall (1982)]. The amplification factors reported in the latter investigation are reproduced in Table 6-4 for damping ratios of 2%, 5% and 10%.

The work of Newmark and Hall was done so that linear response spectra could be constructed from ground motion characteristics. It is used here in reverse: to estimate ground motion characteristics (PGVs) from linear velocity response spectra. To do so first requires a range to be defined for the constant velocity region. Hall et al. (1976) used $T = 0.33$ to 3.33 sec ($f = 0.3$ to 3.0 Hz). The same range is adopted here.

The amplification factors in Table 6-4 were developed for unscaled ground motion records. In most cases in the dataset, ground motion records were scaled with respect to time (i.e. the durations of the records were compressed) because of testing constraints. Some examples of these constraints are simulator limits on PGA, PGV, PGD, and payload limits that restrict the size of specimens that can be tested. To account for this compression, the period range defining the constant velocity region was shifted in proportion to the scale (compression) factor. For example, if a record was compressed by a factor of 3, the constant velocity range must be shifted down from $T = 0.33 - 3.33$ sec to $T = 0.11 - 1.11$ sec. The average spectral velocity, $S_{v,avg}$, was calculated over this shifted period range, and PGV was calculated as:

$$PGV = \frac{S_{v,avg}}{F_v} \quad \text{Equation 6-2}$$

The value of F_v depended on the percentile and the damping coefficient of the spectrum. The mean (50%) was used for the percentile. The preferred damping coefficient was 2%, for which $F_v = 2.03$ was used. If 2% spectra were unavailable, 5% spectra were used instead with $F_v = 1.65$.

In contrast to the method described in Section 6.2.1.1 (which required only a single value to be read from each figure), this procedure required a range of values to be extracted from each velocity spectrum for averaging. To accomplish this, each figure was clipped and imported to DataThief [Van Der Laan and Huyser (2015)]. Using DataThief, the coordinate system was defined, the curve was traced, and the trace was exported as X-Y coordinates. The average spectral velocity, $S_{v,avg}$, was calculated from these data.

For tests conducted on the University of Illinois earthquake simulator, an upper limit of 15 in./sec was set on PGVs calculated using the method described above. This was based on the reported velocity limits of the simulator (15 in./sec) as reported in Sozen et al. (1969).

6.2.1.3. Calculation of T_i and Γ

Initial periods (based on gross cross-sections) and/or modal participation factors were sometimes not reported. In these cases, if the structure had no walls and had fewer than $N = 10$ stories, then Rayleigh's method for frames was used to determine T_i and Γ [Biggs (1964), Ch.3]. Story stiffness estimates for Rayleigh's method were guided by Schultz (1992).

For $N > 10$, as was the case for the test of a 20-story structure in Japan (see Section 6.2.3.3), T_i and Γ were calculated using SAP2000 v17 [Computers and Structures, Inc. (2015)]. This software was used so that axial deformations in the columns would be included.

6.2.2. SDOF Tests

The following SDOF tests were included in the dataset:

- Tests by Gulkan and Sozen (1971) of scaled, 1-bay portal frames
- Tests by Bonacci (1989) of flexural cantilevers
- Tests by Elwood and Moehle (2003) of scaled, 2-bay portal frames
- Tests from this investigation

Specimens in these tests ranged in calculated initial period from 0.02 sec to 0.27 sec. Both Gulkan's and Bonacci's tests were included in Lepage's dataset (1997).

6.2.2.1. Gulkan and Sozen (1971)

The specimens tested by Gulkan and Sozen (1971) were similar to the frames tested in this investigation. They consisted of one-bay planar frames with columns measuring either 2.5 x 2.5 x 13 in. (type H), or 5 x 5 x 26 in. (type F). The frames are illustrated in Figure 6-3. Each frame was subjected to a series of ground motions of increasing demand along one axis. These motions were modeled after records obtained from two different earthquakes. The first was the north-south component of the recording at El Centro obtained during the 1940 Imperial Valley earthquake

(referred to hereafter as El Centro 1940 NS), compressed in time by a factor of 8. The second was the N21E component of the recording at Taft Lincoln School obtained during the 1952 Kern County earthquake (Taft 1952 N21E), compressed in time by a factor of 5. Test data were not available.

6.2.2.2. Bonacci (1989)

Most specimens in the dataset were frame structures, wall structures, or frame-wall structures. The specimens tested by Bonacci (1989) were more idealized. They consisted of a mass that pivoted about a hinge connected to the simulator platform, with a flexural member on one side that resisted lateral demand through single curvature (Figure 6-4). The flexural member was 8 in. deep and 4 in. wide, with a length that varied by specimen. Each specimen was subjected to three different ground motions along one axis. The first motion was modeled after the N21E component of the recording at Castaic obtained during the 1971 San Fernando earthquake (Castaic 1971 N21E). The second was modeled after El Centro 1940 NS. The third was modeled after the S48E component of the recording at Santa Barbara Courthouse obtained during the 1952 Kern County earthquake (Santa Barbara 1952 S48E). All records were compressed in time by a factor of 2. Acceleration recordings were available for these tests [Sozen et al. (2015)].

6.2.2.3. Elwood and Moehle (2003)

The specimens tested by Elwood and Moehle were two-bay planar frames with a clear height of 58 in. (Figure 6-5). The outermost columns in these frames were circular, with a diameter of 10 in. The innermost was square with a 9 in. x 9 in. cross section. The frames were subjected to ground motions along one axis. The input motion was modeled after a recording from Viña del Mar, obtained during the 1985 Chile earthquake. This record was compressed in time by a factor of $\sqrt{2}$. Columns in both specimens failed in shear during the ground motion. They are included in the dataset, but marked using an X in plots. Data were unavailable for these tests.

6.2.3. MDOF Tests

Investigations of MDOFs included in this dataset that also are compiled in Lepage (1997) include:

- Tests by Otani and Sozen (1972) of scaled, 3-story 1-bay frames
- Tests by Aristizabal and Sozen (1976) of scaled, 10-story coupled walls
- Tests by Lybas and Sozen (1977) of scaled, 6-story coupled walls
- Tests by Healey and Sozen (1978) of scaled, 10-story 3-bay frames with a soft first story
- Tests by Moehle and Sozen (1978) of scaled, 10-story 3-bay frames with a soft first story and discontinuous first-level beam
- Tests by Abrams and Sozen (1979) of scaled, 10-story 3-bay frames in parallel with walls
- Tests by Cecen (1979) of scaled, 10-story 3-bay frames
- Tests by Moehle and Sozen (1980) of scaled, 9-story 3-bay frames in parallel with walls of varying height (no wall, 1-story wall, 4-story wall, or 9-story wall)
- Tests by Wolfgram (1984) of scaled, 7-story 3-bay frames with infilled RC walls
- Tests by Schultz (1985) of scaled, 9-story 3-bay frames with yielding columns
- Tests by Eberhard and Sozen (1989) of scaled, 9-story 3-bay frame wall structures

These structures were all tested on the unidirectional earthquake simulator at the University of Illinois Urbana-Champaign [Sozen et al. (1969)]. This is the same earthquake simulator used to test the frames in this investigation (although some of its components have been changed since its installation at Bowen Laboratory). Structures in the aforementioned studies had 3 to 10 stories and first-mode periods ranging from 0.09 sec to 0.22 sec. Summaries for the structures tested in these investigations have been compiled by Lepage (1997).

Tests in the dataset that were not in Lepage's dataset include:

- Tests by Shahrooz and Moehle (1987) on a scaled, 6-story, 2-bay by 2-bay frame building with setbacks
- Tests by Panagiotou et al. (2007) on a full-scale, 7-story building slice with shear walls and frames
- Tests reported on by Sugimoto et al. (2016) on a scaled 20-story, 3-bay by 2-bay frame building

The structures in these studies had 6 to 20 stories and first-mode periods ranging between 0.26 to 0.57 sec.

6.2.3.1. Shahrooz and Moehle (1987)

The structure tested by Shahrooz and Moehle was a 1/4-scale model of a two-bay by two-bay, 6-story moment resisting frame building. The structure is illustrated in Figure 6-6. Stories 4, 5, and 6 were setback so that there was only a single bay in the longitudinal direction on these levels. In the longitudinal direction, 7 in. x 5 in. (depth x width) beams spanned 75 in. (center-to-center). In the transverse direction, 7.5 in. x 4 in. beams spanned 45 in. (center-to-center). Floor slabs were 1.75 in. thick throughout. Each story of the frame measured 36 in. from top-of-slab to top-of-slab. The columns on the first story measured 6.5 in. x 5 in. (dimensions: longitudinal x transverse). The columns were fixed at their base into foundation blocks measuring 16 in. x 16 in. x 12 in. (length x width x depth). These foundation blocks were fastened to the simulator platform. The average concrete compressive strength was 4,200 psi. The average modulus of elasticity was approximately 3,100 ksi.

The structure was tested at the University of California, Berkeley. Before testing, additional lead masses were fastened to each level to simulate service dead load. On the second through fourth floor slabs, the weight of added masses was approximately 10.9 kips. On the fifth floor, sixth floor,

and roof slabs (which had less area than the other floors), the weight of added masses was approximately 6 kips.

The structure was subjected to ten simulated earthquakes. During phase 1 of testing, ground motions were applied along the longitudinal direction of the structure. During phase 2, the structure was rotated 45 degrees on the platform and motions were applied along this 45 degree axis. Only the motions from phase 1 were included in the dataset. These motions were modeled after the El Centro 1940 NS record, compressed in time by a factor of 2. Test data were available for this structure and were used to determine PGA, PGV, and D_{max} . For T_i and Γ , values reported in Shahrooz and Moehle (1987) were used.

6.2.3.2. *Panagiotou et al. (2007)*

The structure tested by Panagiotou et al. (2007) was a full-scale slice of a 7-story prototype residential building. The structure is illustrated in Figure 6-7. It incorporated shear walls in both directions, gravity columns on the north and south sides, and a post-tensioned segmental piers on the west side. In the north-south direction, lateral resistance was provided by a shear wall and post-tensioned concrete columns. The shear wall was 16 ft long with a thickness of 8 in. on the first story and 6 in. on the second through seventh stories. Each post-tensioned column was 18 in. x 18 in. The two post-tensioned columns were connected by a web wall 48 in. long and approximately 8 in. thick. In the east-west direction, lateral resistance was provided by a shear wall with a length of 12 ft. This wall was 8 in. thick on the first and seventh stories, and 6 in. thick on the second through sixth stories.

Each level had a slab measuring 12 ft x 26 ft x 8 in. thick. Each story had a clear height of 100 in. (108 in. top-of-slab to top-of-slab). All vertical members were terminated in foundation blocks fastened to the simulator platform. The average concrete compressive strength was 5,500 psi.

Added masses ranged from 52.2 kip on the seventh floor to 69.5 kips on the first floor. The structure was tested at the University of California, San Diego on the Large High Performance Outdoor Shake Table (LHPOST). It was subjected to four simulated earthquakes of increasing demand. The first motion was the longitudinal component of the recording at Van Nuys obtained during the 1971 San Fernando earthquake. The second motion was the transverse component from the same station and earthquake. The third motion was the longitudinal component of the recording at Woodland Hills Oxnard Boulevard obtained during the 1971 San Fernando earthquake. The final motion was the NS component of the recording from Sylmar Olive View Medical Center obtained during the 1994 Northridge earthquake. Test data were available for this structure, but could not be interpreted with certainty so values from reports were used instead.

6.2.3.3. Sugimoto et al. (2016)

Reports about this structure date back to 2013, but these early reports are available only in Japanese. The first report available in English was published by Sugimoto et al. (2016).

The structure was a 1/4-scale model of a three-bay by two-bay, 20-story frame building as shown in Figure 6-8. In both directions, 7.9 in. x 5.9 in. beams spanned 64 in. center-to-center. Floor slabs were 3.15 in thick throughout. Each story had a height of 29.5 in. from top-of-slab to top-of-slab. Columns were 8.9 in. square throughout, with a clear height of 21.6 in. The columns were fixed at their base into foundation blocks that were fastened to the simulator platform. The concrete compressive strength ranged from 12,300 psi on the bottom eight floors to 6,300 psi on the top top four floors. The modulus of elasticity ranged from 5,700 ksi on the bottom eight floors to 3,700 ksi on the top four floors.

The structure was tested on the E-Defense shake table in Miki City, Japan. The total mass at each level was 38.9 kips. It was subjected to five simulated earthquakes. In phase 1, ground motions

were applied in three directions (longitudinal, transverse, and vertical). These motions were modeled after the Tokyo Observed Wave recorded on 2011-March-11. The original records were compressed in time by a factor of 2. The transverse and vertical components were kept at a constant amplitude while the longitudinal component was increased in amplitude from 100% (test 1), to 200% (test 2), to 300% (test 3). During phase 2, motions were applied in only the longitudinal direction. The motion profiles during this phase were not from a recording obtained during an earthquake. Instead, they were artificial recordings referred to as the “Tsushima Artificial Wave.” These motions were applied at amplitudes of 150% (test 4) and 200% (test 5).

Test data were available for all tests in this structure and were used to determine PGA, PGV, and D_{\max} [NIED (2016)]. The initial period and mode shape were obtained from models created in SAP2000 [Computers and Structures, Inc. (2015)]. Details of the models for this building are described in the Appendices.

One irregularity was observed for the artificial ground motions used in tests 4 and 5. The PGVs obtained from the acceleration histories for these tests were 7.4 in./sec and 9.8 in./sec respectively. The average spectral velocities in the nearly constant velocity region of response were 30 in./sec and 40 in./sec, respectively (for 2% critical damping). These correspond to velocity amplification factors of nearly 4.1. This is twice the mean typical velocity amplification factor $F_v = 2.03$ proposed by Newmark in 1982 (discussed in Section 6.2.1.2). To obtain a better representation of the spectra that governed the response of the structure, the values of PGV used in Equation 6-1 were obtained as $S_{v,avg}/2.03$. The values obtained by integrating ground acceleration were ignored.

6.2.4. Instrumented Buildings

Instrumented buildings offer few, but valuable, data points. The following instrumented buildings were included in the dataset:

- Van Nuys Holiday Inn, Van Nuys, California, United States
- Millikan Library, California Institute of Technology, Pasadena, California, United States
- Building of the Department of Civil Engineering and Architecture, Tohoku University, Sendai, Japan

These buildings had 7 to 9 stories and their first mode periods ranged from 0.4 to 1 sec (considering both longitudinal and transverse directions).

6.2.4.1. Van Nuys Holiday Inn

The Van Nuys Holiday Inn is a 7-story RC frame building that was constructed in 1966. It experienced earthquakes in 1971 (San Fernando), 1987 (Whittier), and 1994 (Northridge). The structure and its response to these earthquakes are detailed in Lepage (1997).

Plan and elevation views of the building are shown in Figure 6-9. The building is rectangular in shape with no setbacks. In the longitudinal direction (east-west), the building has 8 bays at 18 ft 9 in. each (center-to-center). In the transverse direction (north-south), the building has 3 bays with spans of 20 ft, 20 ft 10 in., and 20 ft. The first story is 13 ft 6 in. tall (top-of-slab to top-of-slab). The second through seventh stories are approximately 8 ft 8 in. tall. Exterior columns are 14 in. x 20 in. on all stories. Interior columns are 20 in. x 20 in. on the first story, and 18 in. x 18 in. on upper stories. Beam depths are 30 in. on the first floor, and 22.5 in. on the upper floors. The roof beams are 22 in. deep. Slab thicknesses are 10 in. for the second floor, 8.7 in. for the third through seventh floors, and 7.9 in. for the roof slab. Concrete compressive strength ranged from 4,900 psi in the columns on the first floor to 3,000 psi at the roof.

Accelerometers on the ground floor, third floor, and roof recorded the 1971 San Fernando earthquake. Later, additional accelerometers were installed on additional intermediate floors. These accelerometers were present during the 1987 Whittier earthquake and the 1994 Northridge earthquake. The building experienced minor structural damage during the 1971 San Fernando earthquake and was repaired using epoxy [Blume and Associates (1973)]. All parameters used in the dataset were obtained from Lepage (1997).

6.2.4.2. Millikan Library

The Millikan Library is a 9-story RC frame building that was constructed in 1967. It has been a subject of much investigation, with detailed reports by Kuroiwa (1967), who studied the building using vibration generators during and after construction, and by Iemura and Jennings (1973), who studied the response of the building during the 1971 San Fernando earthquake.

The main portion of the building is 75 ft x 69 ft (east-west x north-south). Additional enclosures on the east and west ends include curved walls. In the north-south direction, lateral resistance is provided by 12-in. thick reinforced concrete shear walls on the exterior of the building. In the east-west direction, lateral resistance is provided by a box of 12-in. thick shear walls that form the service core of the building. The first story is 16 ft tall. Upper stories are 14 ft tall. Slabs are 10 in. thick throughout, and beams are 36 in. x 24 in. (depth x width) throughout.

Before the 1971 San Fernando earthquake, the building was instrumented with triaxial accelerometers in the basement and on the roof. Only the response of the building to this earthquake was included in the dataset. All parameters were obtained from the report by Iemura and Jennings (1973).

6.2.4.3. Building of the Department of Civil Engineering and Architecture

The Building of the Department of Civil Engineering and Architecture was built in 1969. It was a 9-story steel-reinforced concrete (SRC) structure with a 2-story podium (Figure 6-11). The building experienced earthquakes in 1978 (Miyagi-Ken-Oki) and in 2011 (Tohoku). Between these events, the building was retrofitted by replacing shear walls in the north-south direction. For this reason, only the response of the building to the earthquake in 1978 is considered in this dataset. The building is described in Shiga et al. (1981), Wang et al. (2012), and Wang and Pujol (2014).

The building footprint was approximately 210 ft x 110 ft (east-west x north-south, 64 m x 33.6 m). In the lower two stories (i.e. the podium), the floor plan was eight bays by four bays. In the upper seven stories, the floor plan was five bays by two bays. Lateral resistance in the north-south direction was provided by a combination of frames and exterior shear walls bounded by columns. These shear walls were approximately 9.8 in. thick and 22 ft long. Columns were 33.5 in. square. In the east-west direction, lateral resistance was provided by frames and shear walls around a service core. Story heights were approximately 16.4 ft (first story), 14.1 ft (second story), 12.5 ft (third story), and 10.8 ft (remaining stories).

Accelerometers installed on the first and ninth stories recorded response of the building to earthquakes in 1978 and 2011. Parameters for the dataset were obtained from the reports by Wang et al. (2012) and Wang and Pujol (2014).

6.3. Evaluation

A plot of measured versus estimated peak drift ratio (obtained from Equation 6-1) is presented in Figure 6-12. In nearly half of the cases, peak drift was underestimated. To examine possible sources of this lack of conservatism, the ratio of measured-to-estimated peak drift (D_{\max}/S_{dv}) was plotted against:

- Peak ground acceleration (PGA) in Figure 6-13
- Peak ground velocity (PGV) in Figure 6-14
- The ratio of measured-to-calculated initial first-mode period ($T_{\text{meas}}/T_{\text{calc}}$) in Figure 6-15
- Measured drift ratio (D_{\max}/H , where H is structure height) in Figure 6-16

None of these figures shows a clear and consistent trend, prompting the need to consider other combinations of parameters.

In a study of more than 80 ground motions recorded on the west coast of the United States, Hall et al. (1976) observed a minimum ratio of $PGV/PGA = 0.03$ sec. In the dataset compiled in this study, nearly half the cases had PGV/PGA ratios below this value. This is because, for small-scale structural models (which constitute a large portion of the dataset), experimental constraints such as scale and capacities of the earthquake simulator often lead to the need to use “compressed” ground motions that can have lower PGV/PGA ratios than full-scale motions. Compressed ground motions are created by decreasing the time step of the original acceleration record. This leads to records with the same PGA, but lower PGV, than the full-scale source record. The result is a record with a lower ratio of PGV/PGA than the full-scale source record.

In Figure 6-17 and Figure 6-18, D_{\max}/S_{dv} is plotted against PGV/PGA . The minimum and median ratios of PGV/PGA observed by Hall et al. (1976) for ground motions with $PGA > 0.2$ g are also

shown in these figures. A downward trend of D_{\max}/S_{dv} with increasing PGV/PGA can be seen in both figures, crossing the 1:1 line at approximately PGV/PGA = 0.03 sec. This crossing was used to separate the dataset into two parts: (1) tests with PGV/PGA < 0.03 sec, and (2) tests with PGV/PGA \geq 0.03 sec.

Statistics are presented in Table 6-5 for these two ranges of PGV/PGA ratios. In Figure 6-19, measured drift ratio is plotted against estimated drift ratio (from Equation 6-1). For 64% of the cases with PGV/PGA < 0.03 sec, peak drifts were underestimated (i.e. estimated unconservatively). In contrast, for 80% of the cases with PGV/PGA > 0.03 sec, peak drifts were overestimated (i.e. estimated conservatively). In the latter case (PGV/PGA > 0.03 sec), the mean ratio of D_{\max}/S_{dv} was 0.85 and the standard deviation was 0.23. This suggests that Equation 6-1 would produce reasonable and safe estimates for full-scale structures, which supports the idea that drift demand is proportional to initial period (calculated from gross cross-sectional properties). This idea in turn supports the hypothesis stated in Section 3.1.

The scatter in Figure 6-17 suggests that a simplification could be made to Equation 6-1 for MDOF structures without adversely affecting the results:

$$S_{dv} = PGV * T_i \quad \text{Equation 6-3}$$

Using this expression, peak roof drift was recalculated for MDOF structures in the dataset. The new ratios of D_{\max}/S_{dv} obtained from this process are plotted in Figure 6-20 (SDOF cases are shown in gray because calculated S_{dv} were unchanged for SDOFs). Summary statistics are presented in Table 6-6. The trend was similar to what was observed for Equation 6-1. For the 85 cases with PGV/PGA > 0.03 sec, peak drift was overestimated 85% of the time using this simplified equation. The mean ratio of D_{\max}/S_{dv} was 0.81, and the standard deviation was 0.22.

In Equation 6-3, the sole parameter describing the structure is calculated initial period based on gross cross-sectional properties. That peak drift was estimated safely in 85% of cases with $PGV/PGA > 0.03$ sec, and that the mean was 0.81 provides additional support that peak drift is driven by initial period (and stiffness).

6.4. Ground Motions with Low PGV/PGA Ratios

To examine in more detail the effect of low PGV/PGA ratios on peak drift, bilinear numerical models of SDOF systems were subjected to eight full-scale (i.e. uncompressed) ground motion records. Two types of records were used: (1) with PGV/PGA more than 0.1 sec, and (2) with PGV/PGA approximately 0.03 sec or lower. For (1), El Centro 1940 NS and EW were used. For (2), both components of three records obtained during three different earthquakes were used. These records and the criteria for selecting them are described next.

All records were obtained from the PEER NGA database [Chiou et al. (2008)]. This database includes more than 20,000 ground motion recordings from around the world. Of these, approximately 100 had PGV/PGA ratios of 0.03 sec or lower and PGAs more than 0.1 g (<0.5% of all entries in the database). Of these, 37 had PGAs of 0.2 g or more (<0.2% of all entries in the database).

The database was searched to locate records meeting the following criteria: (1) PGV/PGA approximately 0.03 sec or less, (2) PGA larger than 0.2 g, and (3) recorded on the west coast of the United States. The last criterion was set because the lower bound of $PGV/PGA = 0.03$ sec was based on a study of ground motions recorded on the west coast the United States [Hall et al. (1976)]. Of the recordings meeting these criteria, the three with the largest PGVs were selected for use. The selected records and their characteristics are summarized in Table 6-7. The acceleration histories from these records and the El Centro 1940 records were scaled in amplitude so that each would

produce a PGV of 20 in./sec when integrated. The resulting records are referred to as “PGV-normalized” records. Displacement response spectra for these “PGV-normalized” records are presented in Figure 6-21. At periods below $T=0.3$ sec, spectral drifts for records with low PGV/PGA ratios were larger than those with higher PGV/PGA ratios (i.e. El Centro 1940 records). Above $T=0.3$ sec, spectral drifts for records with higher PGV/PGA ratios continued to increase, while spectral drifts for records with low PGV/PGA ratios decreased and then flattened out. This suggested that structures with short periods – below 0.3 sec – could be expected to reach higher drifts when subjected to motions with low PGV/PGA ratios than if subjected to records with higher PGV/PGA ratios.

To study this in more detail, the program PRISM [Jeong et al. (2016)] was used to examine the drift response of numerical models of SDOF systems to each “PGV-normalized” record. The models were bilinear, with periods of 0.1, 0.2, 0.3, 0.4, or 0.5 sec. Two base shear coefficients were considered: 0.2 and 0.3. After each model reached its base shear strength, its stiffness reduced to 2% of its initial stiffness. The peak drifts reached by the models for each ground motion are summarized in Table 6-8. These drifts are plotted Figure 6-22 and Figure 6-23 against period. For models with periods less than 0.3 sec, peak drifts were larger for motions with low PGV/PGA ratios. But for models with periods more than 0.3 sec, peak drifts were larger for records with higher PGV/PGA ratios. This was consistent with the shapes of the linear response spectra.

Overall, the shapes of the displacement response spectra and analyses of bilinear SDOFs suggest that structures with low periods that experience ground motions with low PGV/PGA ratios can reach larger peak drifts than if they had experienced ground motions with the same PGV but higher PGV/PGA ratios. In addition, the scarcity of strong ground motions with PGV/PGA ratios less than 0.03 sec shows that strong ground motions with $PGV/PGA < 0.03$ sec occur infrequently.

6.5. Summary

In this chapter, an equation proposed by Sozen (2003) as an estimate of peak drift in RC structures subjected to ground motions was evaluated using results from more than 160 tests of reinforced concrete structures on earthquake simulators and the measured responses of three instrumented buildings. This equation expresses peak drift in terms of PGV and initial period. Overall, the equation was found to provide safe and reasonable estimates for peak drift for RC structures subjected to ground motions with PGV/PGA ratios above 0.03 sec. Ground motions with PGV/PGA ratios below this have been observed, but are expected to occur infrequently. The findings suggest that initial period (and by association, initial stiffness) calculated from gross cross-sectional properties is a dominant factor driving the peak drift response of RC structures.

CHAPTER 7. SUMMARY AND CONCLUSIONS

This investigation was conducted to test the idea that initial stiffness drives the peak drift response of reinforced concrete (RC) structures subjected to strong ground motions. Experiments were conducted to test the hypothesis that two RC structures with similar initial stiffness and nominal strength, but different post-cracking stiffnesses, would reach similar peak drift during a given ground motion. The results of these experiments prompted the need to evaluate an expression for estimating peak drift in terms of initial period and peak ground velocity [Sozen (2003)].

7.1. Experimental Work

Four reinforced concrete portal frames were tested on an earthquake simulator. The frames were identical except for column longitudinal reinforcement. In type C frames, conventional reinforcing steel was used at a reinforcement ratio of 1.8%. In type H frames, high-strength reinforcing steel was used at a reinforcement ratio of 0.8%. The frames were tested in two series. In Series 1, frames C1 and H1 were subjected to four ground motions of increasing demand, followed by a fifth motion at the strongest demand. In Series 2, frames C2 and H2 were subjected to four ground motions of decreasing demand, followed by a fifth motion at the strongest demand.

The as-tested frames had similar initial periods, but on average type H frames had less than half the post-cracking stiffness and reached half the peak resistance of type C frames. In spite of these differences, peak drifts in type H frames were not systematically larger than in type C frames. In eight out of ten comparisons (all but the weakest ground motion), peak drifts of the two frame types were within 20% of one another. In four out of ten comparisons, peak drifts were smaller in type H frames. Similarly, frames that experienced previous ground motions reached comparable peak

drifts to otherwise identical frames that had experienced fewer or weaker ground motions before the same event. In short, lower post-cracking stiffness, lower strength, and softening caused by damage from previous motions were not observed to lead consistently to larger peak drifts. These results suggest that peak drift was driven by the initial stiffness of the frames.

7.2. Dataset to Evaluate Equation for Estimating Peak Drift

Initial stiffness (or period) has been suggested before as one of the dominant factors that drives peak drift response [Sozen (2003)]. The peak drifts of the frames tested here exceeded (by as much as 120%) the estimated peak drifts obtained from the following expression [Sozen (2003)]:

$$S_{dv} = PGV * T_i * \Gamma / \sqrt{2} \quad \text{Equation 7-1}$$

where S_{dv} is estimated peak drift, PGV is peak ground velocity, T_i is calculated initial first-mode period, and Γ is first-mode participation factor. This expression was proposed as a reasonable upper bound estimate of peak drift caused by earthquake demands in the nonlinear range of response. The fact that the expression did not provide an upper bound estimate of peak drifts for the frames tested here prompted the need for further investigation. To that end, a dataset was created containing summary test results from more than 160 tests of five dozen RC structures, three of which were instrumented buildings. Peak drift estimates obtained from Equation 7-1 were compared to measured peak drifts for each test (or event, in the case of instrumented buildings).

Equation 7-1 was found to provide an upper bound estimate of peak drift for 80% of cases with $PGV/PGA > 0.03$ sec. This lower bound corresponds to the minimum PGV/PGA ratio observed for dozens of full scale ground motion records [Hall et al. (1976)]. For small-scale structural models like those tested in this study, experimental constraints often require the use of “compressed” ground motion records, in which the duration of motion is shortened by decreasing the time step. In the dataset used to evaluate Equation 7-1, compression factors as large as 8 were considered.

Compression of ground motion records can lead to PGV/PGA ratios less than 0.03 sec (i.e. lower than what are commonly seen for full-scale records). For tests with PGV/PGA < 0.03 sec (including the tests conducted as part of this investigation), measured peak drift exceeded S_{dv} in 64% of cases, by as much as 145%. This suggests that, although Equation 7-1 did not provide a conservative estimate of drift for scaled structures with PGV/PGA < 0.03 sec, it should produce reasonable and safe estimates for full-scale RC structures.

7.3. Conclusions

The tests described here supported the hypothesis that peak drift response of a RC structure is dominated by the initial stiffness (and period) of the structure, estimated from gross cross-sectional properties. This implies that the reduction in reinforcement ratio from substituting a reduced amount of higher grade steel reinforcement should not lead to consistently larger peak drifts, because such a substitution does not lead to a large change in initial stiffness. It also implies that softening as a result of damage from previous motions should not consistently lead to larger peak drifts. Evaluation of the expression proposed by Sozen (2003), which states peak drift in terms of initial period and PGV, supported this idea.

TABLES

Table 2-1: Summary of previous quasi-static investigations of high-strength steel reinforced concrete members.

Year	First Author	Specimens	Study Focus	Primary Variables	Longitudinal f_y range	Major Findings
1962	Hognestad	36 rectangular beams	Flexural crack control	Longitudinal bar yield stress, bar diameter, specimen length, concrete strength, concrete cover, reinforcement ratio	45 – 110 ksi	<ul style="list-style-type: none"> • Crack width is proportional to steel stress • Deformed bars are effective for crack control
2002	Ansley	8 rectangular beams	Flexural and shear behavior, splice length	Longitudinal bar yield stress, splice length, specimen geometry, transverse reinforcement, load protocol	not reported	<ul style="list-style-type: none"> • HSSRC has comparable flexural and shear performance • Grade-60 lap splices and embedments may not be adequate for high-strength
2003	Yotakhong	4 rectangular beams	Flexural behavior, response to displacement reversals	Longitudinal bar yield stress, reinforcement ratio, load protocol	63 – 124 ksi	<ul style="list-style-type: none"> • All HSSRC specimens exhibited ductile behavior • Flexural behavior can be modeled using current reinforced concrete theories • Better crack control after yielding in HSSRC specimens
2003	Okamoto	4 rectangular columns	Response to load reversals	Longitudinal bar yield stress, concrete strength	52 – 103 ksi	<ul style="list-style-type: none"> • More yield displacement in HSSRC specimens • Reduced equivalent damping in HSSRC specimens
2006	Restrepo	2 circular columns*	Response to load reversals	Longitudinal bar yield stress, bar diameter, reinforcement ratio	60 – 135 ksi	<ul style="list-style-type: none"> • Bridge columns built using HSSRC can form plastic hinges • Columns built with HSSRC can sustain drifts up to 4%

Table 2-1 (continued): Summary of previous quasi-static investigations of high-strength steel reinforced concrete.

Year	First Author	Specimens	Study Focus	Primary Variables	Longitudinal f_y range	Major Findings
2009	Ousalem	3 square columns	Response to varying axial load and displacement reversals	Longitudinal bar yield stress, Column axial load	107 – 174 ksi	<ul style="list-style-type: none"> • Higher ductility and lower residual deformation in specimen with higher strength longitudinal bars
2011	Rautenberg	11 rectangular columns	Response to displacement reversals	Longitudinal bar yield stress, longitudinal reinforcement ratio, transverse reinforcement ratio, volume fraction of steel fibers	64 – 134 ksi	<ul style="list-style-type: none"> • HSSRC specimens sustained drifts from 4% to 8% • Lower energy dissipation in HSSRC specimens
2011	Tavallali	7 rectangular beams	Response to displacement reversals	Longitudinal bar yield stress, longitudinal reinforcement ratio, transverse reinforcement ratio, volume fraction of steel fibers	65 – 97 ksi	<ul style="list-style-type: none"> • HSSRC specimens had drift ratio capacities comparable to CRC specimens • HSSRC specimens showed approximately 25% more yield displacement than CRC specimens
2015	Ou	8 square columns	Shear behavior of HSSRC columns under low axial load	Column axial load, concrete compressive strength, transverse reinforcement ratio	107 ksi	<ul style="list-style-type: none"> • Specimens failed in shear before longitudinal yielding, as they were designed to

*Transverse reinforcement welds in HSSRC specimen failed before test completion

Table 2-1 (continued): Summary of previous quasi-static investigations of high-strength steel reinforced concrete.

Year	First Author	Specimens	Study Focus	Primary Variables	Longitudinal f_y range	Major Findings
2012	Pfund	4 rectangular beams	Response to displacement reversals	Longitudinal bar yield stress, longitudinal reinforcement ratio, transverse reinforcement ratio, volume fraction of steel fibers	65 – 125 ksi	<ul style="list-style-type: none"> • HSSRC sustained drift cycles of 5% without failure • Calculated maximum probable strength for HSSRC specimens based on $1.5f_y$ was within 5% of the measured value
2012	Tretiakova	2 rectangular columns	Response to displacement reversals	Transverse reinforcement ratio, volume fraction of steel fibers	97 ksi	<ul style="list-style-type: none"> • Specimens maintained more than 80% of their capacity while sustaining drift cycles up to 5% • Specimen crack widths were larger than crack widths of equivalent sections reinforced with conventional steel**

**Equivalent conventionally-reinforced sections were tested by Rautenberg (2011)

Table 2-2: Summary of previous dynamic investigations of conventionally reinforced concrete.

Year	First Author	Dynamic Specimens	Study Focus	Primary Variables	Base Motion*	Major Findings
1970	Takeda	3 rectangular cantilevers	Earthquake response development of hysteretic models	Base motion source, base motion history, base motion intensity	S, P, E	<ul style="list-style-type: none"> • Dynamic response can be estimated satisfactorily using static force-displacement information • Hysteretic model developed
1971	Gulkan	7 one-story one-bay frames	Effect of material nonlinearity on earthquake response	Frame geometry, column reinforcement, base motion source, base motion history intensity	S, E	<ul style="list-style-type: none"> • Maximum response may be estimated using linear response spectrum with reduced stiffness and increased equivalent damping • Slip of anchored reinforcement contributes significantly to total drift
1972	Otani	3 pairs three-story one-bay frames	Earthquake response of multistory frames	Frame strength, base motion source, base motion history intensity	E	<ul style="list-style-type: none"> • First mode equivalent viscous damping factors ranged from 4 - 7% of critical even after severe damage • Maximum displacements calculated from first mode agree favorably with those from response-history analysis
1979	Cecen	2 pairs ten-story three-bay frames	Elastic and inelastic response of multistory frames	Base motion history intensity	E	<ul style="list-style-type: none"> • The same base motion will yield same response regardless of load history, provided that previous load history intensity does not exceed load history under consideration

*Base Motion Types :: S = sinusoidal, P = pulse, E = earthquake

Table 2-2 (continued): Summary of previous dynamic investigations of conventionally reinforced concrete.

Year	First Author	Dynamic Specimens	Study Focus	Primary Variables	Base Motion*	Major Findings
1987	Morrison	3 plate-column assemblies	Static and dynamic response of plate-column assemblies	Slab reinforcement ratio, amount of vertical load, loading protocol	S, E	<ul style="list-style-type: none"> Because of strain rate, dynamic specimens displayed 20-30% increase in strength compared to static specimens
1989	Bonacci	15 rectangular cantilevers	Drift response estimation	Specimen strength and initial period, base motion source, base motion intensity	E	<ul style="list-style-type: none"> Idealized linear response spectrum with 2% damping provides a good estimate of overall drift response
2000	Dodd	14 circular cantilever columns	Strength and ductility capacity of circular columns	Column aspect ratio, axial load, base flexibility, base motion, base motion history	E	<p>Dynamic specimens displayed 10% minimum increase in strength compared to static specimens</p> <p>Analytical models developed from static tests can be used to predict dynamic behavior of columns</p>
2012	Ghannoum	1 three-story three-bay frame	Dynamic response of strong-beam weak-column type construction	Base motion history intensity	E	<p>Column shear and axial behavior was affected by large past deformations and small deformation cycling</p>

*Base Motion Types :: S = sinusoidal, P = pulse, E = earthquake

Table 3-1: Selected properties of four test specimens.

Category			Frame			
			C1	C2	H1	H2
Test series			1	2	1	2
Column Dimensions	b	in.	5	5	5	5
	h	in.	5	5	5	5
	L	in.	42	42	42	42
	d	in.	4	4	4	4
	d'	in.	1	1	1	1
Longitudinal Reinforcement	d _b	in.	3/8	3/8	1/4	1/4
	ρ_ℓ	%	1.8	1.8	0.8	0.8
	f _y	ksi	65	65	162	162
	f _u	ksi	102	102	187	187
	$\rho_\ell f_y$	ksi	1.17	1.17	1.3	1.3
Transverse Reinforcement	d _t	in.	3/16	3/16	3/16	3/16
	s	in.	1	1	1	1
Concrete Properties	f' _c	psi	3,930	3,860	3,660	3,840
	f _t	psi	410	430	420	400
	f _r	psi	--	860	850	--
	E _c	ksi	--	2,620	2,760	--
Series : 1 – motion order: 25%, 50%, 75%, 100%, 100% 2 – motion order: 100%, 75%, 50%, 25%, 100%						
b : Width of compression face of column						
h : Overall thickness of column						
L : Clear height of column						
d : Distance from extreme compression fiber to farthest longitudinal steel layer						
d' : Distance from extreme compression fiber to nearest longitudinal steel layer						
d _b : Diameter of longitudinal reinforcing bar						
ρ_ℓ : Longitudinal reinforcement ratio based on gross cross-sectional area						
f _y : Measured yield stress of longitudinal reinforcement (0.2% offset method)						
f _u : Measured strength of longitudinal reinforcement						
$\rho_\ell f_y$: Product of longitudinal reinforcement ratio and measured yield stress						
d _t : Diameter of transverse reinforcing bars						
s : Spacing of transverse reinforcing bars from end of columns to distance 3d						
f' _c : Measured compressive strength of concrete (established on test day)						
f _t : Measured tensile strength of concrete (established on test day)						
f _r : Measured modulus of rupture of concrete (established on test day)						
E _c : Measured modulus of elasticity of concrete (established on test day)						

Table 3-2: Selected calculated properties of test specimens (used in LARZ models).

Property			Type C	Type H
Modulus of elasticity	E_c	ksi	2,700	2,700
Column moment of inertia	I_g	in. ⁴	52	52
Column trilinear approximation				
Bending moment	M_{cr}	kip-in.	11	11
	M_y	kip-in.	64	65
	M_u	kip-in.	67	68
Curvature	ϕ_y	1/in.	1.5e-3	2.1e-3
	ϕ_u	1/in.	3.5e-3	3.2e-3
Flexural stiffness	$(EI)_g$	kip-in. ²	140,400	140,400
	$(EI)_s$	kip-in. ²	42,700	31,000
	$(EI)_{cr}$	kip-in. ²	37,300	26,700
Effective mass	m	kip-sec ² /in.	0.013	0.013
Fundamental period of frame	T_i	sec	0.11	0.11
	T_s	sec	0.19	0.23
	T_{cr}	sec	0.21	0.24
I_g : Gross moment of inertia, = $bh^3/12$ M_{cr} : Moment at cracking (from FLECHA M- ϕ relationship assuming $f_t=f'_c/10$) M_y : Moment at yielding (from FLECHA, trilinear M- ϕ approximation) M_u : Moment at ultimate (from FLECHA, trilinear M- ϕ approximation) ϕ_{cr} : Curvature at cracking = M_{cr}/E_cI_g ϕ_y : Curvature at yielding (from FLECHA, trilinear M- ϕ approximation) ϕ_u : Curvature at ultimate (from FLECHA, trilinear M- ϕ approximation) $(EI)_i$: Initial stiffness = E_cI_g $(EI)_s$: Secant stiffness to yielding = M_y / ϕ_y $(EI)_{cr}$: Cracked stiffness = $(M_y - M_{cr}) / (\phi_y - \phi_{cr})$ m : Effective mass of system, = W_{me}/g , where $W_{me} = 5$ kip T_i : Initial first-mode period corresponding to gross stiffness, = $2\pi \sqrt{\frac{mL^3}{2*12(EI)_g}}$ T_s : Initial first-mode period corresponding to secant stiffness, = $2\pi \sqrt{\frac{mL^3}{2*12(EI)_s}}$ T_{cr} : Initial first-mode period corresponding to cracked stiffness, = $2\pi \sqrt{\frac{mL^3}{2*12(EI)_{cr}}}$				

Table 3-3: Breakdown of components adding up to effective mass of system.

Component	Quantity	Weight	
		each	total
Reusable mass	1	4,060	4,060
Lower steel plate (in portal)	1	180	180
Plates: PL7x7x1.75 (on top)	6	24	144
Plates: PL9x5x5x2 (underside @ ends)	2	25	50
End threaded rods (1.5"-6)	2	18	36
Portal threaded rods (1.25"-7)	4	12	48
Large nuts (1.5"-6)	4	1.3	5.2
Smalle nuts (1.25"-7)	8	0.8	6.4
Top beam	1	330	320
Two-thirds of columns	1	120	120
Total weight of effective mass, $W_{me} =$			4,980

Table 3-4: Summary of target ground motion characteristics for each base motion.

Characteristic	Ground Motion Amplitude*			
	25%	50%	75%	100%
Peak ground acceleration (PGA), g	0.25	0.50	0.74	1.0
Peak ground velocity (PGV), in./sec	2.7	5.5	8.2	11
Peak ground displacement (PGD), in.	0.32	0.65	0.97	1.3
*As a ratio of the strongest ground motion used in this investigation				

Table 3-5: Typical sequence of test procedure.

Task Nr.	Reps	Task Description
t0	(as needed)	Test instrumentation function
*t1	1	Open manifold
t2	1	Turn on low pressure
t3	1	Turn on high pressure
t4	3	Take zeroes
t5	1	Earthquake motion
t6	3	Take final position measurements
t7	1	Turn pressure off (to low, then off)
t8	5	Hammer tests (5 blows per repetition)*
<p>*Before the first test of a frame, a hammer test was conducted. For subsequent motions on a given frame, the hammer tests conducted after the previous motion were used to compute the initial stiffness of the frame for the run.</p>		

Table 4-1: Measured properties of ground motions during each test.

Property	Ground Motion	Target	Frame				Statistics	
			C1	C2	H1	H2	Mean	CoV*
PGA, g	25%	0.25	0.86	0.89	0.86	0.93	0.89	3.7%
	50%	0.50	1.52	1.32	1.28	1.37	1.37	4.3%
	75%	0.74	1.58	1.93	1.82	1.68	1.75	7.4%
	100%	1.0	2.10	2.58	2.02	1.91	2.15	14.5%
	100% (2)	1.0	1.98	1.98	1.98	1.94	1.97	2.5%
PGV, in./sec	25%	2.7	3.7	3.5	3.4	3.4	3.5	4.0%
	50%	5.5	6.9	6.9	6.5	6.3	6.7	4.5%
	75%	8.2	9.0	9.2	9.1	9.0	9.1	1.1%
	100%	11	11.3	11.9	11.6	11.4	11.6	2.3%
	100% (2)	11	11.8	11.4	11.8	11.1	11.5	3.0%
PGD, in.	25%	0.32	0.32	0.32	0.32	0.32	0.32	0%
	50%	0.65	0.64	0.65	0.65	0.65	0.65	0.8%
	75%	0.97	0.97	0.97	0.97	0.97	0.97	0%
	100%	1.3	1.3	1.3	1.3	1.3	1.3	0%
	100% (2)	1.3	1.3	1.3	1.3	1.3	1.3	0%

*CoV = Coefficient of variation, the ratio of the standard deviation to the average

Table 4-2: Effect of reducing lowpass filter frequency on PGA and PGV. Values generated from acceleration data using Butterworth bandpass filter with highpass frequency 0.5 Hz and lowpass frequency as specified below.

Parameter:		PGA, g				PGV, in./sec			
Lowpass frequency:		15 Hz	30 Hz	45 Hz	60 Hz	15 Hz	30 Hz	45 Hz	60 Hz
25% Motion	C1	0.34	0.55	0.73	0.86	3.55	3.73	3.74	3.74
	C2	0.42	0.62	0.79	0.89	3.24	3.54	3.52	3.50
	H1	0.36	0.59	0.76	0.86	3.22	3.36	3.41	3.43
	H2	0.39	0.66	0.84	0.93	3.06	3.42	3.40	3.42
	<i>Average</i>	<i>0.38</i>	<i>0.61</i>	<i>0.78</i>	<i>0.89</i>	<i>3.26</i>	<i>3.51</i>	<i>3.52</i>	<i>3.52</i>
	<i>CoV</i>	<i>9%</i>	<i>7%</i>	<i>6%</i>	<i>4%</i>	<i>6%</i>	<i>5%</i>	<i>4%</i>	<i>4%</i>
50% Motion	C1	0.60	1.00	1.31	1.52	6.82	6.84	6.85	6.86
	C2	0.64	0.94	1.18	1.32	6.53	6.74	6.82	6.85
	H1	0.65	0.92	1.12	1.28	6.02	6.30	6.44	6.49
	H2	0.65	0.94	1.20	1.37	6.22	6.29	6.32	6.34
	<i>Average</i>	<i>0.64</i>	<i>0.95</i>	<i>1.20</i>	<i>1.37</i>	<i>6.40</i>	<i>6.54</i>	<i>6.61</i>	<i>6.63</i>
	<i>CoV</i>	<i>4%</i>	<i>4%</i>	<i>7%</i>	<i>8%</i>	<i>5%</i>	<i>4%</i>	<i>4%</i>	<i>4%</i>
75% Motion	C1	0.90	1.22	1.45	1.58	8.85	8.97	9.01	9.03
	C2	1.01	1.43	1.72	1.93	9.05	9.30	9.25	9.22
	H1	0.93	1.34	1.65	1.82	8.82	8.95	9.04	9.07
	H2	0.89	1.16	1.49	1.68	9.00	9.04	9.02	9.02
	<i>Average</i>	<i>0.93</i>	<i>1.29</i>	<i>1.58</i>	<i>1.75</i>	<i>8.93</i>	<i>9.07</i>	<i>9.08</i>	<i>9.09</i>
	<i>CoV</i>	<i>6%</i>	<i>9%</i>	<i>8%</i>	<i>9%</i>	<i>1%</i>	<i>2%</i>	<i>1%</i>	<i>1%</i>
100% Motion (1)	C1	1.16	1.65	1.93	2.10	11.14	11.12	11.22	11.25
	C2	1.30	1.98	2.38	2.58	12.01	11.92	11.89	11.87
	H1	1.19	1.55	1.78	2.02	11.46	11.52	11.54	11.55
	H2	1.22	1.62	1.81	1.91	11.42	11.38	11.40	11.42
	<i>Average</i>	<i>1.22</i>	<i>1.70</i>	<i>1.98</i>	<i>2.15</i>	<i>11.51</i>	<i>11.49</i>	<i>11.52</i>	<i>11.52</i>
	<i>CoV</i>	<i>5%</i>	<i>11%</i>	<i>14%</i>	<i>14%</i>	<i>3%</i>	<i>3%</i>	<i>2%</i>	<i>2%</i>
100% Motion (2)	C1	1.15	1.52	1.76	1.98	11.70	11.76	11.79	11.80
	C2	1.16	1.60	1.84	1.98	11.39	11.38	11.37	11.39
	H1	1.13	1.45	1.75	1.98	11.59	11.66	11.76	11.80
	H2	1.22	1.60	1.73	1.94	11.01	10.96	11.04	11.09
	<i>Average</i>	<i>1.17</i>	<i>1.54</i>	<i>1.77</i>	<i>1.97</i>	<i>11.42</i>	<i>11.44</i>	<i>11.49</i>	<i>11.52</i>
	<i>CoV</i>	<i>4%</i>	<i>5%</i>	<i>3%</i>	<i>1%</i>	<i>3%</i>	<i>3%</i>	<i>3%</i>	<i>3%</i>

Table 4-3: Coefficients of variation for linear displacement response spectra (across all tests).

Ground Motion	Period Range	
	0.03 sec - 0.1 sec	0.1 sec - 0.4 sec
25%	19%	7%
50%	15%	6%
75%	14%	4%
100%	14%	4%
100% (2)	12%	4%

Table 4-4: Calculated and measured initial periods.

Parameter	Specimen			
	C1	C2	H1	H2
<u>Period, sec</u>				
Calculated	0.1	0.1	0.1	0.1
Hammer test*	**	0.15	**	0.12
High-pressure jerk	0.16	0.15	0.13	0.12
First test run	0.19	0.19	0.18	0.18
<u>Max displacement considered, in.</u>				
Hammer test*	**	0.004	**	0.003
High-pressure jerk	0.002	0.003	0.002	0.002
First test run	0.032	0.032	0.029	0.035
*Average from multiple tests				
**Frames C1 and H1 were subjected to hammer tests without lumped mass attached to the top beam. See Section A7.1				

Table 4-5: Measured in-plane response, specimen C1 (Figure 4-11 through Figure 4-15).

Parameter	Test ID				
	C1-25 (run 1/5)	C1-50 (run 2/5)	C1-75 (run 3/5)	C1-100 (run 4/5)	C1-100(#2) (run 5/5)
Test Date (2015-)	Sep-12	Sep-12	Sep-17	Sep-21	Sep-27
<u>Base Motion</u>					
Peak acceleration, g	0.86	1.52	1.58	2.10	1.98
Peak velocity, in./sec	3.7	6.9	9.0	11.3	11.8
Peak displacement, in.	0.32	0.64	0.97	1.3	1.3
<u>Response</u>					
Acceleration (abs.)					
Peak value, g	1.26	1.28	1.72	1.94	1.32
Time at peak, sec	2.88	3.28	4.69	4.03	5.44
Velocity					
Peak value, in./sec	9.5	17	30	38	27
Time at peak, sec	3.20	4.75	4.79	4.11	4.03
Displacement					
Peak value, in.*	0.27	0.78	1.25	1.69	1.37
Time at peak, sec	3.64	4.79	6.07	4.06	5.66
Residual drift at end of run, in.	0	0.05	-0.17	-0.16	0
Cumul. residual drift, in.	0	0.05	-0.12	-0.28	-0.28
<u>Period</u>					
Before run, sec	0.16**	0.30	0.32	0.32	0.47
After run, sec	0.30	0.32	0.32	0.47	0.55
*Single amplitude peak					
**Hammer test was only conducted without mass for this specimen. This value is taken from the platform jolt at the beginning of the test.					

Table 4-6: Measured in-plane response, specimen C2 (Figure 4-16 through Figure 4-20).

Parameter	Test ID				
	C2-25 (run 4/5)	C2-50 (run 3/5)	C2-75 (run 2/5)	C2-100 (run 1/5)	C2-100(#2) (run 5/5)
Test Date (2015-)	Dec-22	Dec-22	Dec-23	Dec-23	Dec-23
<u>Base Motion</u>					
Peak acceleration, g	0.89	1.32	1.93	2.58	1.98
Peak velocity, in./sec	3.5	6.9	9.2	11.9	11.4
Peak displacement, in.	0.32	0.65	0.97	1.29	1.29
<u>Response</u>					
Acceleration (abs.)					
Peak value, g	0.20	0.87	1.15	1.74	1.50
Time at peak, sec	4.11	6.54	6.49	4.06	4.07
Velocity					
Peak value, in./sec	8.3	16	21	39	33
Time at peak, sec	4.05	4.72	4.70	4.10	4.03
Displacement					
Peak value, in.*	0.45	0.90	1.06	1.70	1.67
Time at peak, sec	3.94	6.35	6.49	5.41	3.91
Residual drift at end of run, in.	-0.02	-0.03	-0.02	-0.31	-0.04
Cumul. residual drift, in.	-0.38	-0.36	-0.33	-0.31	-0.42
<u>Period</u>					
Before run, sec	0.45	0.45	0.43	0.16	0.47
After run, sec	0.47	0.45	0.45	0.43	0.50
*Single amplitude peak					

Table 4-7: Measured in-plane response, specimen H1 (Figure 4-21 through Figure 4-25).

Parameter	Test ID				
	H1-25 (run 1/5)	H1-50 (run 2/5)	H1-75 (run 3/5)	H1-100 (run 4/5)	H1-100(#2) (run 5/5)
Test Date (2015-)	Jul-15	Jul-16	Jul-29	Aug-04	Aug-06
<u>Base Motion</u>					
Peak acceleration, g	0.86	1.28	1.82	2.02	1.98
Peak velocity, in./sec	3.4	6.5	9.1	11.6	11.8
Peak displacement, in.	0.32	0.65	0.97	1.29	1.29
<u>Response</u>					
Acceleration (abs.)					
Peak value, g	0.48	0.68	0.70	0.76	1.31
Time at peak, sec	5.42	4.75	4.75	4.58	4.05
Velocity					
Peak value, in./sec	10	16	21	28	29
Time at peak, sec	4.11	4.70	4.69	4.71	4.04
Displacement					
Peak value, in.*	0.45	0.87	1.10	1.43	1.61
Time at peak, sec	5.41	4.74	4.74	4.59	3.94
Residual drift at end of run, in.	-0.005	-0.007	0.017	-0.032	0.023
Cumul. residual drift, in.	-0.005	-0.012	0.005	-0.027	0
<u>Period</u>					
Before run, sec	0.13**	0.22***	0.46	0.48	0.42
After run, sec	N/A	0.46	0.48	0.42	0.42
*Single amplitude peak					
**Hammer test was only conducted without mass for this specimen. This value is taken from the platform jolt at the beginning of the test.					
***This value taken from platform jolt because no hammer test after test H1-25.					

Table 4-8: Measured in-plane response, specimen H2 (Figure 4-26 through Figure 4-30).

Parameter	Test ID				
	H2-25 (run 4/5)	H2-50 (run 3/5)	H2-75 (run 2/5)	H2-100 (run 1/5)	H2-100(#2) (run 5/5)
Test Date (2015-)	Dec-05	Dec-05	Dec-06	Dec-06	Dec-06
<u>Base Motion</u>					
Peak acceleration, g	0.93	1.37	1.68	1.91	1.94
Peak velocity, in./sec	3.4	6.3	9.0	11.4	11.1
Peak displacement, in.	0.32	0.65	0.97	1.29	1.29
<u>Response</u>					
Acceleration (abs.)					
Peak value, g	0.17	0.40	0.58	0.89	0.73
Time at peak, sec	3.95	3.95	4.61	4.58	3.94
Velocity					
Peak value, in./sec	7.0	15	21	26	28
Time at peak, sec	4.05	4.06	4.70	4.69	4.03
Displacement					
Peak value, in.*	0.51	0.99	1.25	1.39	1.48
Time at peak, sec	3.96	3.95	4.60	4.60	3.94
Residual drift at end of run, in.	0.03	0.09	-0.03	-0.04	-0.11
Cumul. residual drift, in.	0.05	0.02	-0.07	-0.04	-0.06
<u>Period</u>					
Before run, sec	0.48	0.38	0.41	0.13	0.49
After run, sec	0.49	0.48	0.38	0.41	0.42
*Single amplitude peak					

Table 4-9: Summary of peak displacement response for each test.

Parameter	Ground motion	Frame				Statistics	
		C1	C2	H1	H2	Mean	CoV
Peak drift, in.	25%	0.27	0.38	0.45	0.51	0.40	26%
	50%	0.78	0.90	0.87	0.99	0.89	10%
	75%	1.25	1.06	1.10	1.25	1.17	9%
	100%	1.69	1.70	1.43	1.39	1.55	11%
	100% (2)	1.37	1.67	1.61	1.48	1.53	9%
Peak vertical displacement, in.	25%	0.04	0.04	0.04	0.03	0.04	13%
	50%	0.06	0.08	0.08	0.04	0.07	29%
	75%	0.09	0.08	0.10	0.06	0.08	21%
	100%	0.09	0.15	0.09	0.12	0.11	26%
	100% (2)	0.10	0.07	0.10	0.08	0.09	17%
Peak out-of-plane displacement, in.	25%	0.08	0.04	0.13	0.06	0.08	50%
	50%	0.07	0.17	0.11	0.13	0.12	35%
	75%	0.18	0.22	0.15	0.13	0.17	23%
	100%	0.18	0.17	0.15	0.12	0.16	17%
	100% (2)	0.17	0.16	0.14	0.17	0.16	9%

Note: All values are relative to position at start of test run (i.e. in-run drift)

Table 5-1: Calculated versus measured initial periods (from free vibration tests) for past dynamic tests of SDOF reinforced concrete structures.

Study and Specimen	Calculated (T_{calc}), sec	Measured (T_{meas}), sec	$\frac{T_{meas}}{T_{calc}}$
<u>Bonacci (1989)</u>			<u>1.12</u>
B-01	0.10	0.11	1.07
B-02	0.15	0.15	1.04
B-03	0.10	0.12	1.16
B-04	0.18	0.19	1.07
B-05	0.15	0.18	1.22
B-06	0.15	0.17	1.16
B-07	0.18	0.18	1.01
B-08	0.18	0.17	0.98
B-09	0.15	0.15	1.02
B-10	0.18	0.21	1.18
B-11	0.10	0.11	1.14
B-12	0.10	0.14	1.39
B-13	0.10	0.11	1.15
B-14	0.10	0.12	1.17
B-15	0.15	0.16	1.05
<u>Gulkan and Sozen (1971)</u>			<u>1.64</u>
HD1	0.023	-	-
HD2	0.023	0.036	1.58
HE1	0.023	0.038	1.69
HE2	0.023	0.043	1.90
FD1	0.040	0.063	1.55
FE1	0.040	0.062	1.55
FE2	0.040	0.064	1.60
Overall average =			<u>1.27</u>
<p><u>Notes:</u> Underlined values indicate averages. Dashes indicate that the value was not measured. Modulus of elasticity was taken as the reported value from the investigation.</p>			

Table 5-2: Calculated versus measured initial first mode periods (from free vibration tests) for past dynamic tests of MDOF reinforced concrete structures with walls [adapted from Lepage (1997)].

Study and Specimen	Calculated (T_{calc}), sec	Measured (T_{meas}), sec	$\frac{T_{meas}}{T_{calc}}$
<u>Abrams and Sozen</u> (1979)			<u>1.69</u>
FW1	0.19	0.31	1.69
FW2	0.17	0.30	1.76
FW3	0.19	0.31	1.69
FW4	0.18	0.29	1.62
<u>Aristizabal and Sozen</u> (1976)			<u>1.12</u>
D1	0.19	0.22	1.16
D2	0.19	0.21	1.08
D3	0.19	0.21	1.08
M1	0.19	0.22	1.16
<u>Lybas and Sozen</u> (1977)			<u>1.27</u>
D1	0.09	0.08	0.94
D2	0.09	0.13	1.38
D3	0.10	0.13	1.34
D4	0.10	0.14	1.51
D5	0.10	0.12	1.19
<u>Moehle and Sozen</u> (1980)			<u>1.08</u>
FFW	0.18	0.20	1.12
FHW	0.19	0.19	1.04
FSW	0.19	0.20	1.08
<u>Wolfgram (1984)</u>			<u>1.05</u>
NS1	0.09	0.10	1.09
NS2	0.09	0.09	1.00
NS3	0.09	0.10	1.06
Overall average =			<u>1.26</u>
Note: Underlined values indicate averages.			

Table 5-3: Calculated versus measured initial first mode periods for past dynamic tests of MDOF reinforced concrete structures without walls [adapted from Lepage (1997)].

Study and Specimen	Calculated (T_{calc}), sec	Measured (T_{meas}), sec	$\frac{T_{meas}}{T_{calc}}$
<u>Cecen (1979)</u>			<u>1.35</u>
H1	0.20	0.33	1.63
H2	0.21	0.23	1.07
<u>Eberhard and Sozen (1989)</u>			<u>1.00</u>
ES1	0.17	0.18	1.05
ES2	0.17	0.16	0.95
<u>Healey and Sozen (1978)</u>			
MF1	0.20	0.31	1.53
<u>Moehle and Sozen (1978)</u>			
MF2	0.21	0.23	1.07
<u>Moehle and Sozen (1980)</u>			
FNW	0.22	0.24	1.10
<u>Otani and Sozen (1972)</u>			<u>1.20</u>
D1	0.15	0.18	1.16
D2	0.15	-	-
D3	0.15	0.19	1.25
<u>Schultz (1985)</u>			<u>1.14</u>
SS1	0.21	0.26	1.23
SS2	0.21	0.22	1.04
<u>Wood (1985)</u>			<u>1.08</u>
STEPPED	0.16	0.17	1.07
TOWER	0.16	0.18	1.09
Overall average =			<u>1.17</u>
<u>Note:</u> Underlined values indicate averages. Dashes indicate that the value was not measured.			

Table 5-4: Mean effective periods calculated using zero crossing rate from $t = 1.5 - 11$ sec.

Specimen	Ground Motion					Mean
	25%	50%	75%	100%(1)	100%(2)	
C1	0.28	0.34	0.37	0.39	0.42	0.36
C2	0.42	0.39	0.41	0.37	0.40	0.40
H1	0.28	0.46	0.44	0.50	0.54	0.44
H2	0.61	0.46	0.50	0.40	0.56	0.51
<u>Comparison: Type</u>						
H1/C1	1.00	1.35	1.19	1.28	1.29	1.22
H2/C2	1.45	1.18	1.22	1.08	1.40	1.27
<u>Comparison: Series</u>						
C2/C1	1.50	1.15	1.11	0.95	0.95	1.13
H2/H1	2.18	1.00	1.14	0.80	1.04	1.23

Table 5-5: Percent difference* in peak drift for frame type C versus frame type H.

Drift Type	Series	Ground Motion					Mean
		25%	50%	75%	100%(1)	100%(2)	
In-run	1	67%	11%	-12%	-16%	18%	14%
	2	35%	10%	18%	-18%	-11%	7%
	Mean	51%	11%	3%	-17%	3%	10%
Cumulative	1	67%	12%	-7%	-21%	0%	10%
	2	-27%	-23%	-12%	-18%	-25%	-21%
	Mean	20%	-6%	-9%	-20%	-13%	-5%

* Percent difference = $\Delta_H / \Delta_C - 1$, negative indicates less drift in type H

Table 5-6: Percent difference** in peak drift for frames in Series 1 versus Series 2.

Drift Type	Type	Ground Motion					Mean
		25%	50%	75%	100%(1)	100%(2)	
In-run	C	39%	15%	-15%	0%	22%	12%
	H	13%	14%	14%	-3%	-8%	6%
	Mean	26%	15%	-1%	-1%	7%	9%
Cumulative	C	167%	55%	15%	-6%	28%	52%
	H	18%	6%	9%	-3%	-4%	5%
	Mean	92%	30%	12%	-5%	12%	29%

** Percent difference = $\Delta_{Series2} / \Delta_{Series1} - 1$, negative indicates less drift in Series 2

Table 5-7: Percent change^{***} in peak drift for a given frame type from first 100% motion to second 100% motion.

Drift Type	Frame				Mean
	C1	C2	H1	H2	
In-run	-19%	-2%	13%	7%	0%
Cumulative	-13%	20%	11%	10%	7%
*** Percent change = $\Delta_{100\%(2)} / \Delta_{100\%(1)} - 1$, negative indicates less drift in run 2					

Table 6-1: Summary of single-degree-of-freedom experiments.

Reference	D O F	Structure	Run	Parameters				Peak Drift			Sources			
				T _{i,calc} sec	Γ	PGV in./sec	PGA g	Meas. (D _{max}) in.	Calc. (S _{dv}) in.	$\frac{D_{max}}{S_{dv}}$	T _{i,calc}	Γ	PGV	PGA
Gulkan and Sozen (1971)	1	HE1	1	0.02	1	10.9	1.18	0.10	0.2	0.56	C	N/A	E	R
			2	0.02	1	15.0	-	-	-	-	C	N/A	E	R
		HE2	2	0.02	1	10.8	1.45	0.32	0.2	1.81	C	N/A	E	R
			3	0.02	1	10.8	1.51	0.28	0.2	1.59	C	N/A	E	R
		FE1	1	0.04	1	15.0	2.20	0.65	0.4	1.53	C	N/A	E	R
			2	0.04	1	15.0	2.54	0.70	0.4	1.66	C	N/A	E	R
			3	0.04	1	15.0	2.50	0.66	0.4	1.56	C	N/A	E	R
			4	0.04	1	15.0	2.40	0.66	0.4	1.56	C	N/A	E	R
		FE2	1	0.04	1	15.0	4.20	0.85	0.4	1.99	C	N/A	E	R
			2	0.04	1	15.0	2.60	0.81	0.4	1.92	C	N/A	E	R
			3	0.04	1	15.0	3.94	0.86	0.4	2.02	C	N/A	E	R
			4	0.04	1	15.0	2.90	0.97	0.4	2.29	C	N/A	E	R
			5	0.04	1	15.0	3.05	1.04	0.4	2.44	C	N/A	E	R
			6	0.04	1	15.0	2.90	1.04	0.4	2.45	C	N/A	E	R
Bonacci (1989)	1	B01	R1	0.10	1	12.6	1.35	0.58	0.9	0.66	R	N/A	D	D
			R2	0.10	1	14.6	2.41	1.08	1.0	1.06	R	N/A	D	D
		B02	R1	0.15	1	11.8	0.94	1.08	1.2	0.87	R	N/A	D	D
			R2	0.15	1	15.3	3.38	2.12	1.6	1.32	R	N/A	D	D
		B03	R1	0.10	1	11.8	0.88	0.62	0.8	0.75	R	N/A	D	D
			R2	0.10	1	16.1	3.29	1.59	1.1	1.41	R	N/A	D	D
		B04	R1	0.18	1	11.7	0.94	1.40	1.5	0.95	R	N/A	D	D
			R2	0.18	1	14.1	3.21	2.08	1.8	1.18	R	N/A	D	D
		B05	R1	0.15	1	13.0	0.96	1.10	1.4	0.81	R	N/A	D	D
			R2	0.15	1	15.3	3.50	1.88	1.6	1.17	R	N/A	D	D

Sources: R – Obtained from reference publication (i.e. reports, theses) | L – Obtained from Lepage (1997)
D – Obtained from original test data | E – Extracted from figures | C – Calculated (continued next page)

Table 6-1 (cont'd): Summary of single-degree-of-freedom experiments.

Reference	D O F	Structure	Run	Parameters				Peak Drift			Sources			
				T _{i,calc} sec	Γ	PGV in./sec	PGA g	Meas. (D _{max}) in.	Calc. (S _{dv}) in.	$\frac{D_{max}}{S_{dv}}$	T _{i,calc}	Γ	PGV	PGA
Bonacci (1989)	1	B06	R1	0.15	1	4.9	0.43	0.39	0.5	0.76	R	N/A	D	D
			R2	0.15	1	9.4	0.90	0.90	1.0	0.92	R	N/A	D	D
		B07	R1	0.18	1	11.1	0.66	0.72	1.4	0.52	R	N/A	D	D
			R2	0.18	1	15.5	1.33	1.50	1.9	0.78	R	N/A	D	D
		B08	R1	0.18	1	6.7	0.34	0.59	0.8	0.70	R	N/A	D	D
			R2	0.18	1	10.1	0.60	1.73	1.3	1.37	R	N/A	D	D
		B09	R1	0.15	1	8.6	0.42	0.49	0.9	0.55	R	N/A	D	D
			R2	0.15	1	14.0	1.17	2.14	1.5	1.45	R	N/A	D	D
		B10	R1	0.18	1	8.5	0.56	1.10	1.1	1.03	R	N/A	D	D
			R2	0.18	1	13.4	1.42	1.68	1.7	1.00	R	N/A	D	D
		B11	R1	0.10	1	3.6	0.40	0.28	0.3	1.10	R	N/A	D	D
			R2	0.10	1	9.8	0.87	0.71	0.7	1.04	R	N/A	D	D
		B12	R1	0.10	1	7.0	0.58	0.49	0.5	1.00	R	N/A	D	D
			R2	0.10	1	10.5	1.03	0.63	0.7	0.85	R	N/A	D	D
		B13	R1	0.10	1	11.2	0.75	0.42	0.8	0.53	R	N/A	D	D
			R2	0.10	1	15.8	1.61	0.70	1.1	0.63	R	N/A	D	D
		B14	R1	0.10	1	8.8	0.55	0.25	0.6	0.41	R	N/A	D	D
			R2	0.10	1	14.6	1.28	0.85	1.0	0.83	R	N/A	D	D
B15	R1	0.15	1	7.9	0.50	0.51	0.8	0.62	R	N/A	D	D		
	R2	0.15	1	14.6	1.30	1.14	1.5	0.74	R	N/A	D	D		
Elwood and Moehle (2003)	1	Spec. 1	1	0.27	1	15.5	0.79	3.50	3.0	1.18	R	N/A	R	R
		Spec. 2	1	0.27	1	15.2	0.73	4.20	2.9	1.45	R	N/A	R	R
Sources: R – Obtained from reference publication (i.e. reports, theses) L – Obtained from Lepage (1997) D – Obtained from original test data E – Extracted from figures C – Calculated (continued next page)														

Table 6-1 (cont'd): Summary of single-degree-of-freedom experiments.

Reference	D O F	Structure	Run	Parameters				Peak Drift			Sources			
				$T_{i,calc}$ sec	Γ	PGV in./sec	PGA g	Meas. (D_{max}) in.	Calc. (S_{dv}) in.	$\frac{D_{max}}{S_{dv}}$	$T_{i,calc}$	Γ	PGV	PGA
Laughery (this study)	1	C1	C1-25	0.10	1	3.7	0.86	0.27	0.3	1.02	C	N/A	D	D
			C1-50	0.10	1	6.9	1.52	0.78	0.5	1.61	C	N/A	D	D
			C1-75	0.10	1	9.0	1.58	1.25	0.6	1.95	C	N/A	D	D
			C1-100	0.10	1	11.2	2.10	1.69	0.8	2.13	C	N/A	D	D
			C1-100(2)	0.10	1	11.8	1.98	1.37	0.8	1.64	C	N/A	D	D
		C2	C2-25	0.10	1	3.5	0.89	0.38	0.2	1.52	C	N/A	D	D
			C2-50	0.10	1	6.8	1.32	0.90	0.5	1.86	C	N/A	D	D
			C2-75	0.10	1	9.2	1.93	1.06	0.7	1.63	C	N/A	D	D
			C2-100	0.10	1	11.9	2.58	1.70	0.8	2.03	C	N/A	D	D
			C2-100(2)	0.10	1	11.4	1.98	1.67	0.8	2.08	C	N/A	D	D
		H1	H1-25	0.10	1	3.4	0.86	0.45	0.2	1.86	C	N/A	D	D
			H1-50	0.10	1	6.5	1.28	0.87	0.5	1.89	C	N/A	D	D
			H1-75	0.10	1	9.1	1.82	1.10	0.6	1.71	C	N/A	D	D
			H1-100	0.10	1	11.6	2.02	1.43	0.8	1.75	C	N/A	D	D
			H1-100(2)	0.10	1	11.8	1.98	1.61	0.8	1.93	C	N/A	D	D
		H2	H2-25	0.10	1	3.4	0.93	0.51	0.2	2.11	C	N/A	D	D
			H2-50	0.10	1	6.3	1.37	0.99	0.4	2.21	C	N/A	D	D
			H2-75	0.10	1	9.0	1.68	1.25	0.6	1.96	C	N/A	D	D
			H2-100	0.10	1	11.4	1.91	1.39	0.8	1.72	C	N/A	D	D
			H2-100(2)	0.10	1	11.1	1.94	1.48	0.8	1.89	C	N/A	D	D
Sources: R – Obtained from reference publication (i.e. reports, theses) L – Obtained from Lepage (1997) D – Obtained from original test data E – Extracted from figures C – Calculated														

Table 6-2: Summary of multiple-degree-of-freedom experiments.

Reference	D O F	Structure	Run	Parameters				Peak Drift			Sources			
				T _{i,calc} sec	Γ	PGV in./sec	PGA g	Meas. (D _{max}) in.	Calc. (S _{dv}) in.	$\frac{D_{max}}{S_{dv}}$	T _{i,calc}	Γ	PGV	PGA
Otani and Sozen (1972)	3	D1	D1-1	0.15	1.26	4.0	0.24	0.34	0.5	0.63	L	L	E	R
			D1-2	0.15	1.26	6.1	0.40	0.55	0.8	0.67	L	L	E	R
			D1-3	0.15	1.26	9.4	0.53	0.79	1.3	0.62	L	L	E	R
			D1-4	0.15	1.26	14.7	0.84	1.22	2.0	0.62	L	L	E	R
			D1-5	0.15	1.26	15.0	1.42	1.57	2.0	0.78	L	L	E	R
			D1-6	0.15	1.26	15.0	3.16	1.95	2.0	0.96	L	L	E	R
		D2	D2-1	0.15	1.26	14.0	0.86	1.26	1.8	0.69	L	L	E	R
			D2-2	0.15	1.26	15.0	1.10	1.70	2.0	0.86	L	L	E	R
			D2-3	0.15	1.26	15.0	1.21	1.91	2.0	0.97	L	L	E	R
			D2-4	0.15	1.26	15.0	3.43	2.27	2.0	1.16	L	L	E	R
		D3	D3-1	0.15	1.26	10.6	0.61	1.06	1.4	0.74	L	L	E	R
			D3-2	0.15	1.26	15.0	1.10	1.65	2.0	0.81	L	L	E	R
			D3-3	0.15	1.26	15.0	0.93	1.92	2.0	0.95	L	L	E	R
			D3-4	0.15	1.26	15.0	2.14	2.23	2.0	1.10	L	L	E	R
Aristizabal and Sozen (1976)	10	D1	D1-1	0.19	1.44	4.4	0.51	1.12	0.9	1.31	L	L	D	D
			D1-2	0.19	1.44	10.9	1.98	1.82	2.1	0.85	L	L	D	D
		D2	D2-1	0.18	1.44	6.1	0.41	1.16	1.1	1.03	L	L	E	R
			D2-2	0.18	1.44	12.0	0.94	2.13	2.2	0.96	L	L	E	R
			D2-3	0.18	1.44	15.0	1.72	2.96	2.8	1.07	L	L	E	R
		D3	D3-1	0.19	1.44	6.2	0.46	0.95	1.2	0.78	L	L	E	R
			D3-2	0.19	1.44	12.2	1.06	1.48	2.4	0.62	L	L	E	R
		M1	M1-1	0.19	1.44	9.2	0.91	2.05	1.8	1.14	L	L	D	D

Sources: R – Obtained from reference publication (i.e. reports, theses) | L – Obtained from Lepage (1997)
D – Obtained from original test data | E – Extracted from figures | C – Calculated (continued next page)

Table 6-2 (cont'd): Summary of multiple-degree-of-freedom experiments.

Reference	D O F	Structure	Run	Parameters				Peak Drift			Sources			
				T _{i,calc} sec	Γ	PGV in./sec	PGA g	Meas. (D _{max}) in.	Calc. (S _{dv}) in.	$\frac{D_{max}}{S_{dv}}$	T _{i,calc}	Γ	PGV	PGA
Lybas and Sozen (1977)	6	D1	D1-1	0.09	1.29	1.2	0.12	0.06	0.1	0.61	L	L	E	R
			D1-2	0.09	1.29	2.5	0.22	0.15	0.2	0.74	L	L	E	R
			D1-3	0.09	1.29	4.8	0.50	0.28	0.4	0.72	L	L	E	R
			D1-4	0.09	1.29	9.2	1.06	0.50	0.7	0.67	L	L	E	R
			D1-5	0.09	1.29	15.0	2.20	1.07	1.2	0.88	L	L	E	R
		D2	D2-1	0.09	1.29	6.0	1.28	0.45	0.5	0.88	L	L	E	R
			D2-2	0.09	1.29	12.0	3.59	1.36	1.0	1.34	L	L	E	R
		D3	D3-1	0.10	1.29	9.0	1.12	0.46	0.8	0.57	L	L	E	R
			D3-2	0.10	1.29	14.0	2.10	1.00	1.3	0.80	L	L	E	R
		D4	D4-1	0.10	1.29	7.0	1.12	0.50	0.6	0.81	L	L	E	R
			D4-2	0.10	1.29	15.0	2.40	1.13	1.3	0.86	L	L	E	R
		D5	D5-1	0.10	1.29	7.0	1.07	0.48	0.6	0.75	L	L	E	R
			D5-2	0.10	1.29	15.0	2.10	1.19	1.4	0.87	L	L	E	R
		Healey and Sozen (1978)	10	MF1	R1	0.20	1.33	5.2	0.41	0.94	1.0	0.94	L	L
R2	0.20				1.33	9.0	0.93	2.01	1.7	1.16	L	L	D	D
R3	0.20				1.33	9.3	1.42	2.68	1.8	1.50	L	L	D	D
Moehle and Sozen (1978)	10	MF2	R1	0.21	1.31	6.0	0.37	0.94	1.2	0.80	L	L	D	D
			R2	0.21	1.31	10.2	0.83	1.73	2.0	0.86	L	L	D	D
			R3	0.21	1.31	11.8	1.28	2.28	2.3	0.99	L	L	D	D
Sources: R – Obtained from reference publication (i.e. reports, theses) L – Obtained from Lepage (1997) D – Obtained from original test data E – Extracted from figures C – Calculated														

(continued next page)

Table 6-2 (cont'd): Summary of multiple-degree-of-freedom experiments.

Reference	D O F	Structure	Run	Parameters				Peak Drift			Sources			
				T _{i,calc} sec	Γ	PGV in./sec	PGA g	Meas. (D _{max}) in.	Calc. (S _{dv}) in.	$\frac{D_{max}}{S_{dv}}$	T _{i,calc}	Γ	PGV	PGA
Abrams and Sozen (1979)	10	FW1	R1	0.19	1.36	6.1	0.55	1.10	1.1	1.02	L	L	D	D
			R2	0.19	1.36	10.5	1.84	1.50	1.9	0.80	L	L	D	D
			R3	0.19	1.36	11.6	2.41	2.68	2.1	1.30	L	L	D	D
		FW2	R1	0.17	1.36	6.5	0.48	1.10	1.1	1.02	L	L	D	D
			R2	0.17	1.36	10.6	0.92	1.69	1.8	0.96	L	L	D	D
			R3	0.17	1.36	8.9	1.10	2.20	1.5	1.49	L	L	D	D
		FW3	R1	0.19	1.36	5.7	0.43	0.67	1.0	0.66	L	L	D	D
			R2	0.19	1.36	-	0.92	1.89	-	-	L	L	N/A	N/A
		FW4	R1	0.18	1.36	6.9	0.47	0.71	1.2	0.59	L	L	D	D
			R2	0.18	1.36	12.5	0.95	1.81	2.2	0.83	L	L	D	D
			R3	0.18	1.36	11.3	1.26	2.56	2.0	1.29	L	L	D	D
		Cecen (1979)	10	H1	R1	0.20	1.31	5.2	0.37	1.14	1.0	1.16	L	L
R2	0.20				1.31	10.9	0.84	2.05	2.1	0.99	L	L	D	D
R3	0.20				1.31	13.7	1.57	4.06	2.6	1.57	L	L	D	D
H2	R1			0.21	1.31	2.0	0.19	0.37	0.4	0.96	L	L	D	D
	R2			0.21	1.31	3.8	0.34	0.71	0.7	0.95	L	L	D	D
	R3			0.21	1.31	6.2	0.51	0.94	1.2	0.77	L	L	D	D
	R4			0.21	1.31	6.2	0.48	1.02	1.2	0.84	L	L	D	D
	R5			0.21	1.31	8.9	0.72	1.54	1.8	0.87	L	L	D	D
	R6			0.21	1.31	11.7	1.01	2.28	2.3	0.99	L	L	D	D
	R7			0.21	1.31	14.6	2.61	3.91	2.9	1.36	L	L	D	D

Sources: R – Obtained from reference publication (i.e. reports, theses) | L – Obtained from Lepage (1997)

D – Obtained from original test data | E – Extracted from figures | C – Calculated

(continued next page)

Table 6-2 (cont'd): Summary of multiple-degree-of-freedom experiments.

Reference	D O F	Structure	Run	Parameters				Peak Drift			Sources			
				$T_{i,calc}$ sec	Γ	PGV in./sec	PGA g	Meas. (D_{max}) in.	Calc. (S_{dv}) in.	$\frac{D_{max}}{S_{dv}}$	$T_{i,calc}$	Γ	PGV	PGA
Moehle and Sozen (1980)	9	FNW	R1	0.22	1.25	5.4	0.43	1.02	1.1	0.97	L	L	D	D
			R2	0.22	1.25	9.3	0.74	1.73	1.8	0.95	L	L	D	D
			R3	0.22	1.25	14.0	1.22	3.61	2.7	1.31	L	L	D	D
		FSW	R1	0.19	1.31	5.1	0.36	0.87	0.9	0.97	L	L	D	D
			R2	0.19	1.31	9.6	0.57	1.57	1.7	0.94	L	L	D	D
			R3	0.19	1.31	15.3	1.11	2.99	2.7	1.12	L	L	D	D
		FHW	R1	0.19	1.32	5.6	0.41	0.91	1.0	0.93	L	L	D	D
FFW	R1	0.18	1.34	5.0	0.32	1.02	0.9	1.20	L	L	D	D		
Wolfgram (1984)	7	NS1	R1	0.09	1.41	-	0.60	0.71	-	-	L	L	N/A	R
			R2	0.09	1.41	-	1.80	1.85	-	-	L	L	N/A	R
		NS2	R1	0.09	1.41	7.3	0.59	0.59	0.7	0.86	L	L	D	D
			R2	0.09	1.41	-	1.00	1.14	-	-	L	L	N/A	R
			R3	0.09	1.41	-	1.60	1.14	-	-	L	L	N/A	R
			R4	0.09	1.41	-	1.50	2.20	-	-	L	L	N/A	R
		NS3	R1	0.09	1.41	6.9	0.49	0.55	0.6	0.86	L	L	D	D
			R2	0.09	1.41	10.2	0.82	0.91	0.9	0.96	L	L	D	D
			R3	0.09	1.41	14.4	1.54	0.94	1.3	0.71	L	L	D	D
			R4	0.09	1.41	-	1.50	1.97	-	-	L	L	N/A	R
Sources: R – Obtained from reference publication (i.e. reports, theses) L – Obtained from Lepage (1997)														
D – Obtained from original test data E – Extracted from figures C – Calculated (continued next page)														

Table 6-2 (cont'd): Summary of multiple-degree-of-freedom experiments.

Reference	D O F	Structure	Run	Parameters				Peak Drift			Sources			
				T _{i,calc} sec	Γ	PGV in./sec	PGA g	Meas. (D _{max}) in.	Calc. (S _{dv}) in.	$\frac{D_{max}}{S_{dv}}$	T _{i,calc}	Γ	PGV	PGA
Schultz (1985)	9	SS1	R1	0.21	1.26	6.2	0.35	0.98	1.2	0.85	L	L	D	D
			R2	0.21	1.26	5.7	0.34	0.87	1.1	0.82	L	L	D	D
			R3	0.21	1.26	8.5	0.53	1.26	1.6	0.80	L	L	D	D
			R4	0.21	1.26	15.7	1.44	2.17	2.9	0.74	L	L	D	D
		SS2	R1	0.21	1.26	5.4	0.35	0.91	1.0	0.89	L	L	D	D
			R2	0.21	1.26	5.3	0.40	1.10	1.0	1.10	L	L	D	D
			R3	0.21	1.26	5.0	0.35	0.87	0.9	0.92	L	L	D	D
Shahrooz and Moehle (1987)	6	6F Setback	EC7.7L	0.26	1.25	1.4	0.08	0.27	0.3	0.82	R	0	D	D
			EC16.6L	0.26	1.25	3.2	0.17	0.61	0.7	0.82	R	0	D	D
			EC49.3L	0.26	1.25	9.0	0.49	2.48	2.1	1.19	R	0	D	D
Eberhard and Sozen (1989)	9	ES1	R1	0.17	1.3	5.0	0.36	0.71	0.8	0.90	L	L	D	D
			R2	0.17	1.3	7.5	0.52	1.22	1.2	1.03	L	L	D	D
			R3	0.17	1.3	9.8	0.62	1.69	1.6	1.09	L	L	D	D
		ES2	R1	0.17	1.3	4.8	0.35	0.67	0.8	0.89	L	L	D	D
			R2	0.17	1.3	7.2	0.52	1.26	1.1	1.13	L	L	D	D
			R3	0.17	1.3	9.6	0.61	1.61	1.5	1.08	L	L	D	D
Panagiotou et al. (2007)	7	7F slice	EQ1	0.50	1.46	10.2	0.15	1.97	5.3	0.37	R	R	R	R
			EQ2	0.50	1.46	12.6	0.27	5.51	6.5	0.85	R	R	R	R
			EQ3	0.50	1.46	16.9	0.35	6.30	8.7	0.72	R	R	R	R
			EQ4	0.50	1.46	40.2	0.91	15.75	20.7	0.76	R	R	R	R

Sources: R – Obtained from reference publication (i.e. reports, theses) | L – Obtained from Lepage (1997)
D – Obtained from original test data | E – Extracted from figures | C – Calculated (continued next page)

Table 6-2 (cont'd): Summary of multiple-degree-of-freedom experiments.

Reference	D O F	Structure	Run	Parameters				Peak Drift			Sources			
				$T_{i,calc}$ sec	Γ	PGV in./sec	PGA g	Meas. (D_{max}) in.	Calc. (S_{dv}) in.	$\frac{D_{max}}{S_{dv}}$	$T_{i,calc}$	Γ	PGV	PGA
Sugimoto et al. (2016)	20	20F	#1-5long	0.55	1.38	3.9	0.06	1.92	2.1	0.92	C	C	D	D
			#1-5tran	0.61	1.4	3.8	0.07	1.33	2.3	0.58	C	C	D	D
			#2-2long	0.55	1.38	8.3	0.13	2.91	4.5	0.65	C	C	D	D
			#2-2tran	0.61	1.4	3.8	0.07	1.20	2.3	0.52	C	C	D	D
			#2-6long	0.55	1.38	13.0	0.19	4.37	7.0	0.63	C	C	D	D
			#2-6tran	0.61	1.4	3.9	0.07	1.37	2.4	0.58	C	C	D	D
			#3-2long	0.55	1.38	14.7	0.14	6.32	7.9	0.80	C	C	E	D
			#3-5long	0.55	1.38	19.8	0.19	9.39	10.6	0.88	C	C	E	D
<p>Sources: R – Obtained from reference publication (i.e. reports, theses) L – Obtained from Lepage (1997) D – Obtained from original test data E – Extracted from figures C – Calculated</p>														

Table 6-3: Summary of instrumented buildings that experienced earthquakes.

Reference	D O F	Structure	Run	Parameters				Peak Drift			Sources			
				$T_{i,calc}$ sec	Γ	PGV in./sec	PGA g	Meas. (D_{max}) in.	Calc. (S_{dv}) in.	$\frac{D_{max}}{S_{dv}}$	$T_{i,calc}$	Γ	PGV	PGA
Lepage (1997)	7	Van Nuys Holiday Inn	Whittier 1987 NS	0.97	1.3	3.2	0.16	1.10	2.9	0.38	L	L	D	D
			Northridge 1994 NS	0.97	1.3	15.8	0.39	9.84	14.1	0.70	L	L	D	D
			Northridge 1994 EW	0.89	1.28	20.1	0.45	9.45	16.2	0.58	L	L	D	D
Iemura and Jennings (1973)	9	Millikan Library	San Fernando 1971 EW	0.66	1.44	9.0	0.19	2.40	6.0	0.40	R	R	R	R
Wang et al. (2012)	9	Bldg of Dept of Civ Eng.	1978 Miyagi- Ken-Oki NS	0.40	1.52	14.6	0.26	8.27	6.3	1.32	R	R	R	R
<p>Sources: R – Obtained from reference publication (i.e. reports, theses) L – Obtained from Lepage (1997) D – Obtained from original test data E – Extracted from figures C – Calculated</p>														

Table 6-4: Amplification factors for selected damping coefficients [reproduced from Newmark and Hall (1982)].

Damping, % critical	One Sigma (84.1%)			Median (50%)		
	F _a	F _v	F _d	F _a	F _v	F _d
2%	3.66	2.92	2.42	2.74	2.03	1.63
5%	2.71	2.30	2.01	2.12	1.65	1.39
10%	1.99	1.84	1.69	1.64	1.37	1.20

Table 6-5: Summary of D_{\max}/S_{dv} ratios for different PGV/PGA ranges.

PGV/PGA Range	D_{\max}/S_{dv}				Number of cases		
	min	mean	max	Std. Dev.	Total	Underestimated (% total)	Overestimated (% total)
< 0.03 sec	0.56	1.31	2.45	0.50	87	56 (64%)	31 (36%)
> 0.03 sec	0.37	0.85	1.45	0.23	85	17 (20%)	68 (80%)
ALL	0.37	1.08	2.45	0.45	172	73 (42%)	99 (58%)

Table 6-6: Summary of D_{\max}/S_{dv} ratios for different PGV/PGA ranges if $\Gamma=\sqrt{2}$ is assumed for MDOF systems.

PGV/PGA Range	D_{\max}/S_{dv}				Number of cases		
	min	mean	max	Std. Dev.	Total	Underestimated (% total)	Overestimated (% total)
< 0.03 sec	0.52	1.28	2.45	0.52	87	54 (62%)	33 (38%)
> 0.03 sec	0.35	0.81	1.45	0.22	85	13 (15%)	72 (85%)
ALL	0.35	1.05	2.45	0.46	172	67 (39%)	105 (61%)

Table 6-7: Ground motion records used for analyses of bilinear SDOF systems.

Earthquake	Imperial Valley		Parkfield		Stone Canyon		Coalinga	
Date & Time	1940-05-19		2004-09-28, 17:15		1972-09-04		1983-05-09, 02:49	
Station	El Centro Array #9		Parkfield – Fault Zone 11		Melendy Ranch		Oil Fields, Skunk Hollow	
Component	0	90	90	360	61	331	90	0
Time step (dt), sec	0.01	0.01	0.005	0.005	0.02	0.02	0.005	0.005
PGA, g*	0.28	0.21	0.60	1.13	0.48	0.52	0.35	0.30
PGV, in./sec*	12.2	12.3	6.0	10.9	6.1	5.0	4.0	3.8
PGV/PGA, sec	0.11	0.15	0.026	0.025	0.033	0.025	0.029	0.033
*Unscaled value								

Table 6-8: Summary of peak drifts from analyses of bilinear SDOF systems with specified initial periods and base shear coefficients.

Earthquake	Imperial Valley		Parkfield		Stone Canyon		Coalinga	
Station	El Centro Array #9		Parkfield – Fault Zone 11		Melendy Ranch		Oil Fields, Skunk Hollow	
Component	0	90	90	360	61	331	90	0
Period, sec	Peak drift, systems with base shear coefficient = 0.2							
0.1	0.8	0.5	1.5	1.0	1.1	1.1	1.2	1.3
0.2	1.0	1.3	2.7	1.0	1.2	1.9	1.5	1.6
0.2	1.9	2.5	3.4	1.5	1.0	2.7	1.9	1.1
0.4	2.4	2.9	3.0	1.9	0.9	2.9	2.4	1.2
0.5	3.3	3.2	2.6	1.7	1.5	2.7	2.3	1.3
Period, sec	Peak drift, systems with base shear coefficient = 0.3							
0.1	0.4	0.1	1.2	0.8	1.1	1.0	1.1	1.3
0.2	0.7	0.5	2.4	1.1	1.3	1.5	1.5	1.8
0.2	1.3	1.6	3.3	1.3	1.0	1.8	2.1	1.5
0.4	2.4	2.5	3.0	1.6	1.4	1.9	2.1	1.3
0.5	3.0	2.3	2.5	1.6	1.6	1.9	2.2	1.3

FIGURES



Figure 1-1: Reinforcement congestion at a beam-column joint [Risser and Hoffman (2011)].



Figure 1-2: Honeycombing as a result of reinforcement congestion [from Kenai and Bahar (2003)].

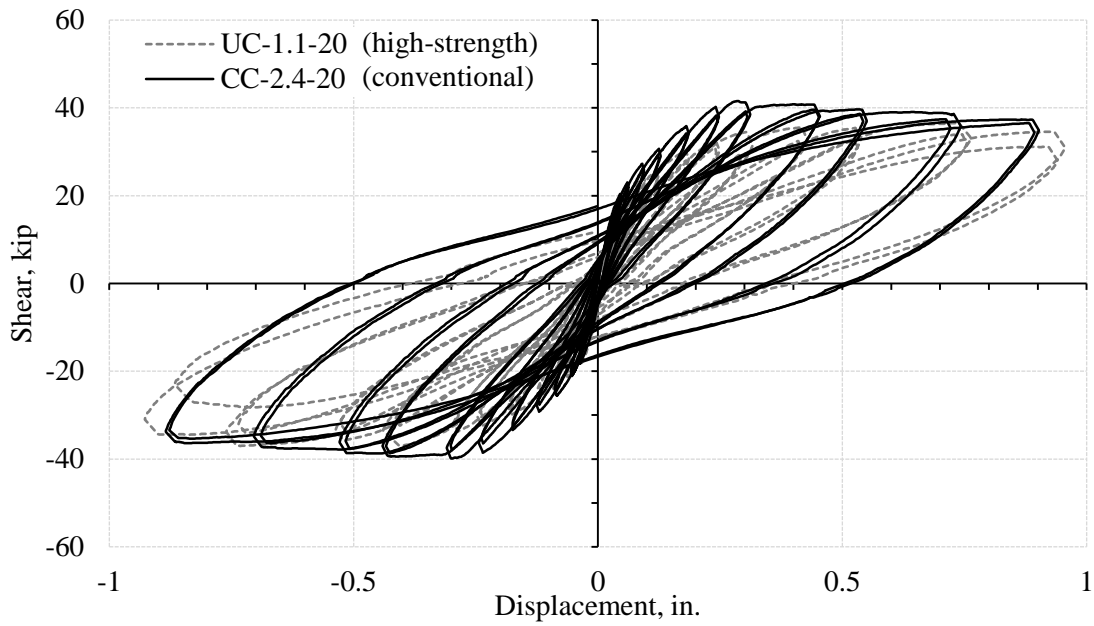


Figure 2-1: Comparison of hysteresis loops for HSSRC (gray) and CRC (black) columns, with HSSRC exhibiting a lower unloading stiffness [from Rautenberg (2011)].

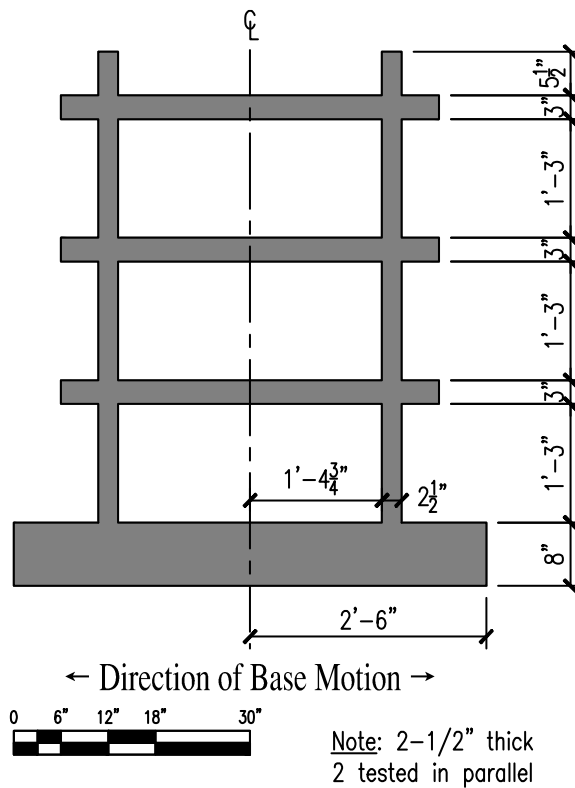


Figure 2-2: Illustration of frames tested by Otani and Sozen (1972).

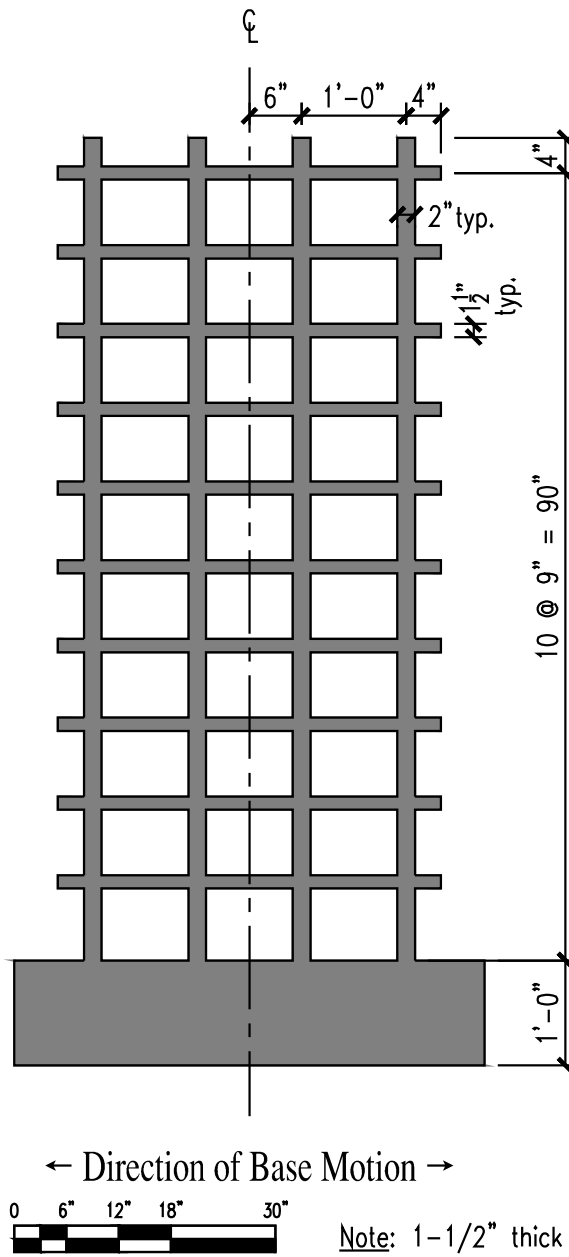


Figure 2-3: Illustration of frames tested by Cecen (1979).

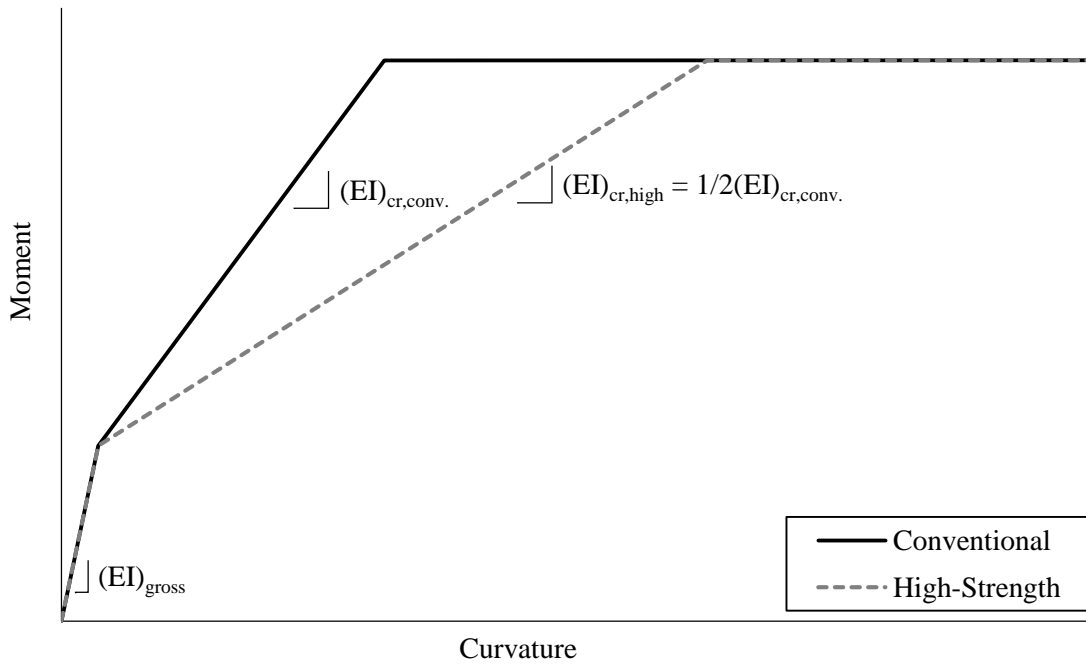


Figure 2-4. Qualitative moment-curvature diagrams for Rautenberg’s (2011) two column types. (Note: EI is flexural stiffness, subscript “g” denotes gross stiffness and “cr” denotes post-cracking stiffness)

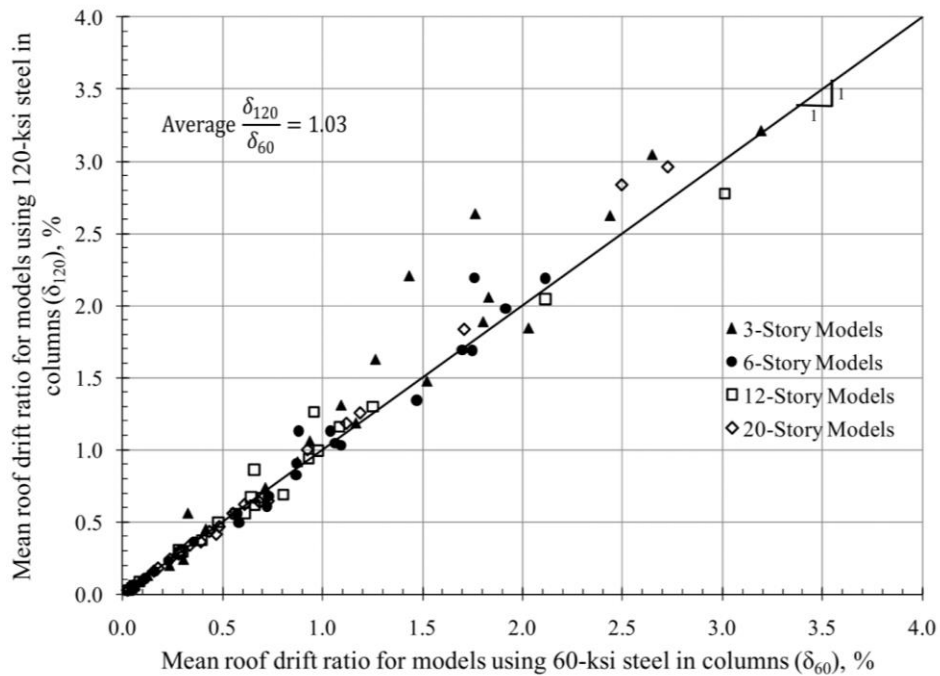


Figure 2-5: Comparison of computed mean roof drift ratios in multi-degree-of-freedom models using Gr.-60 steel and models using Gr.-120 steel in the columns [from Rautenberg (2011)].

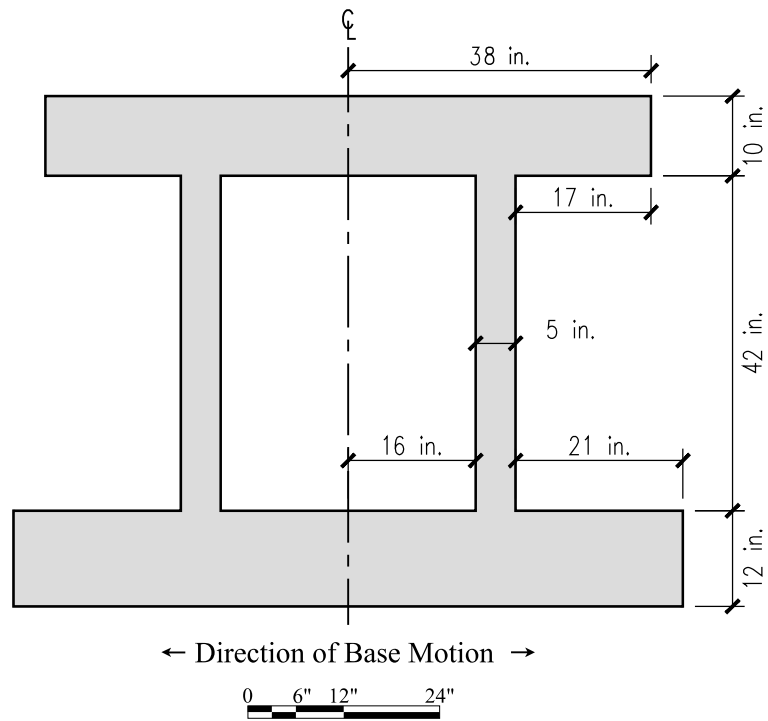


Figure 3-1: Test structure elevation view.

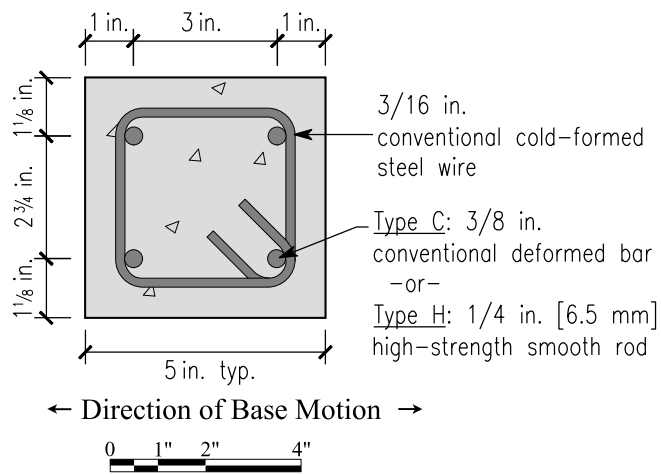


Figure 3-2: Typical column cross-section.

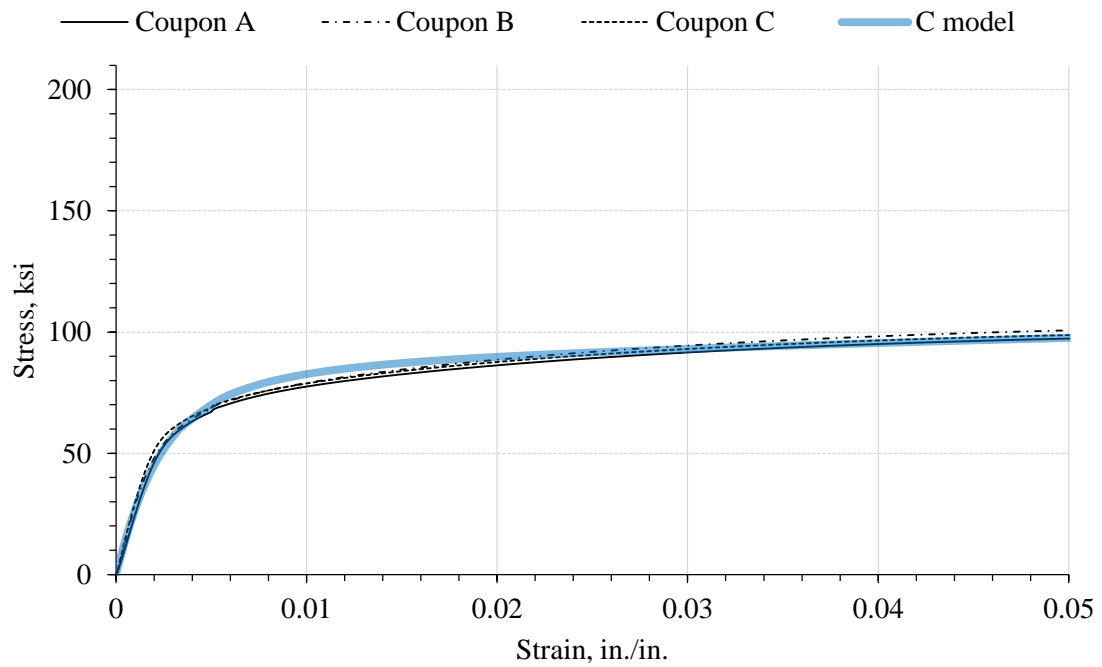


Figure 3-3: Measured stress-strain curves for conventional steel alongside model curve.

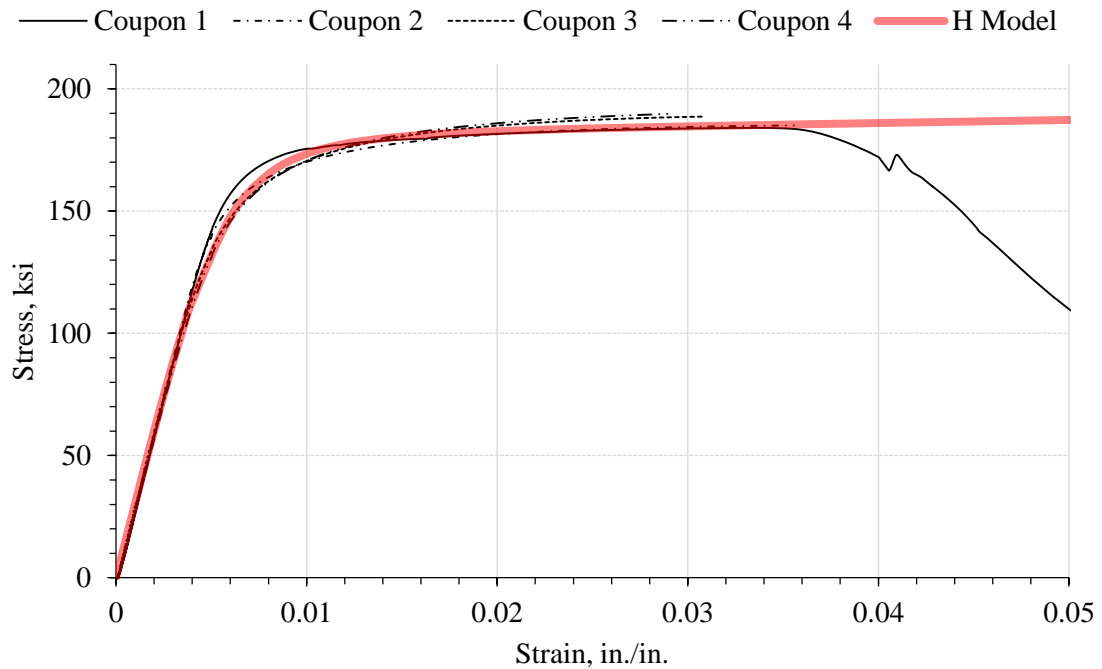
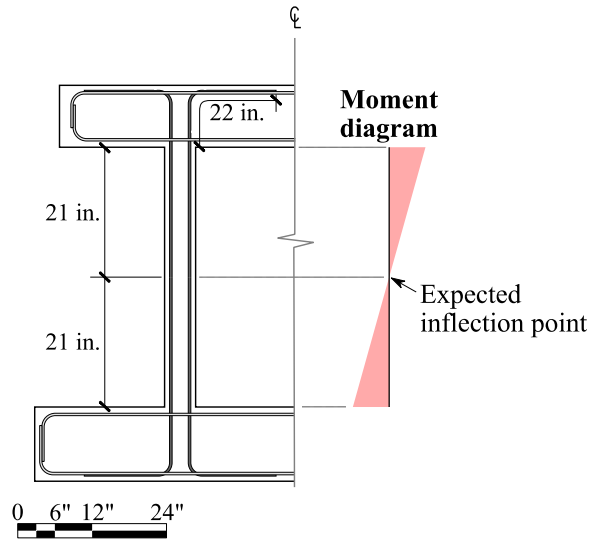


Figure 3-4: Measured stress-strain curves for high-strength steel alongside model curve.
(Note: Extensometer was removed at 0.03 in./in. for samples 2, 3, and 4).



Column Longitudinal Reinforcement
(Transverse reinforcement hidden for clarity)

Figure 3-5: Column longitudinal reinforcement development lengths.

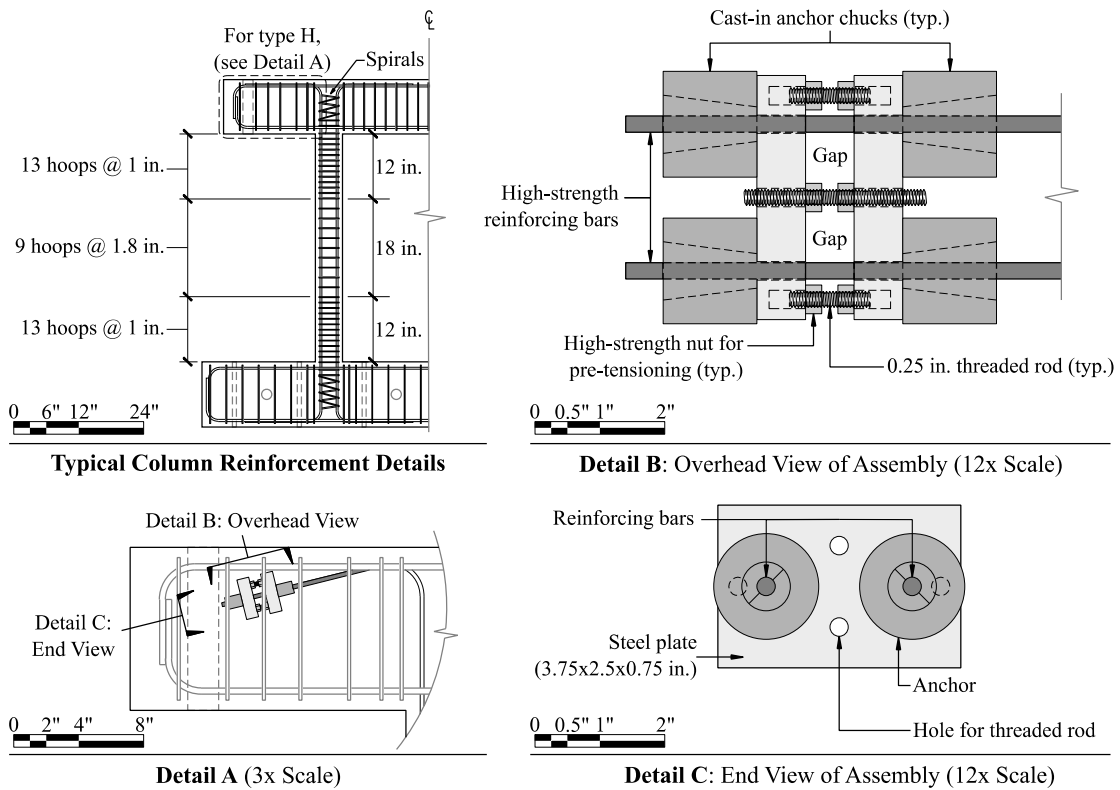


Figure 3-6: Column reinforcement plans showing anchorage assemblies in type H columns.

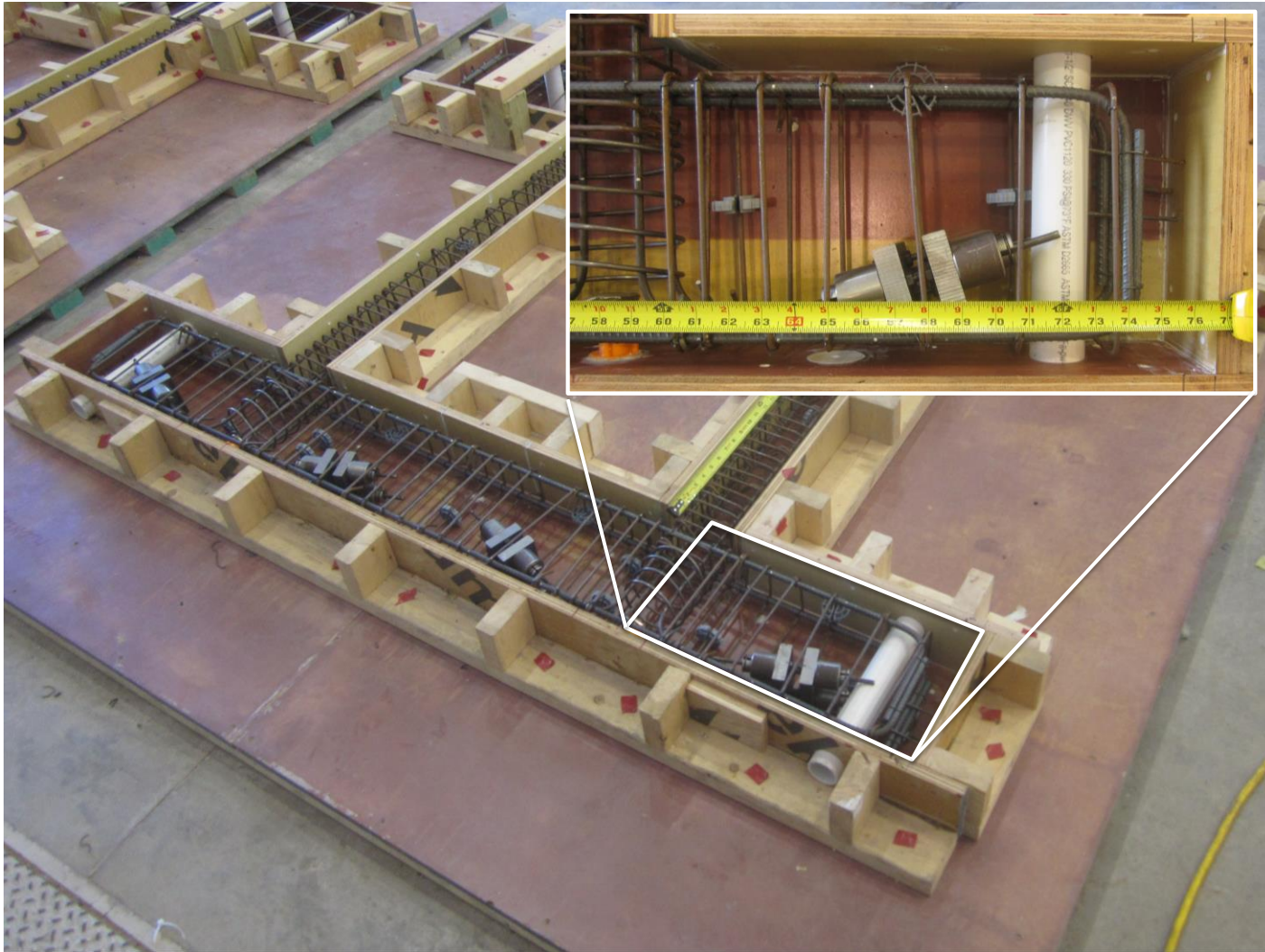


Figure 3-7: Photograph of anchorage assembly in type H frame.

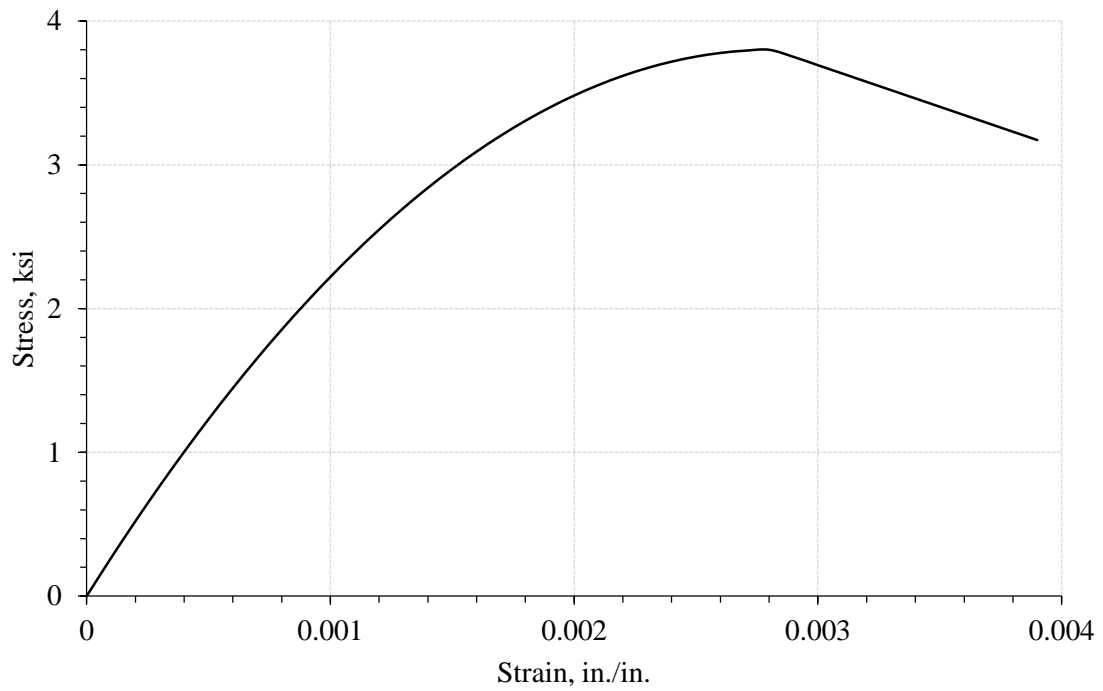


Figure 3-8: Concrete stress-strain model used in FLECHA.

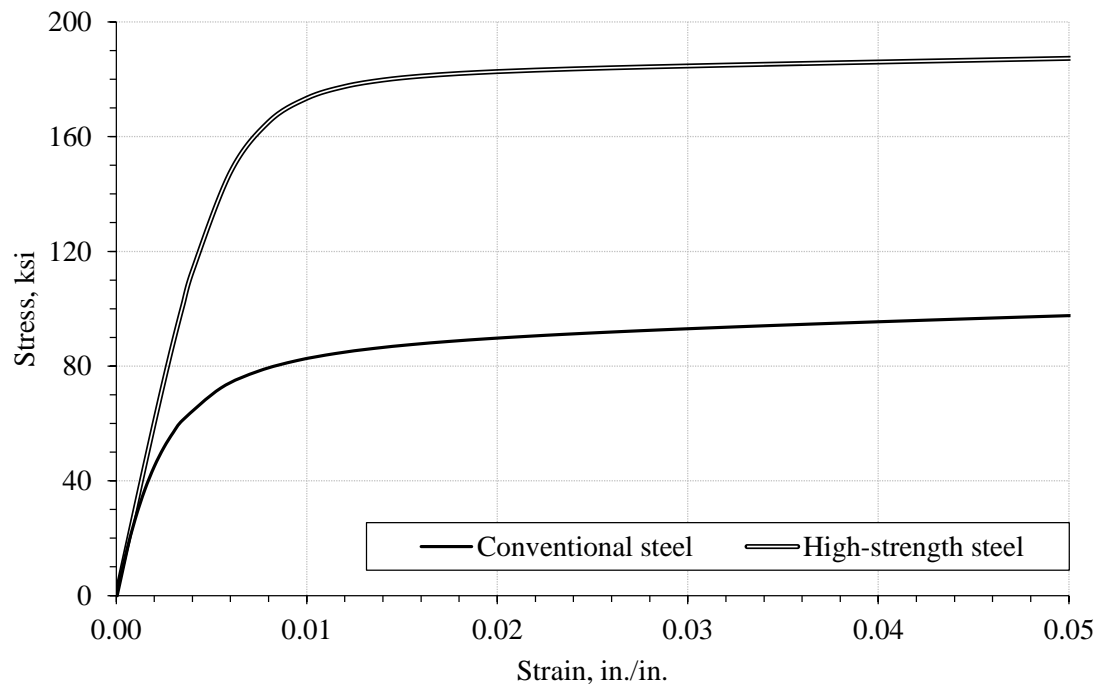


Figure 3-9: Model stress-strain curves for column longitudinal reinforcing steel.

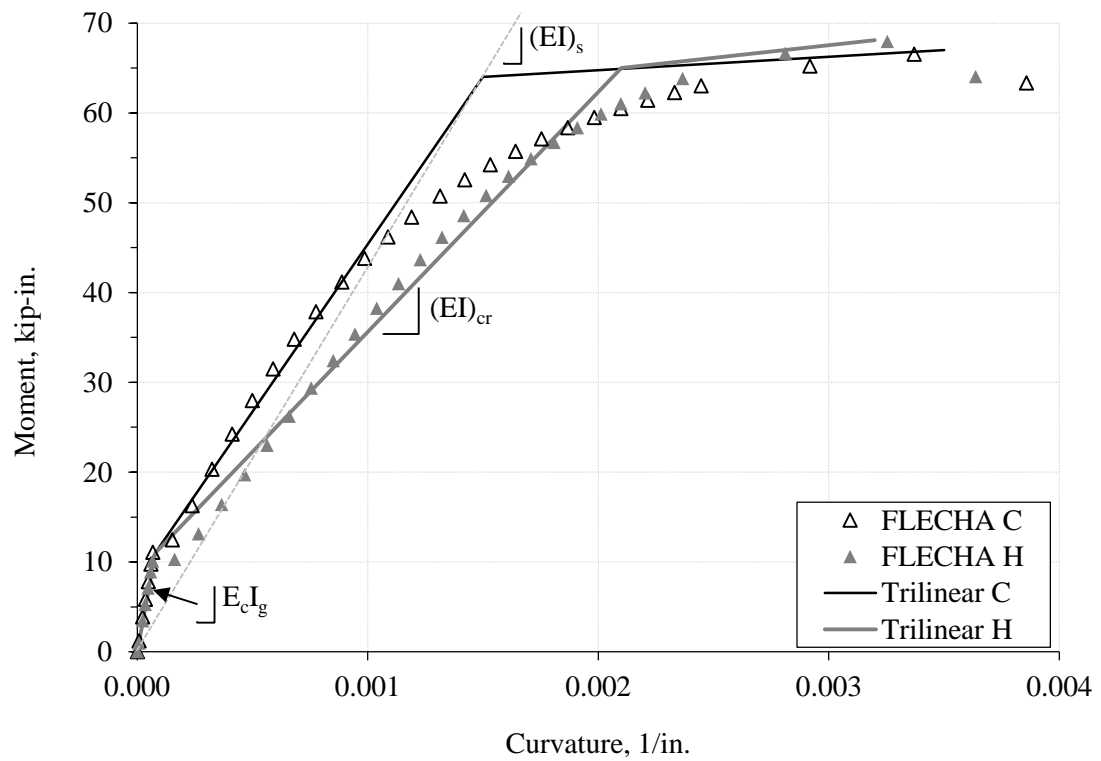


Figure 3-10: Idealized trilinear moment curvature relationships for columns (axial load = $0.025A_g f'_c$).

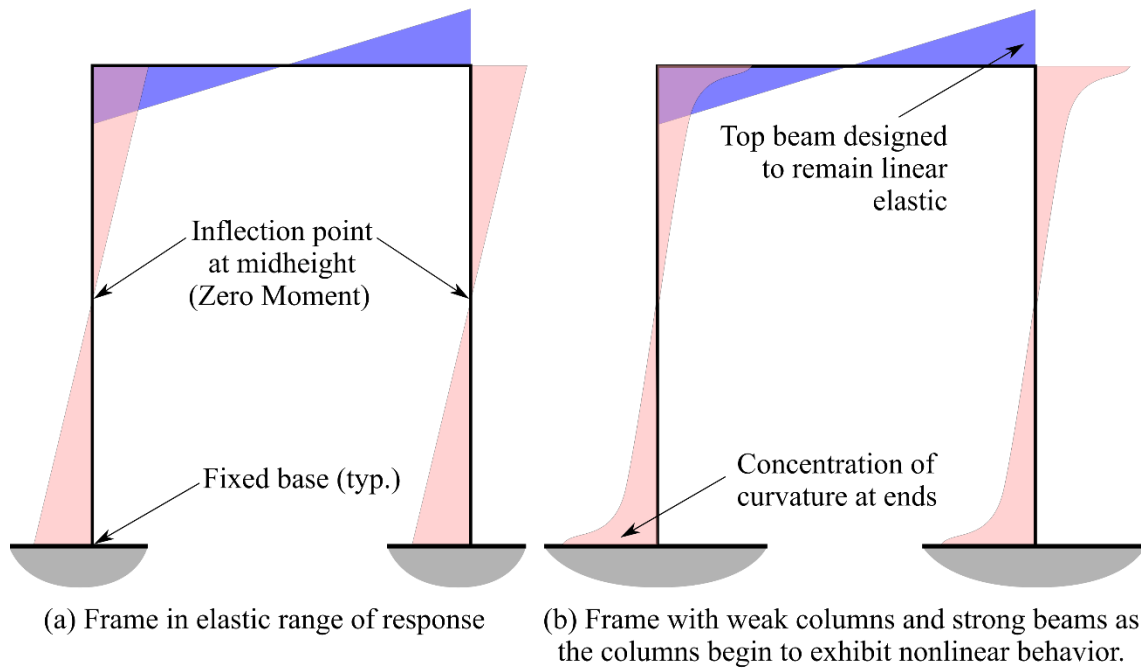


Figure 3-11: Elastic bending moment diagram for a portal frame subject to lateral load at the top.

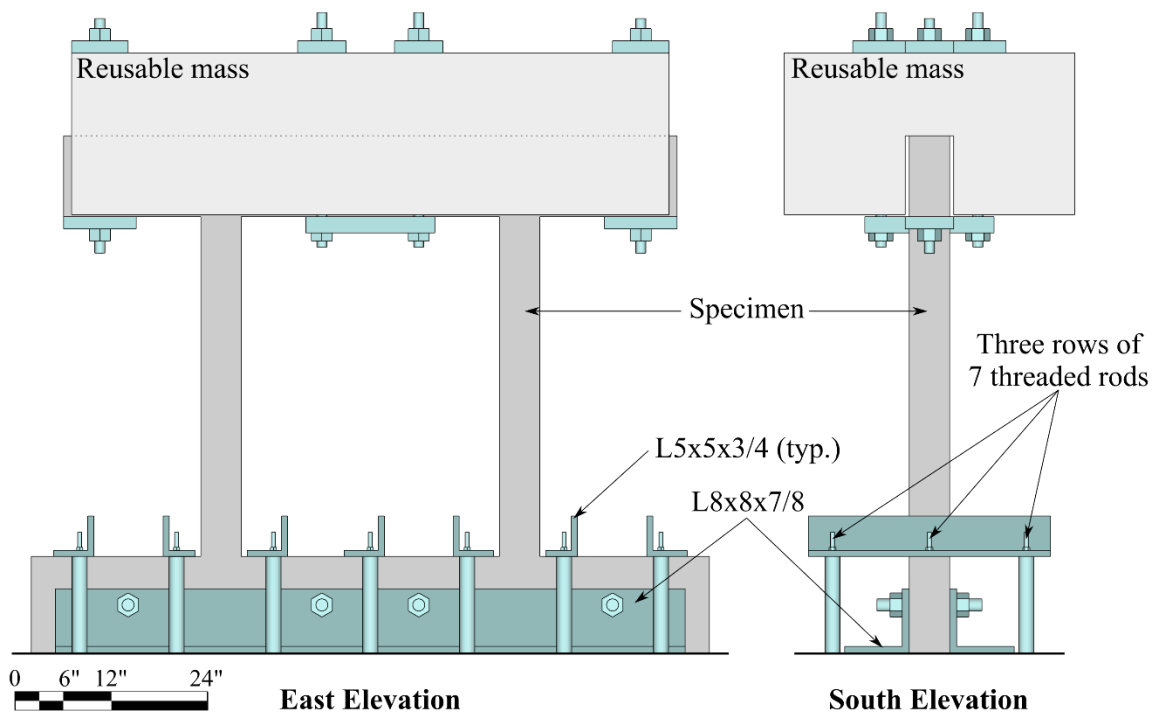


Figure 3-12: Renderings of specimen, mass, and connection components.

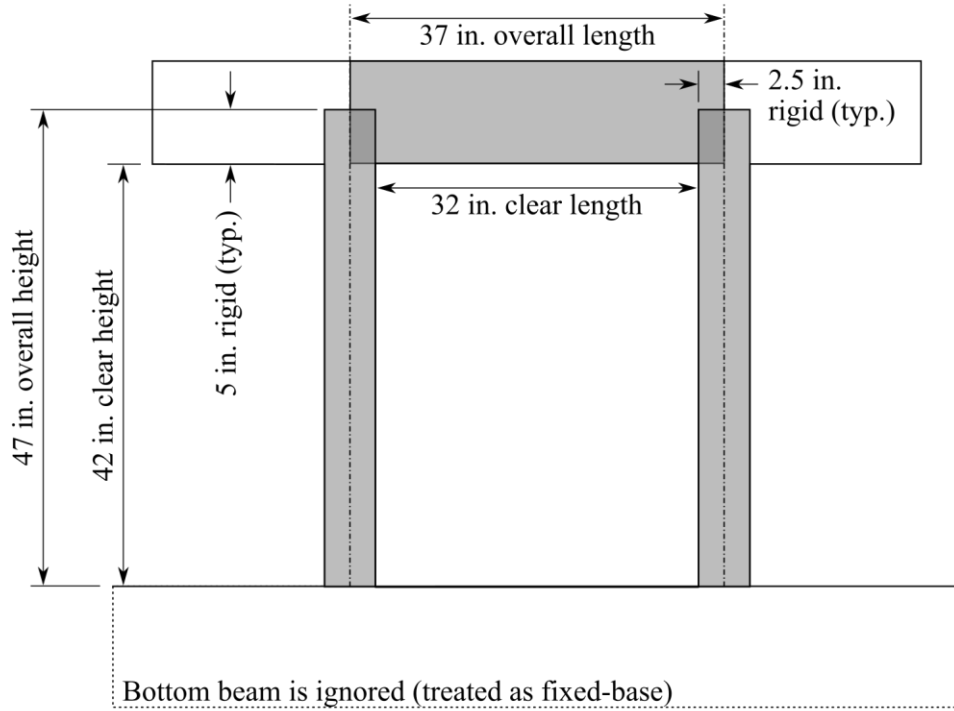


Figure 3-13: Assumed geometry for LARZ models.

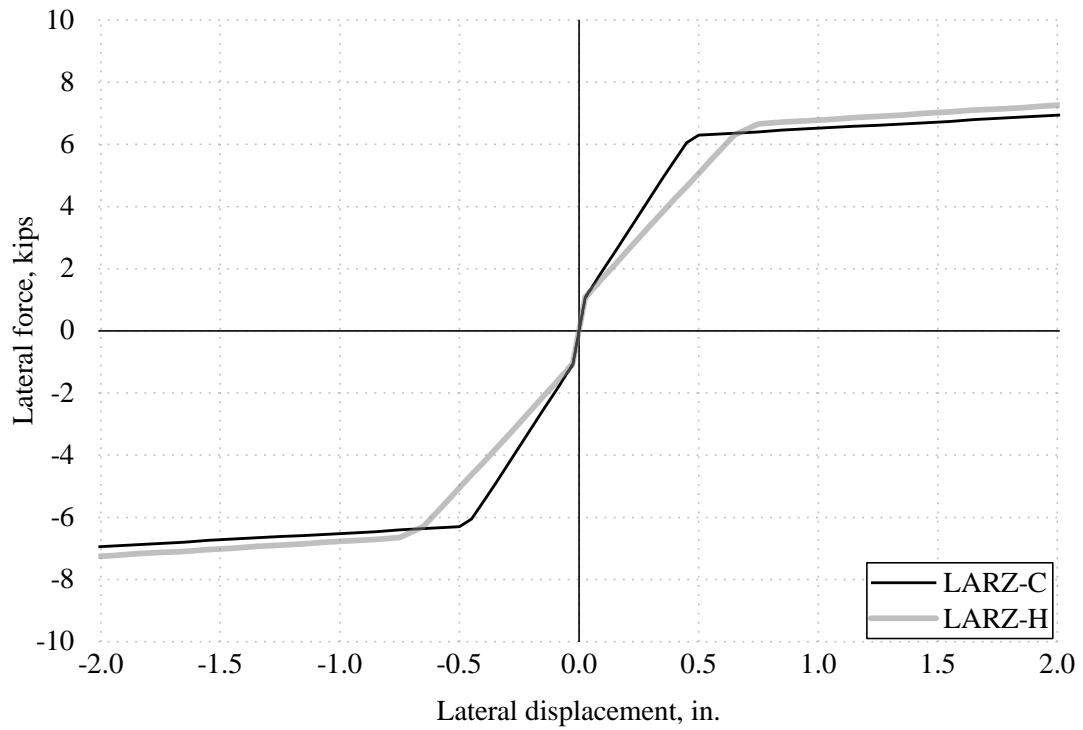


Figure 3-14: Lateral force versus displacement curves for C and H frames (from LARZ).

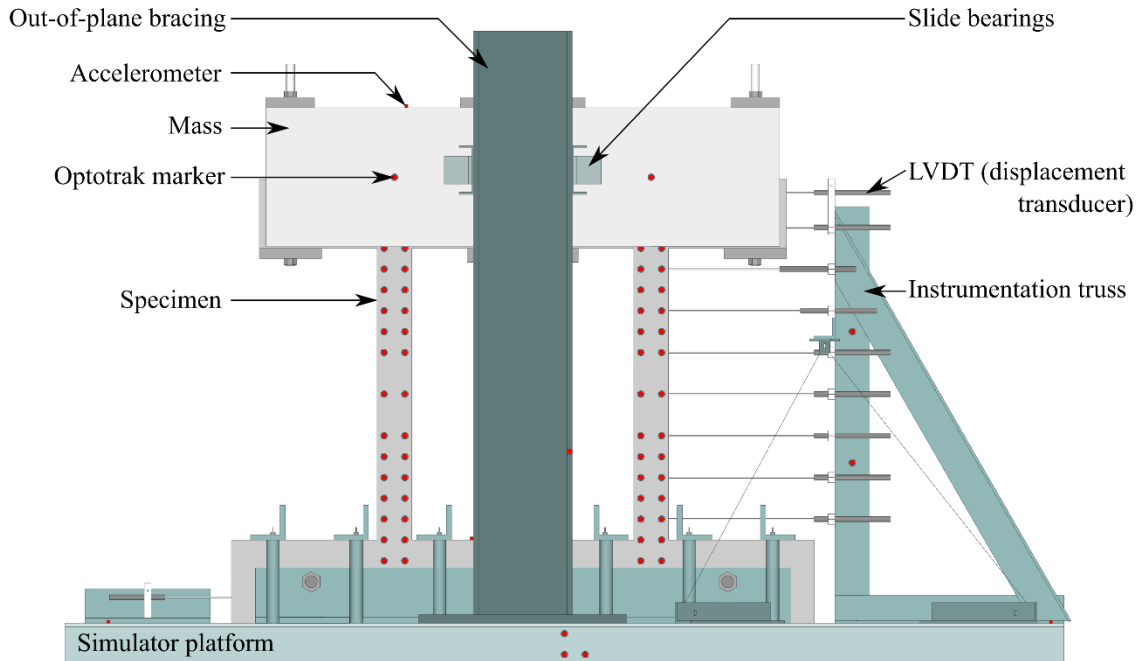


Figure 3-15: Rendering of west elevation of test setup highlighting primary components.

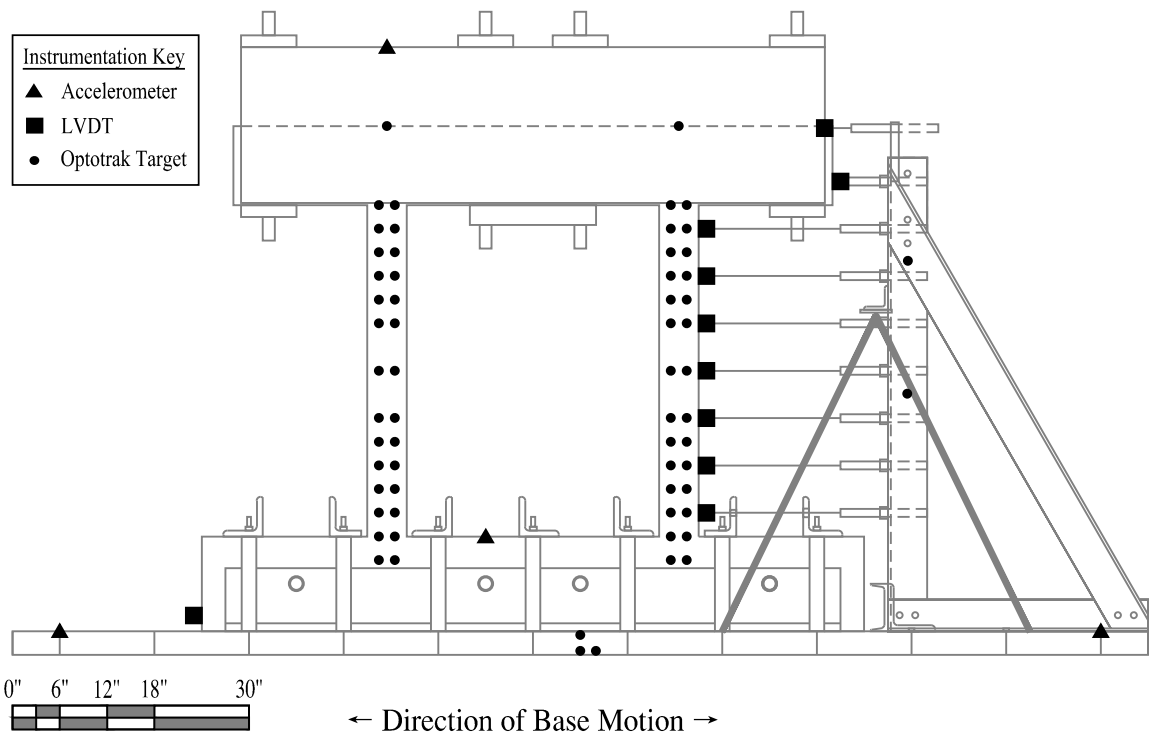
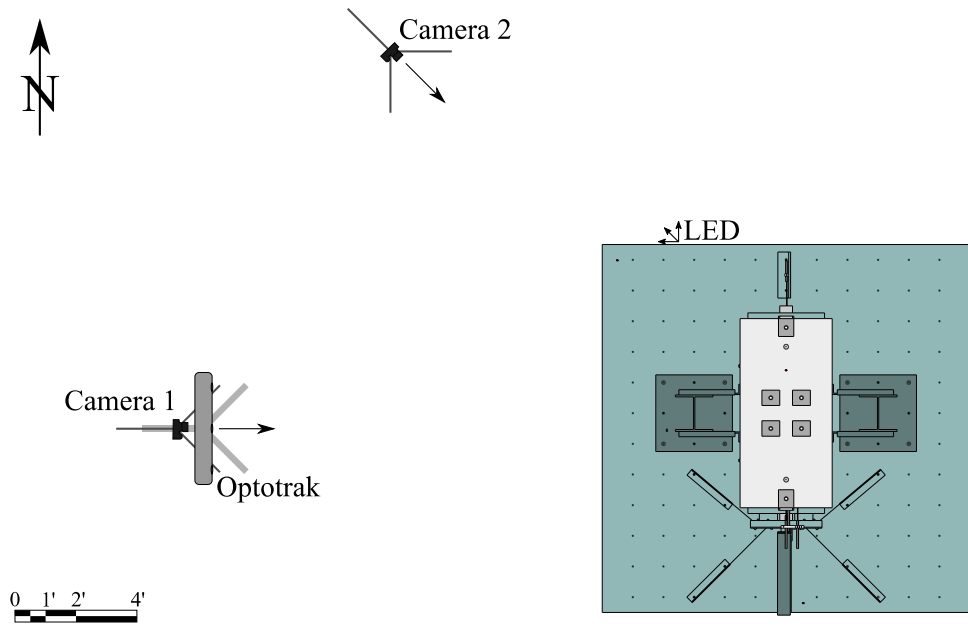


Figure 3-16: Instrumentation layout.



Plan View of Test Setup

Note: Camera positions are approximate.

Figure 3-17: Plan view of setup showing camera and Optotrak positions.

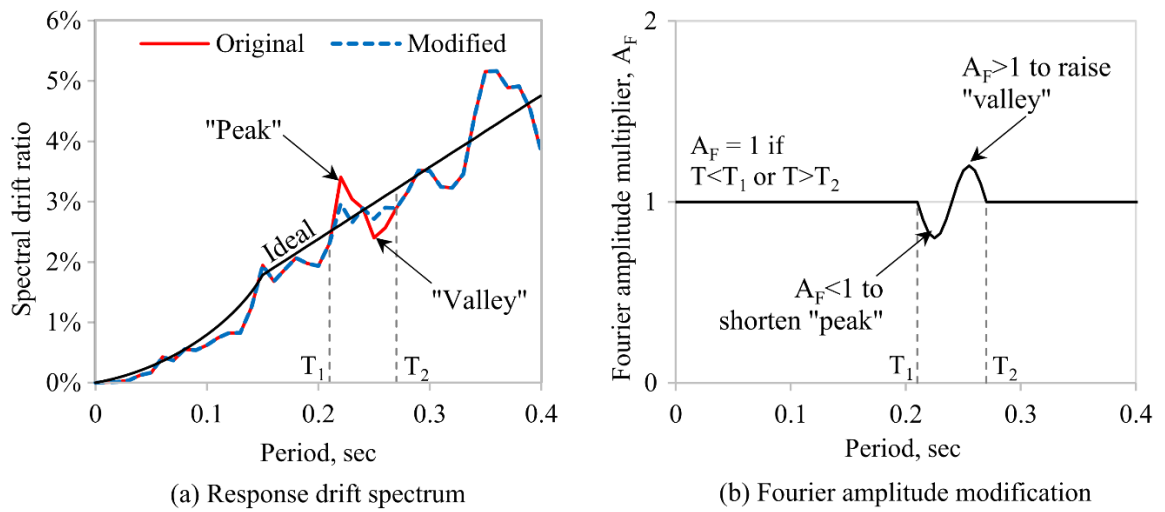


Figure 3-18: Fourier spectrum modification process used to smoothen displacement spectrum.

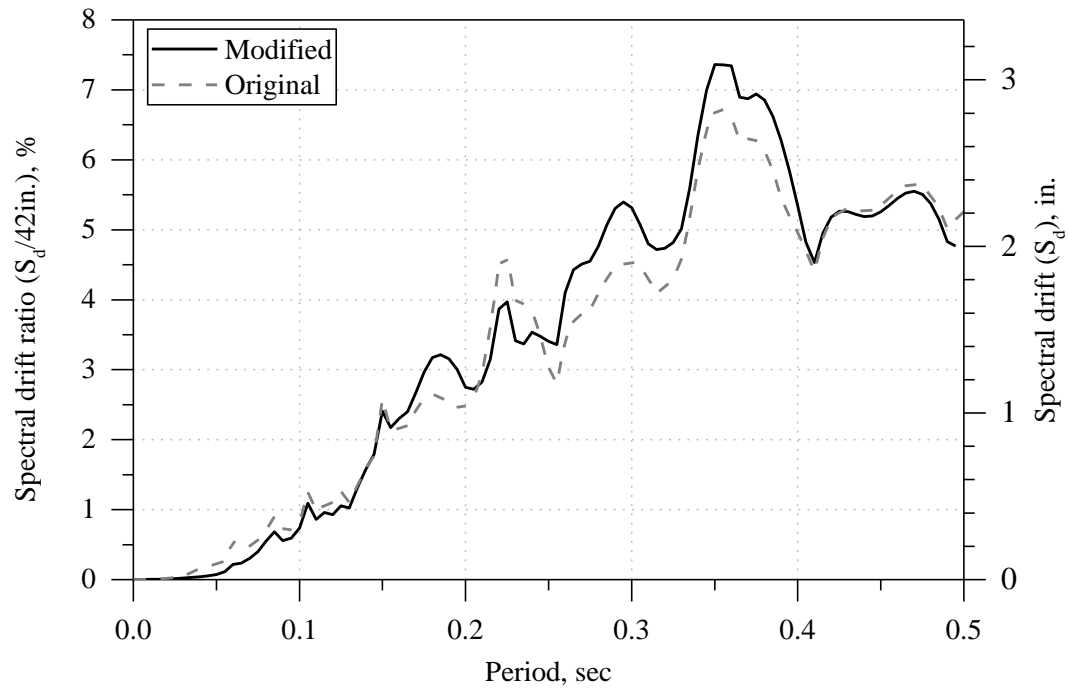


Figure 3-19: Comparison of linear displacement spectra of modified and original ground motions.

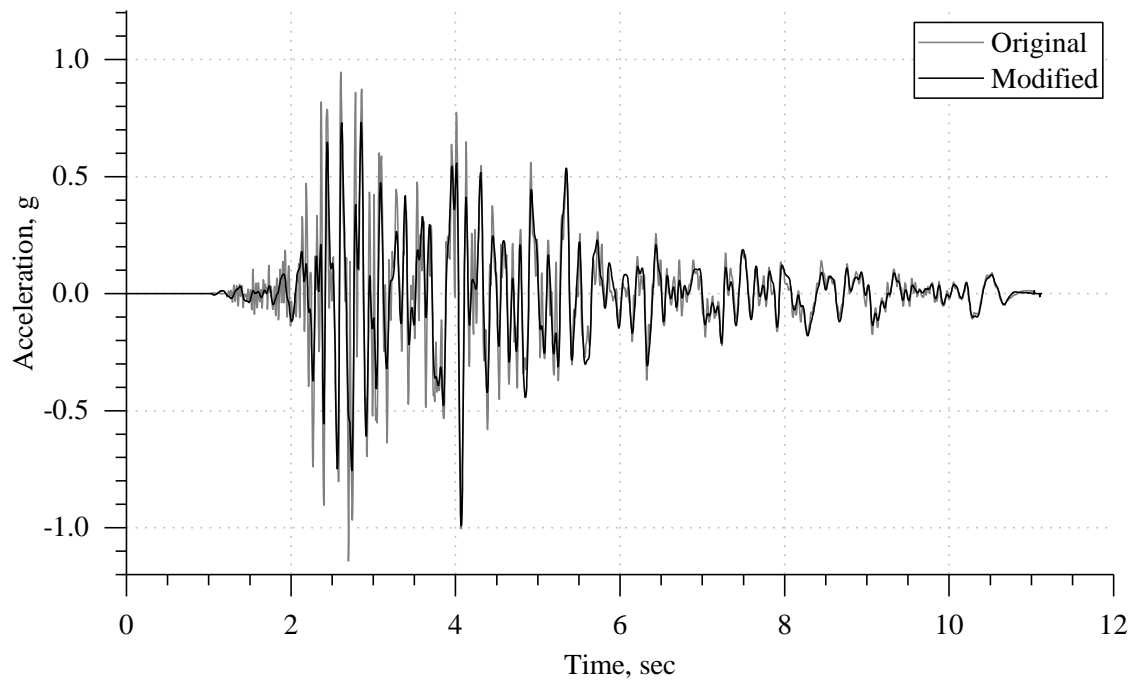


Figure 3-20: Comparison of original and modified acceleration histories.

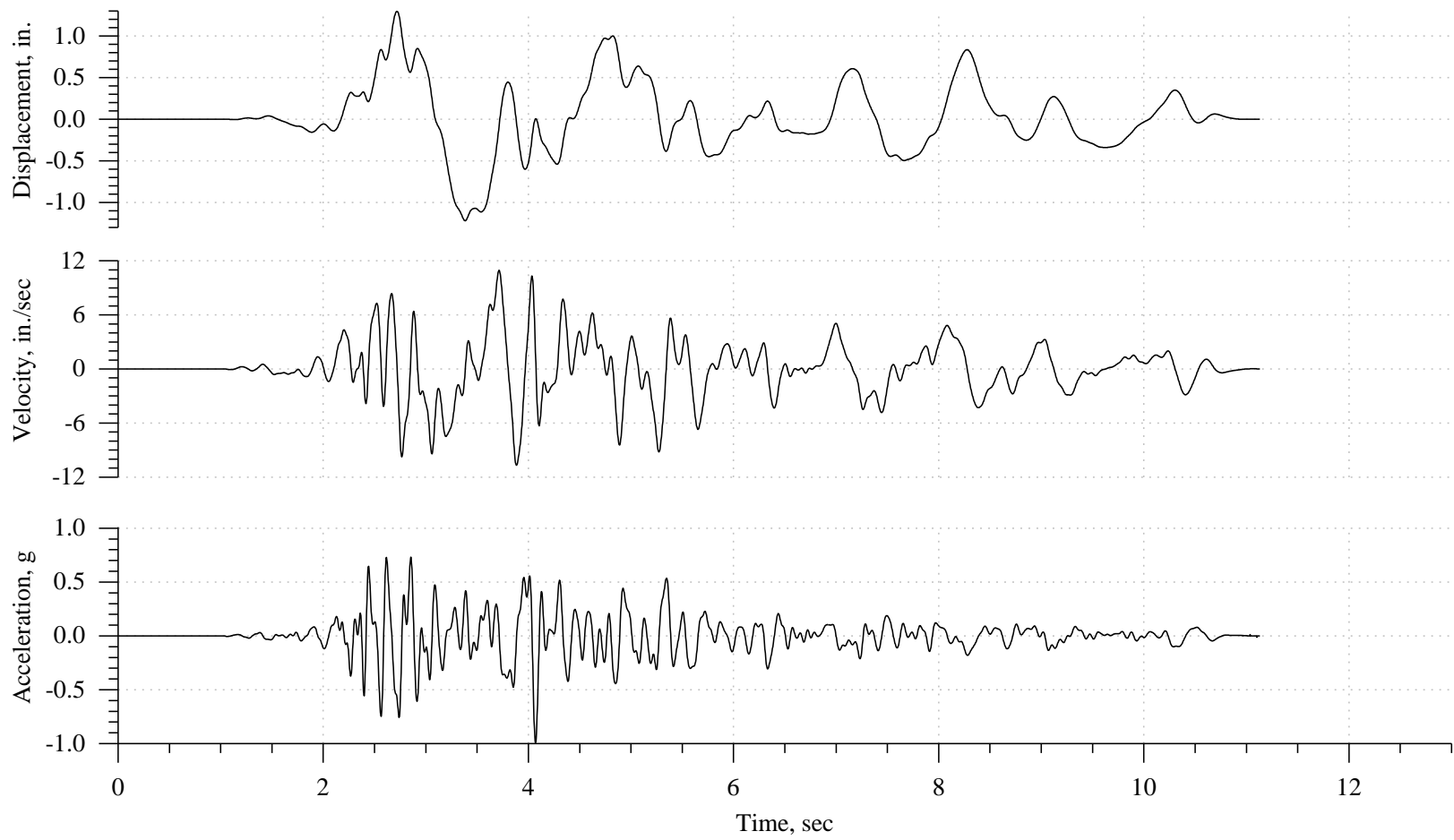


Figure 3-21: Ground motion histories for target 100% motion.

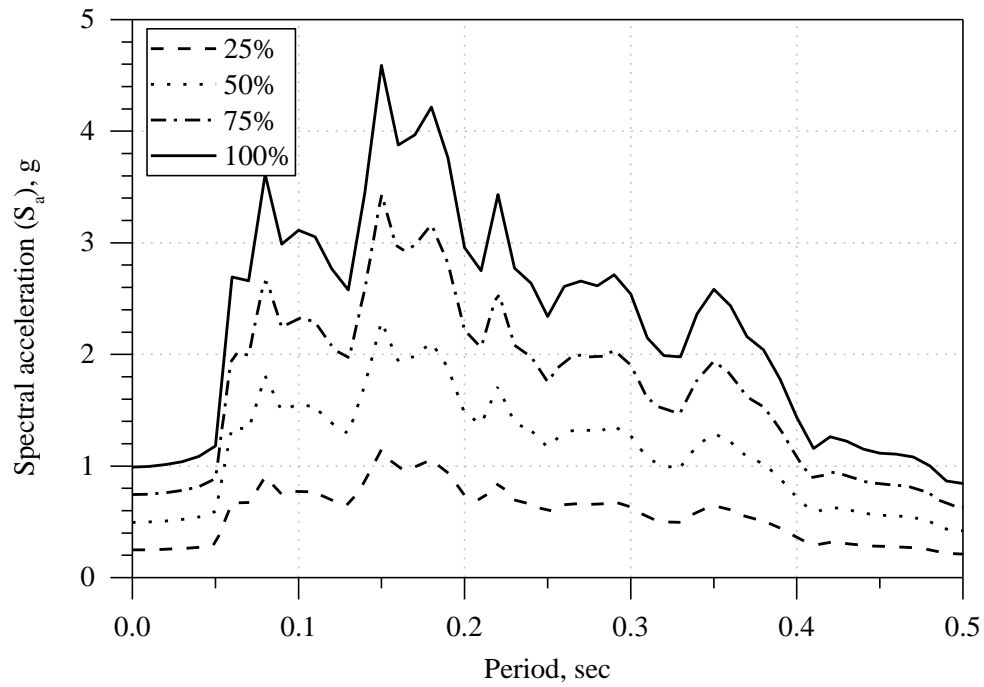


Figure 3-22: Linear acceleration response spectra for scaled ground motion records (2% damped).

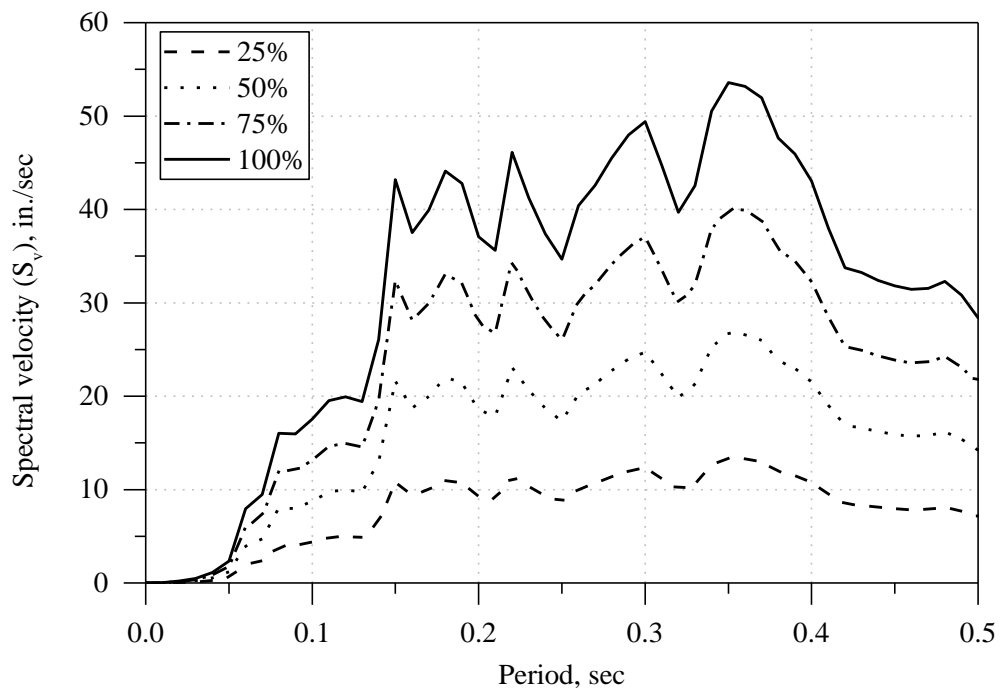


Figure 3-23: Linear velocity response spectra for scaled ground motion records (2% damped).

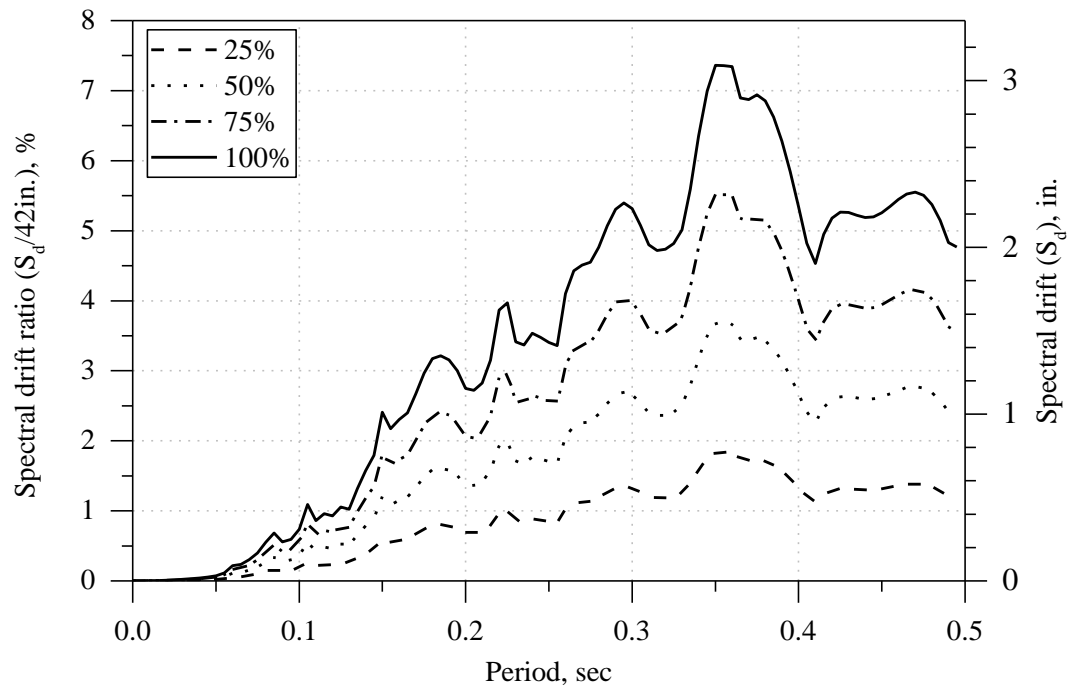


Figure 3-24: Linear displacement (drift) response spectra for scaled ground motion records (2% damped).

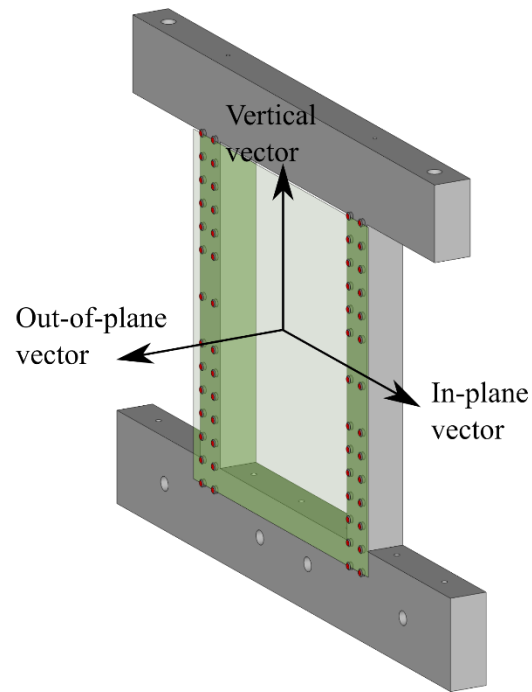
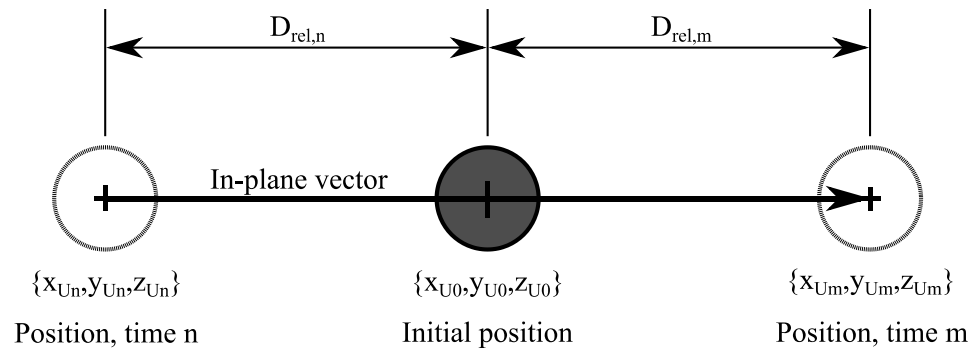


Figure 4-1: Illustration of experiment coordinate system vectors.



where $\frac{D_{rel,n}}{D_{rel,m}} < 0$

and $\frac{|D_{rel,n}| - |D_{rel,m}|}{(|D_{rel,n}| + |D_{rel,m}|)/2}$ is minimized

Figure 4-2: Method for obtaining in-plane transformation vector for Optotrak targets.

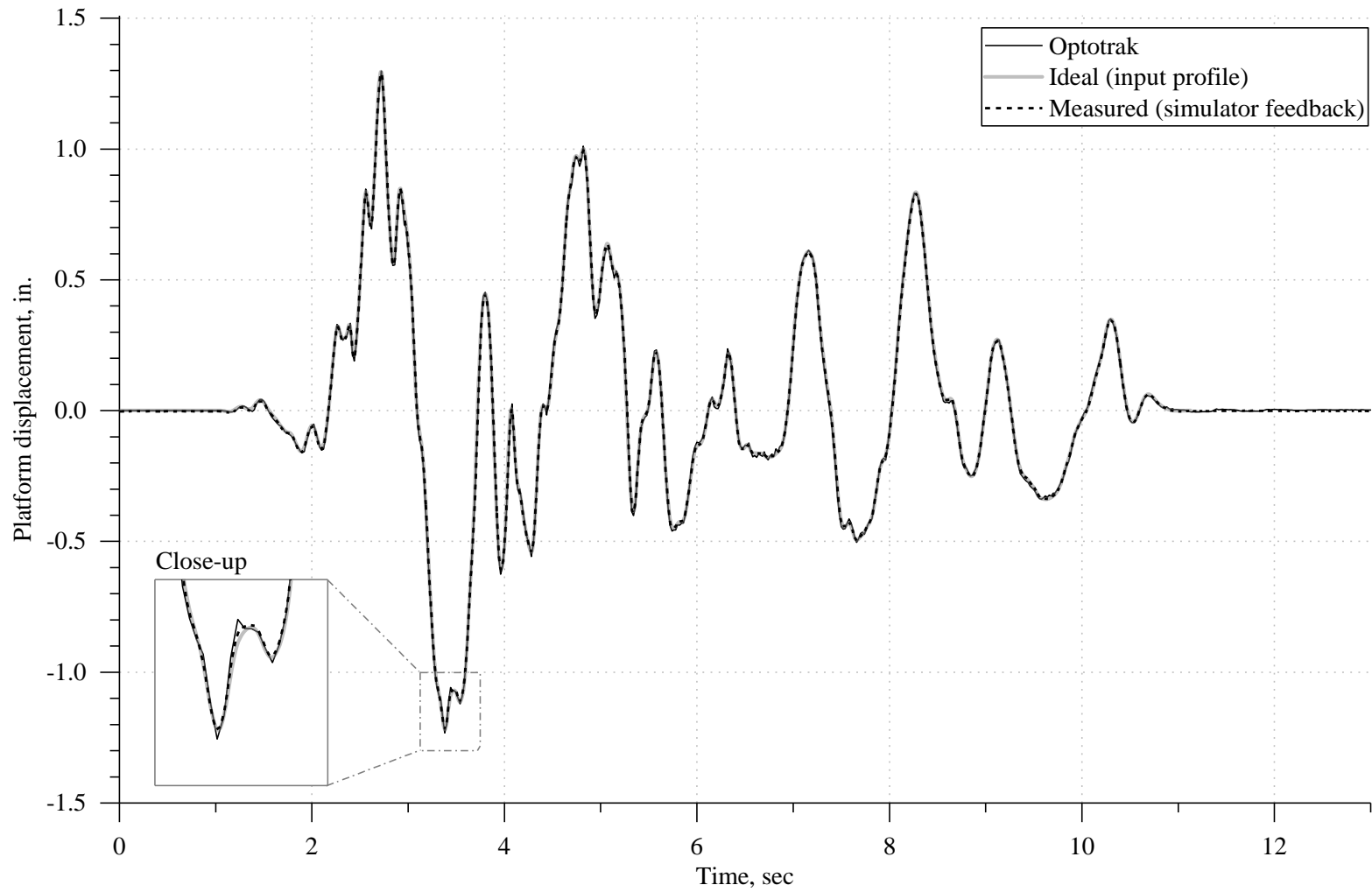


Figure 4-3: Comparison of ideal platform displacement with Optotrak and feedback.

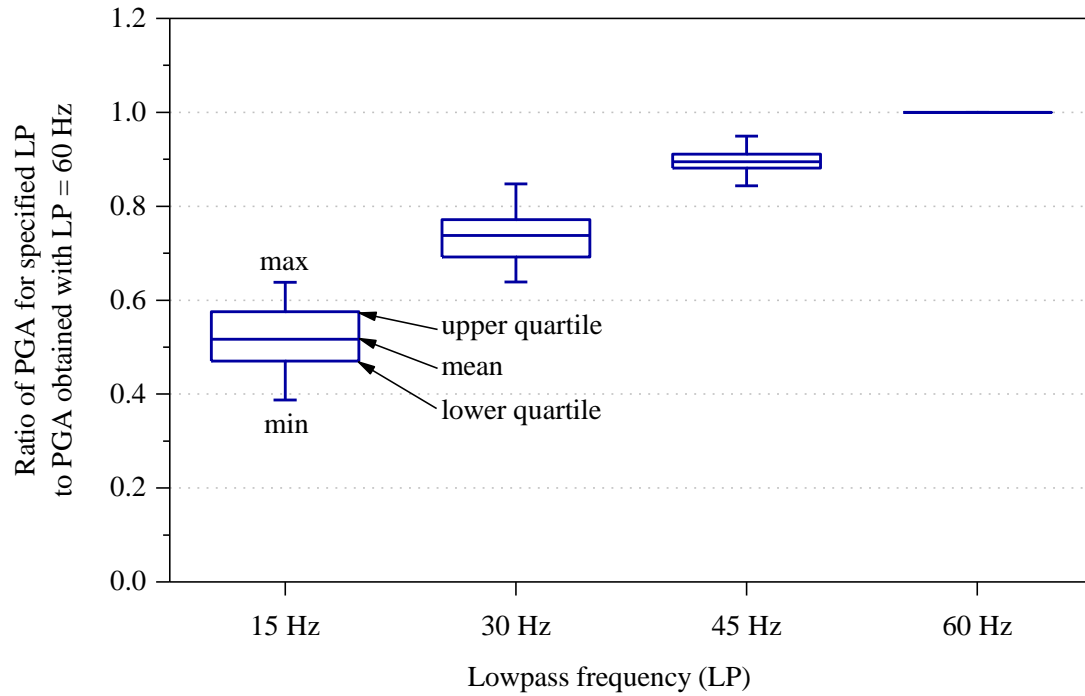


Figure 4-4: Effect on PGA of reducing lowpass frequency from 60 Hz to 15 Hz.

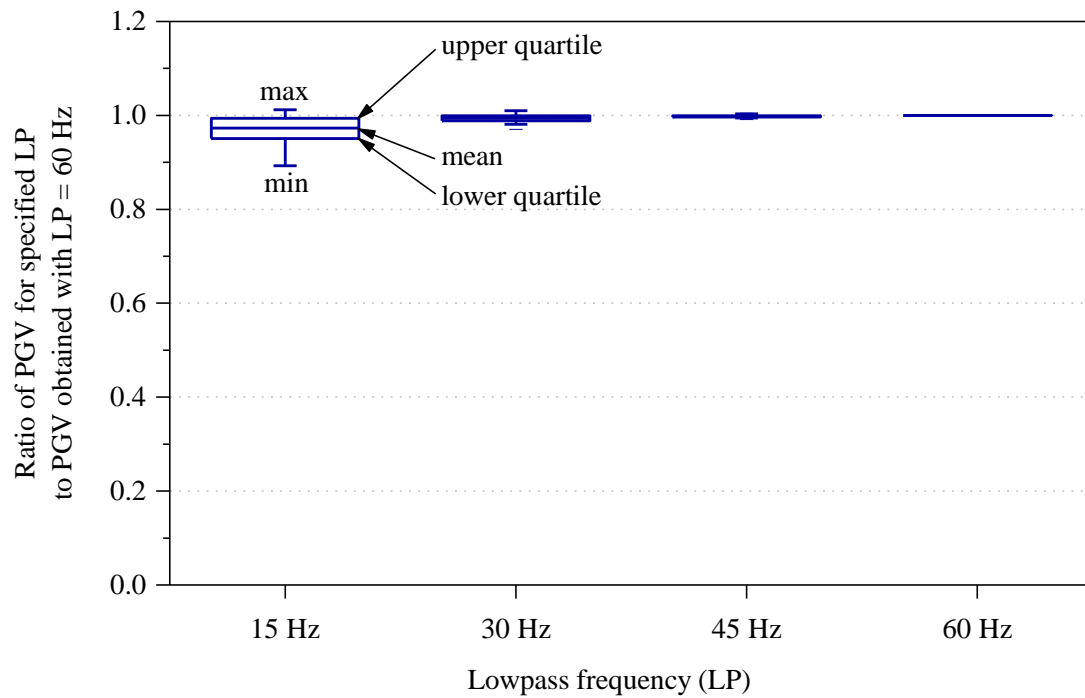


Figure 4-5: Effect on PGV of reducing lowpass frequency from 60 Hz to 15 Hz.

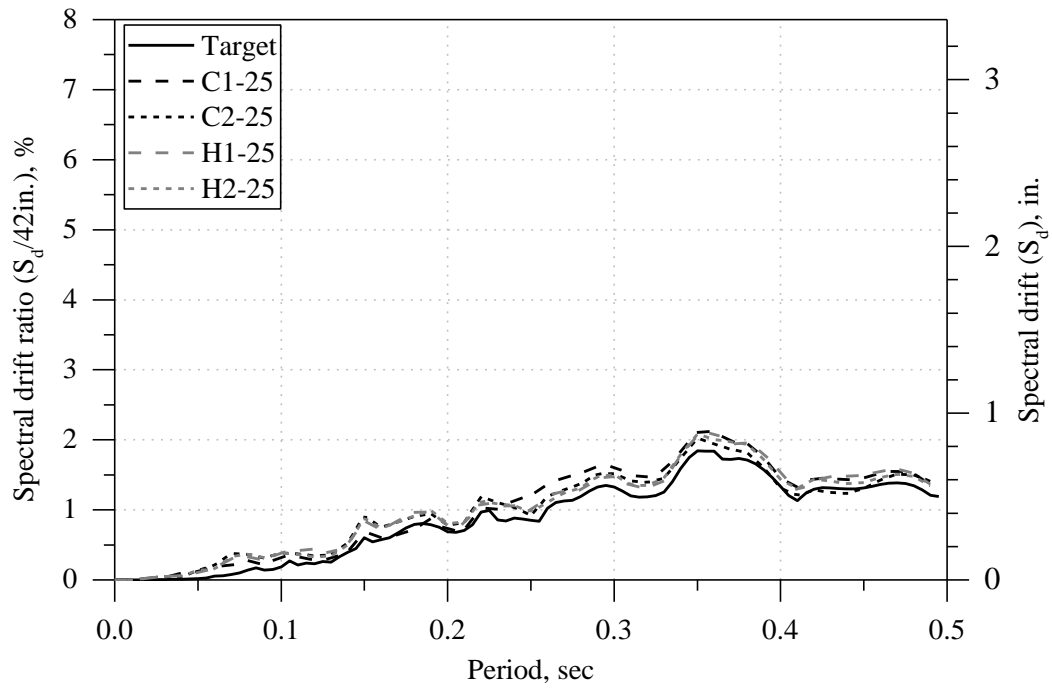


Figure 4-6: Comparison of linear displacement response spectra obtained from 25% runs with target spectrum (2% damped).

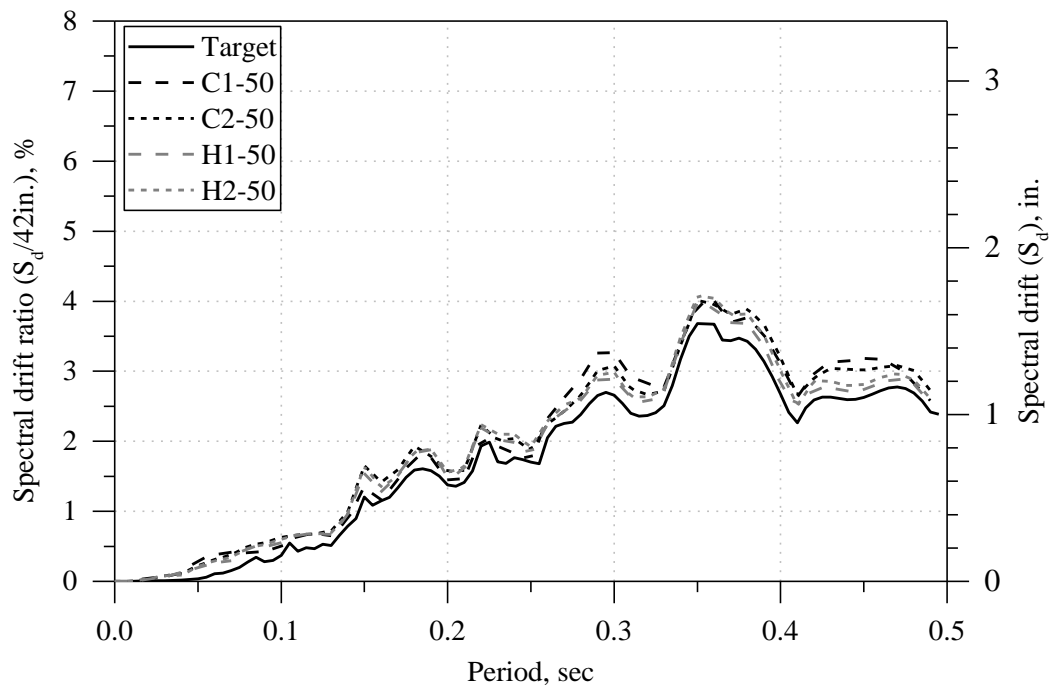


Figure 4-7: Comparison of linear displacement response spectra obtained from 50% runs with target spectrum (2% damped).

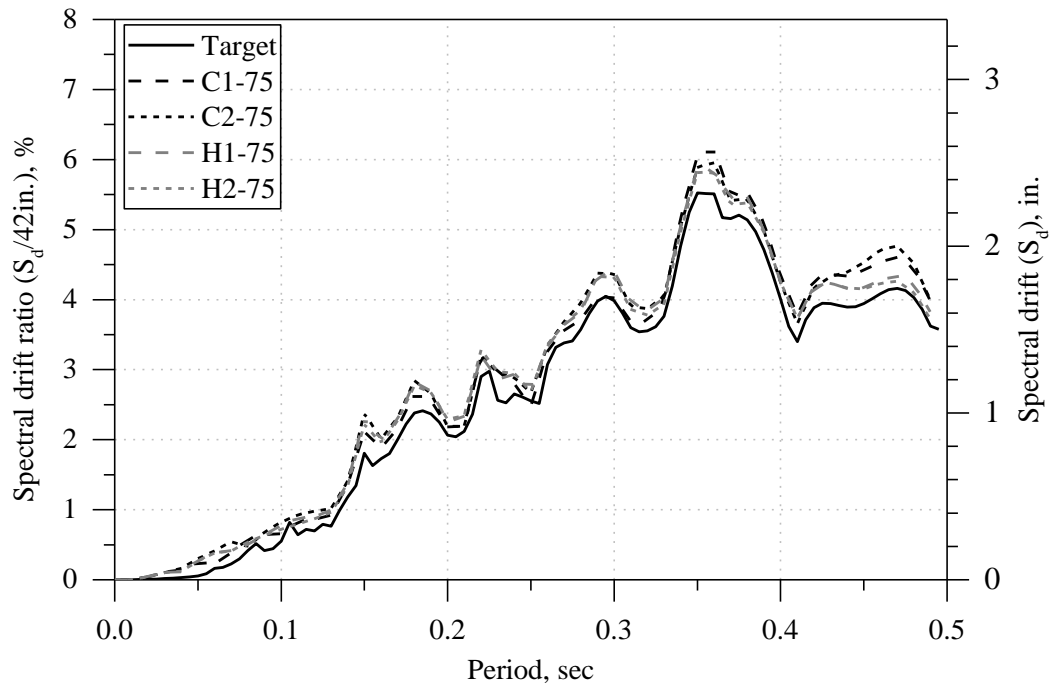


Figure 4-8: Comparison of linear displacement response spectra obtained from 75% runs with target spectrum (2% damped).

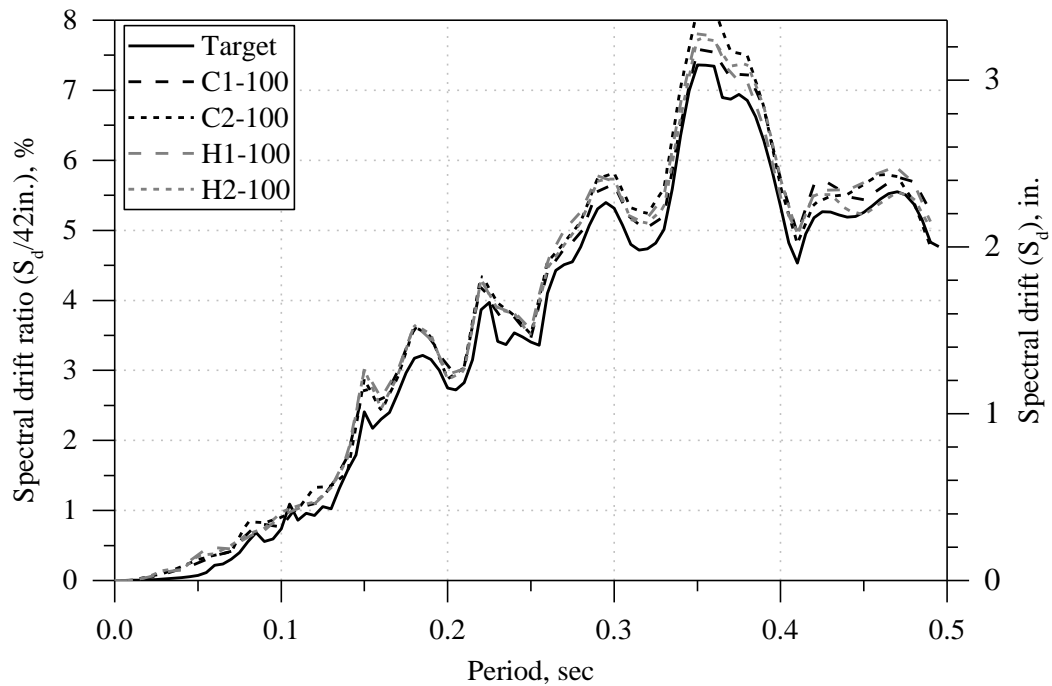


Figure 4-9: Comparison of linear displacement response spectra obtained from first 100% runs with target spectrum (2% damped).

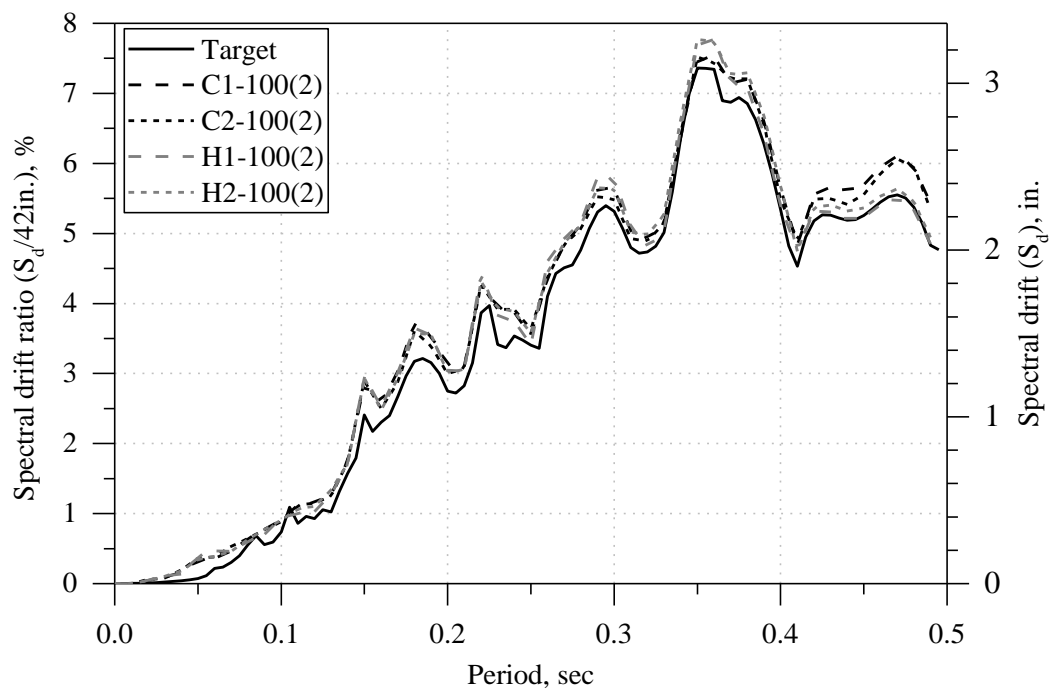


Figure 4-10: Comparison of linear displacement response spectra obtained from second 100% runs with target spectrum (2% damped).

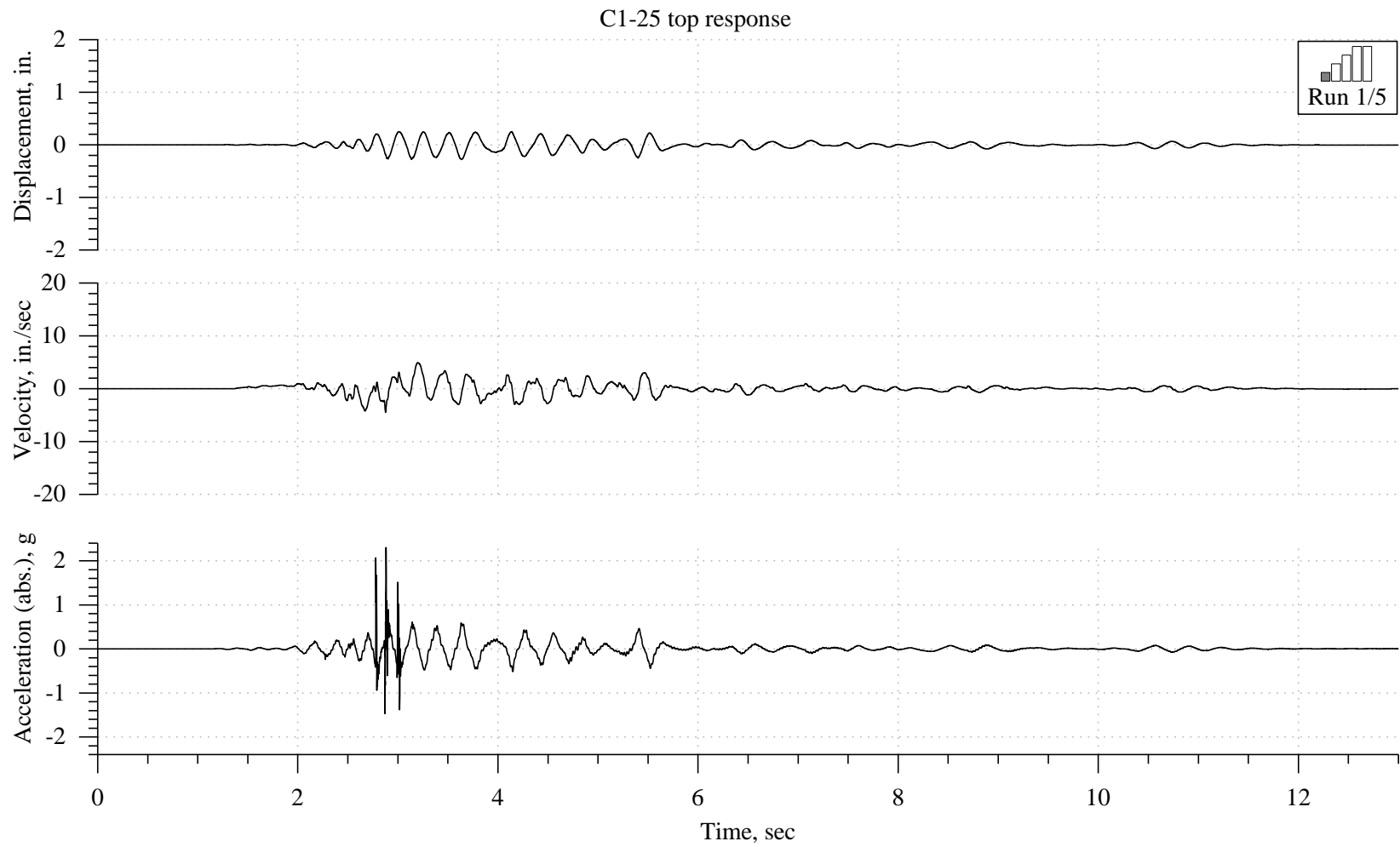


Figure 4-11: Response histories for specimen C1, 25% run (first of five runs).

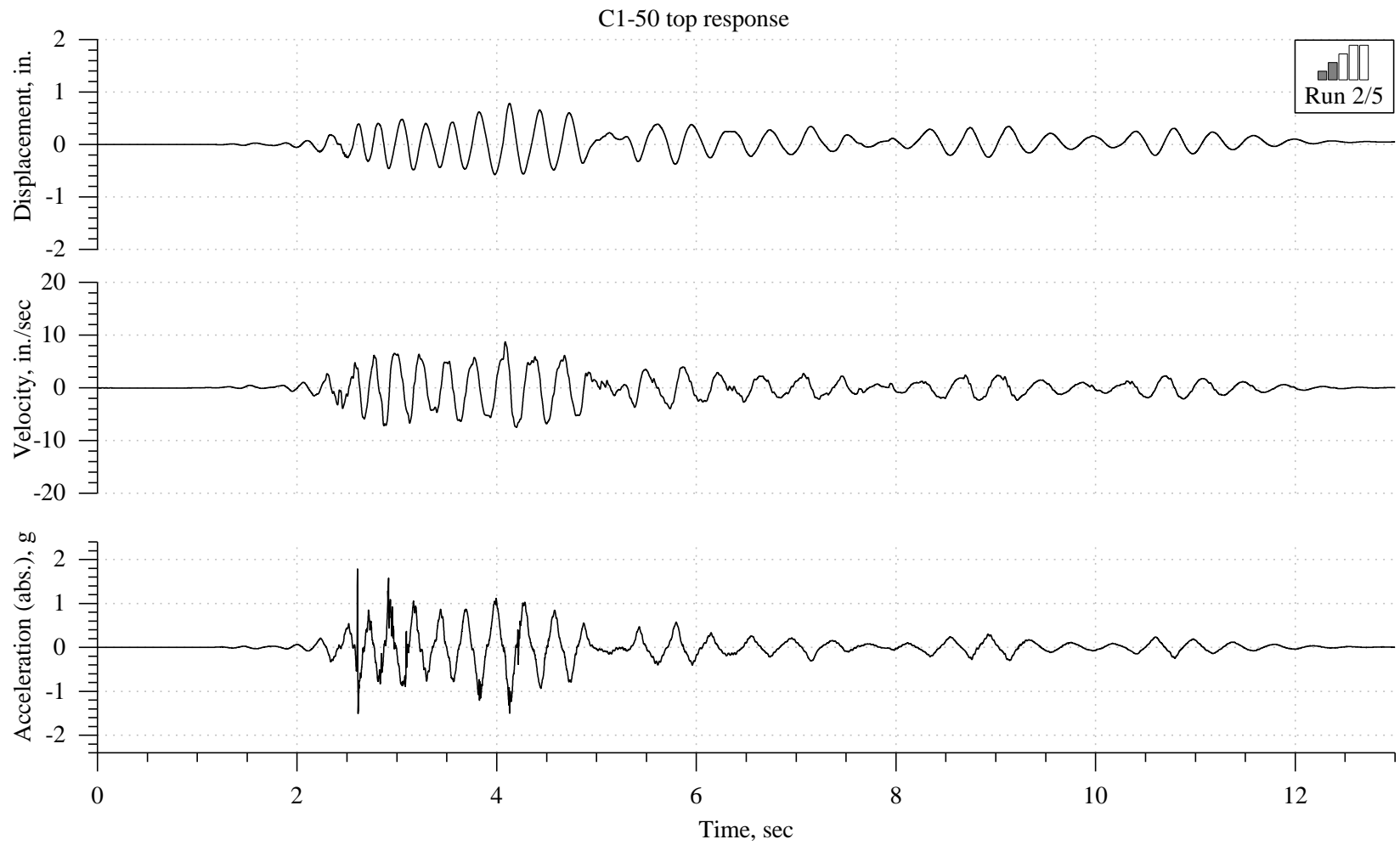


Figure 4-12: Response histories for specimen C1, 50% run (second of five runs).

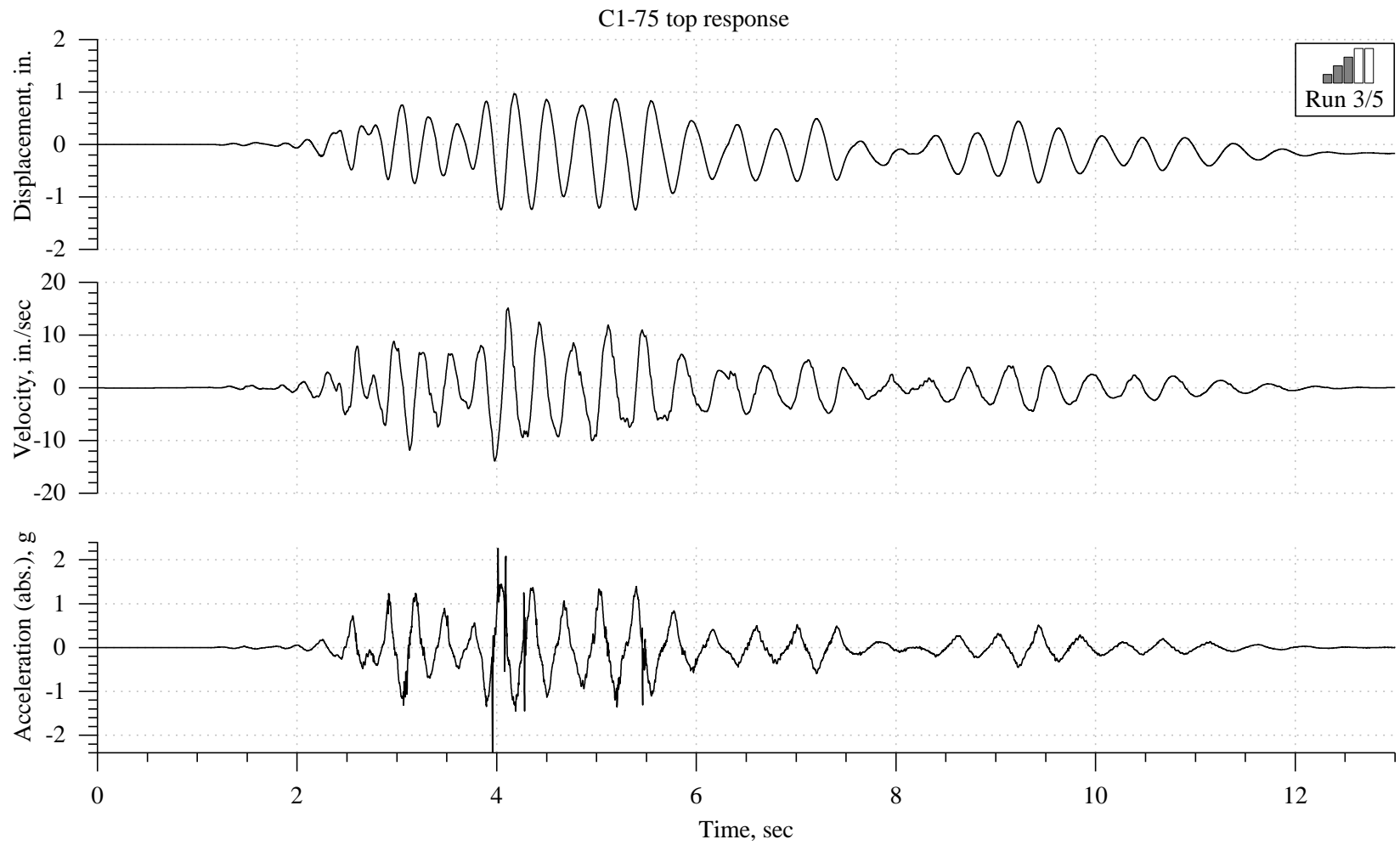


Figure 4-13: Response histories for specimen C1, 75% run (third of five runs).

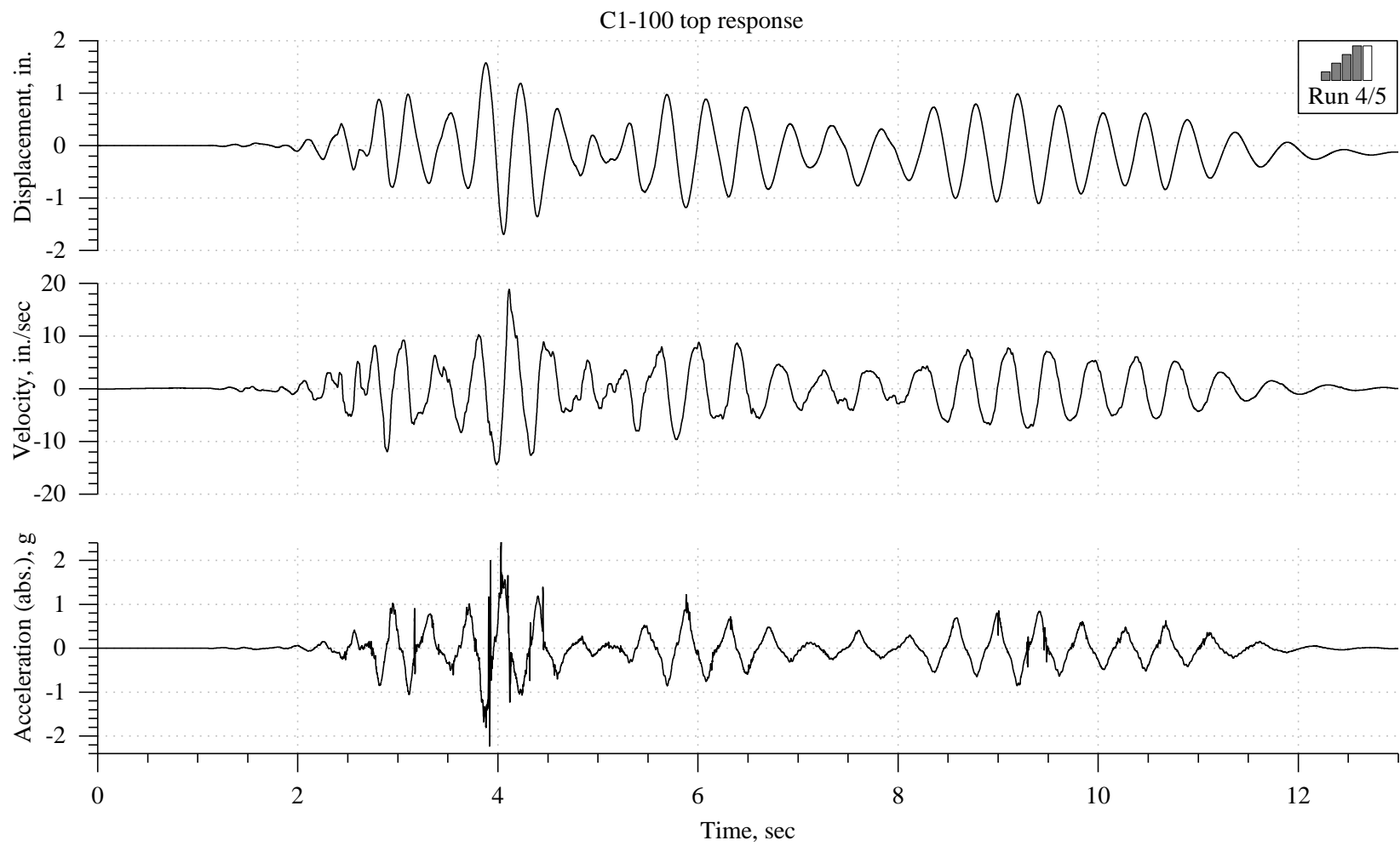


Figure 4-14: Response histories for specimen C1, 100% run (fourth of five runs).

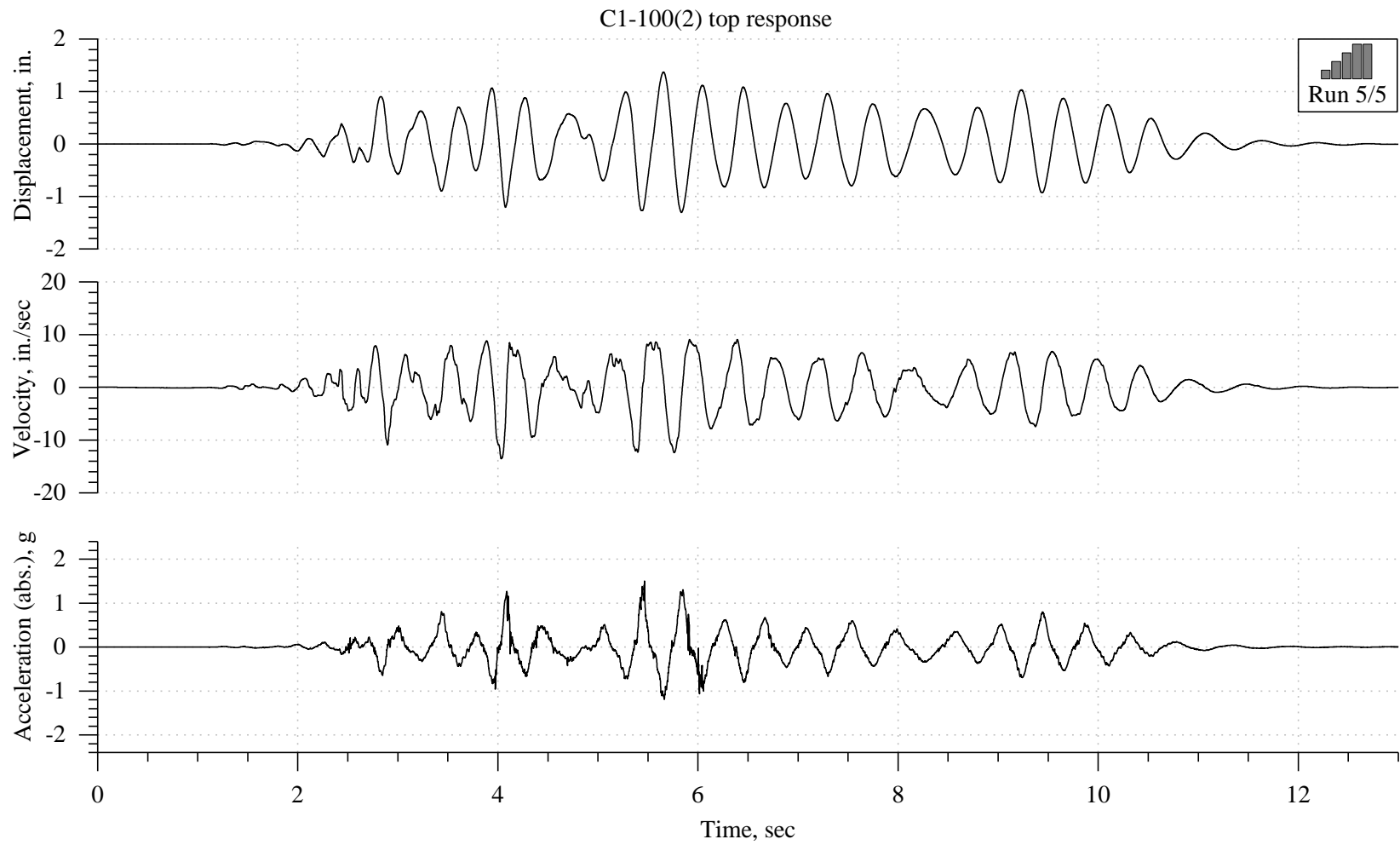


Figure 4-15: Response histories for specimen C1, second 100% run (fifth of five runs).

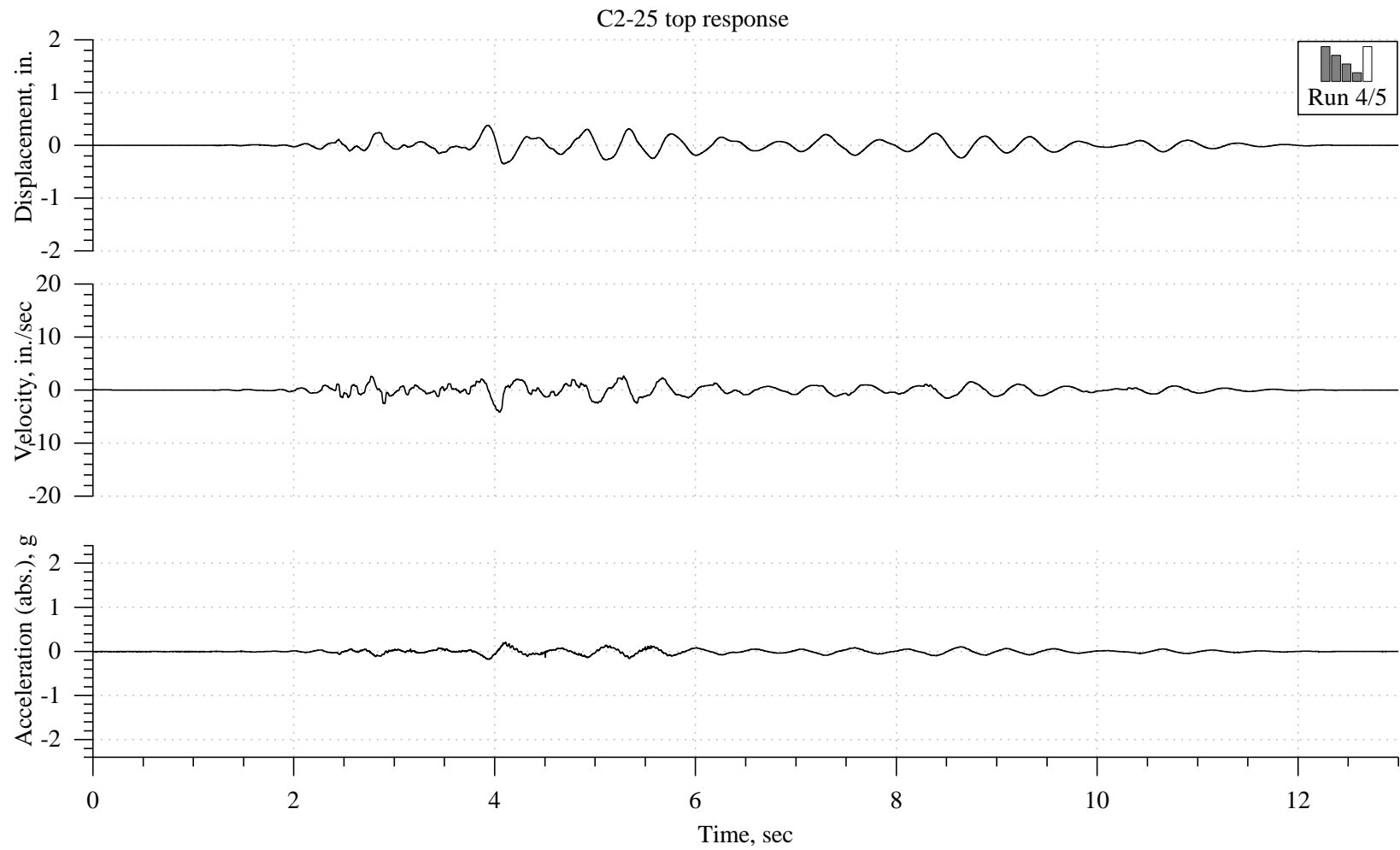


Figure 4-16: Response histories for specimen C2, 25% run (fourth of five runs).

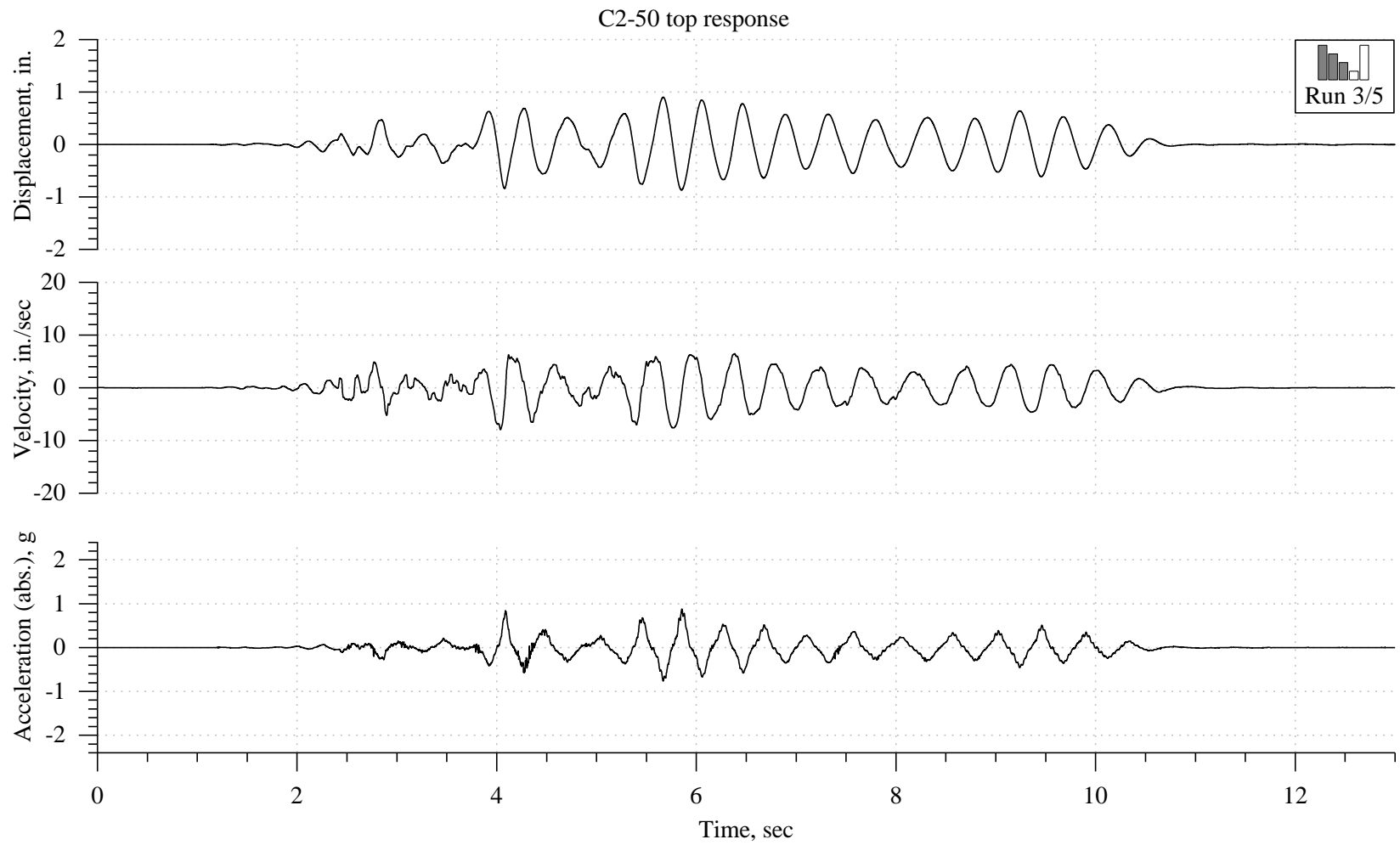


Figure 4-17: Response histories for specimen C2, 50% run (third of five runs).

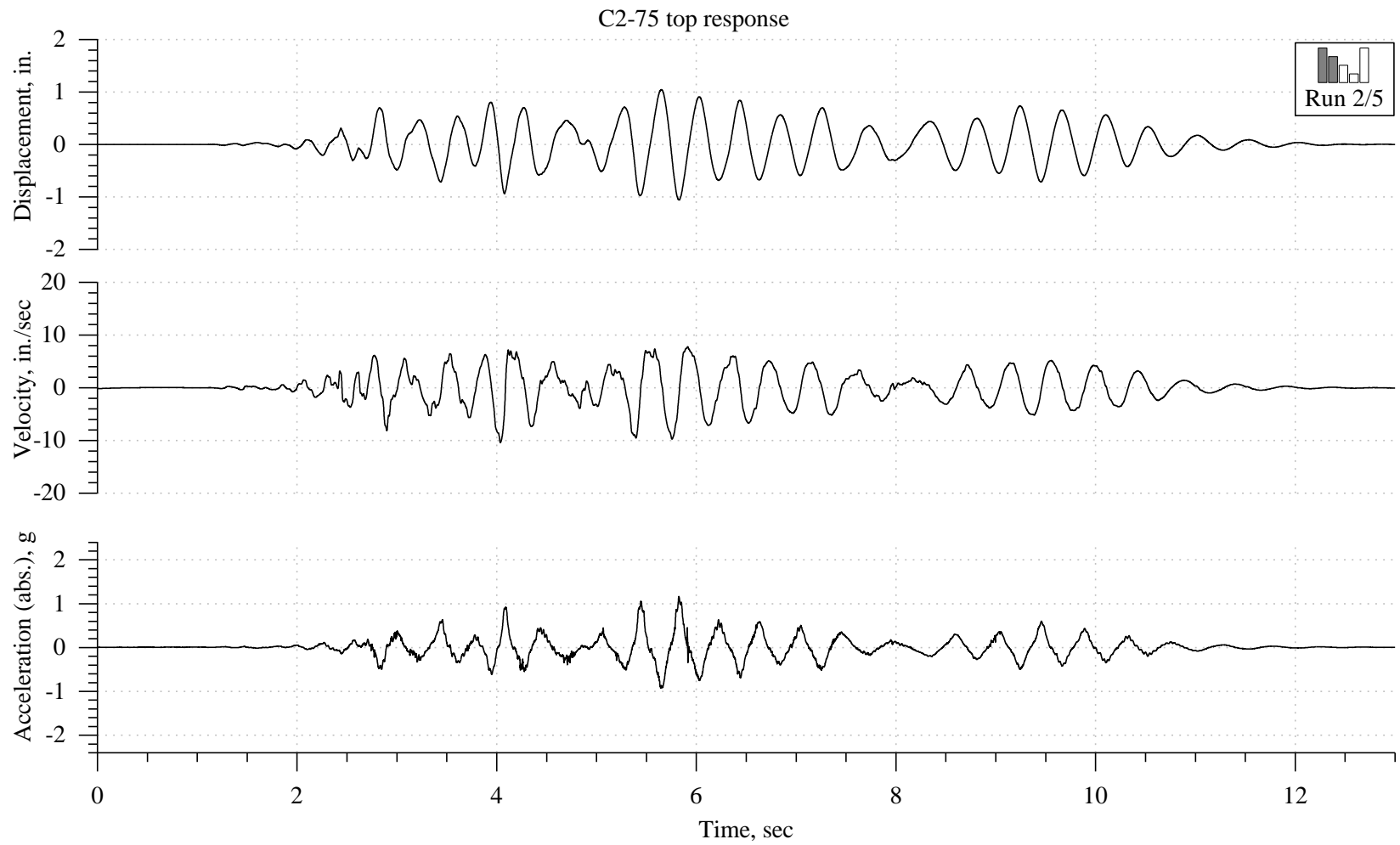


Figure 4-18: Response histories for specimen C2, 75% run (second of five runs).

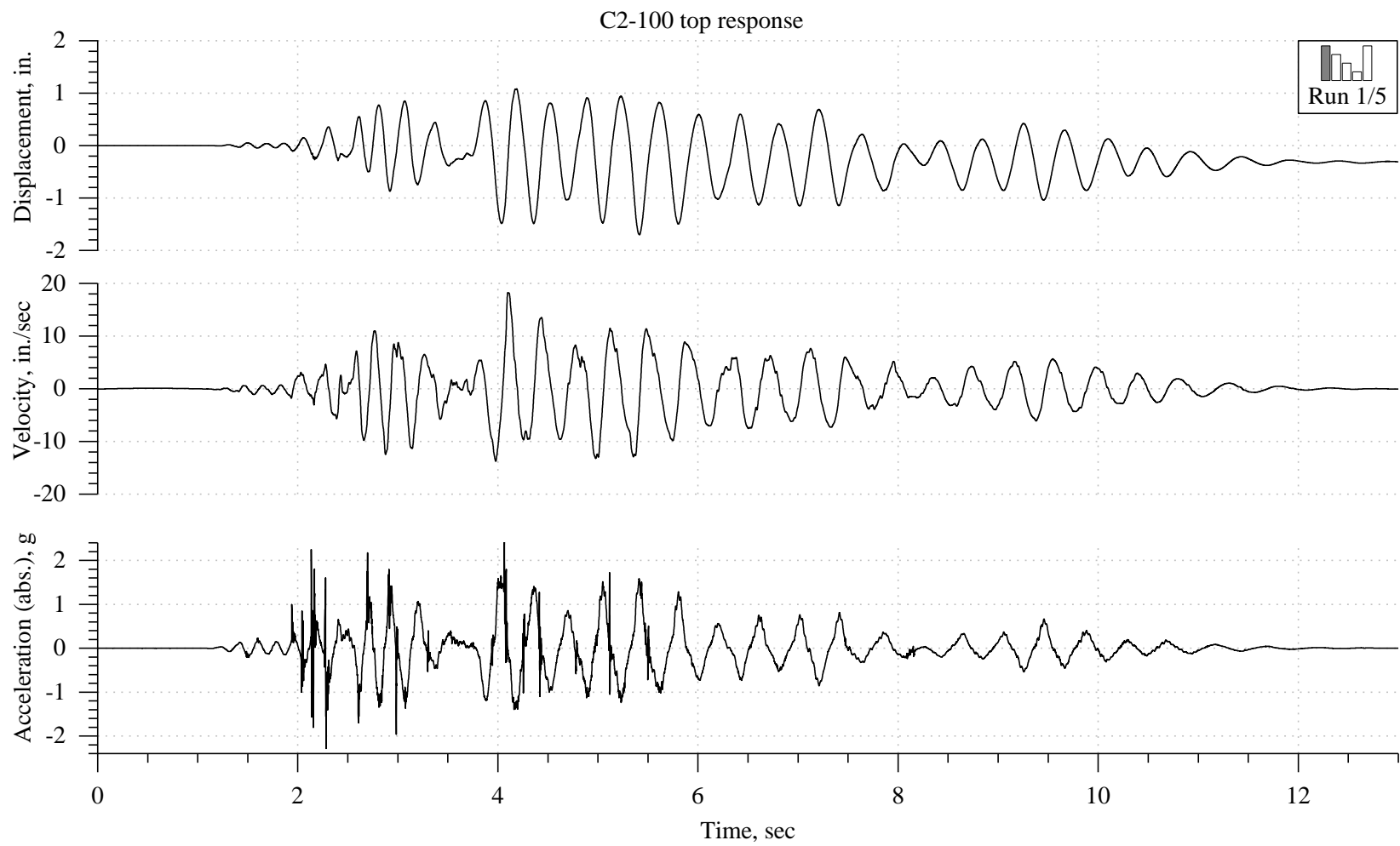


Figure 4-19: Response histories for specimen C2, 100% run (first of five runs).

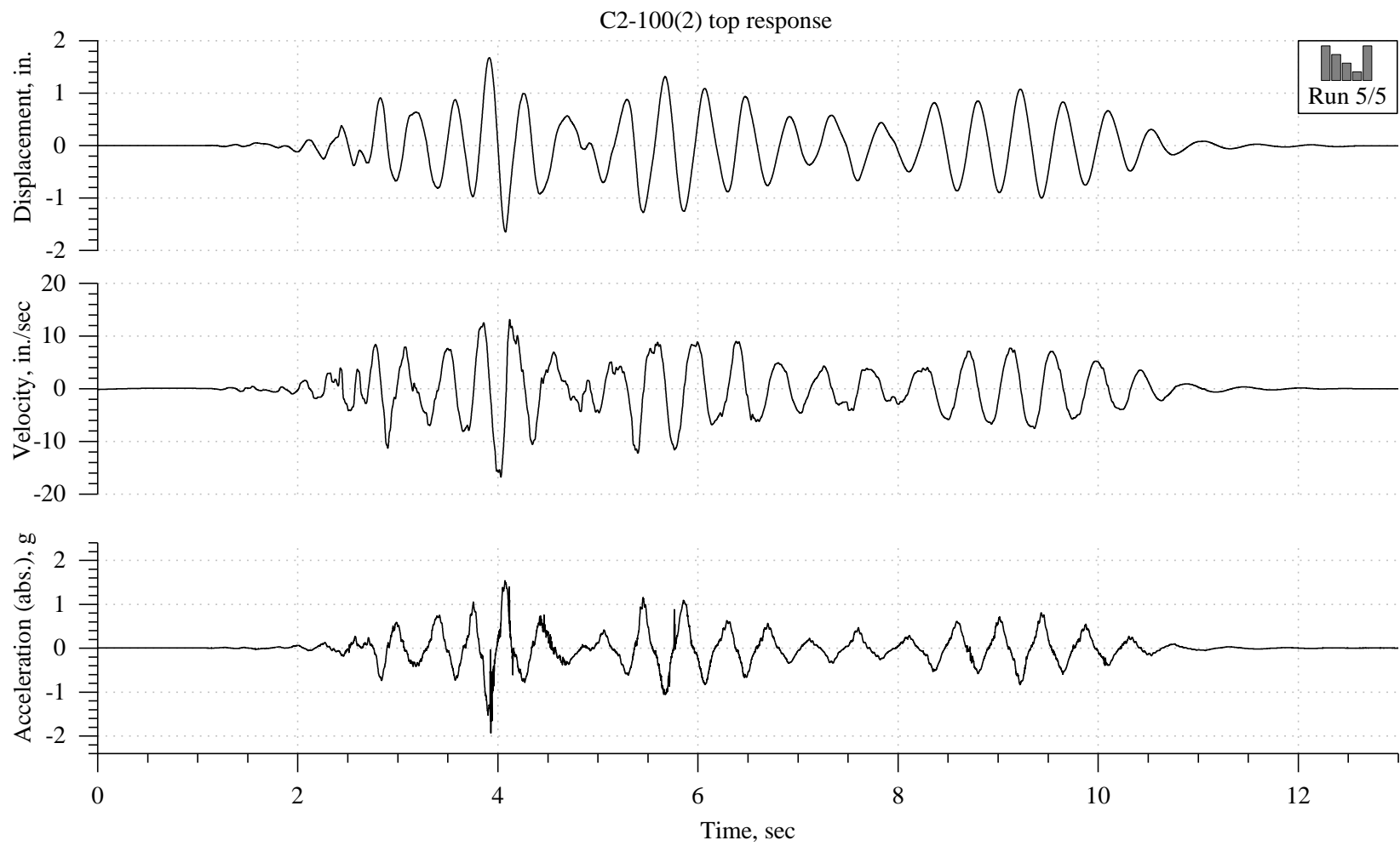


Figure 4-20: Response histories for specimen C2, second 100% run (fifth of five runs).

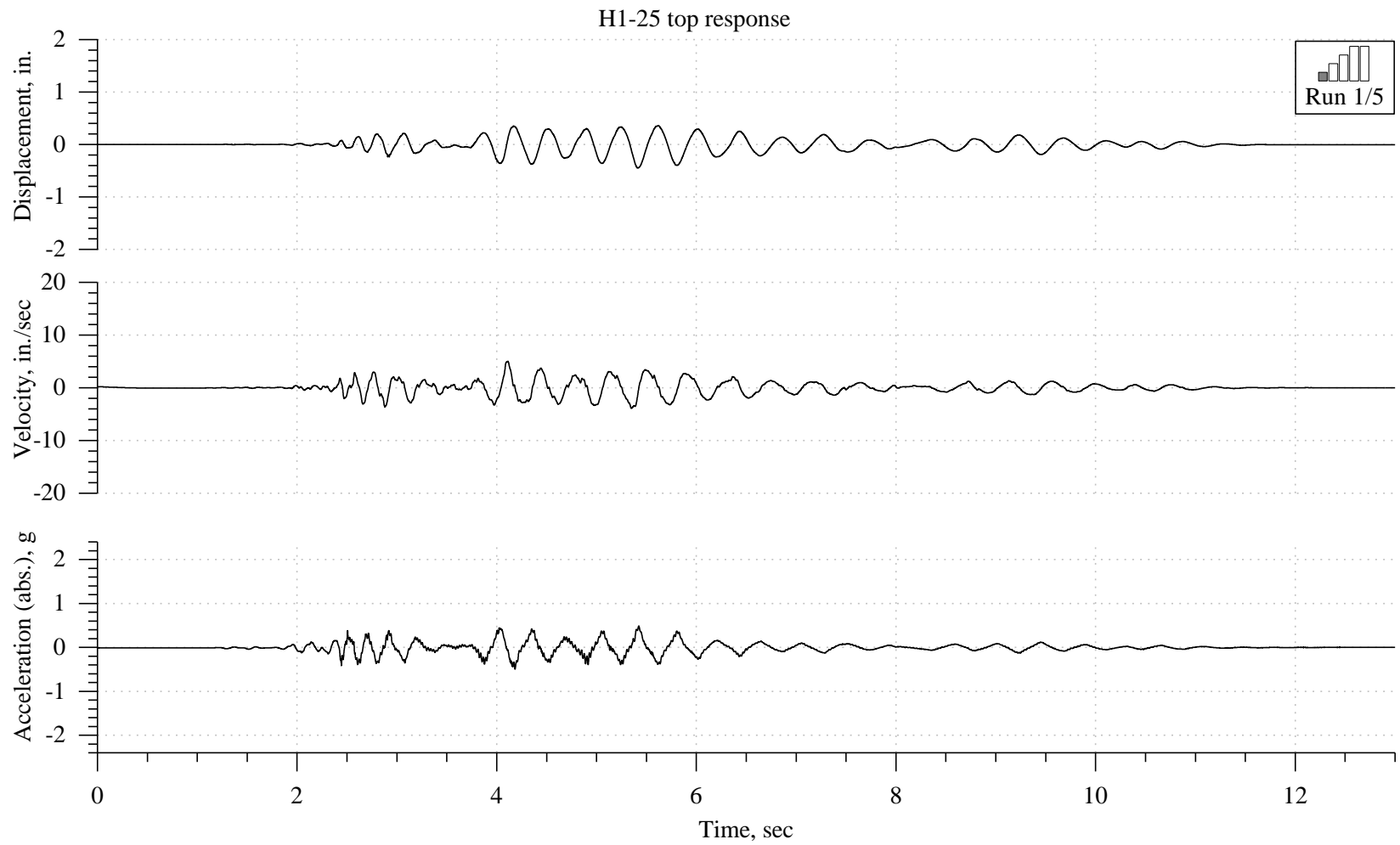


Figure 4-21: Response histories for specimen H1, 25% run (first of five runs).

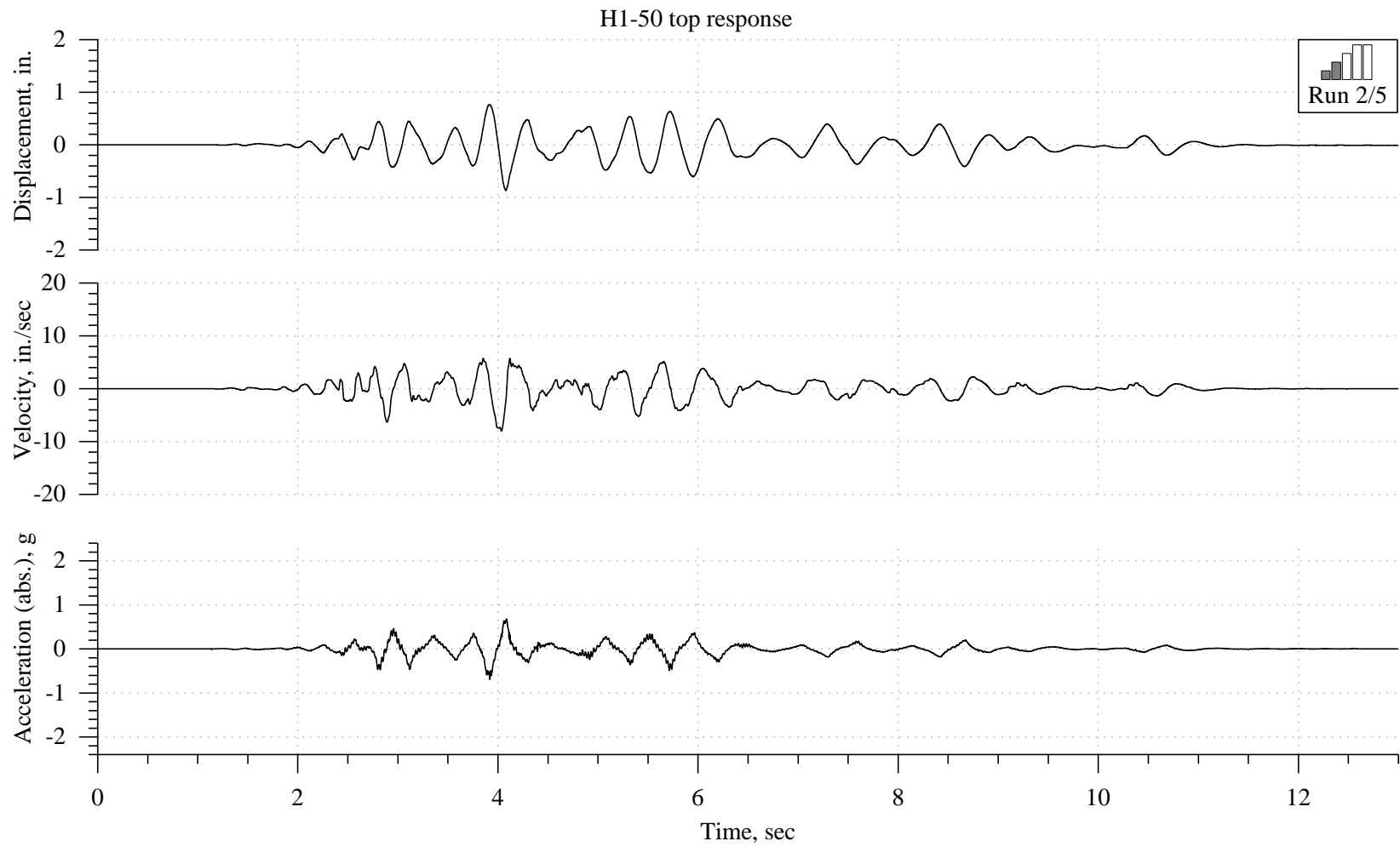


Figure 4-22: Response histories for specimen H1, 50% run (second of five runs).

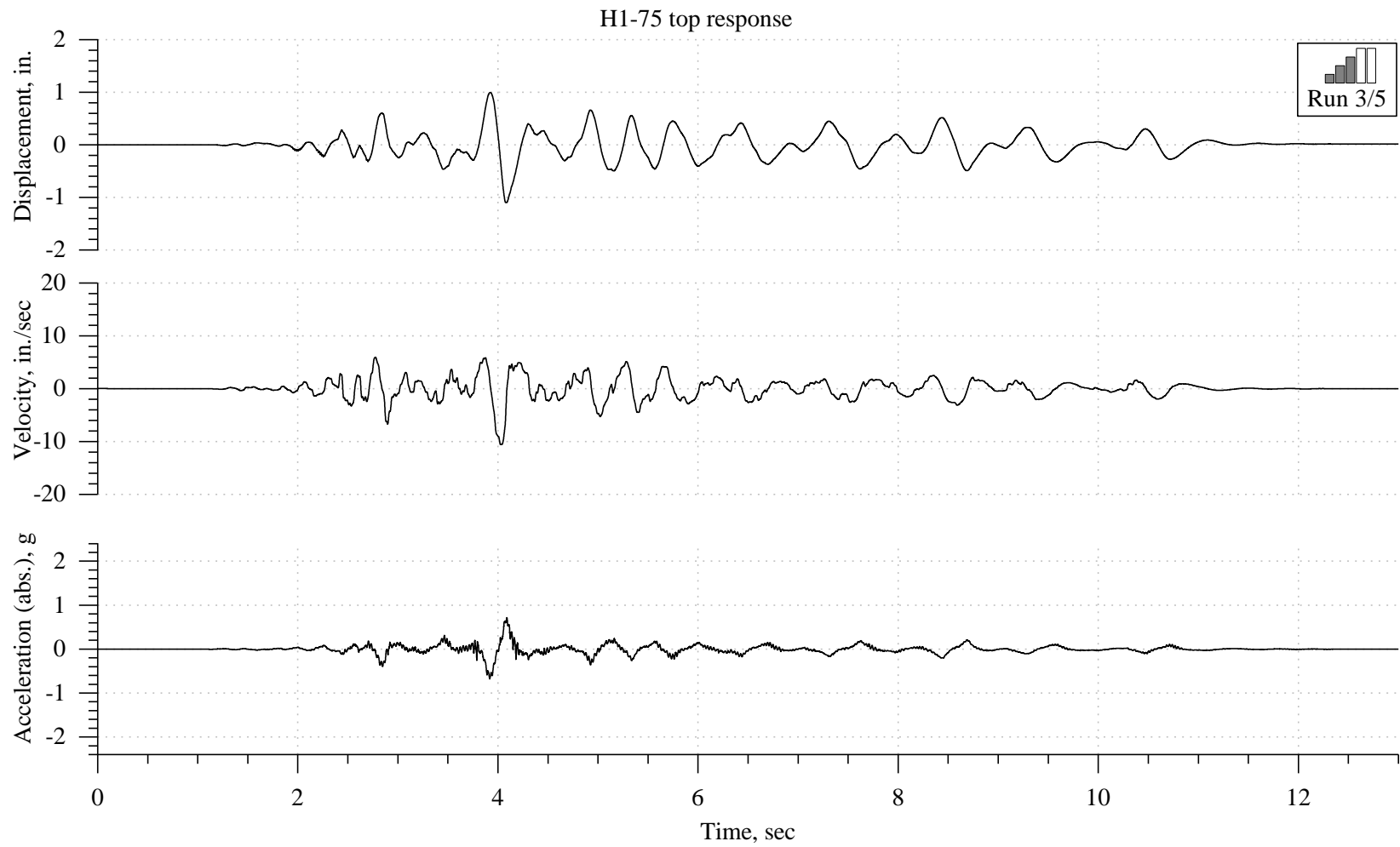


Figure 4-23: Response histories for specimen H1, 75% run (third of five runs).

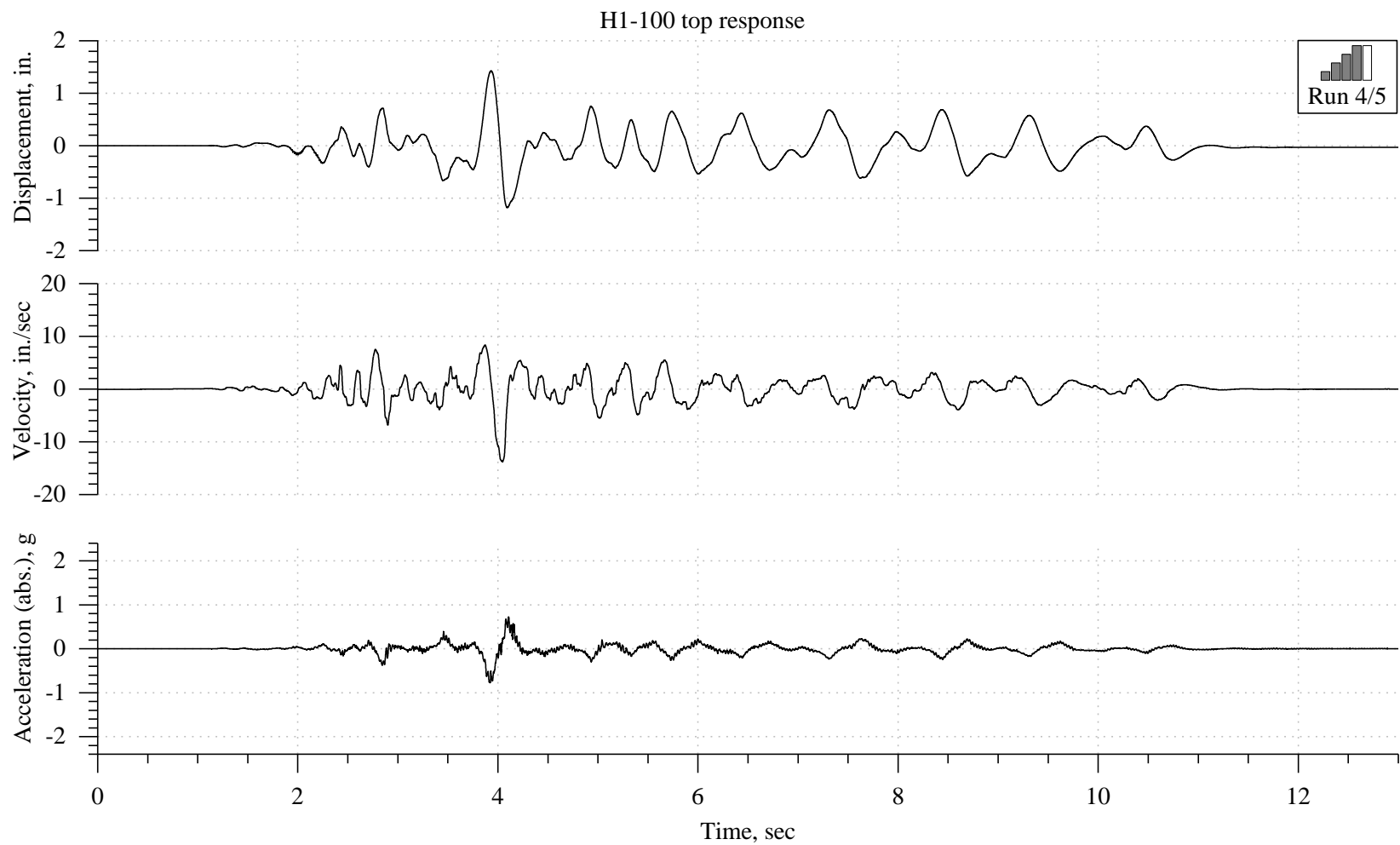


Figure 4-24: Response histories for specimen H1, 100% run (fourth of five runs).

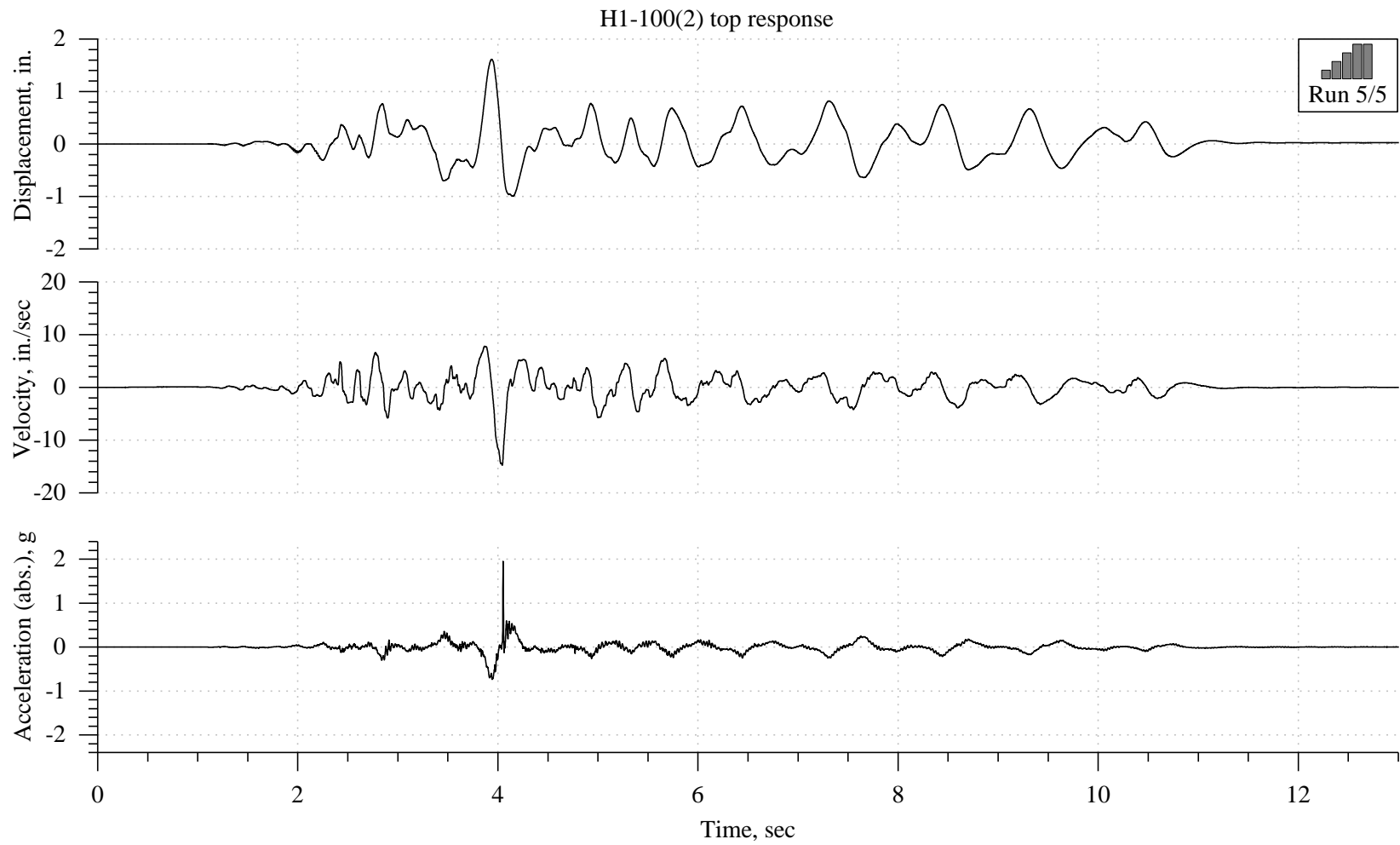


Figure 4-25: Response histories for specimen H1, second 100% run (fifth of five runs).

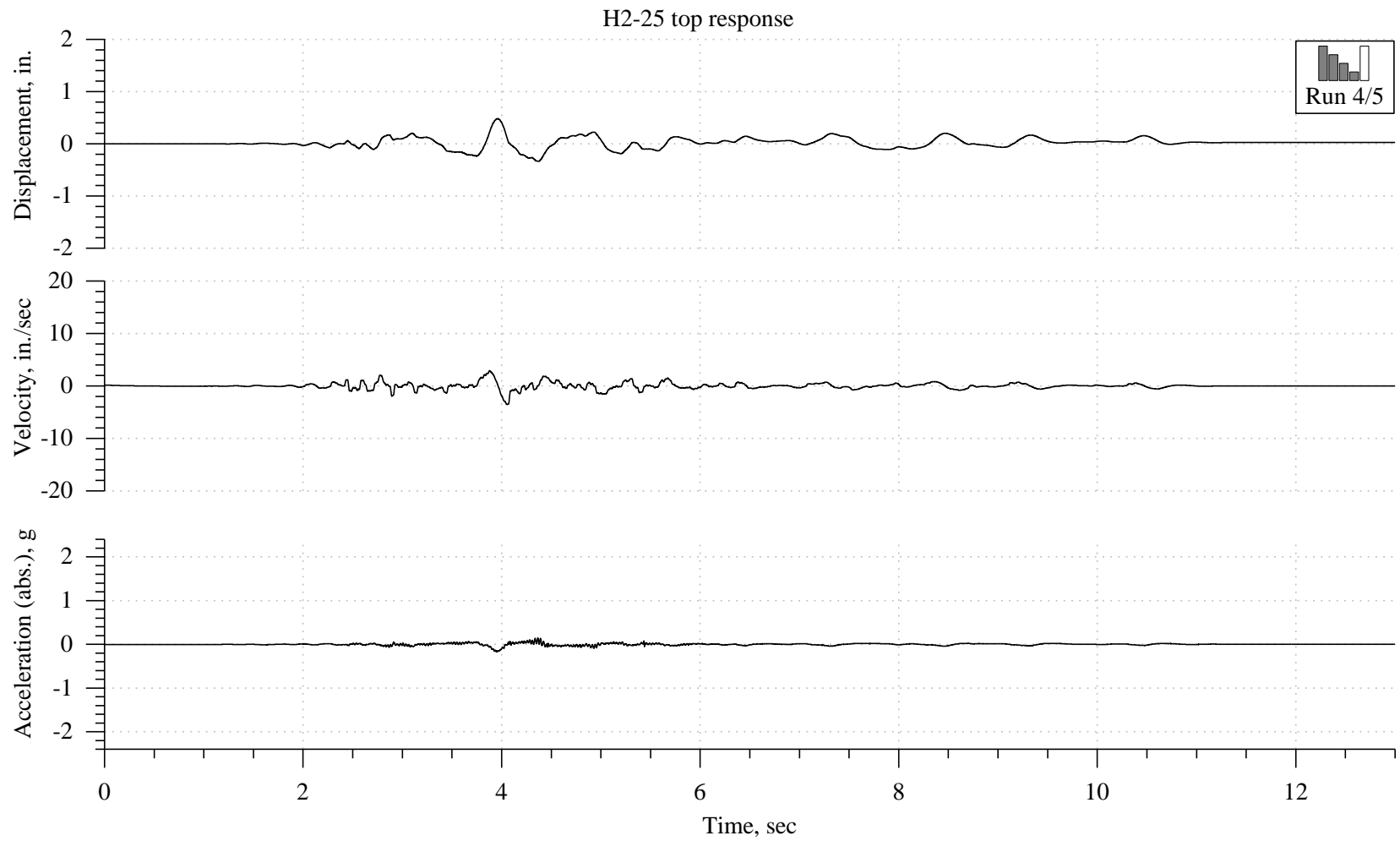


Figure 4-26: Response histories for specimen H2, 25% run (fourth of five runs).

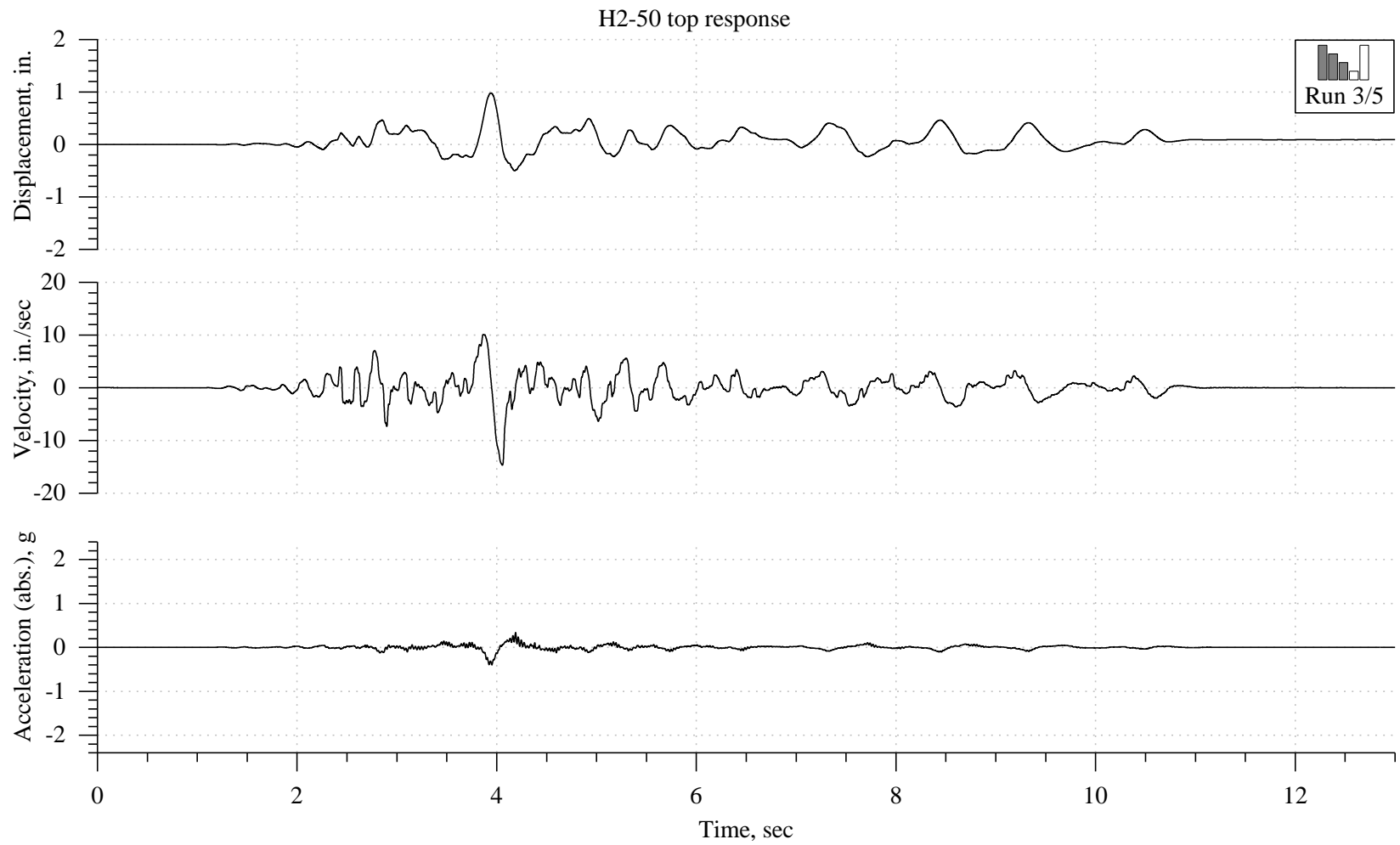


Figure 4-27: Response histories for specimen H2, 50% run (third of five runs).

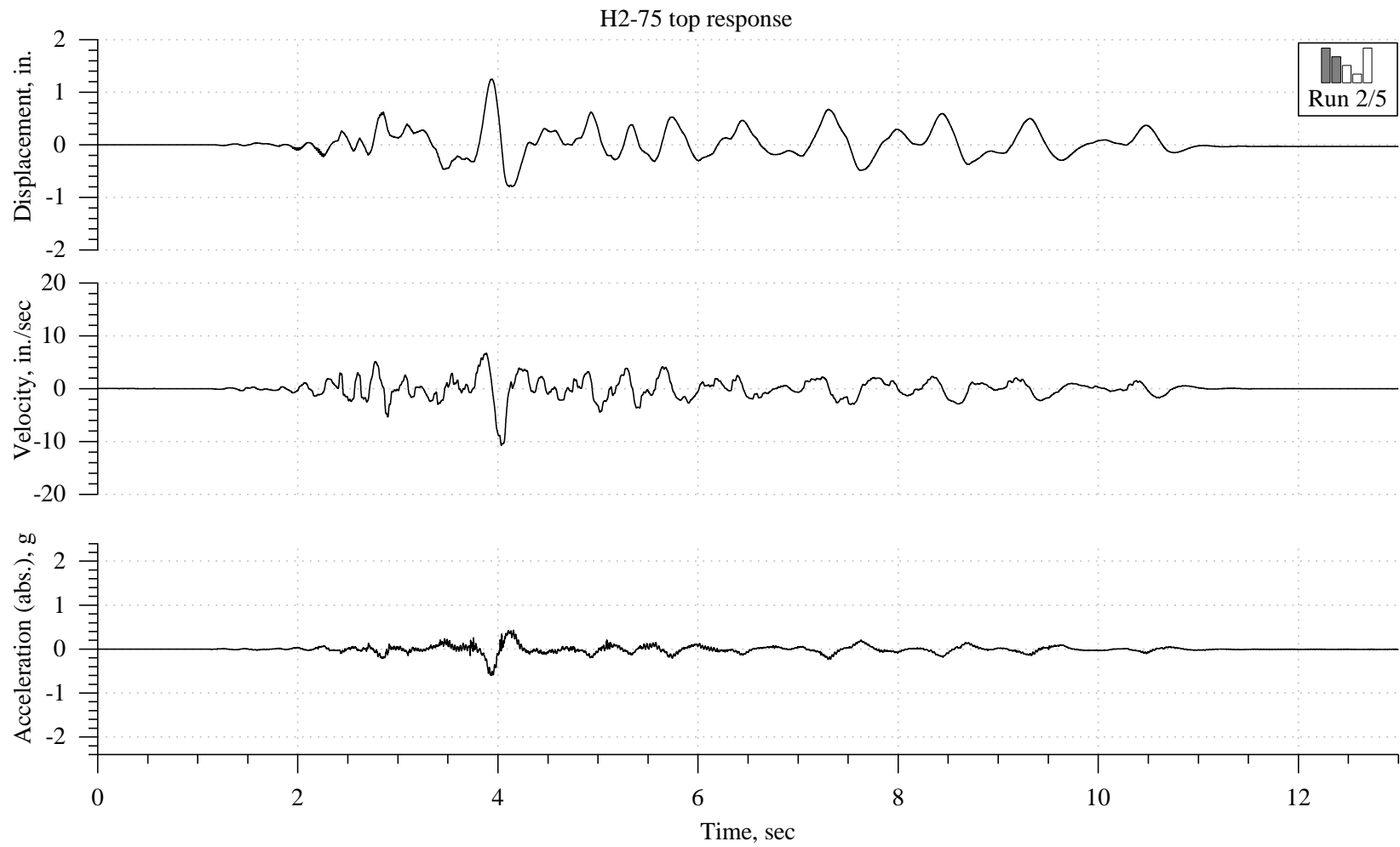


Figure 4-28: Response histories for specimen H2, 75% run (second of five runs).

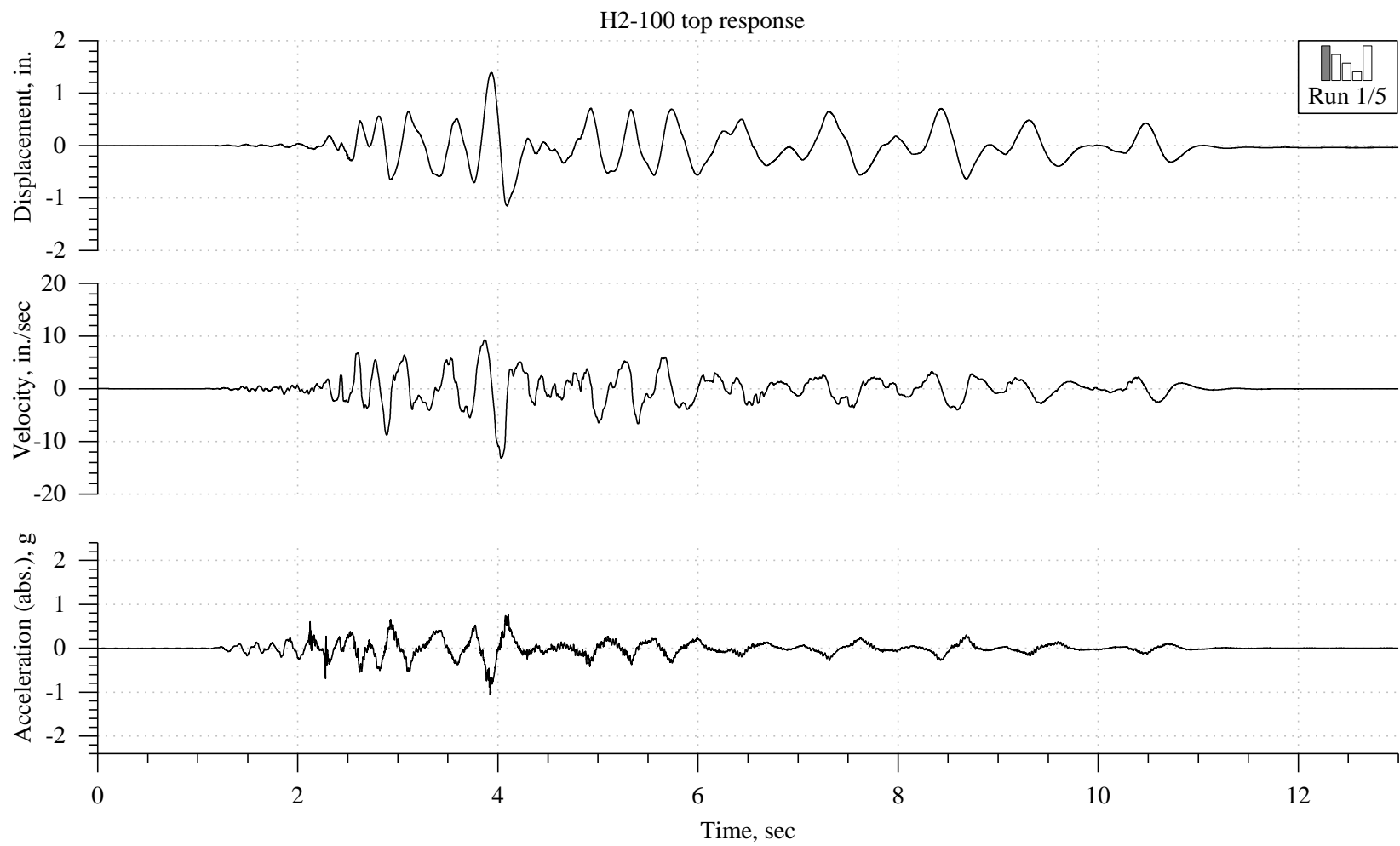


Figure 4-29: Response histories for specimen H2, 100% run (first of five runs).

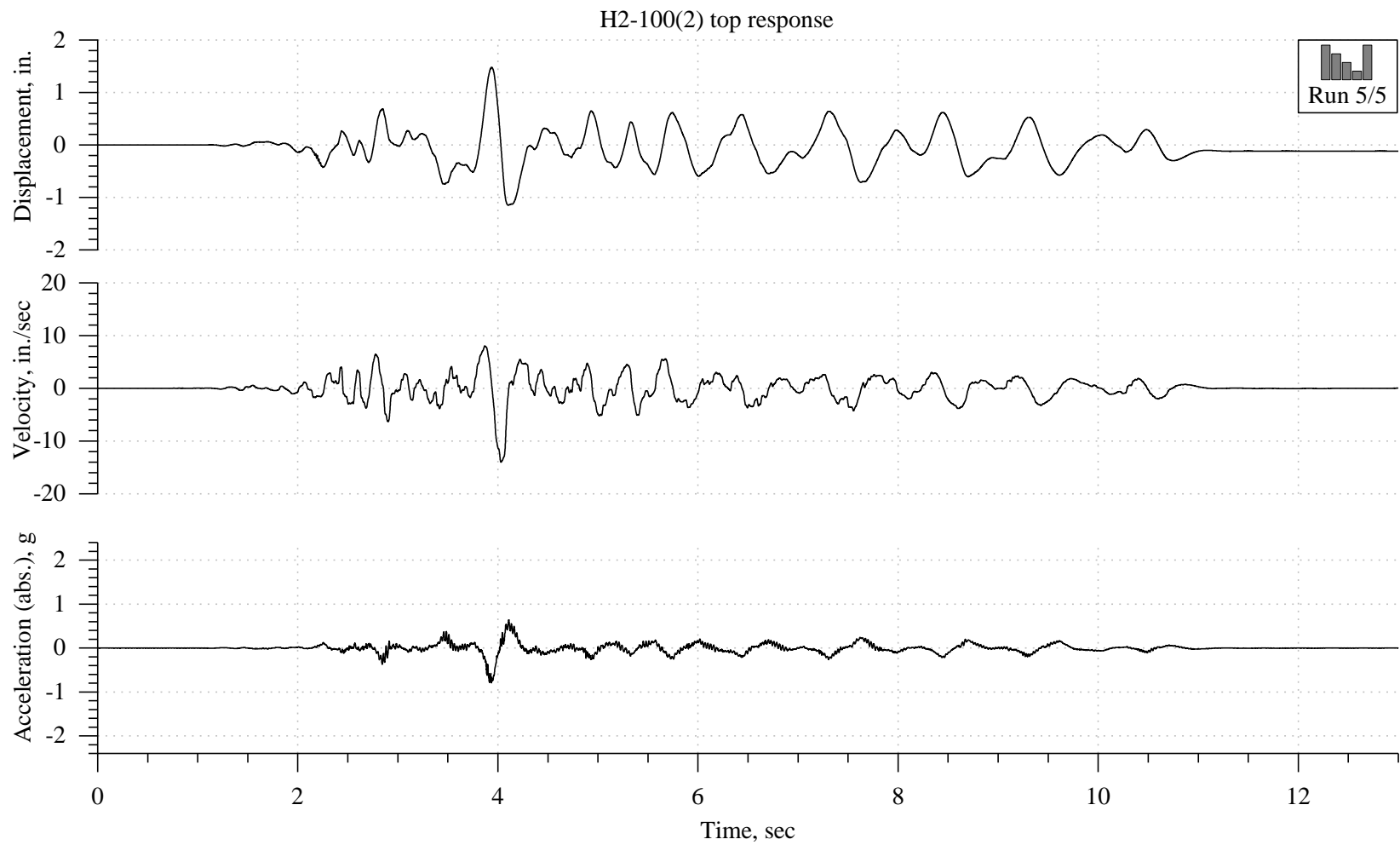


Figure 4-30: Response histories for specimen H2, second 100% run (fifth of five runs).

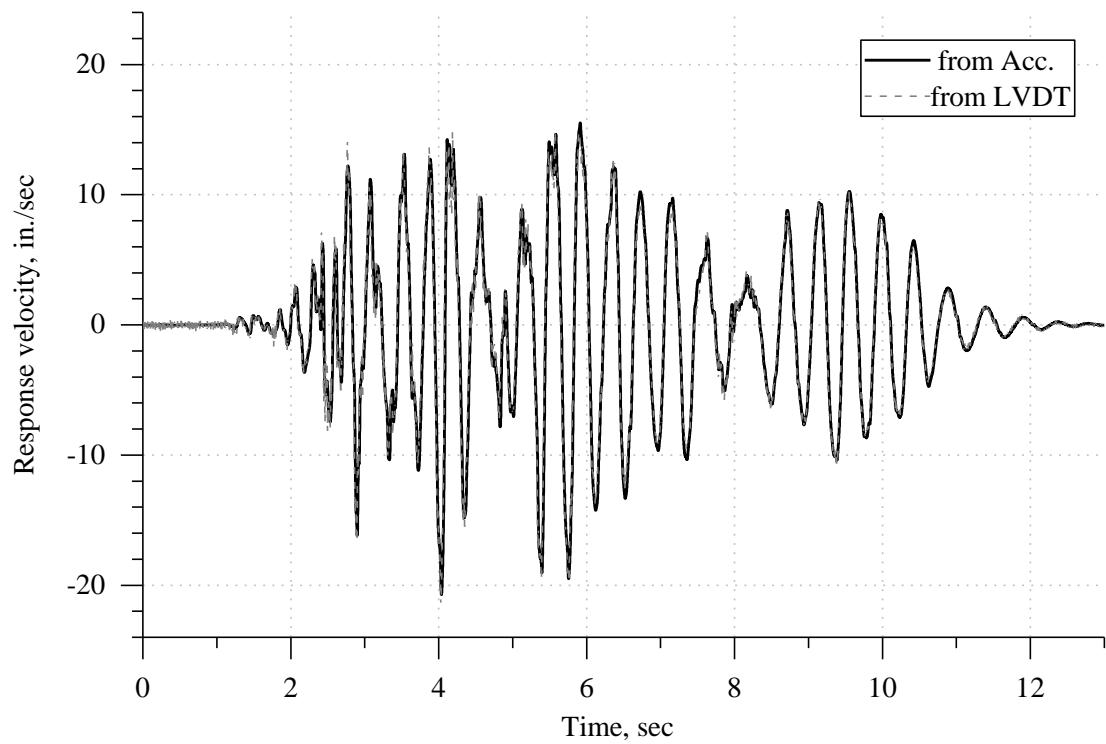


Figure 4-31: Comparison of velocity history derived from accelerometers to velocity history derived from LVDT (C2-75).

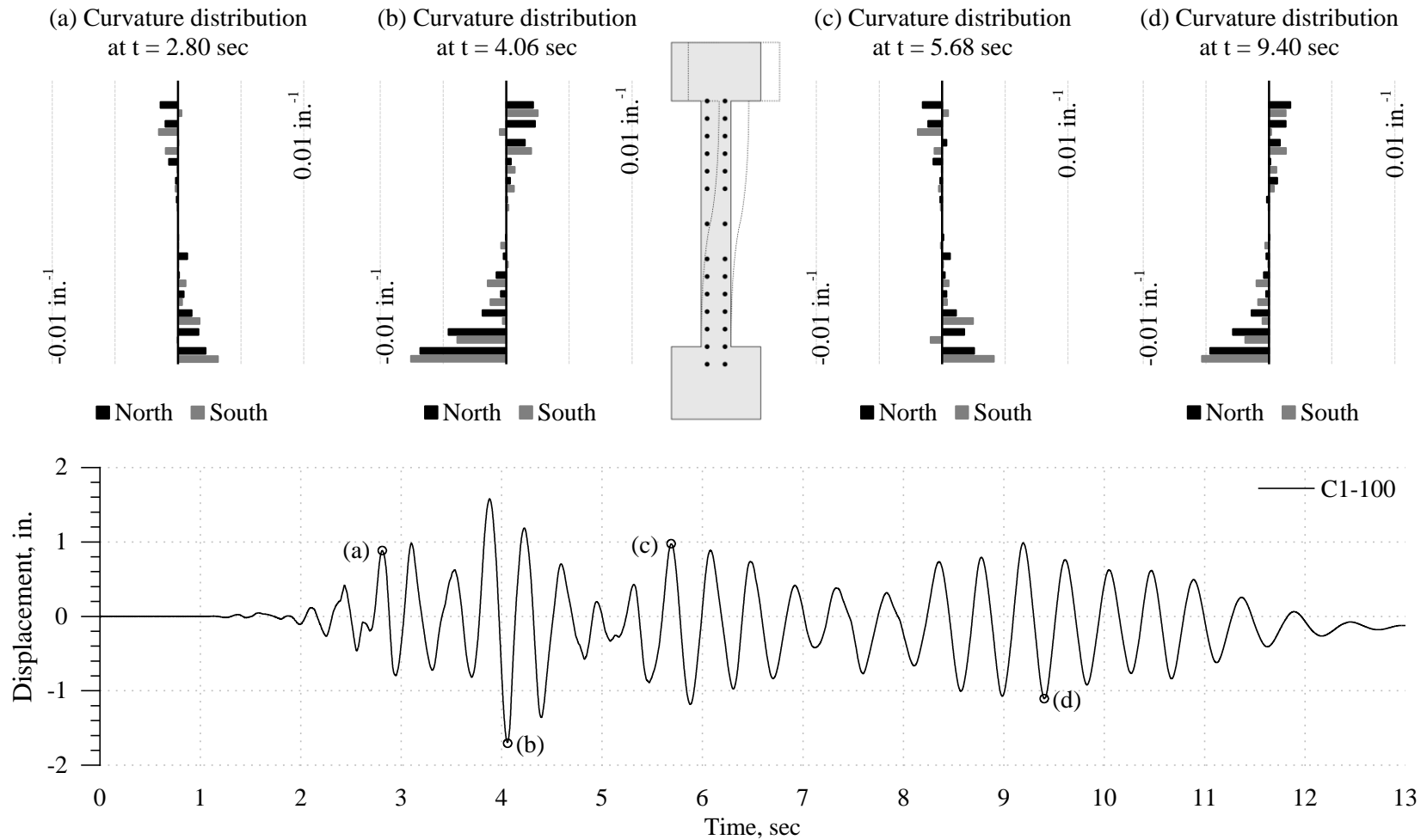


Figure 4-32: Curvature distributions at selected times for test C1-100. [Note: Top curvatures could not be measured.]

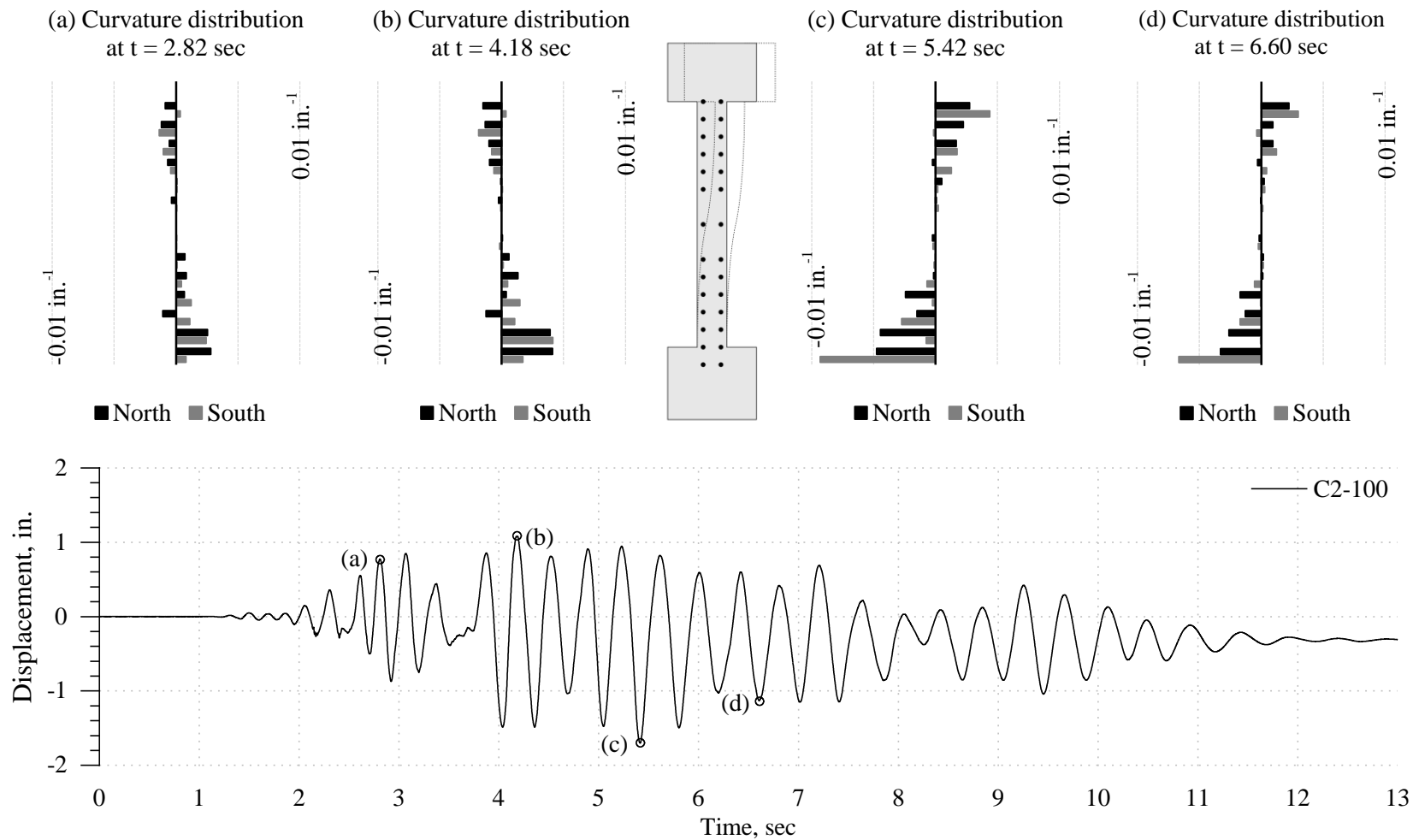


Figure 4-33: Curvature distributions at selected times for test C2-100. [Note: Top curvatures could not be measured.]

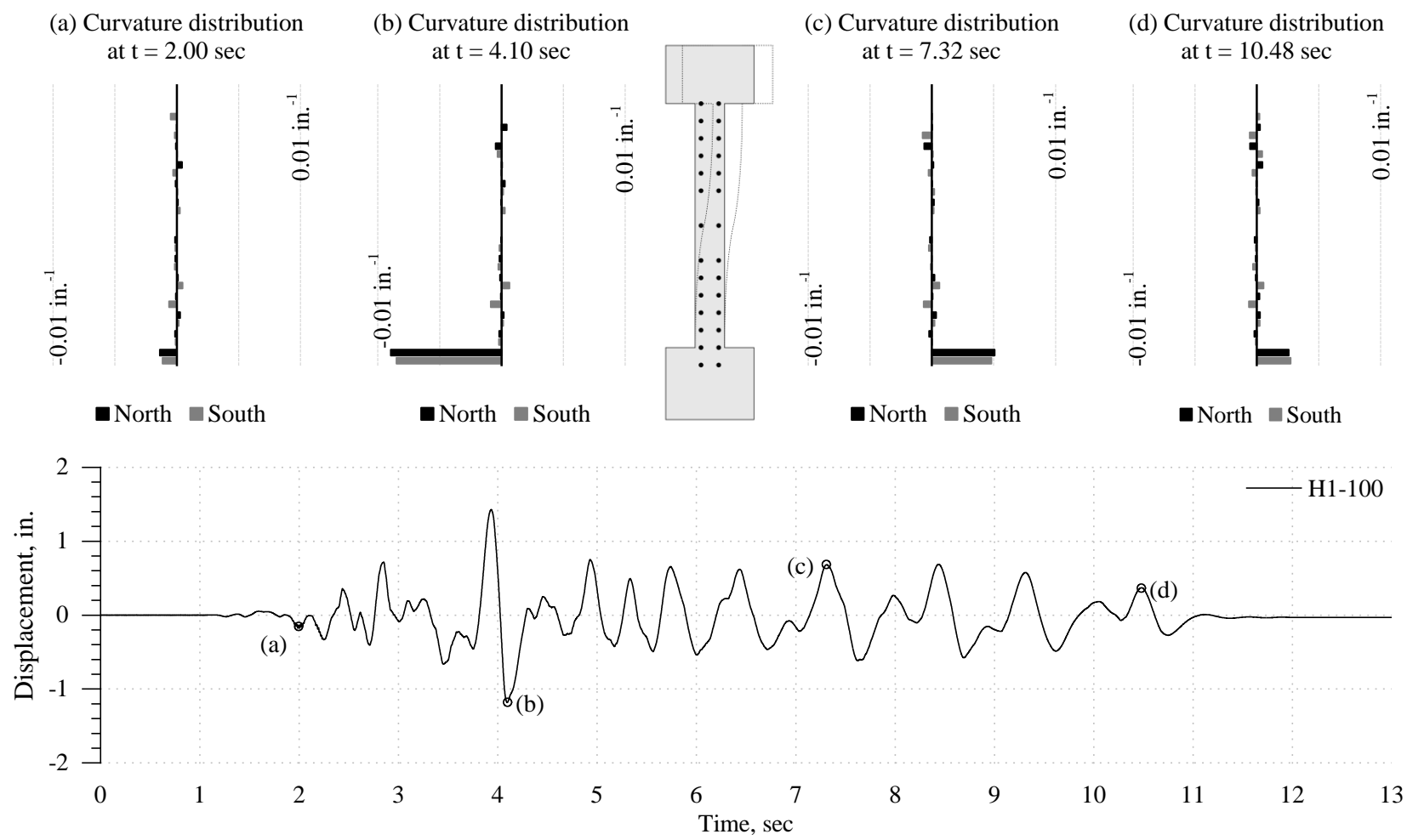


Figure 4-34: Curvature distributions at selected times for test H1-100. [Note: Top curvatures could not be measured.]

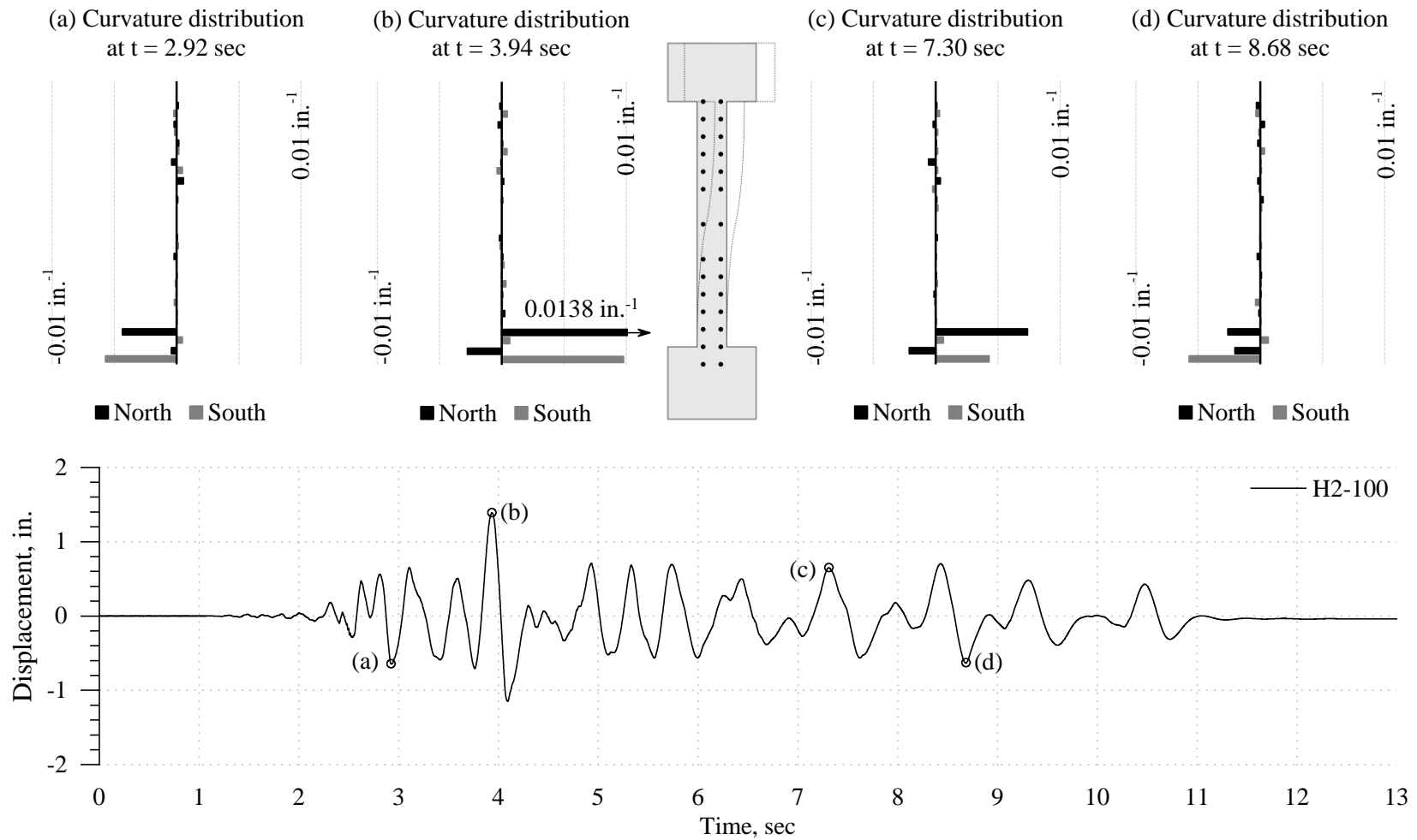


Figure 4-35: Curvature distributions at selected times for test H2-100. [Note: Top curvatures could not be measured.]

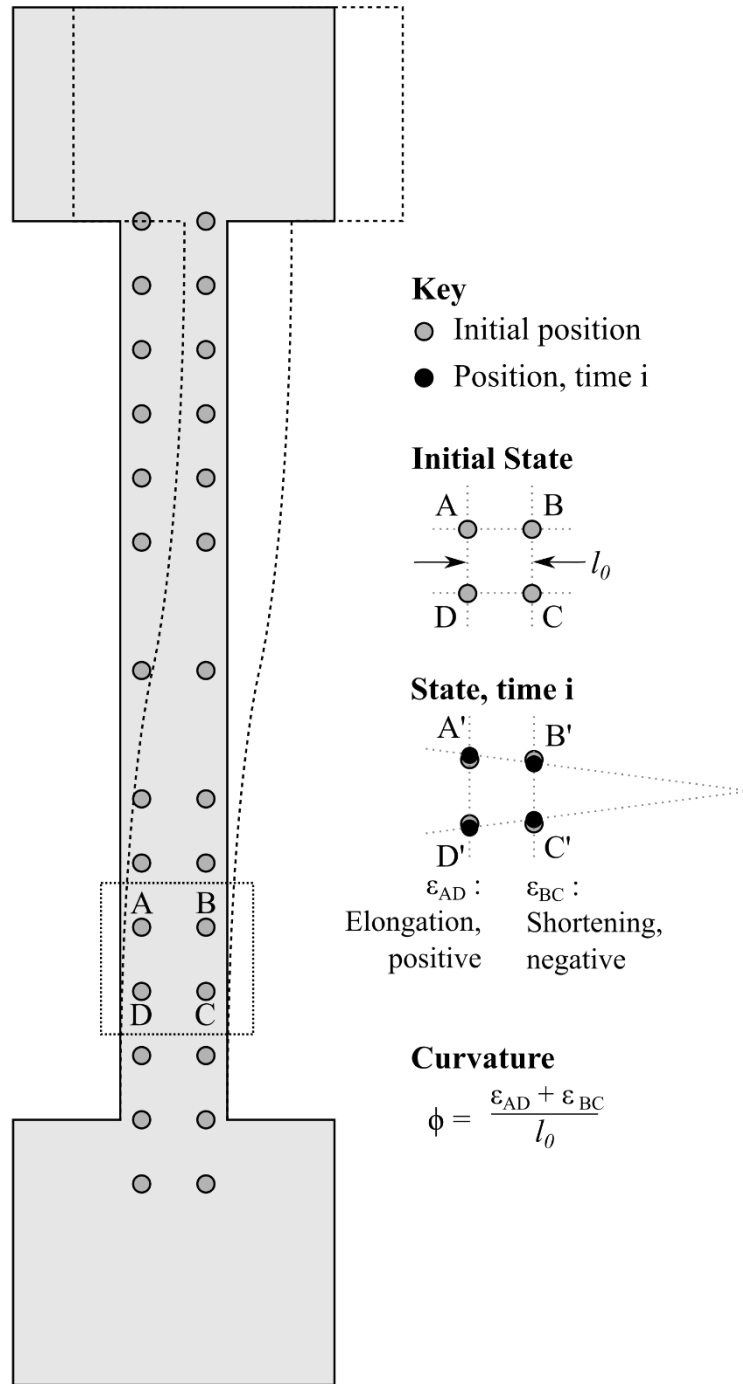


Figure 4-36: Diagram showing method of calculating curvatures using optical targets.

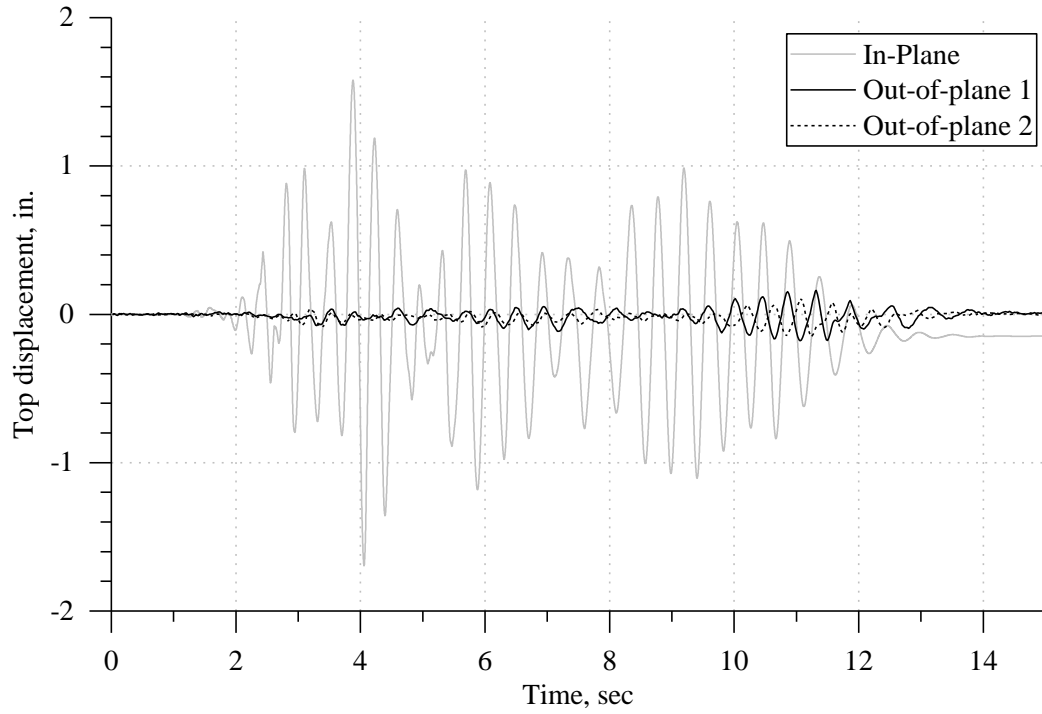


Figure 4-37: Out-of-plane movement measured during test C1-100.

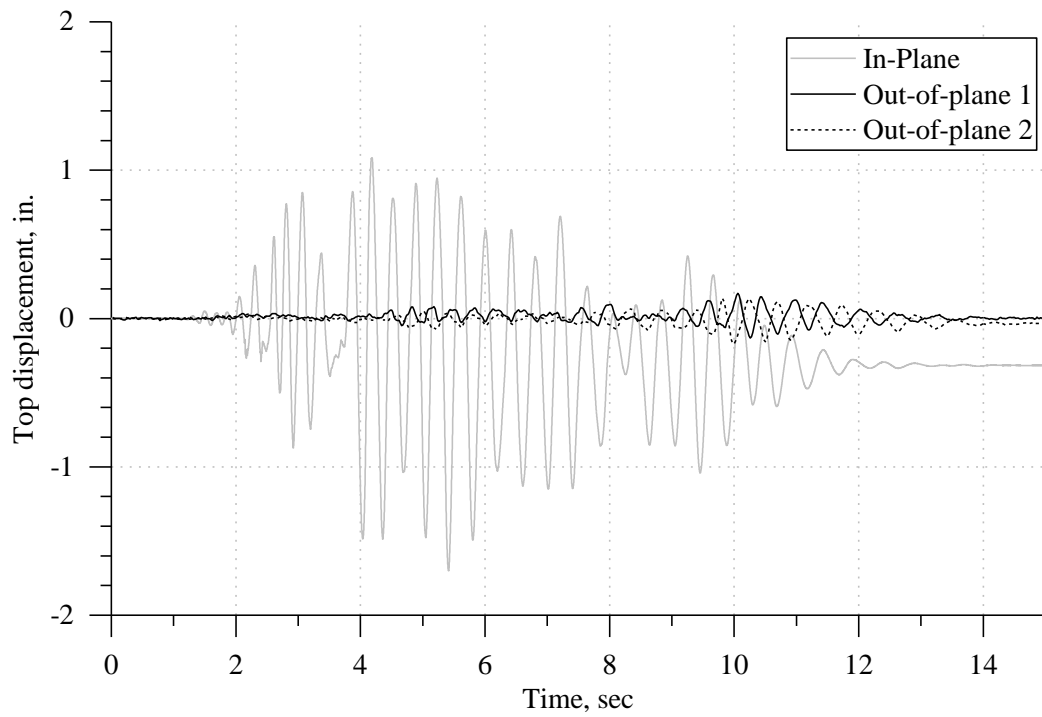


Figure 4-38: Out-of-plane movement measured during test C2-100.

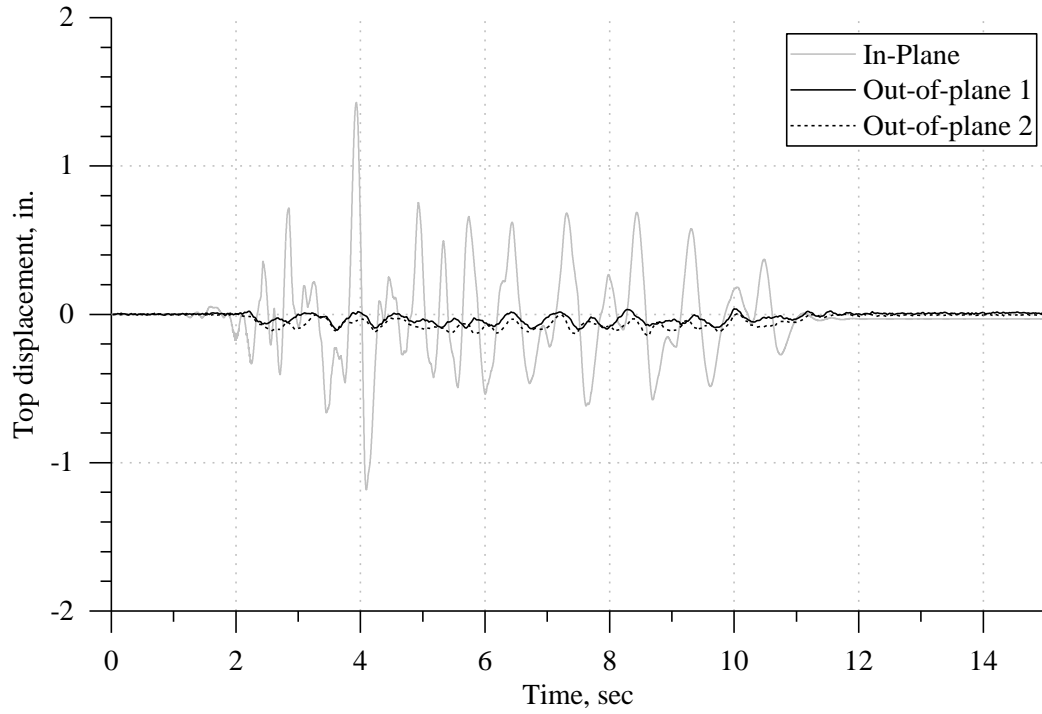


Figure 4-39: Out-of-plane movement measured during test H1-100.

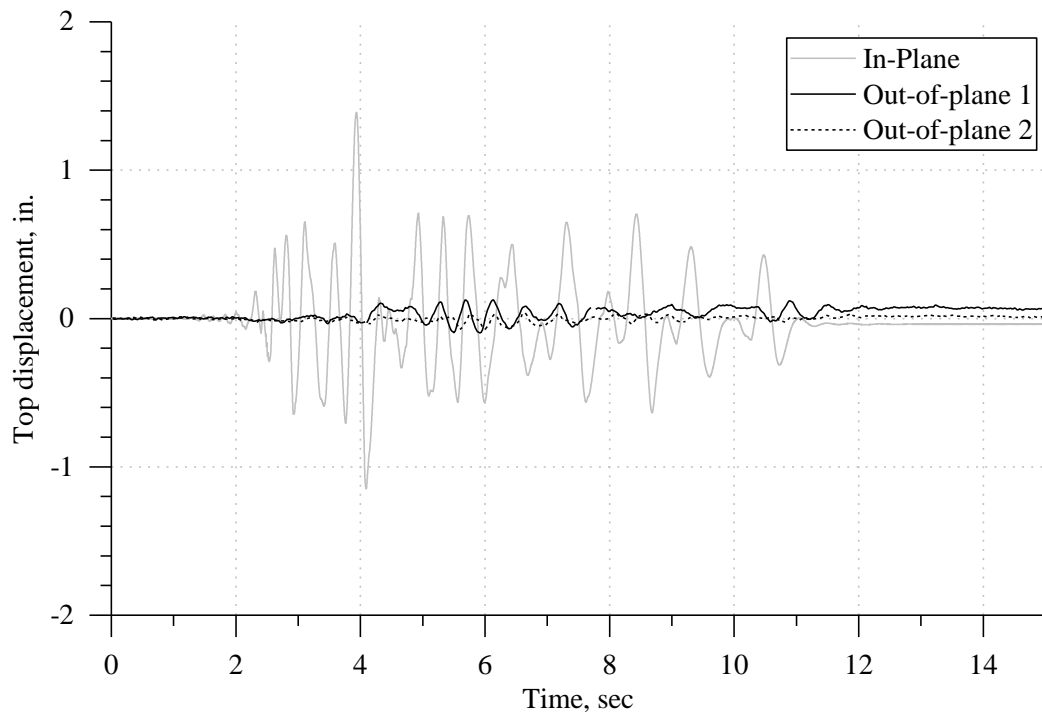


Figure 4-40: Out-of-plane movement measured during test H2-100.

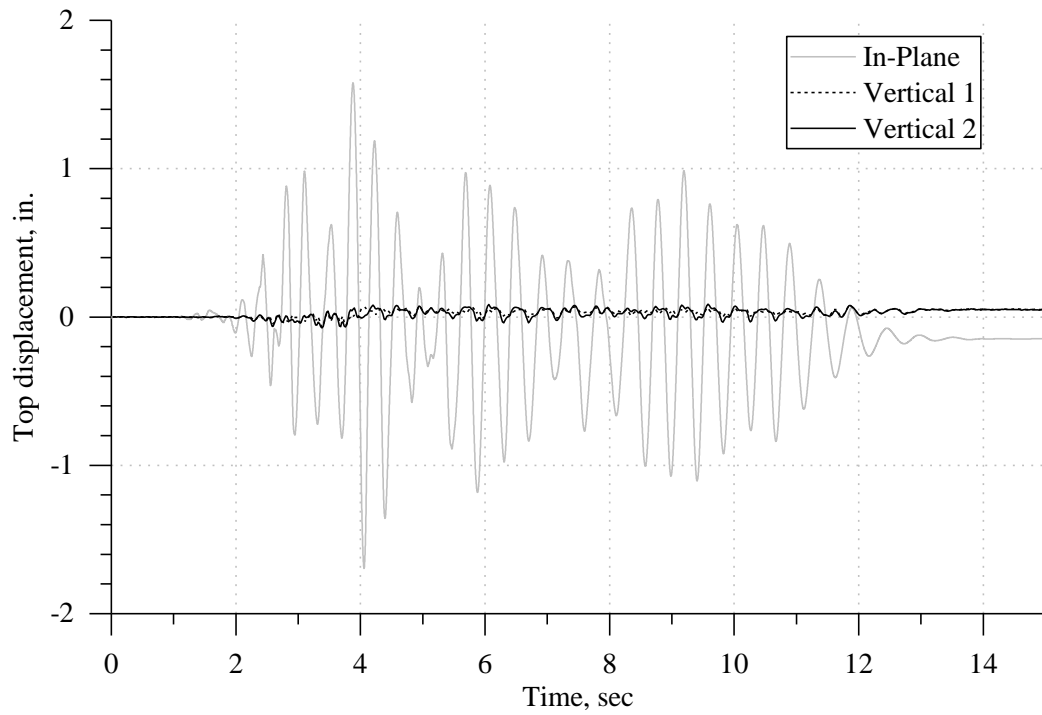


Figure 4-41: Vertical movement measured during test C1-100.

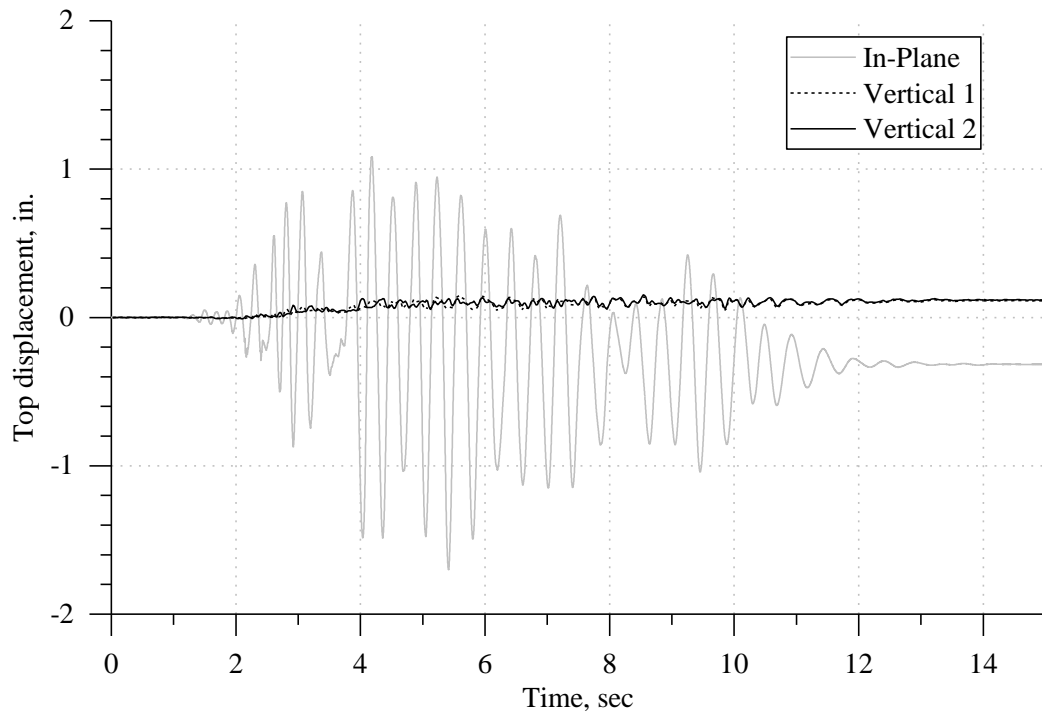


Figure 4-42: Vertical movement measured during test C2-100.

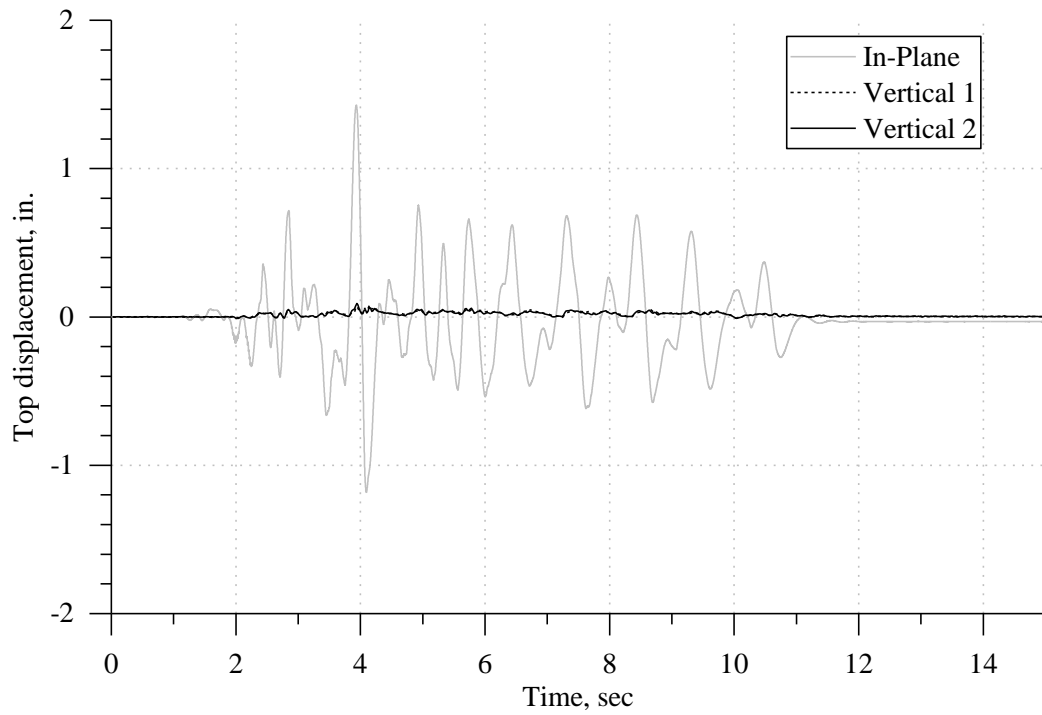


Figure 4-43: Vertical movement measured during test H1-100.

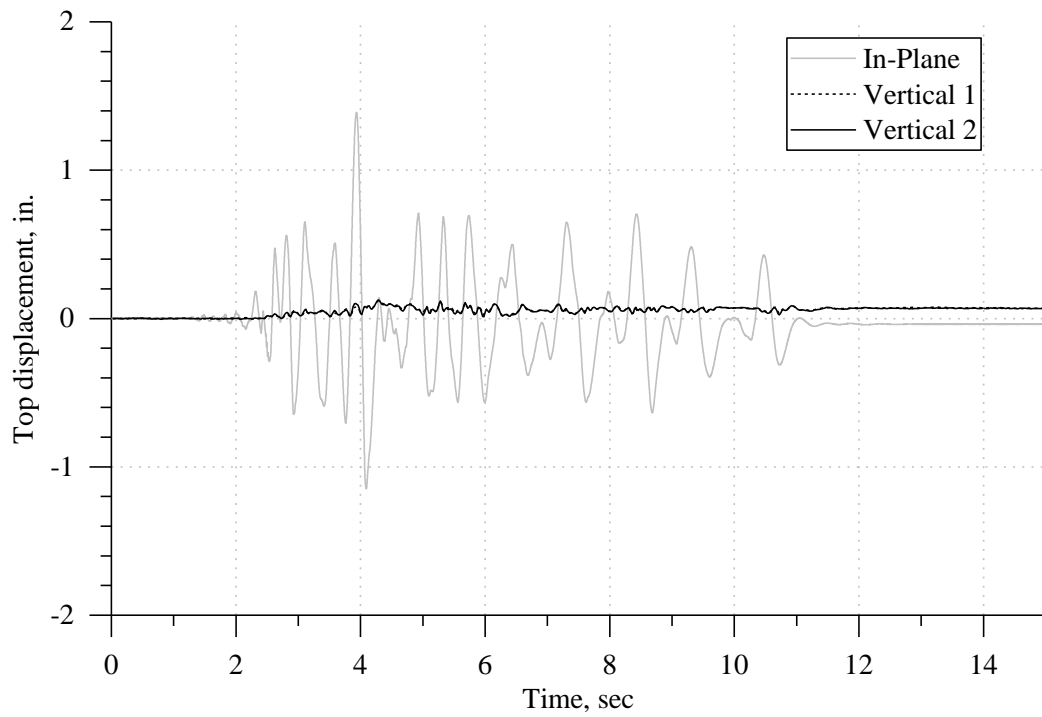


Figure 4-44: Vertical movement measured during test H2-100.

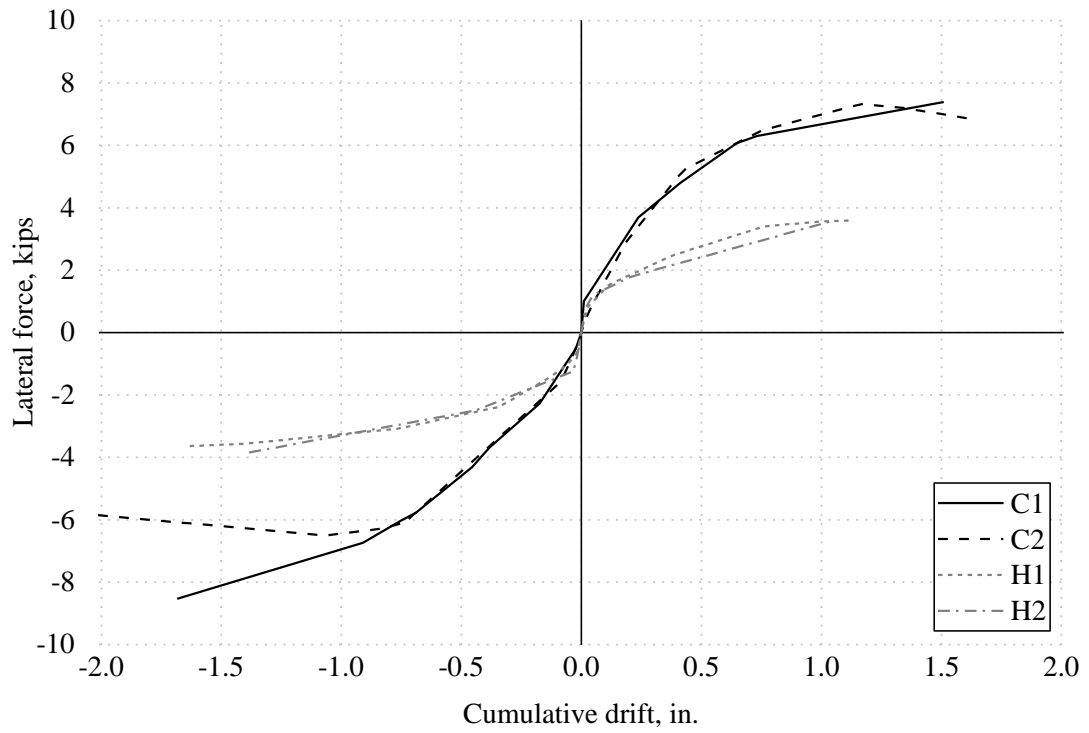


Figure 4-45: Envelopes derived from response histories.

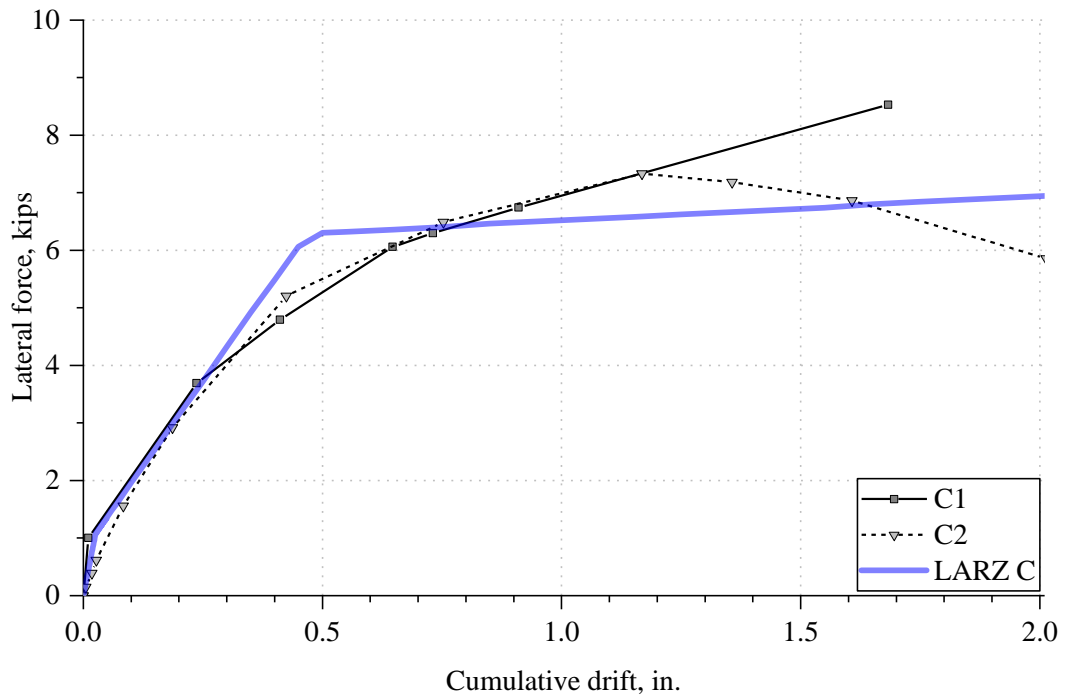


Figure 4-46: LARZ predicted envelope alongside measured envelopes for specimens C1 and C2 (measured are uppermost points from positive and negative directions).

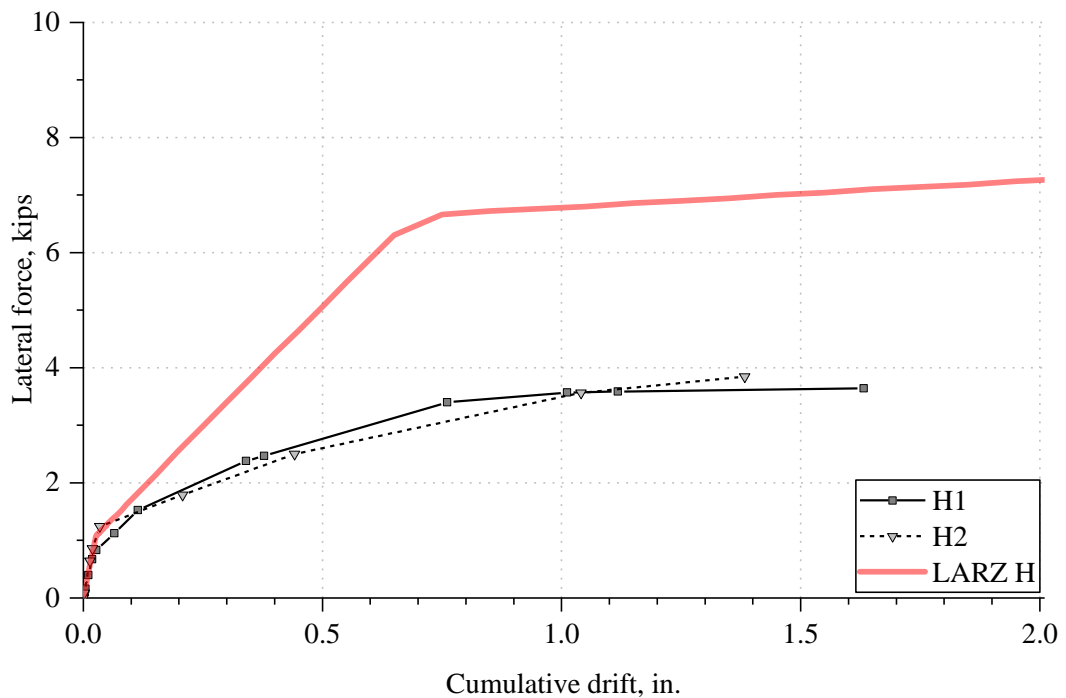
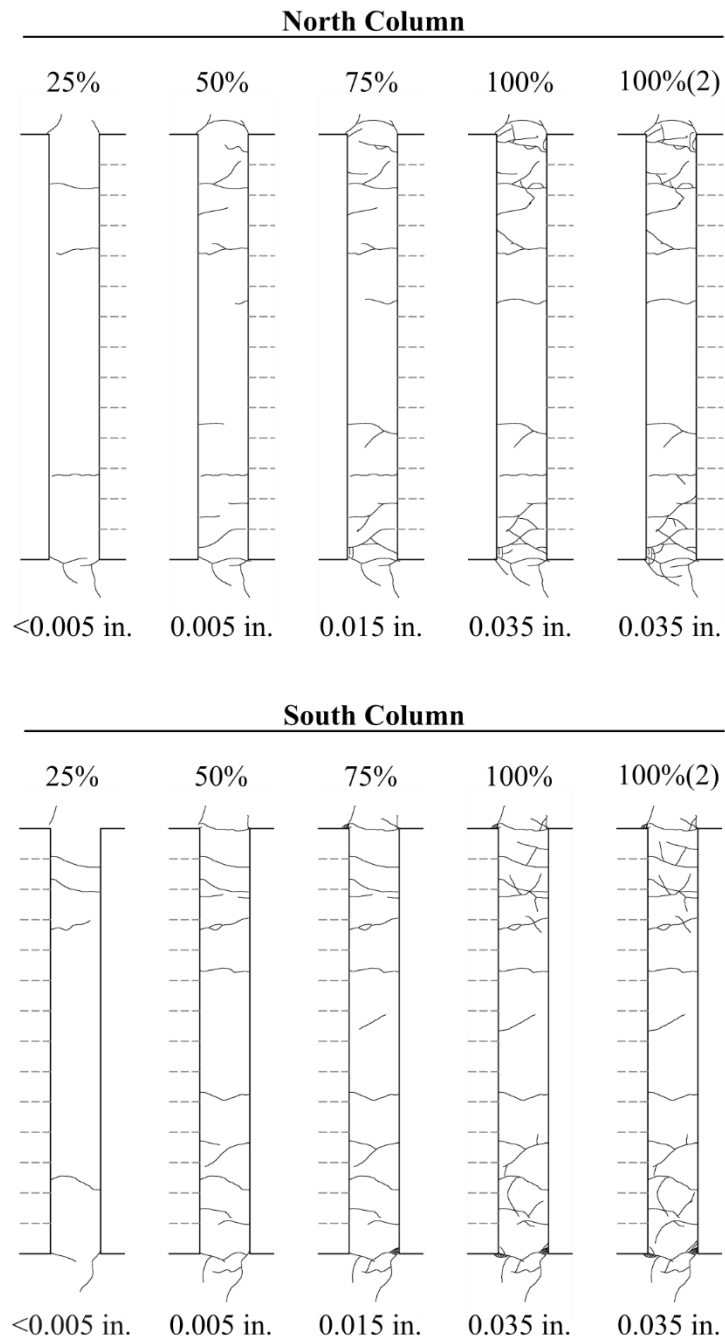


Figure 4-47: LARZ predicted envelope alongside measured envelopes for specimens H1 and H2 (measured are uppermost points from positive and negative directions).

Damage - Frame C1 - West Face

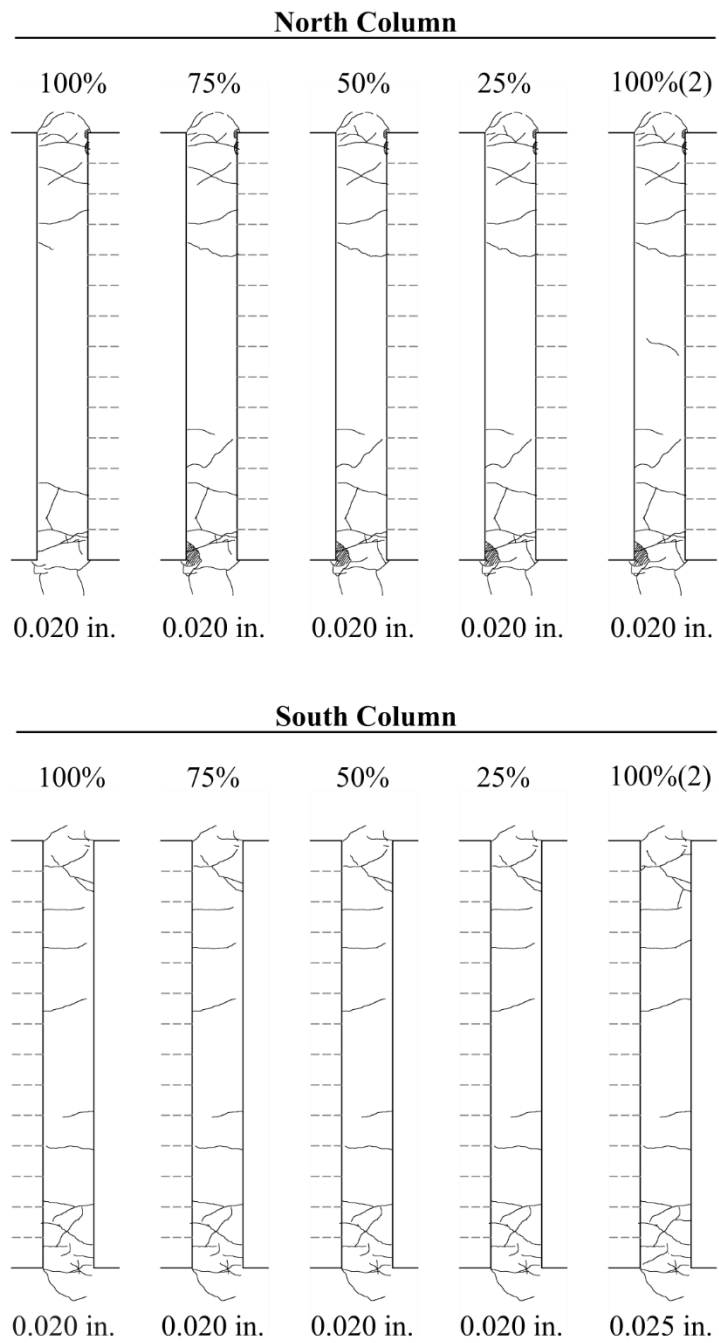


Note:

1. Dashed gray reference lines are spaced at 3 in. and point towards portal.
2. Values below damage maps are maximum crack width measured after test.

Figure 4-48: Crack map for specimen C1, west face.

Damage - Frame C2 - West Face

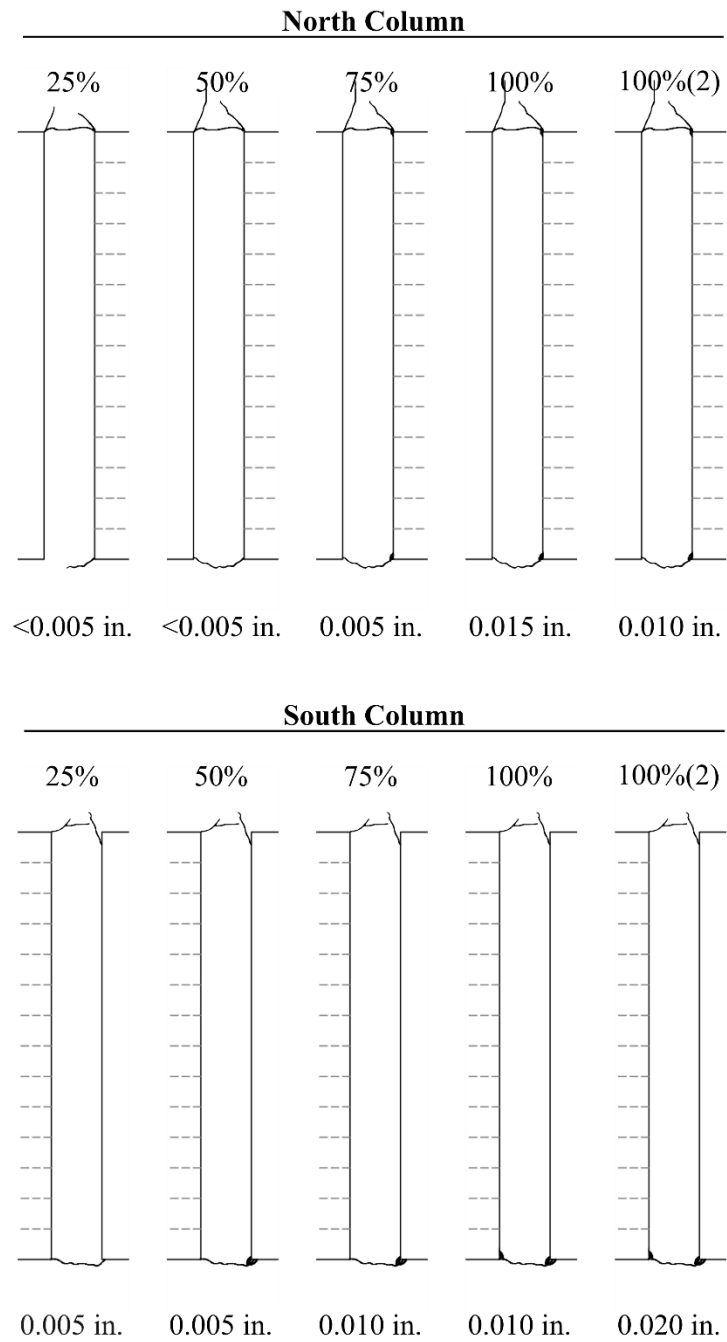


Note:

1. Dashed gray reference lines are spaced at 3 in. and point towards portal.
2. Values below damage maps are maximum crack width measured after test.

Figure 4-49: Crack map for specimen C2, west face.

Damage - Frame H1 - West Face

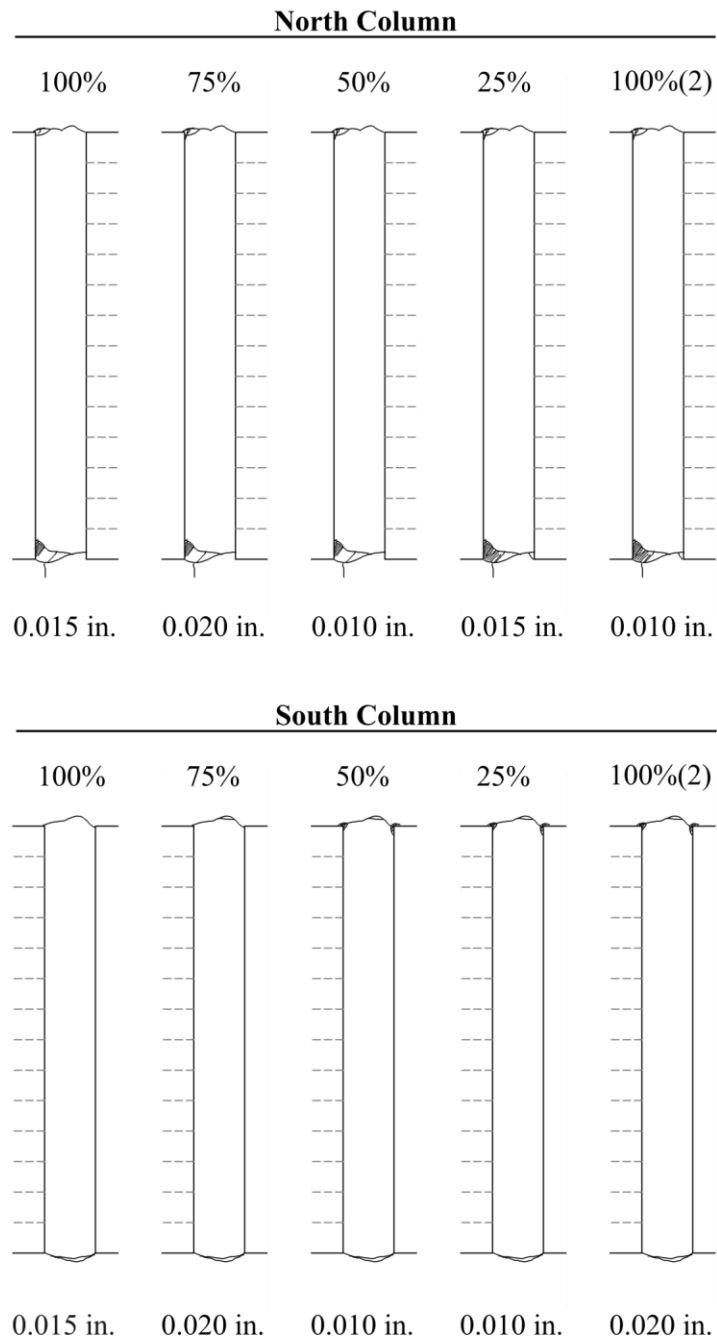


Note:

1. Dashed gray reference lines are spaced at 3 in. and point towards portal.
2. Values below damage maps are maximum crack width measured after test.

Figure 4-50: Crack map for specimen H1, west face.

Damage - Frame H2 - West Face



Note:

1. Dashed gray reference lines are spaced at 3 in. and point towards portal.
2. Values below damage maps are maximum crack width measured after test.

Figure 4-51: Crack map for specimen H2, west face.

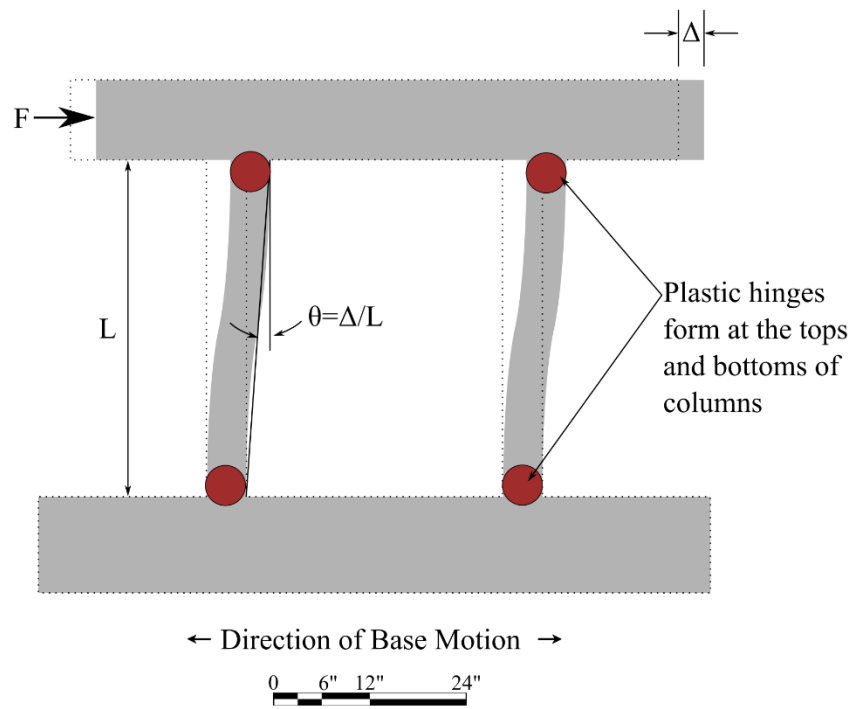


Figure 5-1: Illustration of expected limit state for portal frames (based on flexural behavior).

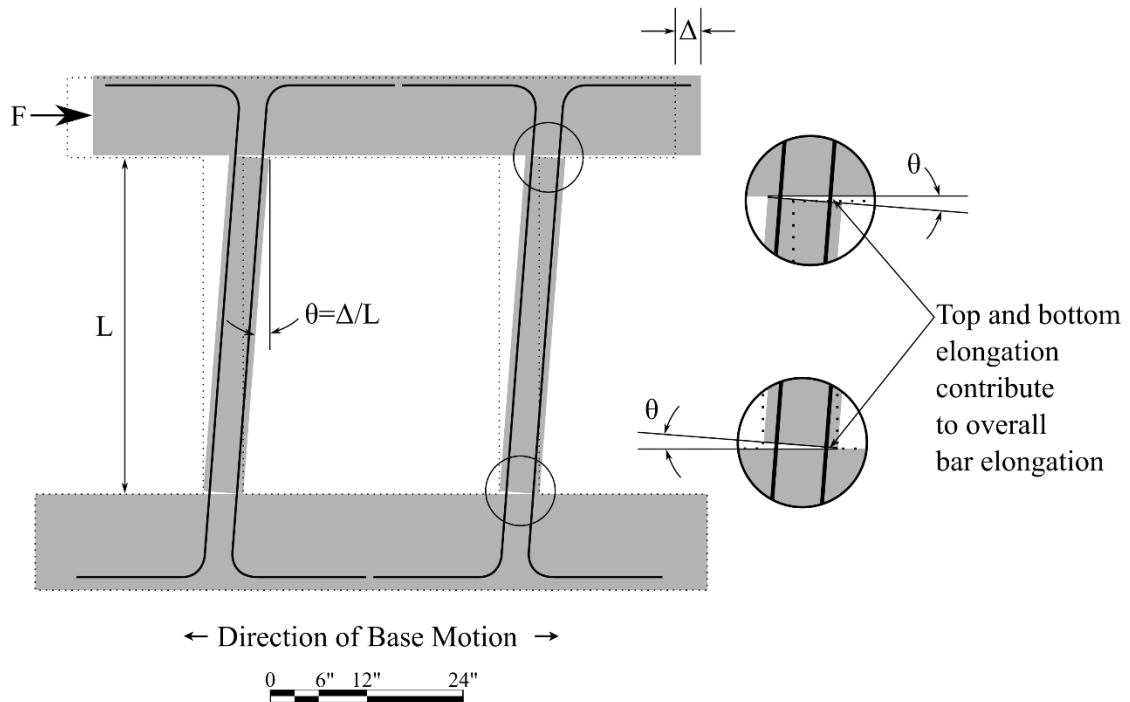


Figure 5-2: Illustration of possible limit state for type H frames (assuming slip).

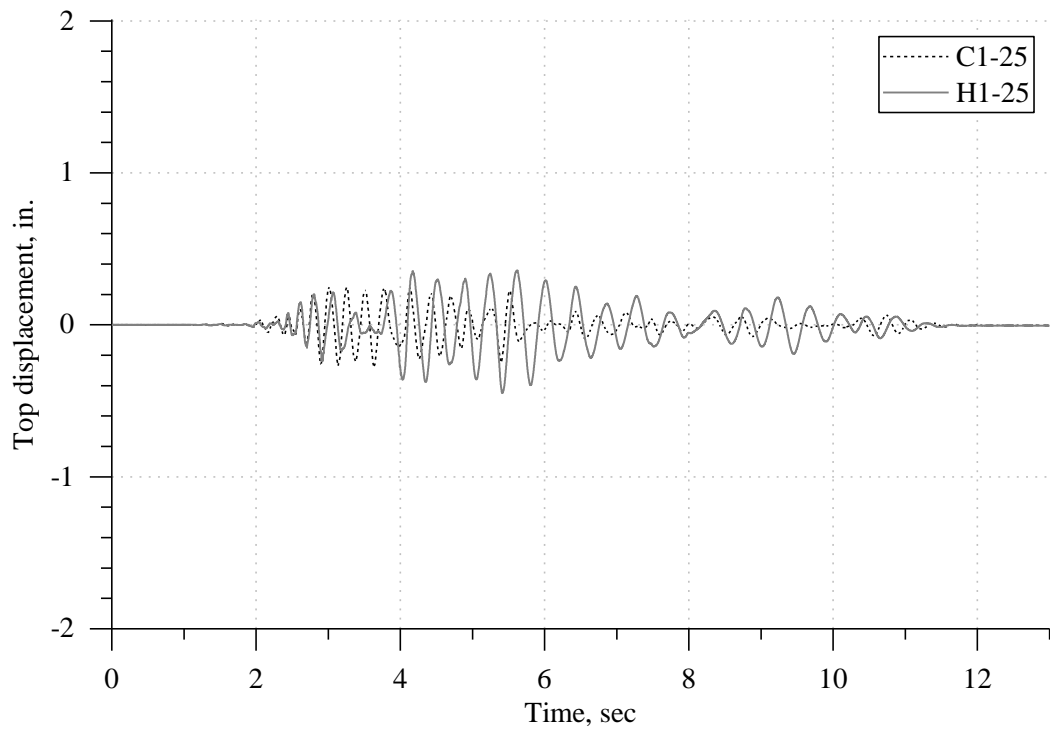


Figure 5-3: Comparison of top drift responses of tests C1-25 and H1-25.

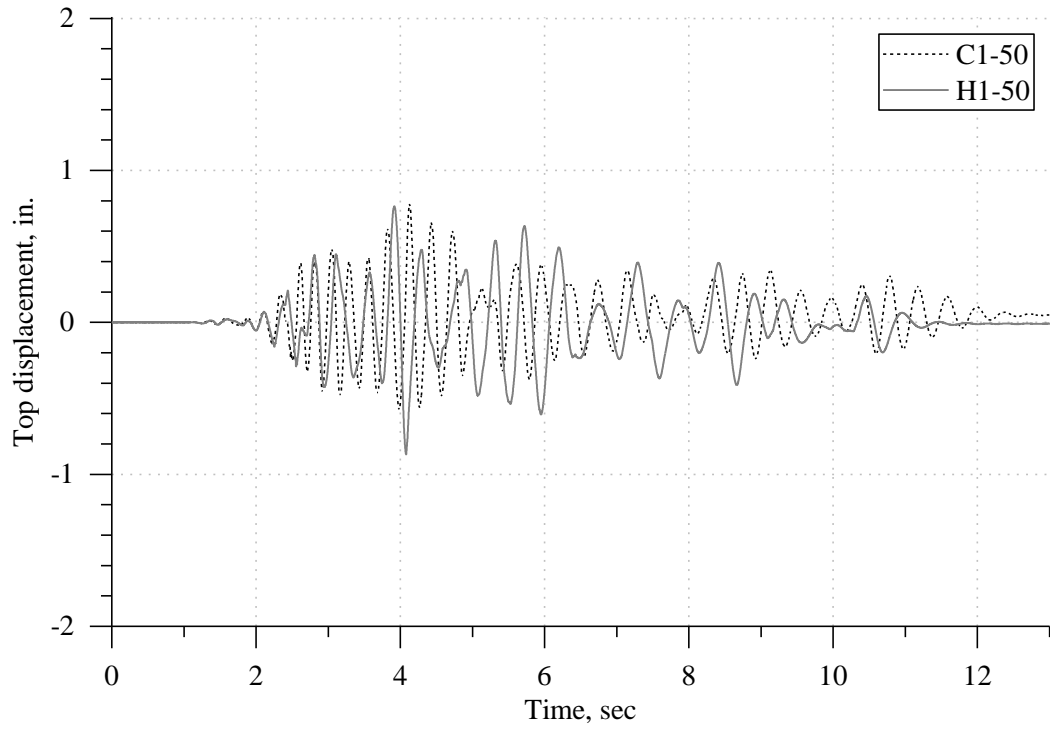


Figure 5-4: Comparison of top drift responses of tests C1-50 and H1-50.

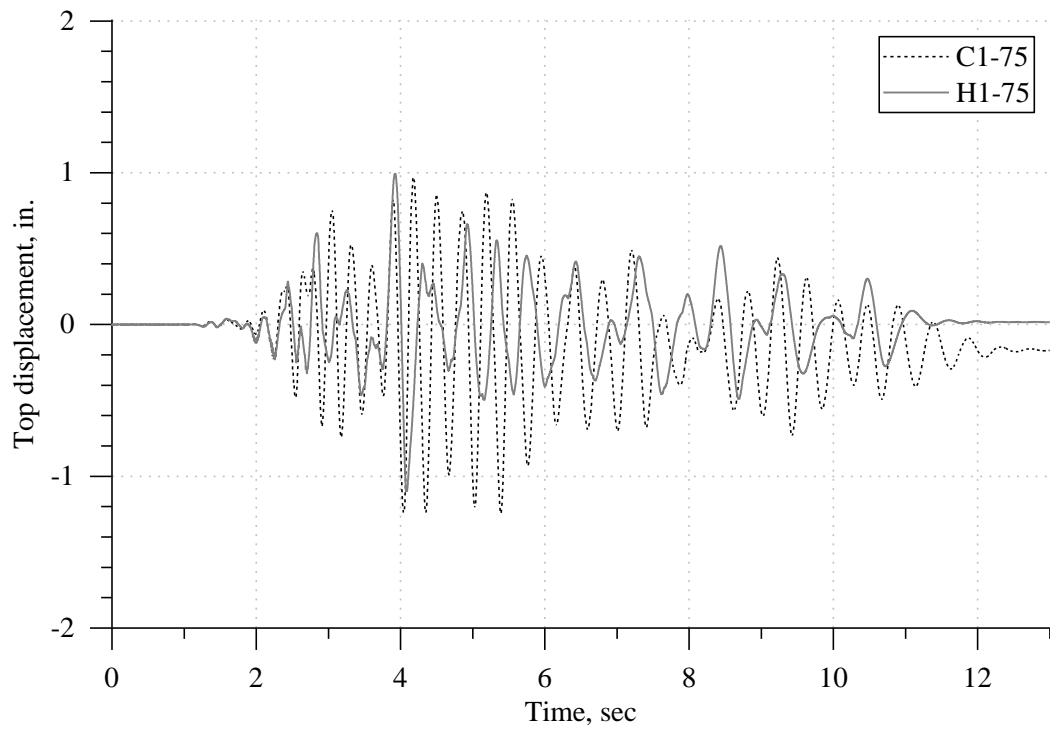


Figure 5-5: Comparison of top drift responses of tests C1-75 and H1-75.

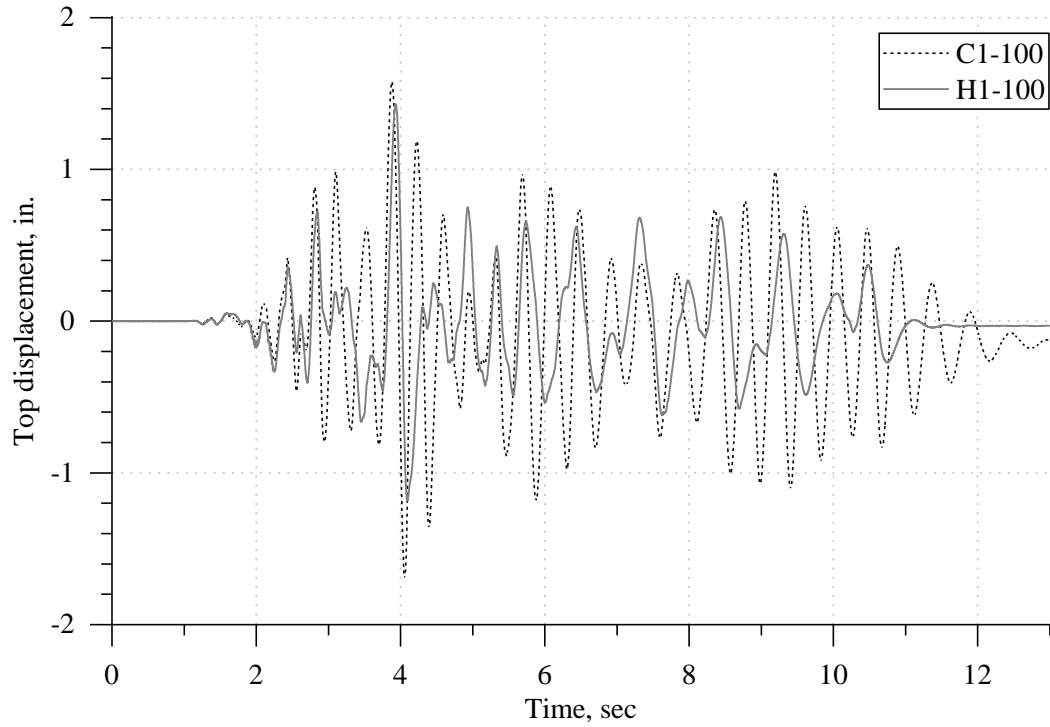


Figure 5-6: Comparison of top drift responses of tests C1-100 and H1-100.

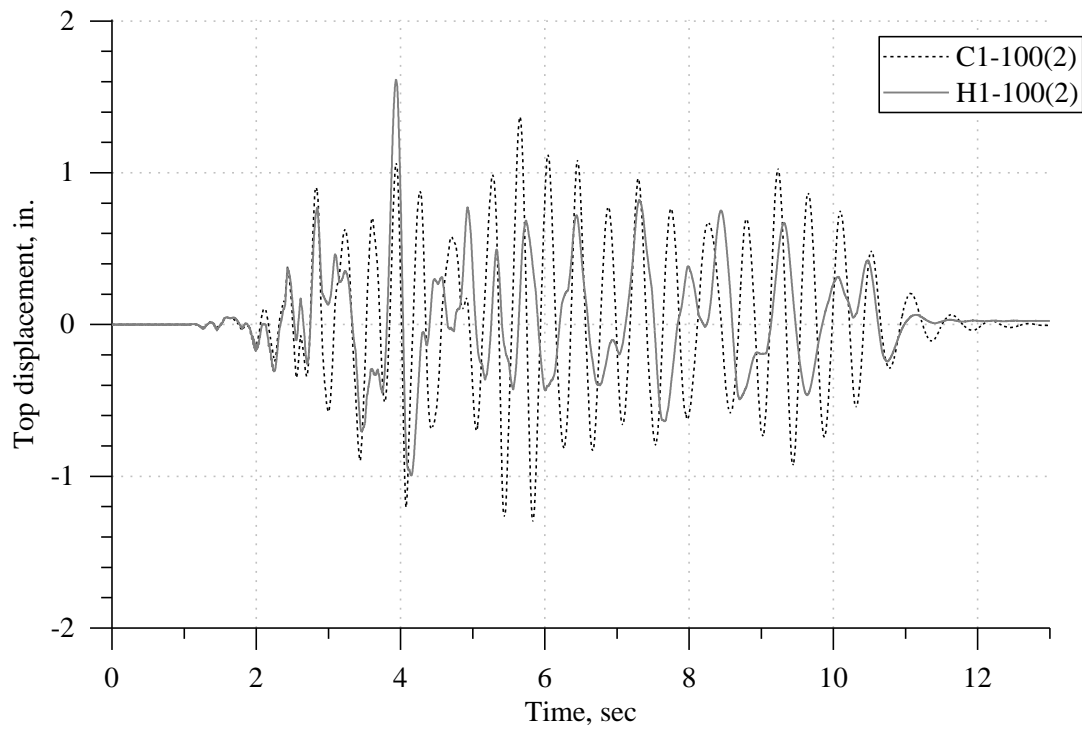


Figure 5-7: Comparison of top drift responses of tests C1-100(2) and H1-100(2).

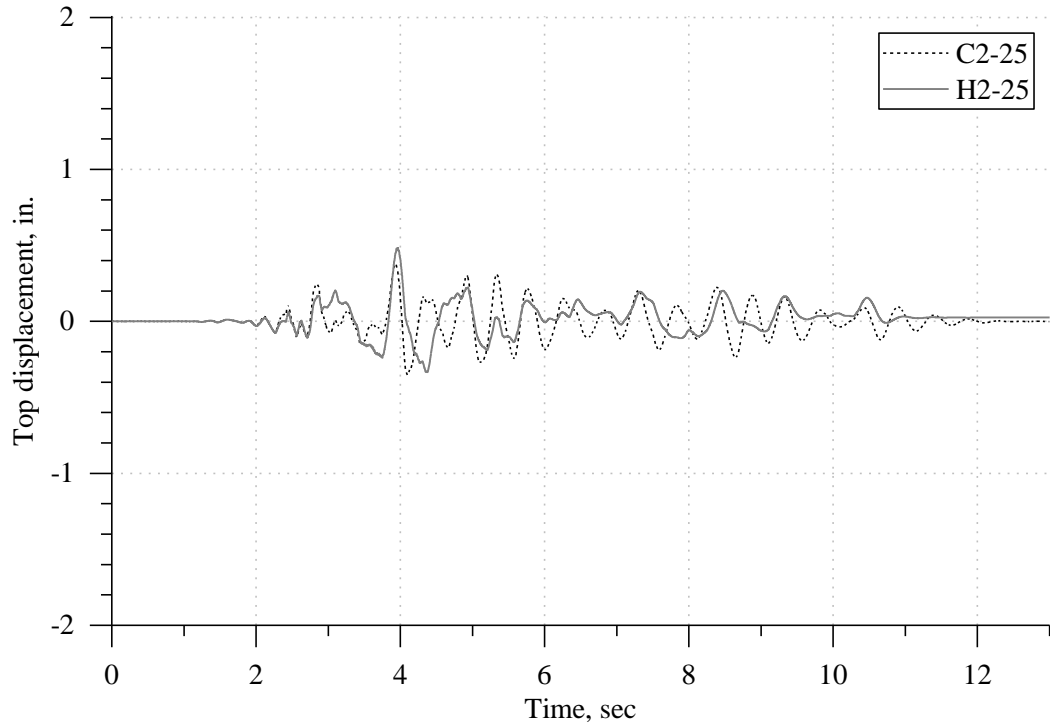


Figure 5-8: Comparison of top drift responses of tests C2-25 and H2-25.

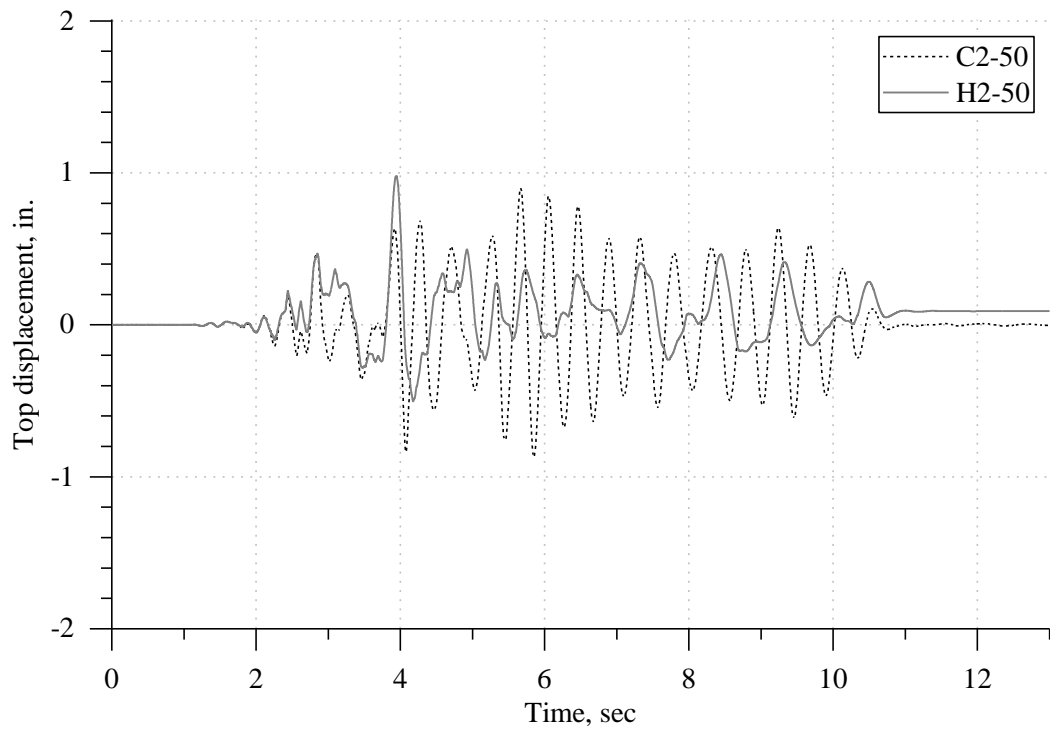


Figure 5-9: Comparison of top drift responses of tests C2-50 and H2-50.

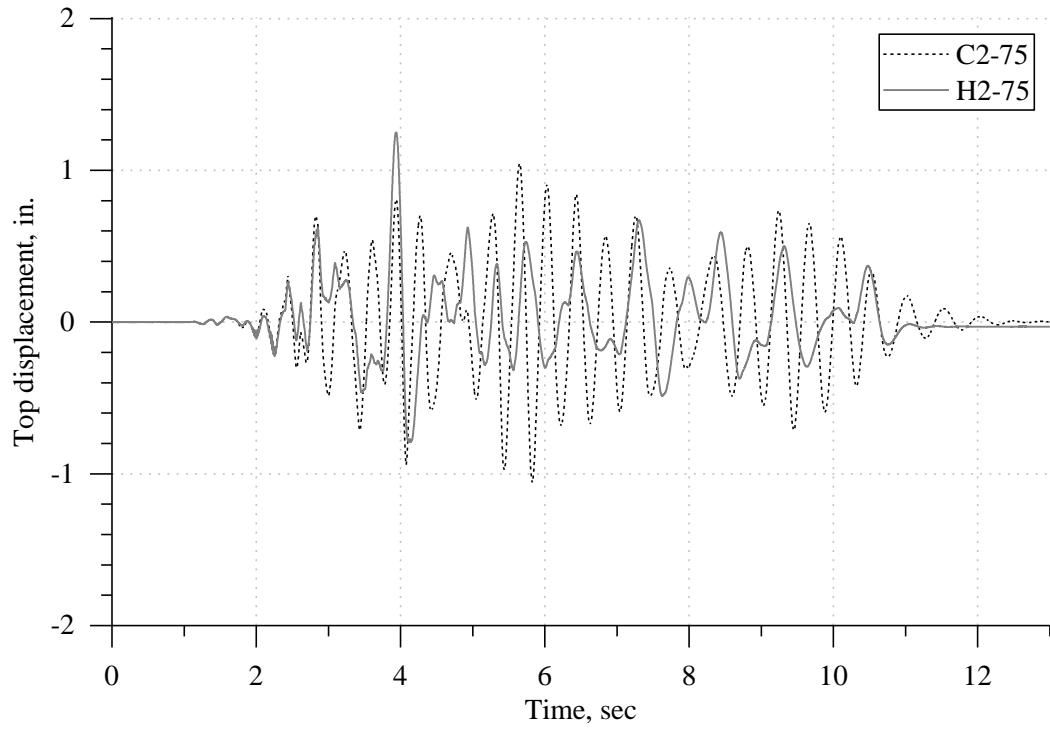


Figure 5-10: Comparison of top drift responses of tests C2-75 and H2-75.

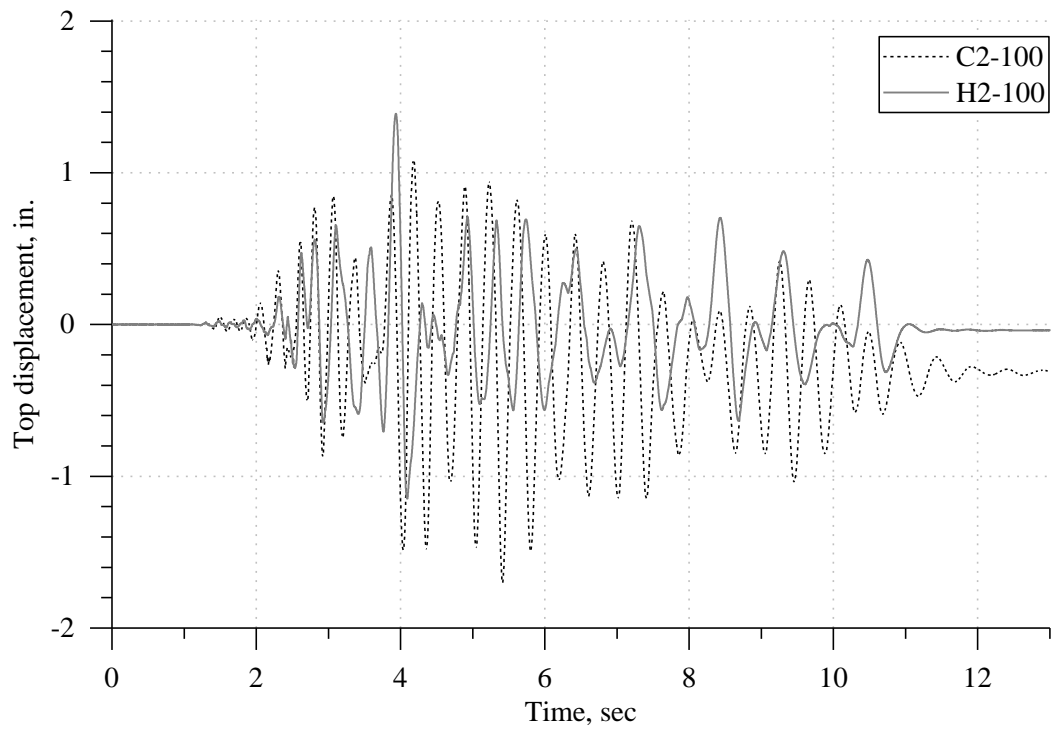


Figure 5-11: Comparison of top drift responses of tests C2-100 and H2-100.

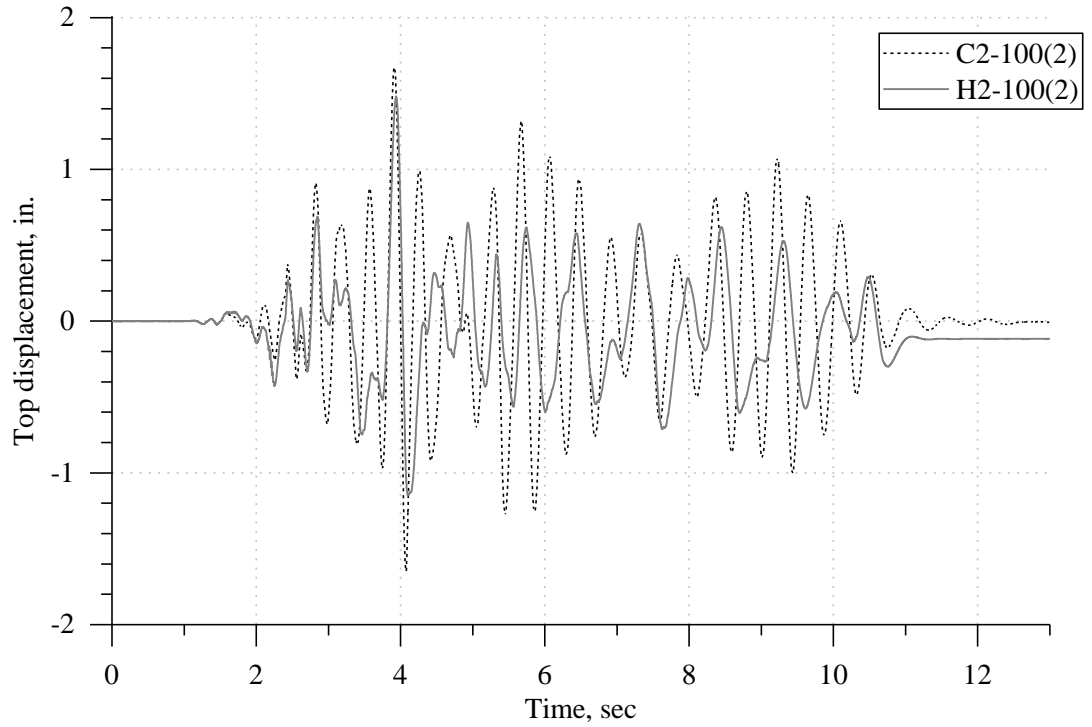


Figure 5-12: Comparison of top drift responses of tests C2-100(2) and H2-100(2).

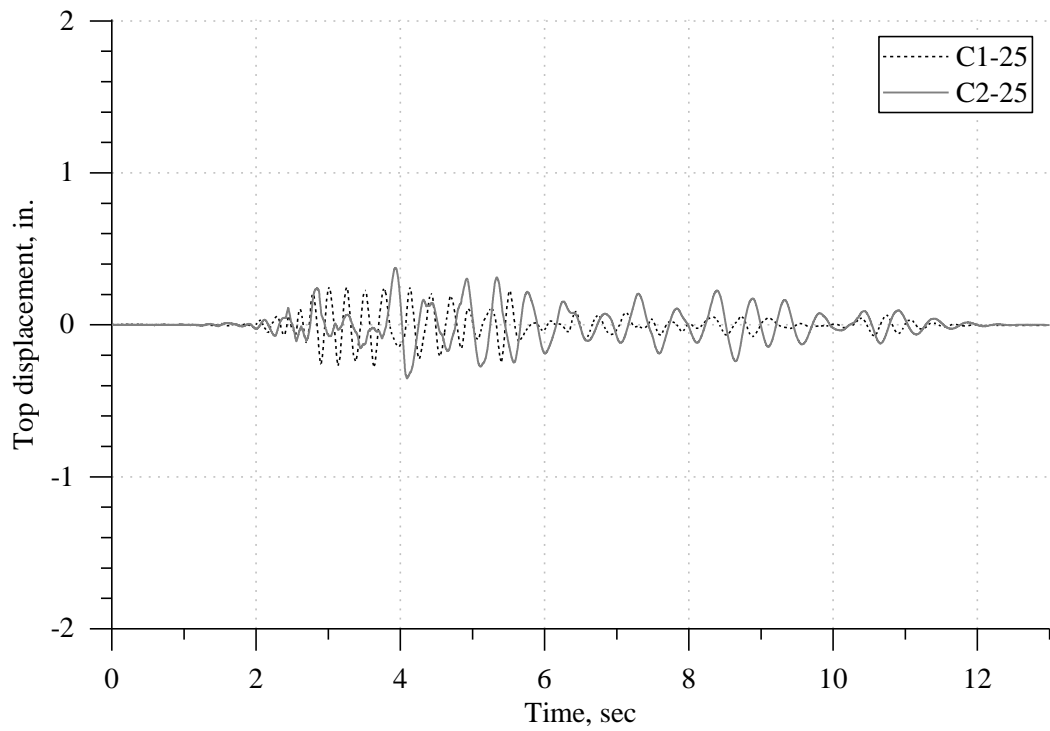


Figure 5-13: Comparison of top drift responses of tests C1-25 and C2-25.

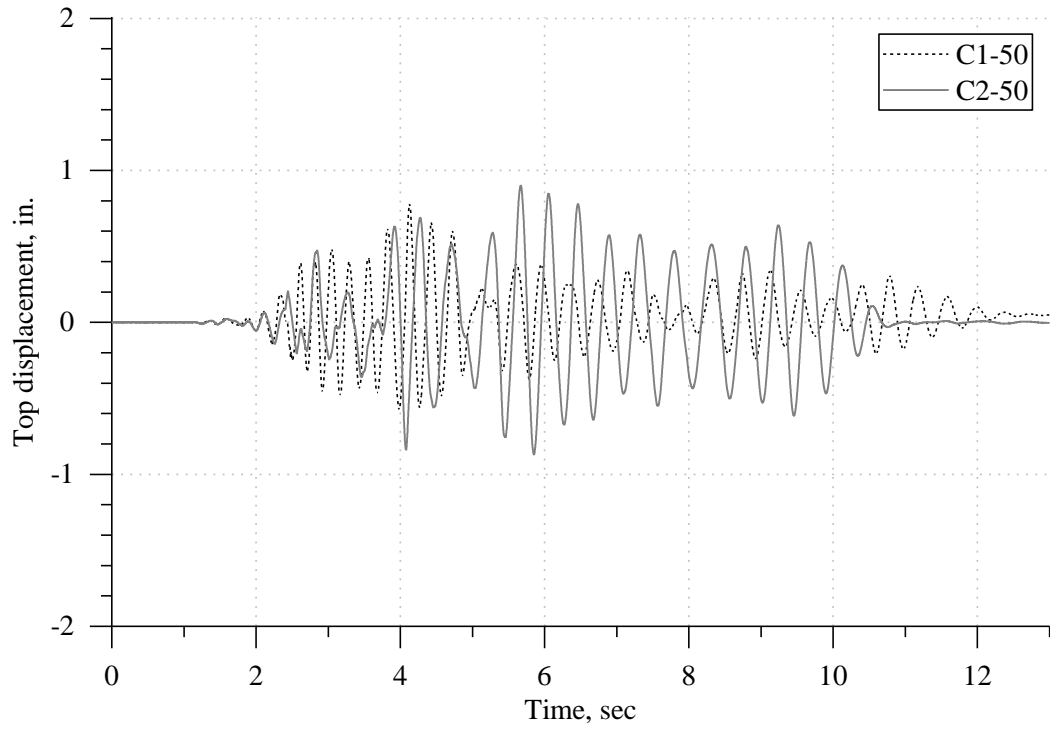


Figure 5-14: Comparison of top drift responses of tests C1-50 and C2-50.

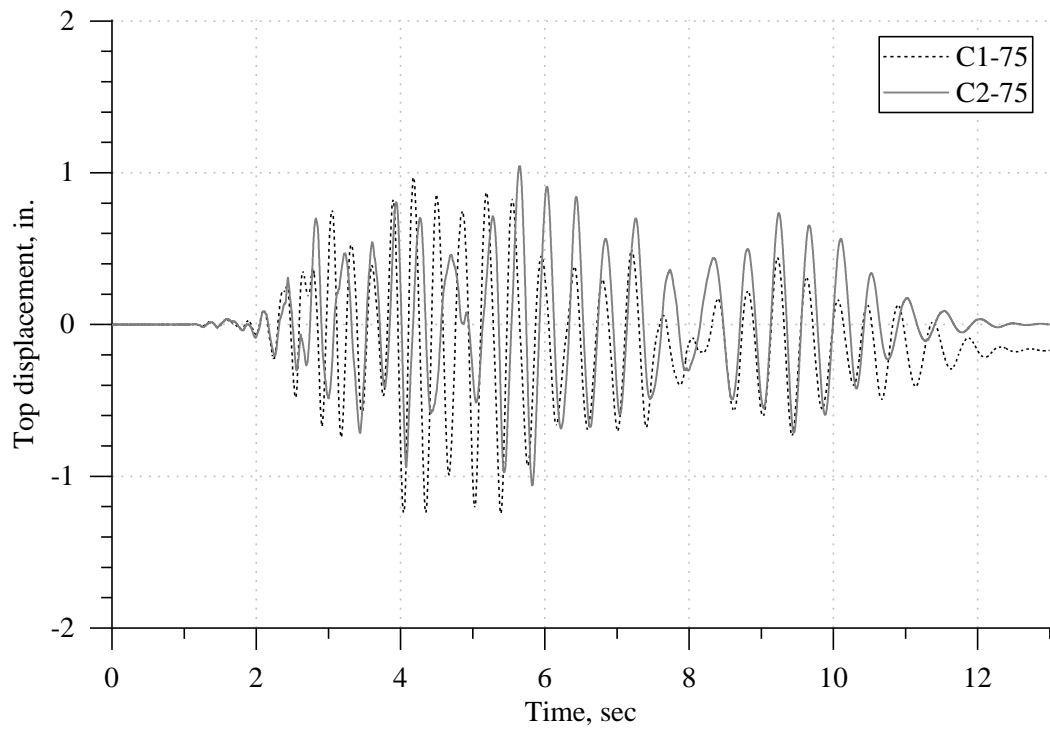


Figure 5-15: Comparison of top drift responses of tests C1-75 and C2-75.

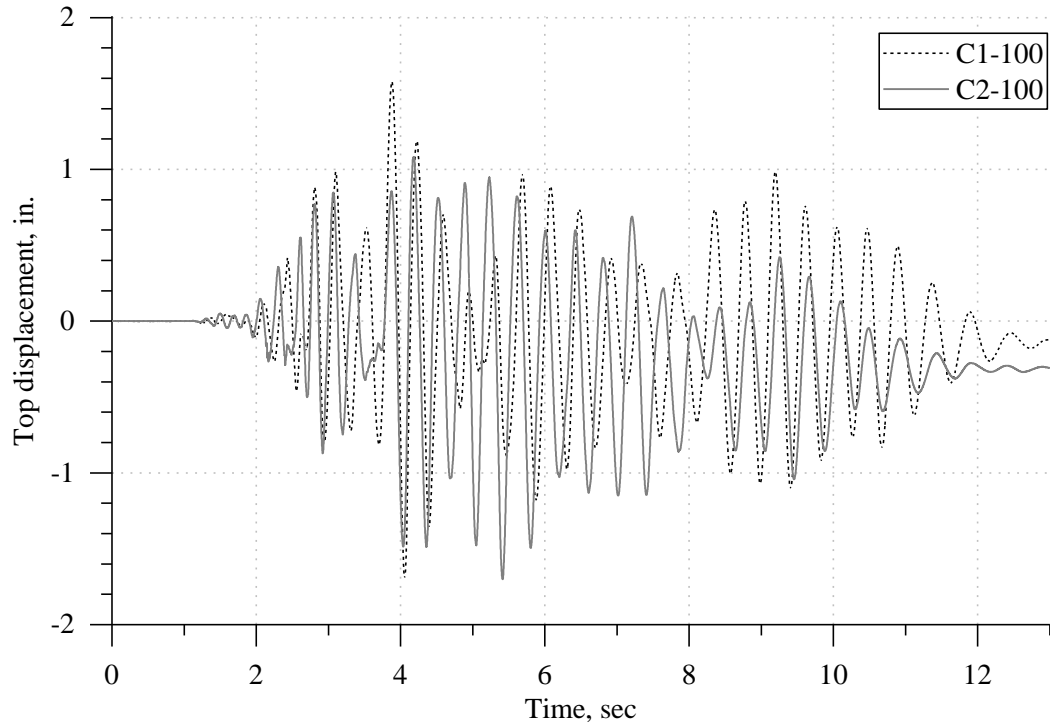


Figure 5-16: Comparison of top drift responses of tests C1-100 and C2-100.

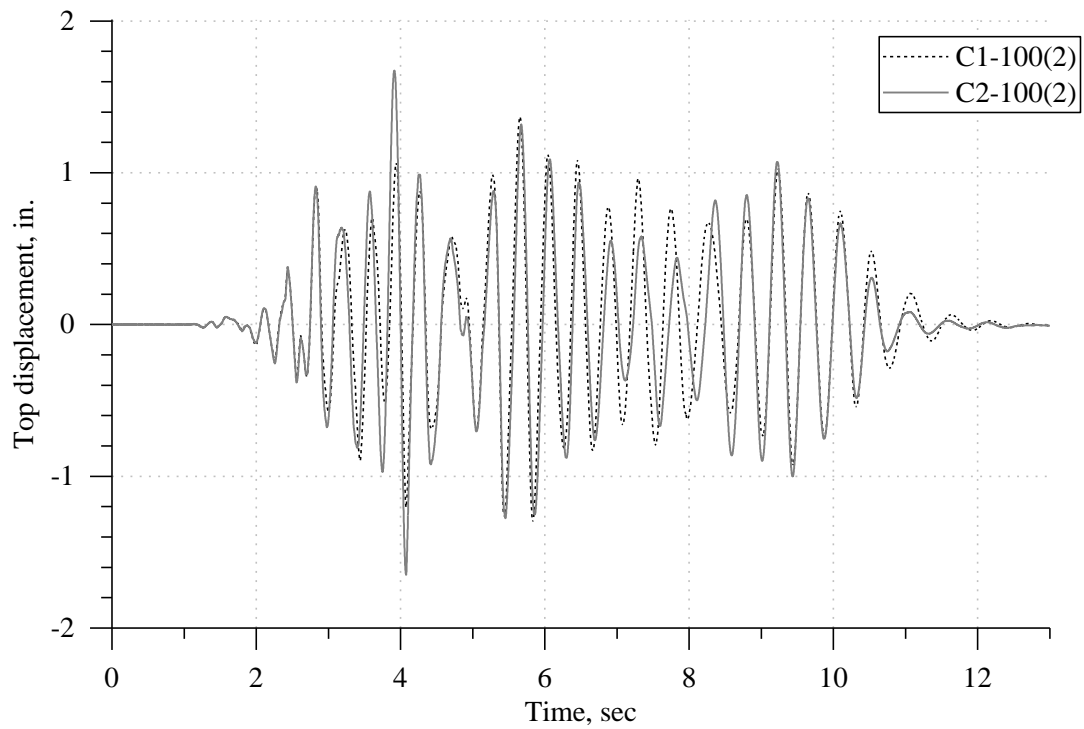


Figure 5-17: Comparison of top drift responses of tests C1-100(2) and C2-100(2).

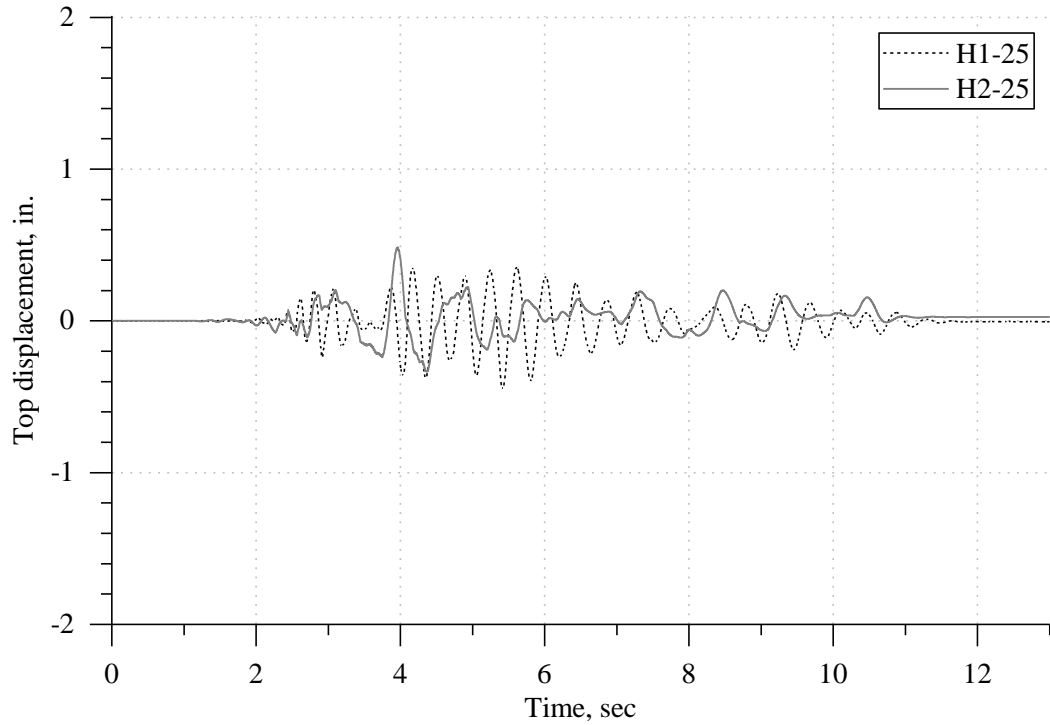


Figure 5-18: Comparison of top drift responses of tests H1-25 and H2-25.

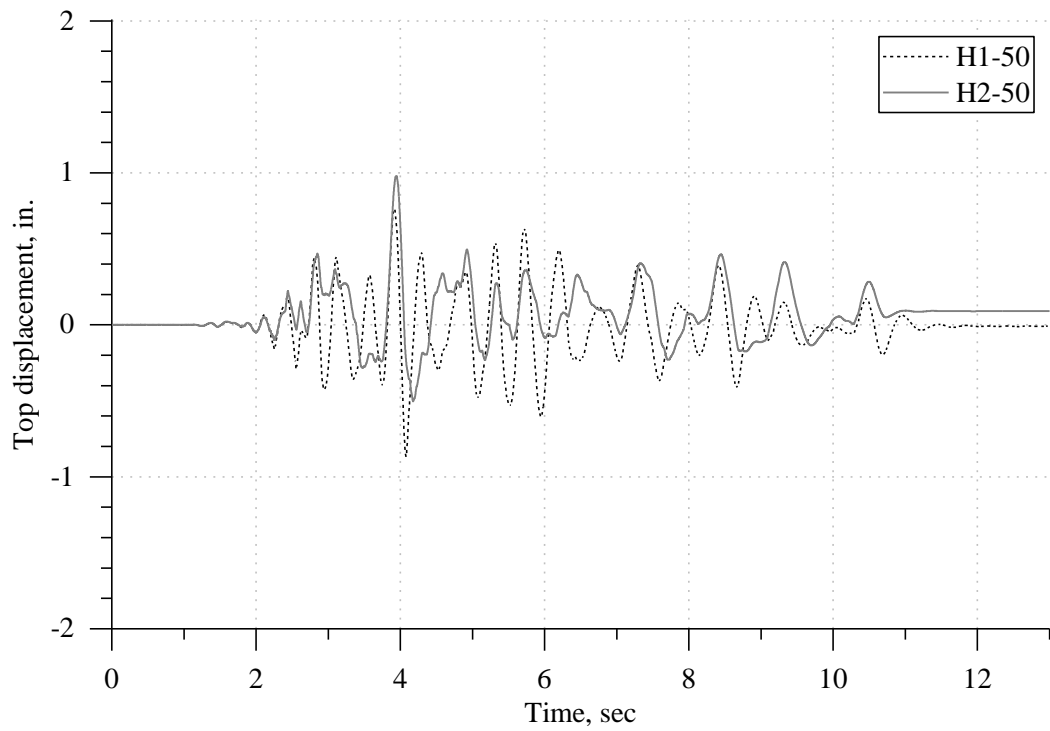


Figure 5-19: Comparison of top drift responses of tests H1-50 and H2-50.

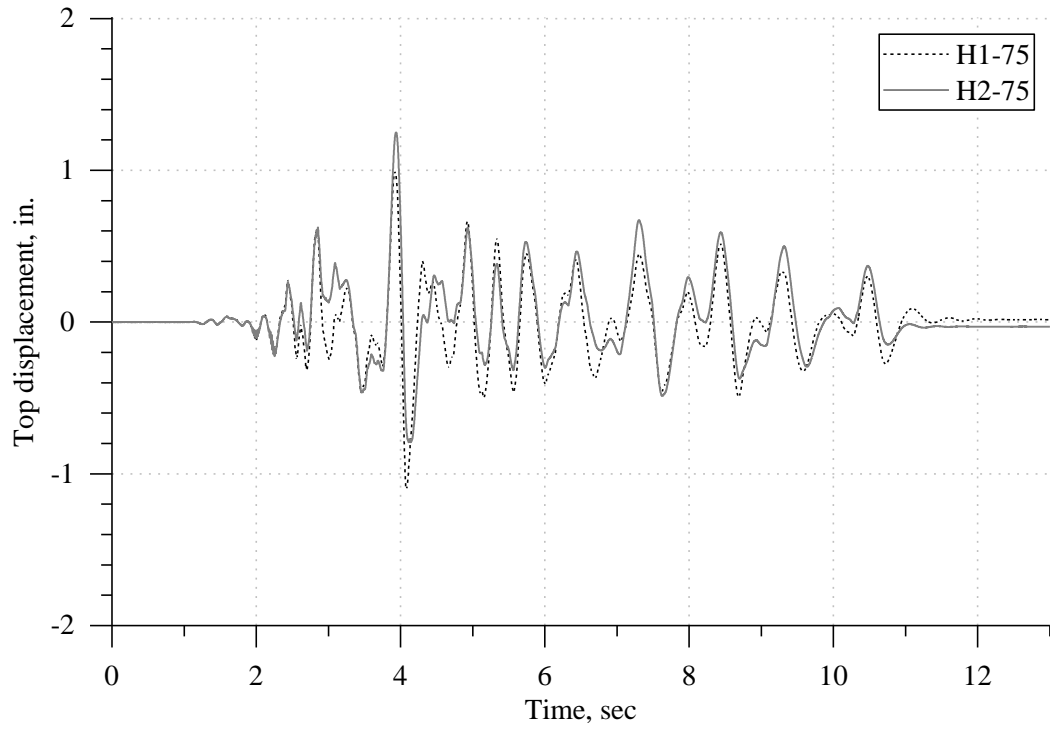


Figure 5-20: Comparison of top drift responses of tests H1-75 and H2-75.

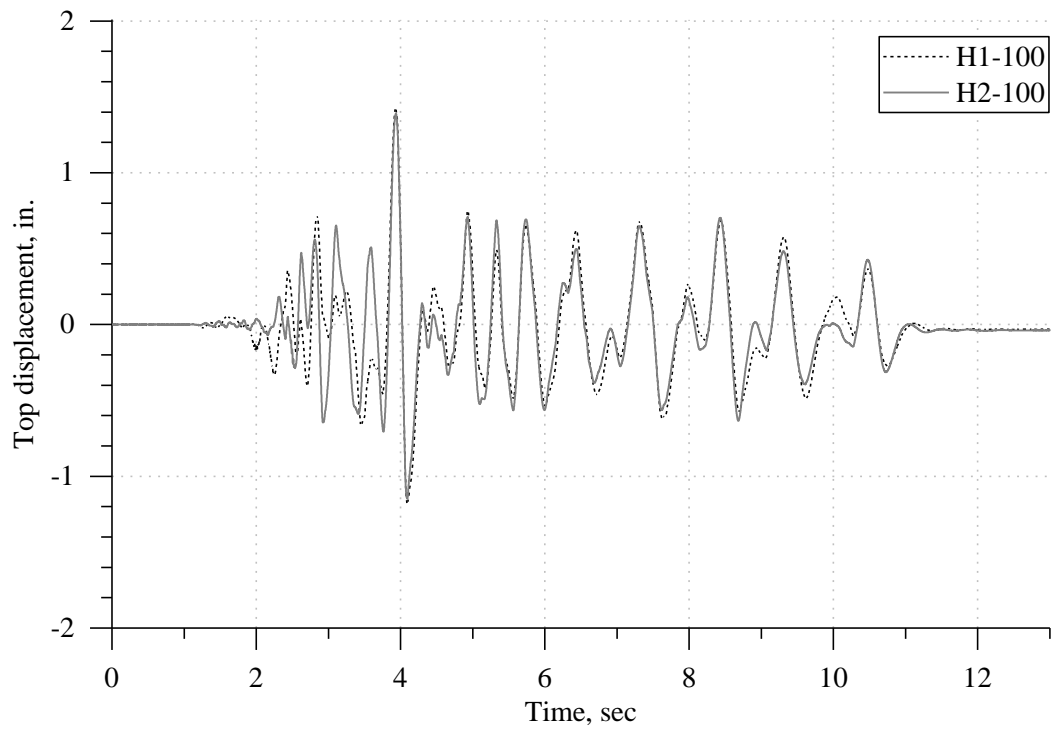


Figure 5-21: Comparison of top drift responses of tests H1-100 and H2-100.

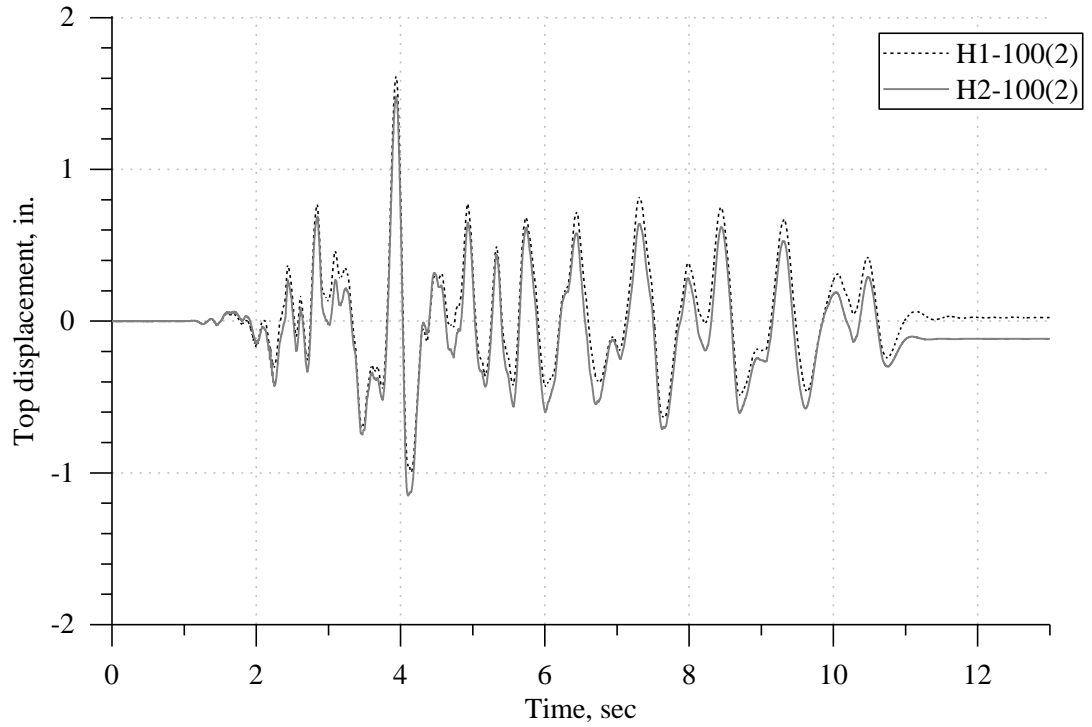


Figure 5-22: Comparison of top drift responses of tests H1-100(2) and H2-100(2).

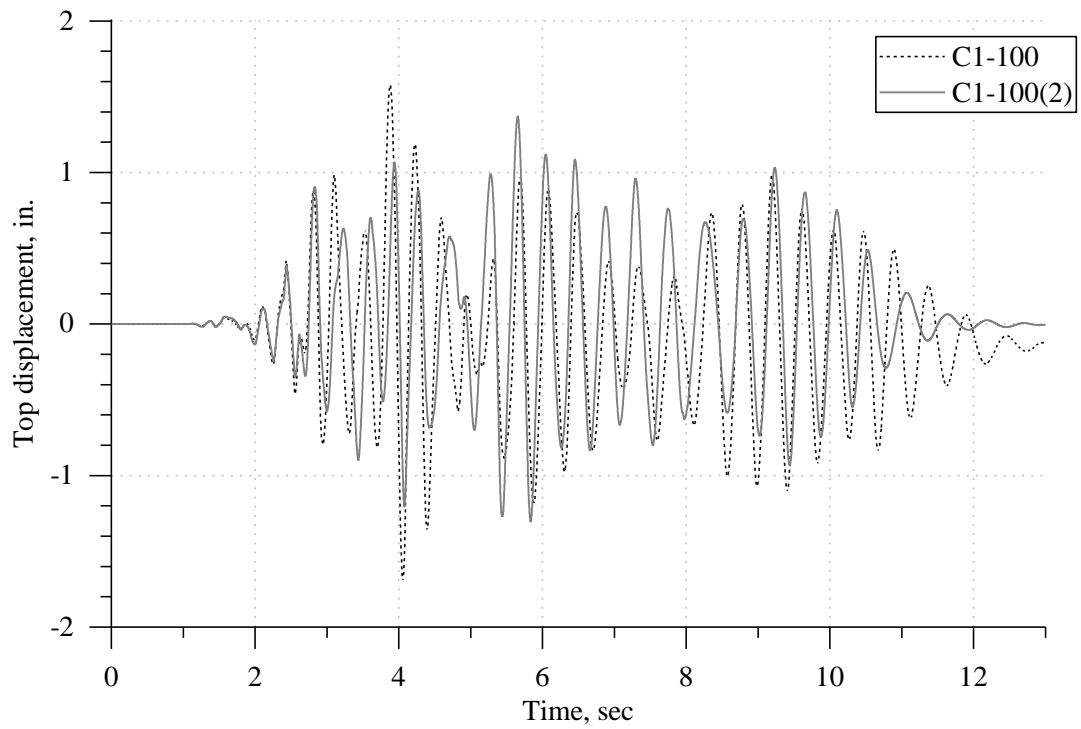


Figure 5-23: Comparison of top drift responses of tests C1-100(1) and C1-100(2).

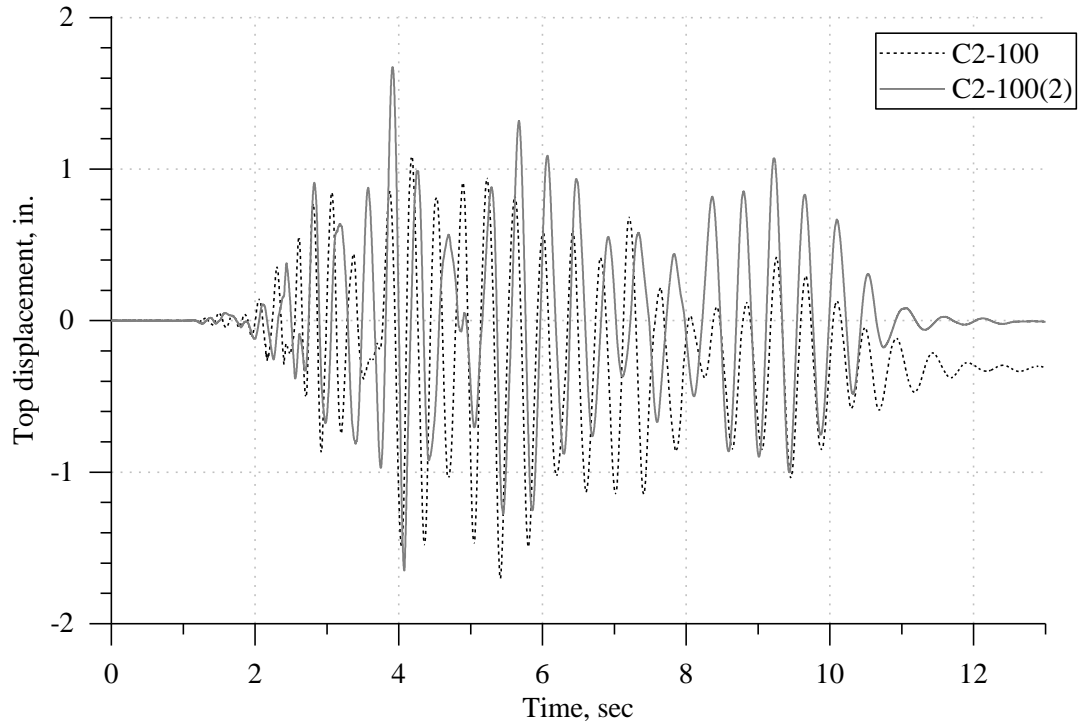


Figure 5-24: Comparison of top drift responses of tests C2-100(1) and C2-100(2).

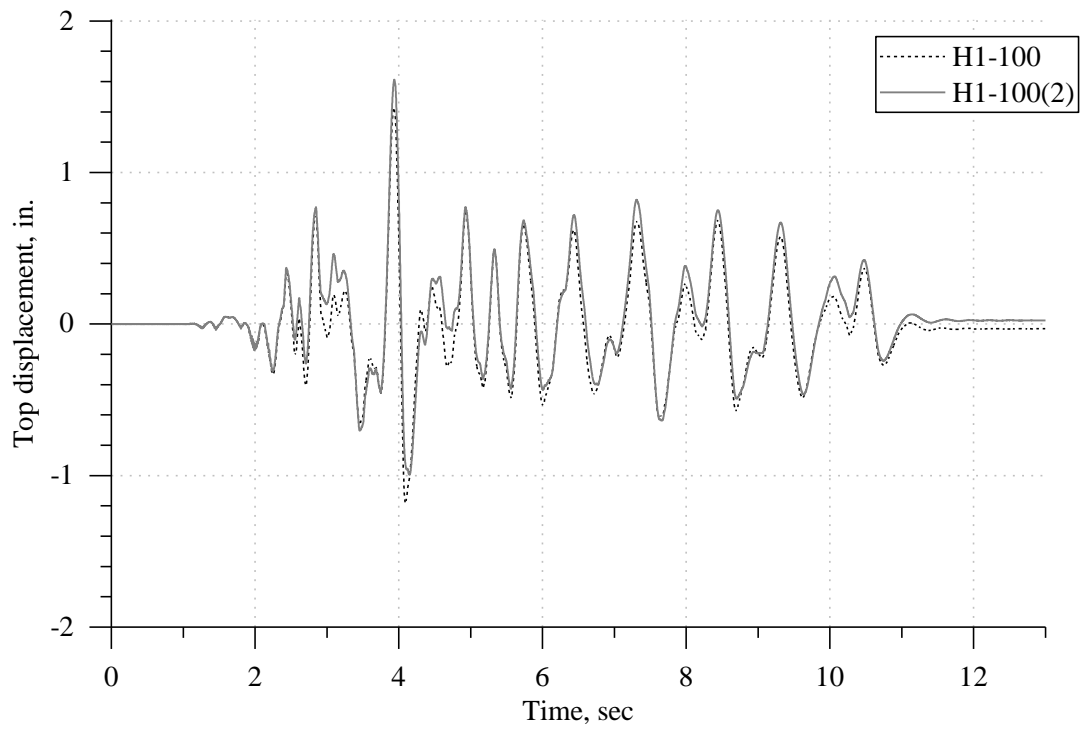


Figure 5-25: Comparison of top drift responses of tests H1-100(1) and H1-100(2).

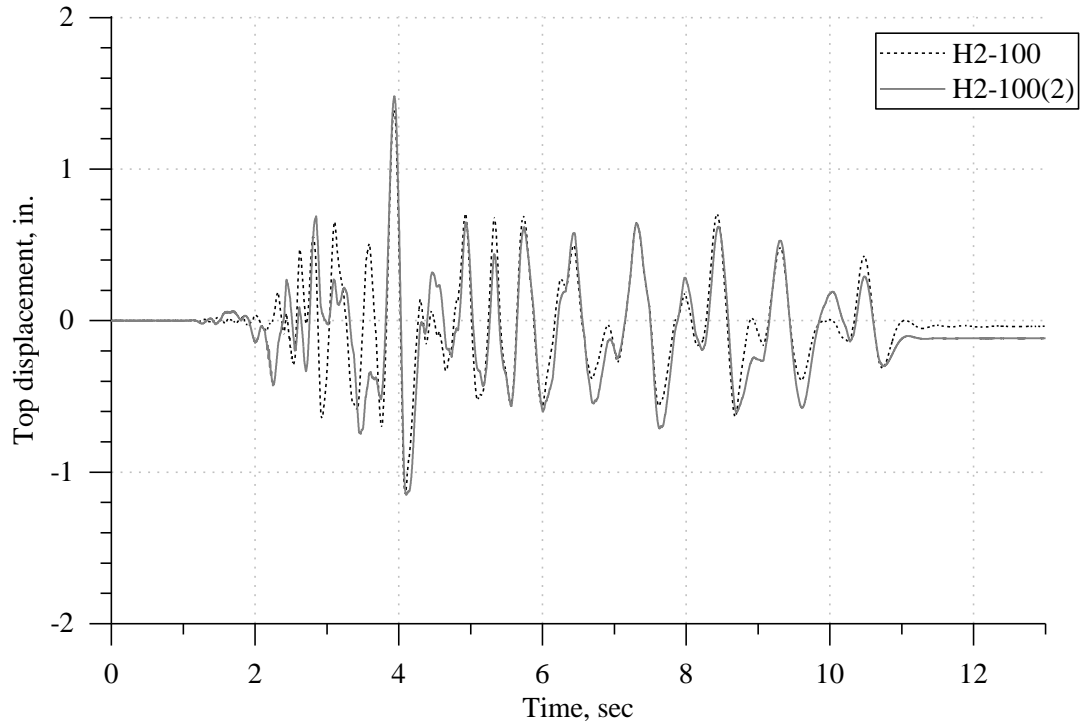


Figure 5-26: Comparison of top drift responses of tests H2-100(1) and H2-100(2).

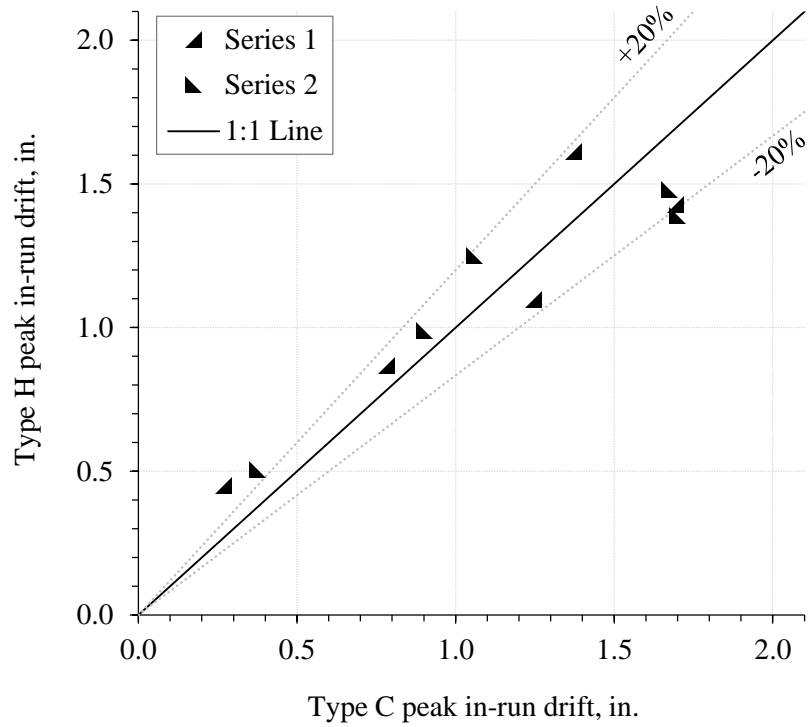


Figure 5-27: Measured peak in-run drift of H frames vs. C frames.

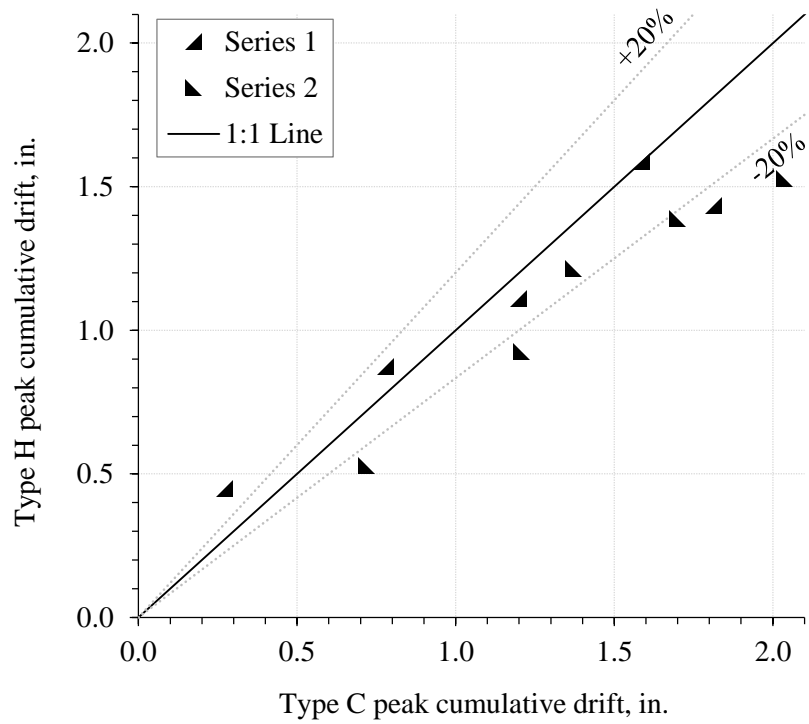


Figure 5-28: Measured peak cumulative drift of H frames vs. C frames.

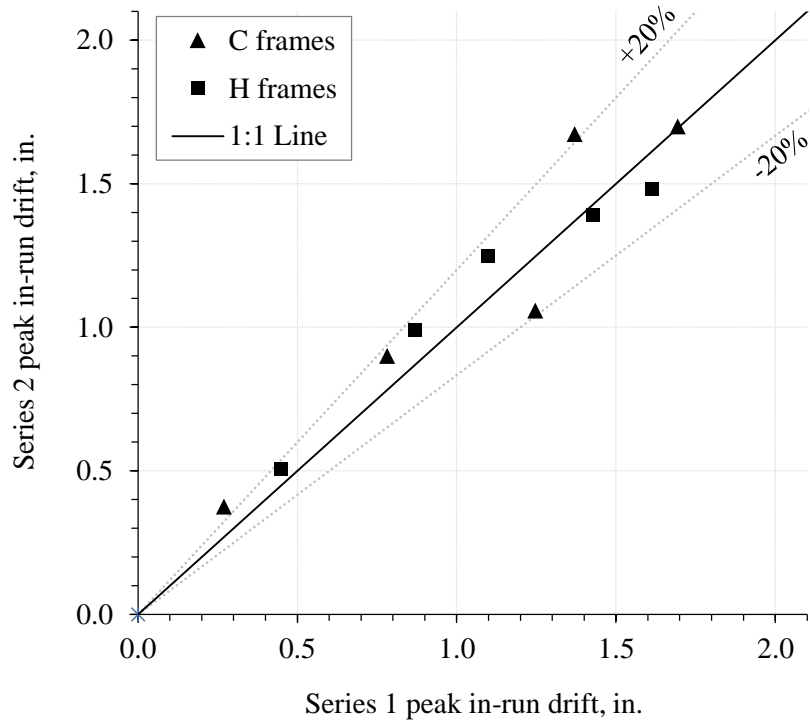


Figure 5-29: Measured peak in-run drift of Series 2 frames vs. Series 1 frames.

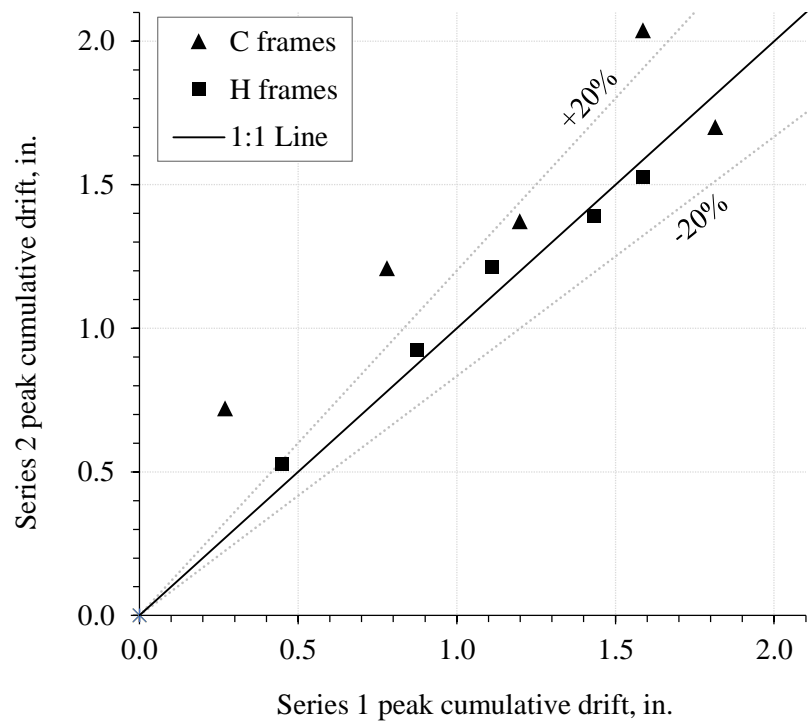


Figure 5-30: Measured peak cumulative drift of Series 2 frames vs. Series 1 frames.

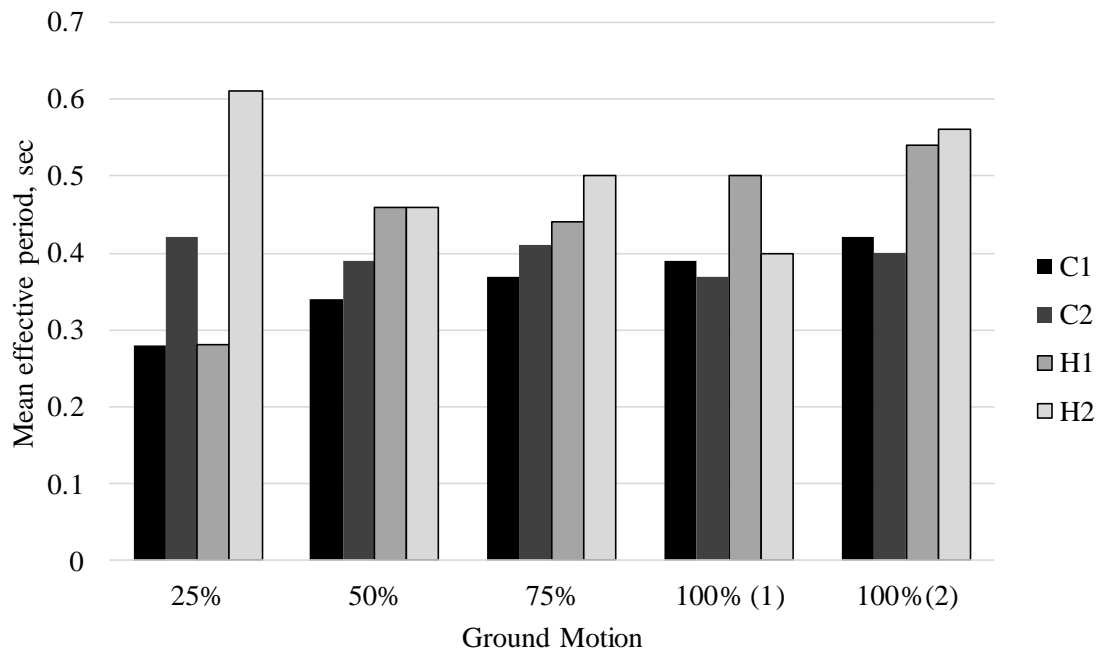


Figure 5-31: Comparison of mean effective periods for each test.

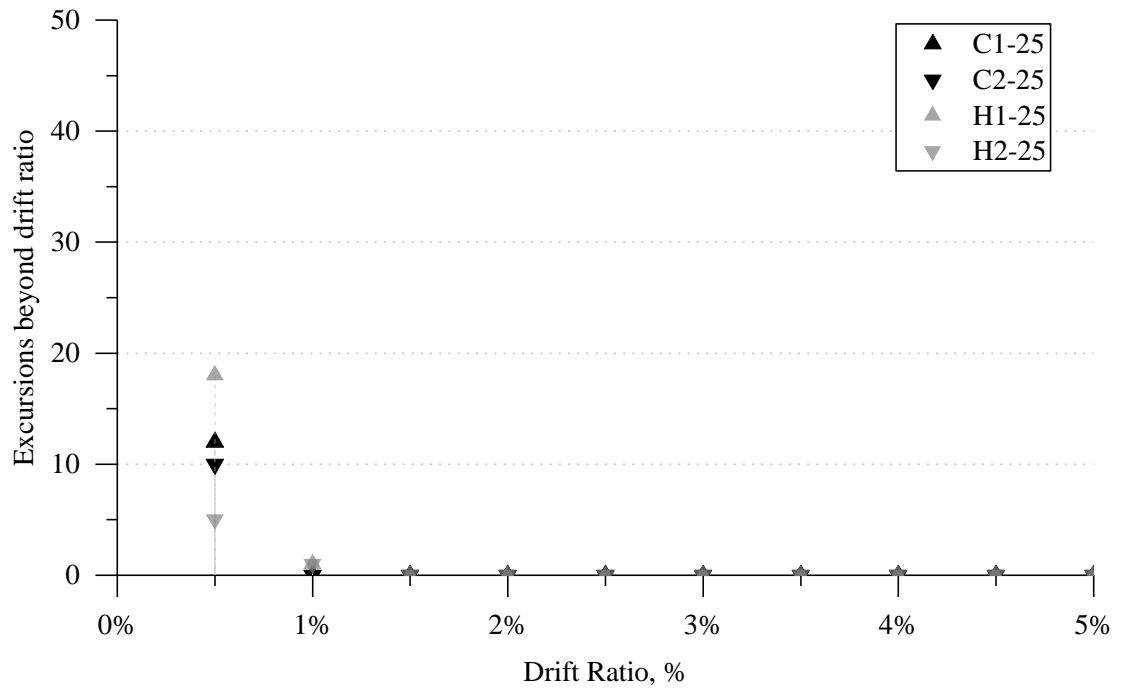


Figure 5-32: Excursions beyond drift versus drift for tests at 25%.

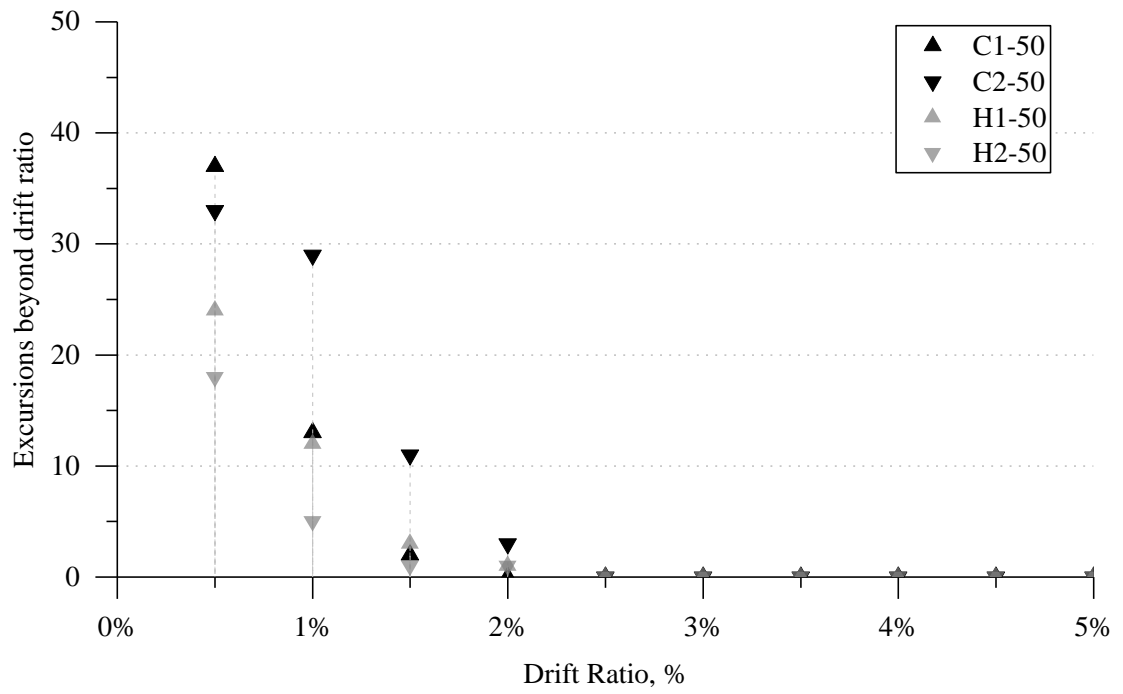


Figure 5-33: Excursions beyond drift versus drift for tests at 50%.

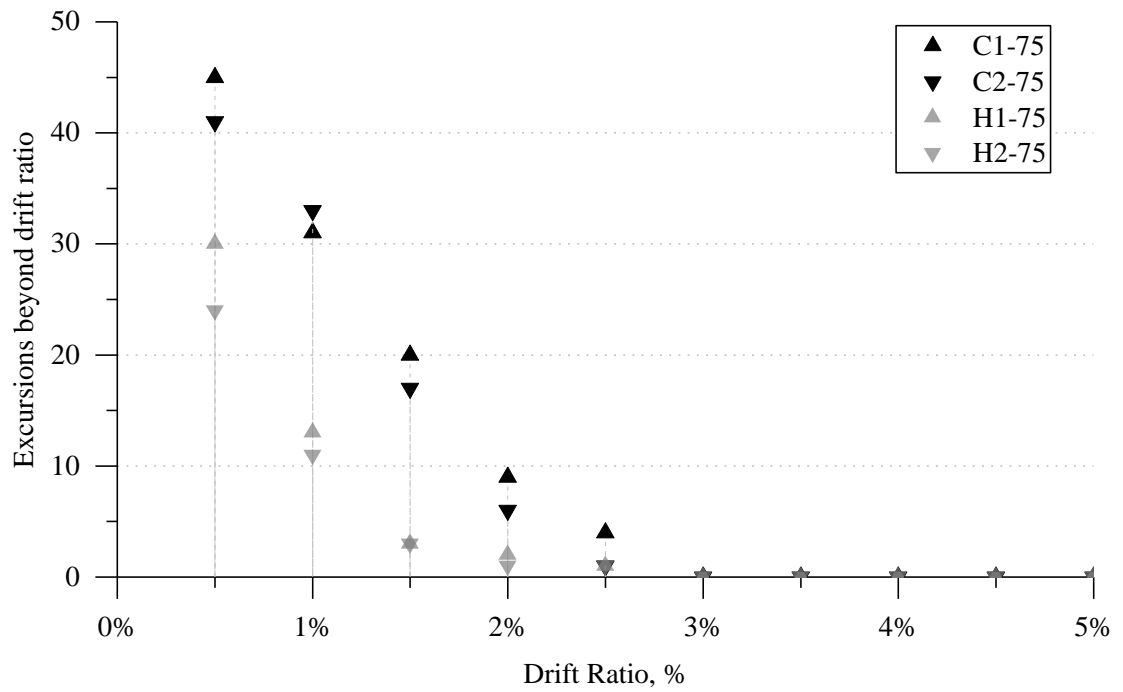


Figure 5-34: Excursions beyond drift versus drift for tests at 75%.

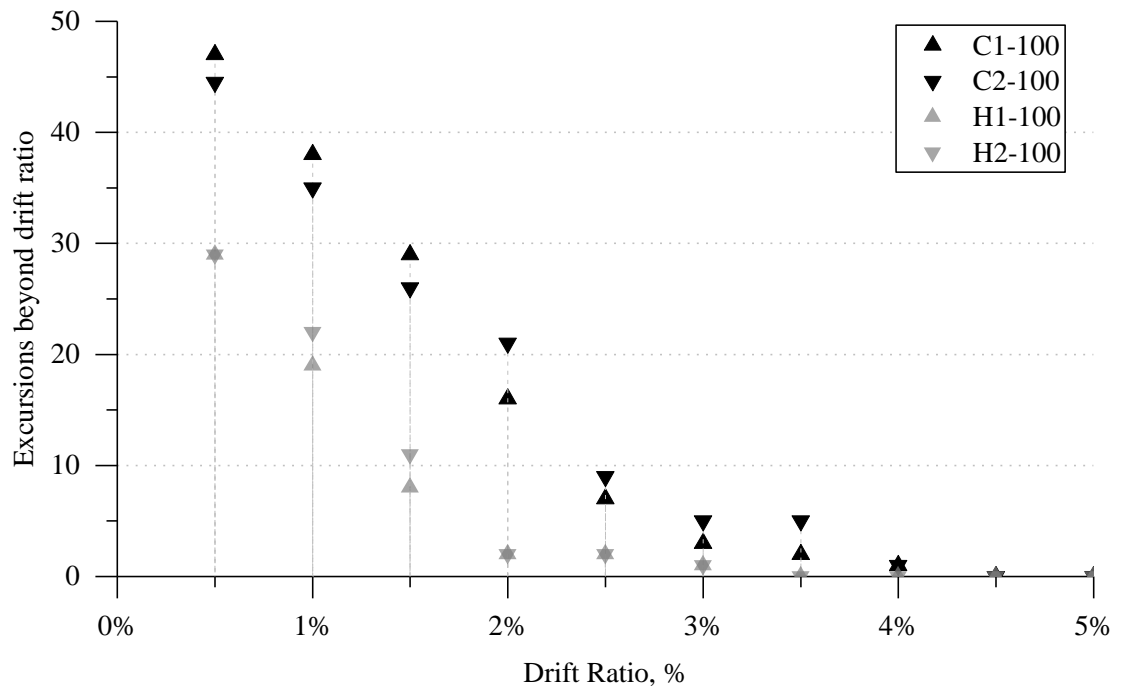


Figure 5-35: Excursions beyond drift versus drift for tests at 100%.

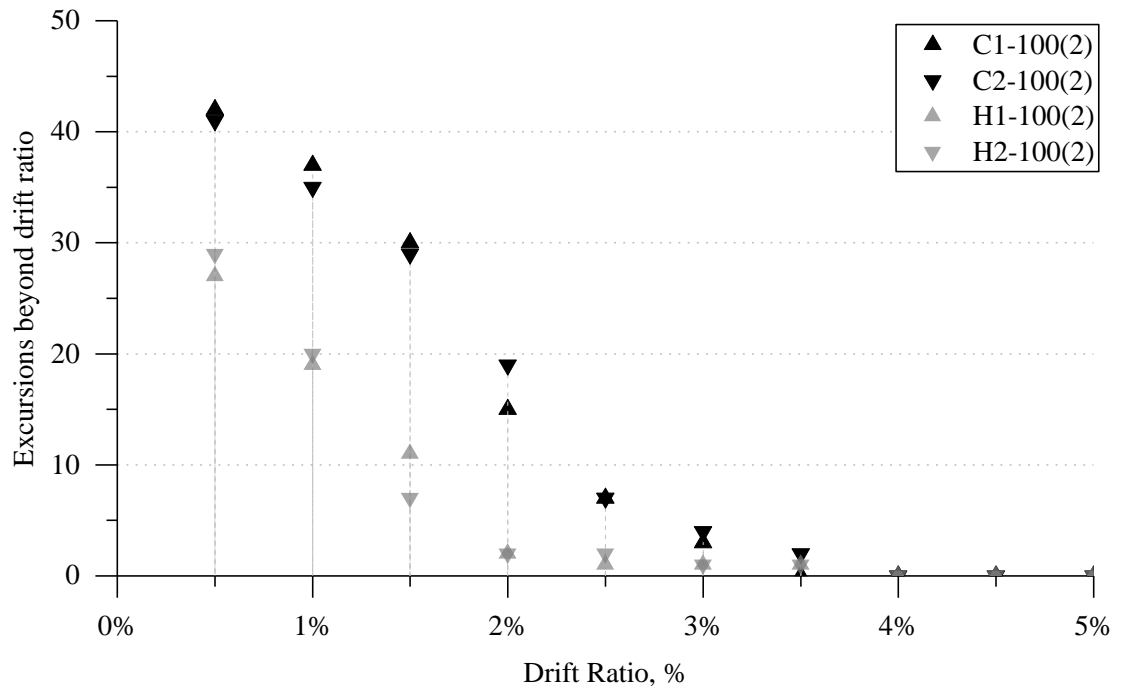


Figure 5-36: Excursions beyond drift versus drift for second tests at 100%(2).

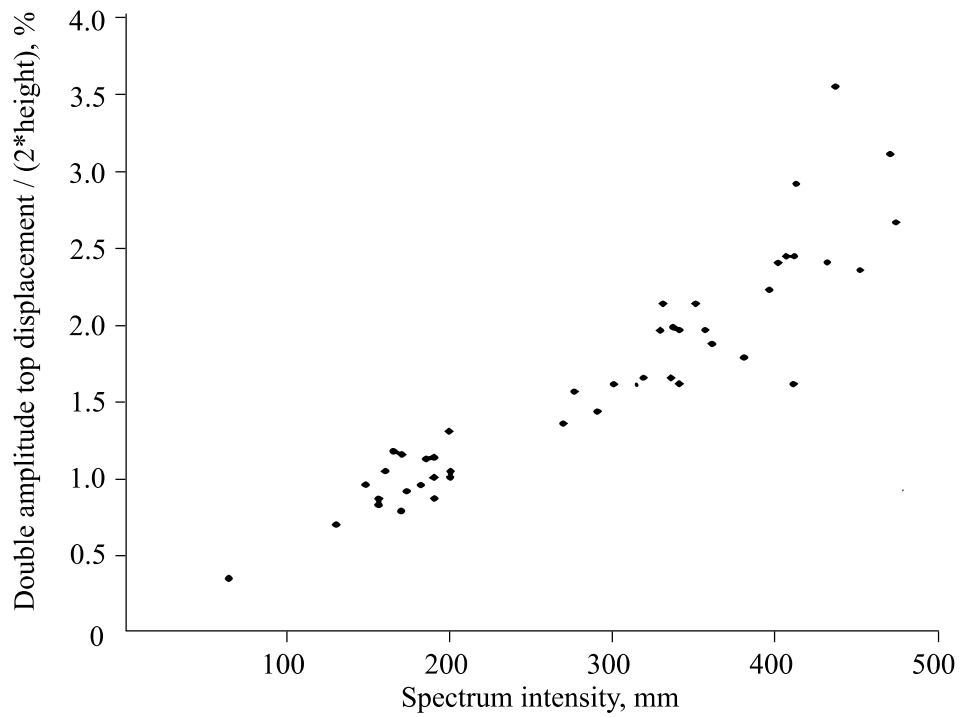


Figure 6-1: Reproduction of Sozen's (1980) plot of peak drift ratio versus spectrum intensity.

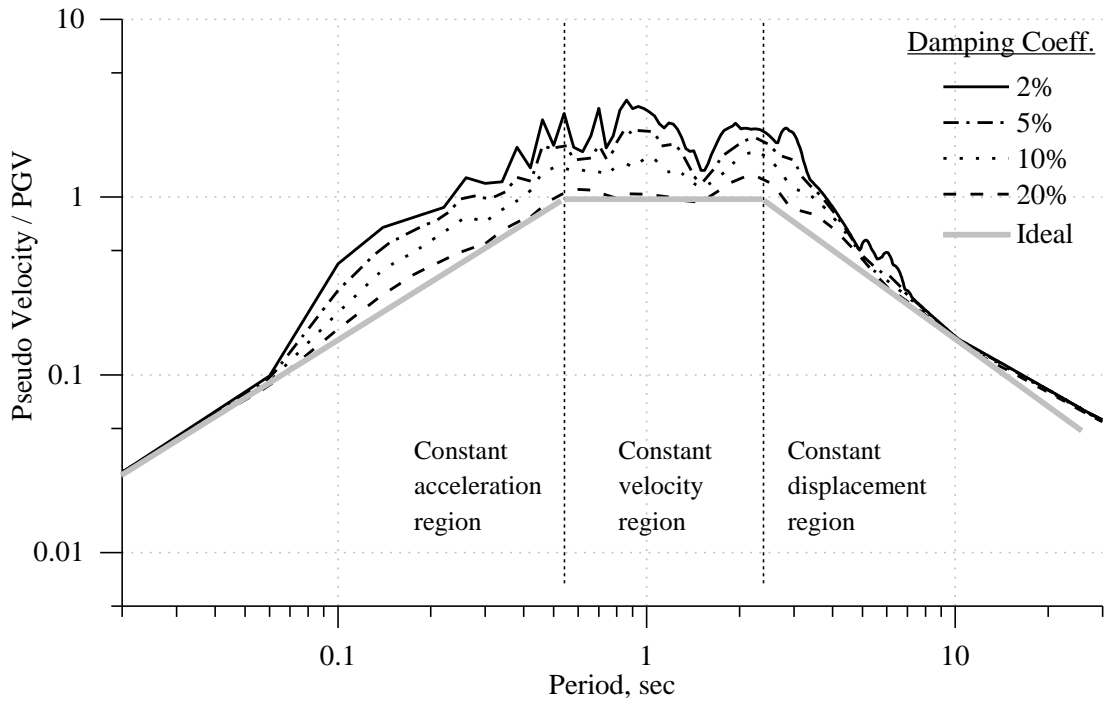


Figure 6-2: Illustration of idealized constant acceleration, velocity, and displacement regions of response (based on 1940 El Centro 180 component).

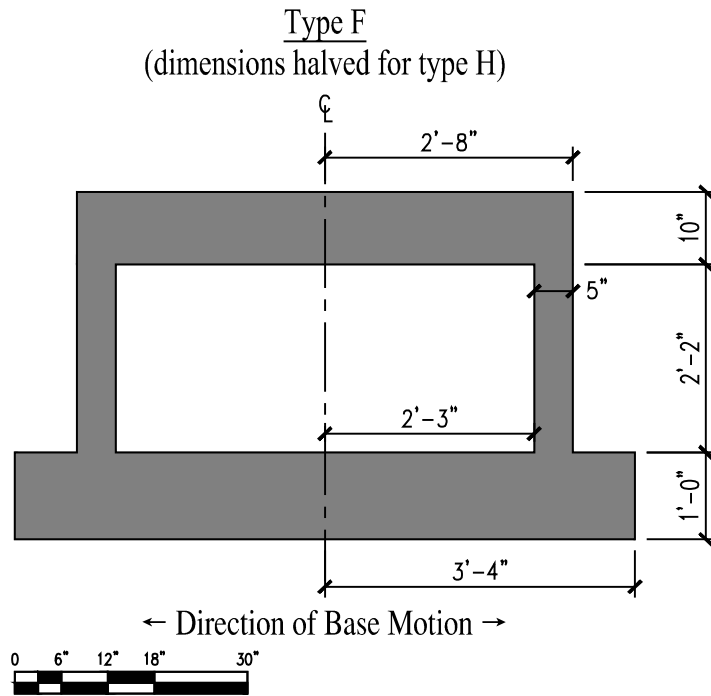


Figure 6-3: Frames tested by Gulkan and Sozen (1971).

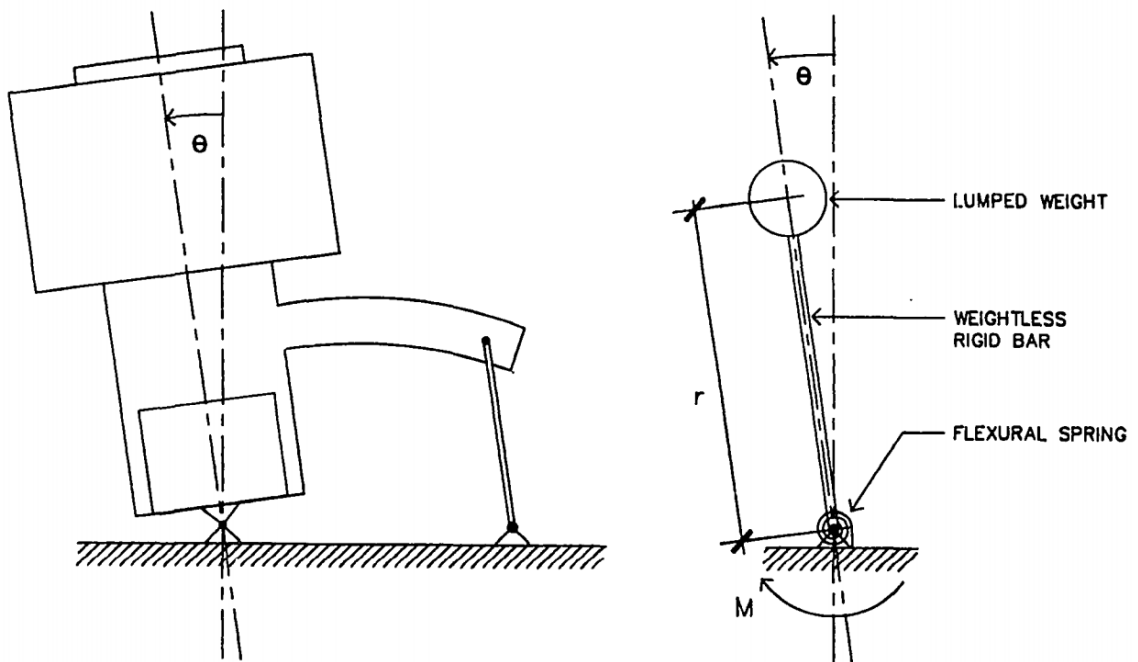


Figure 6-4: Schematic showing idealized response of specimens tested by Bonacci [from Bonacci (1989), Fig. 2.2].

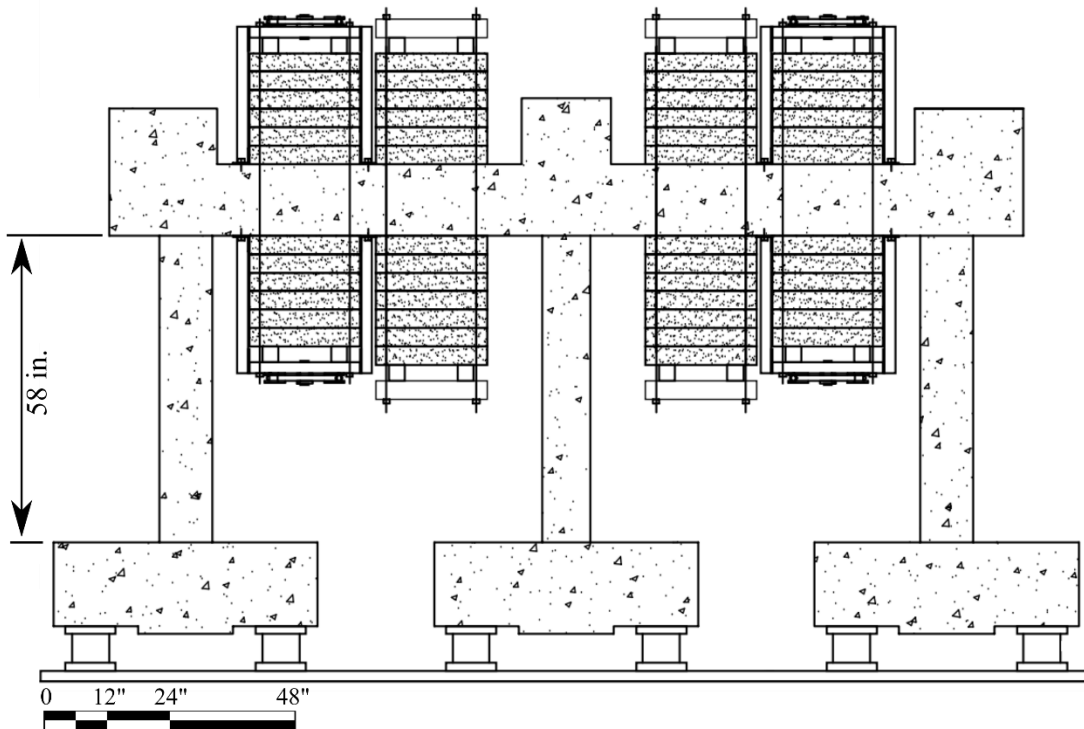
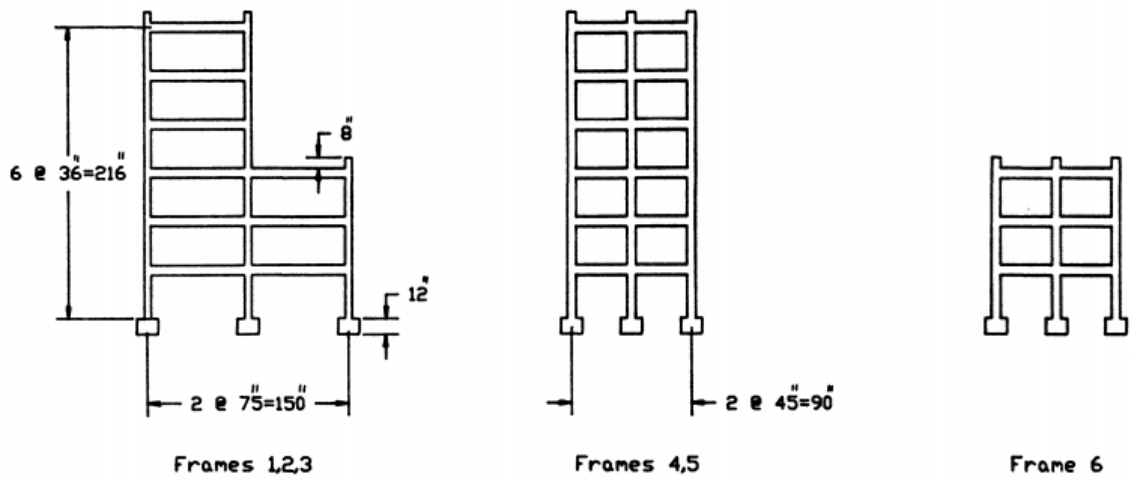
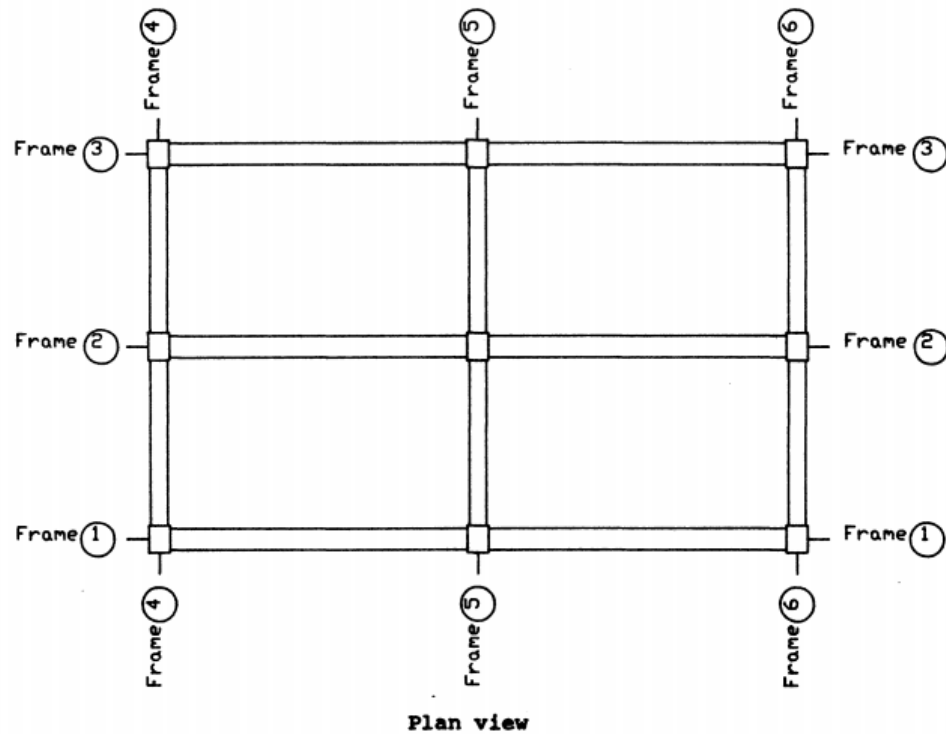


Figure 6-5: Frames tested by Elwood and Moehle (2003). Outer columns are circular, inner column is square [from Elwood and Moehle (2003), Fig. B-1].



Elevation views



Plan view

Figure 6-6: Schematics of building tested by Shahrooz and Moehle [from Shahrooz and Moehle (1987), Fig. 2.1].

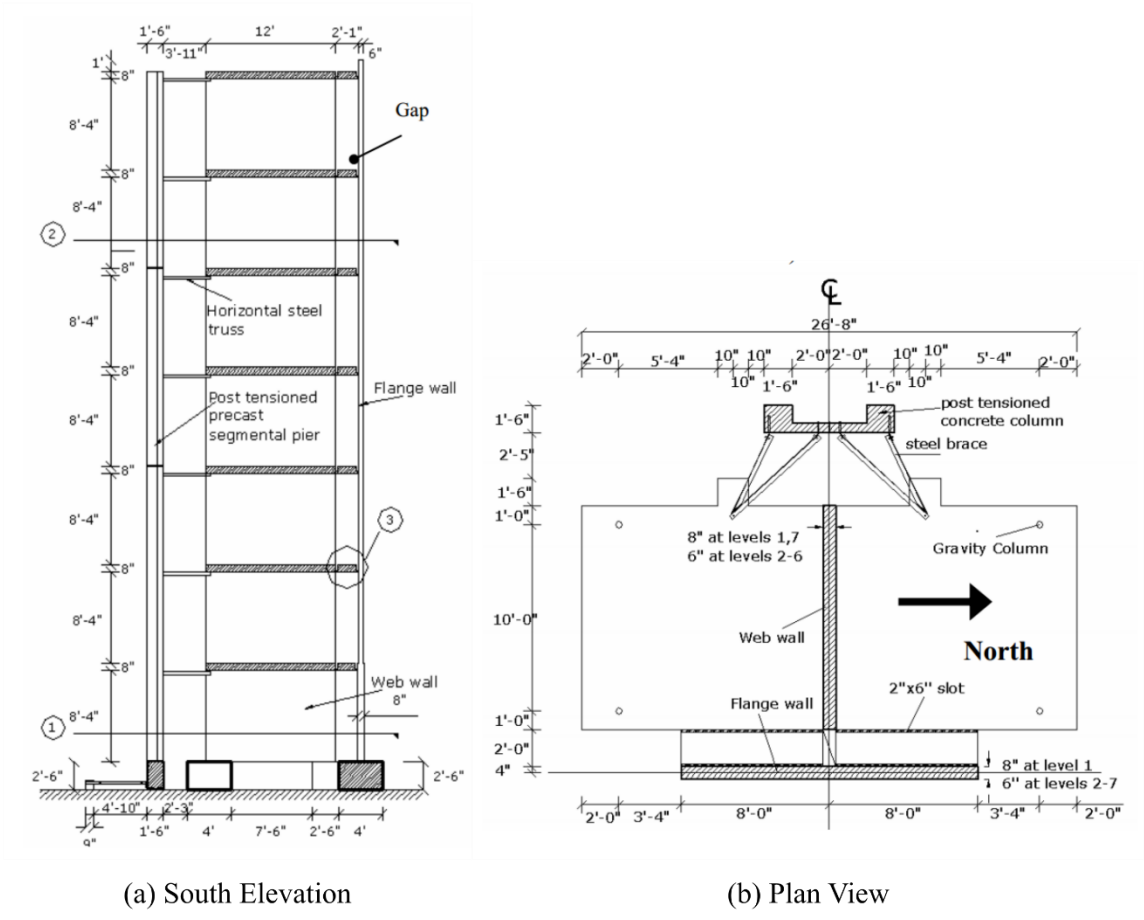


Figure 6-7: Elevation and plan view of building slice tested by Panagiotou et al. [from Panagiotou et al. (2007), Fig. 2.1].

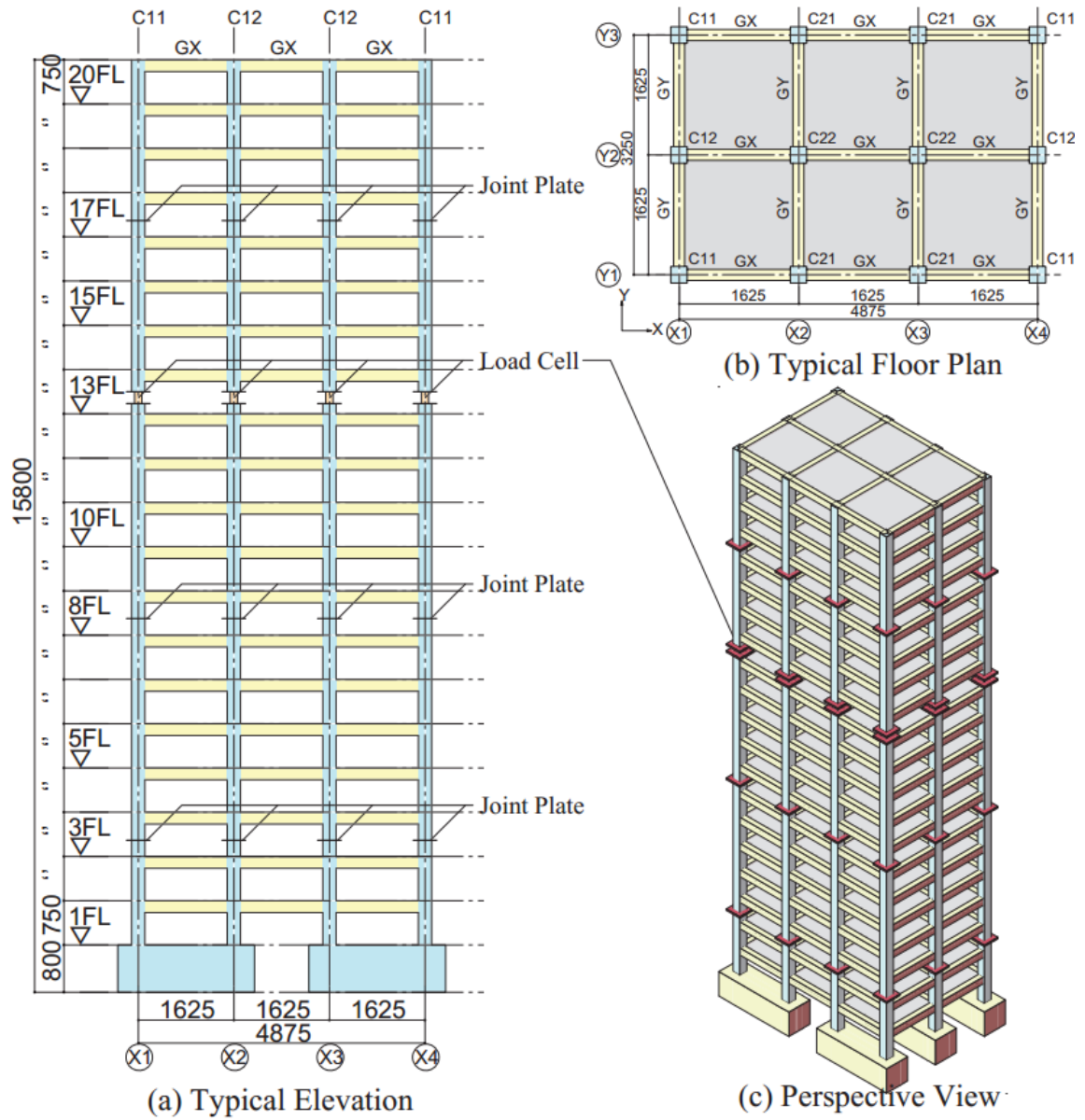


Figure 6-8: Building tested at E-Defense [from Sugimoto et al. (2016), Fig. 2].

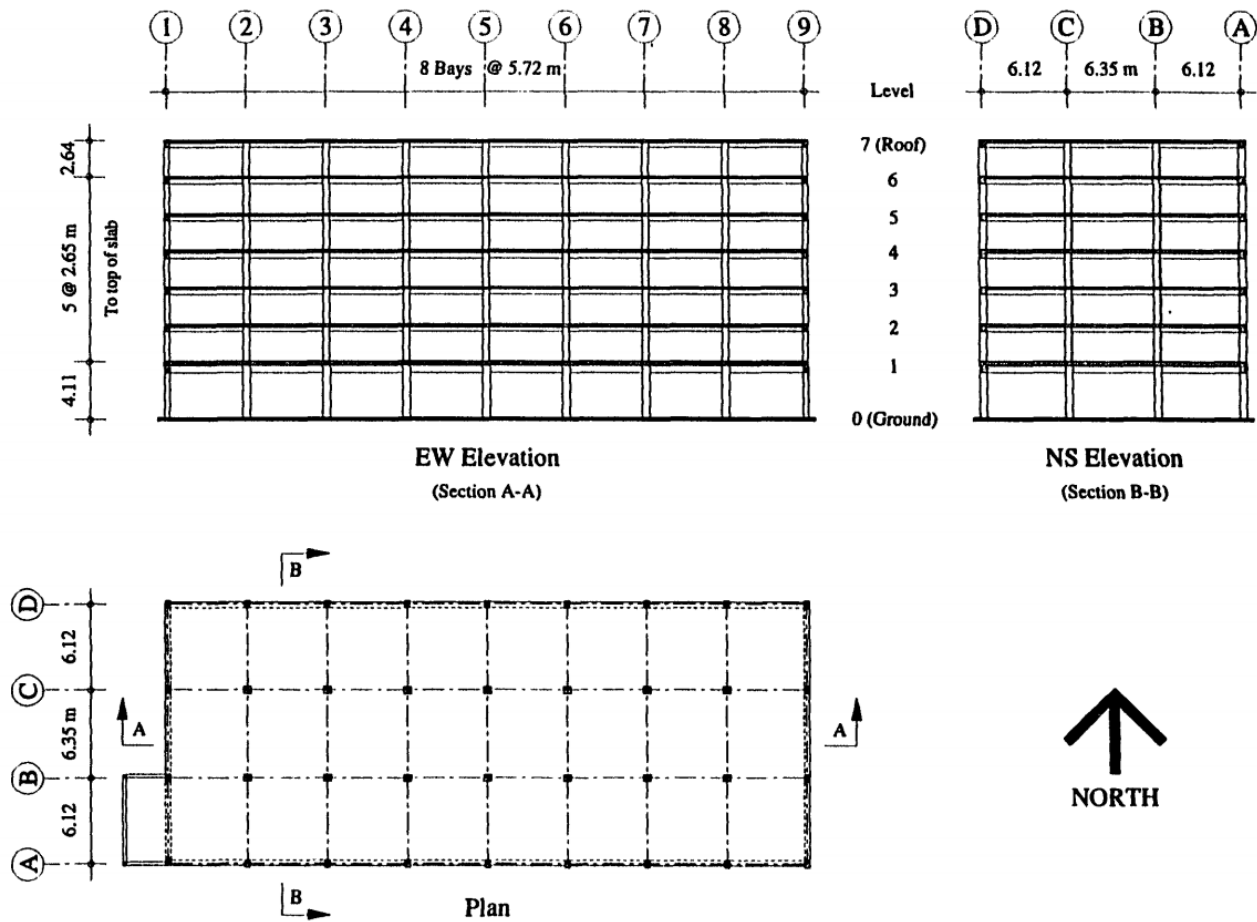


Figure 6-9: Plan and elevation views of Van Nuys Holiday Inn [from Lepage (1997), Fig. 5.1].

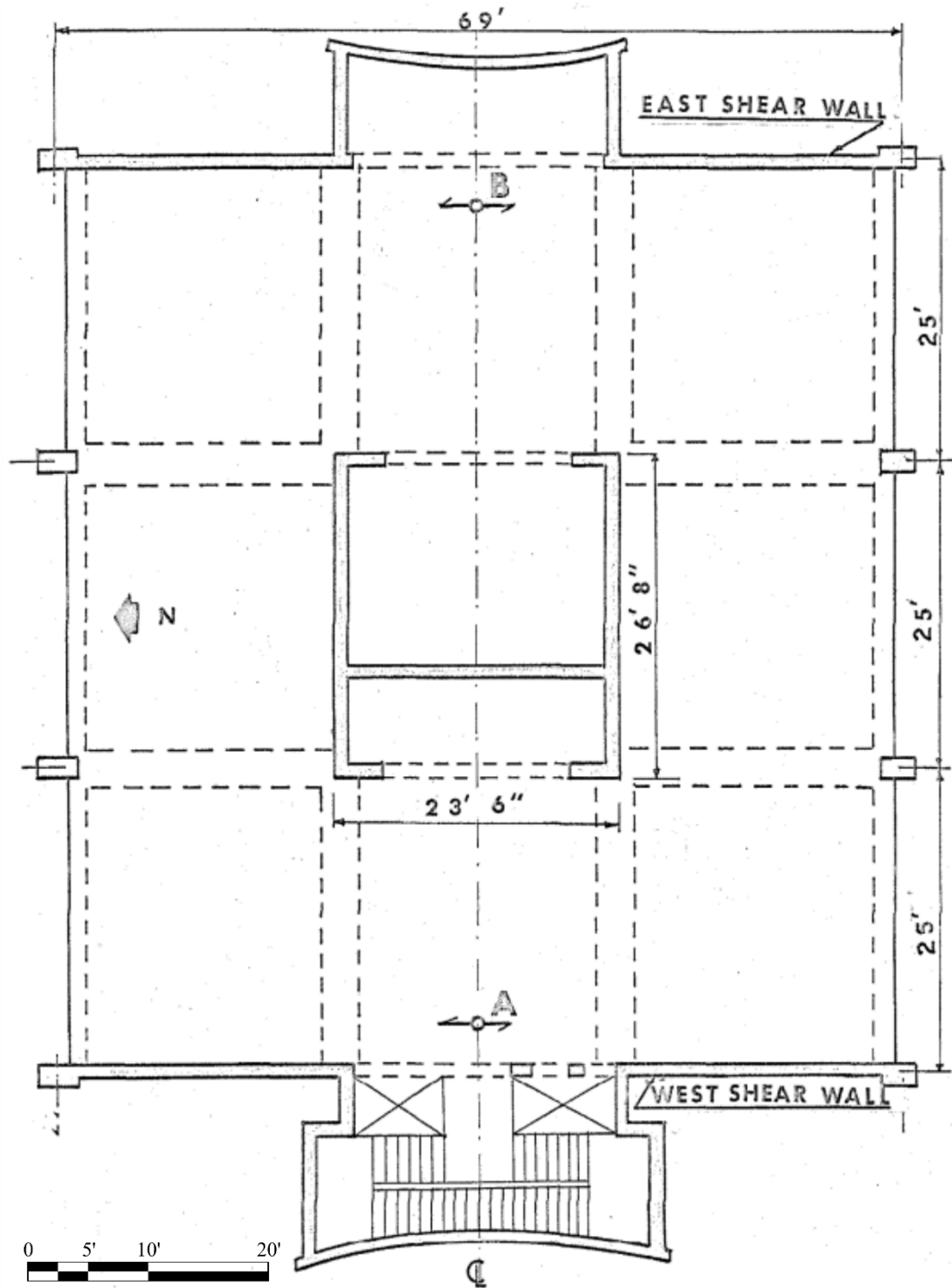


Figure 6-10: Floor plan of Millikan Library [from Kuroiwa (1967), Fig. 1.1].

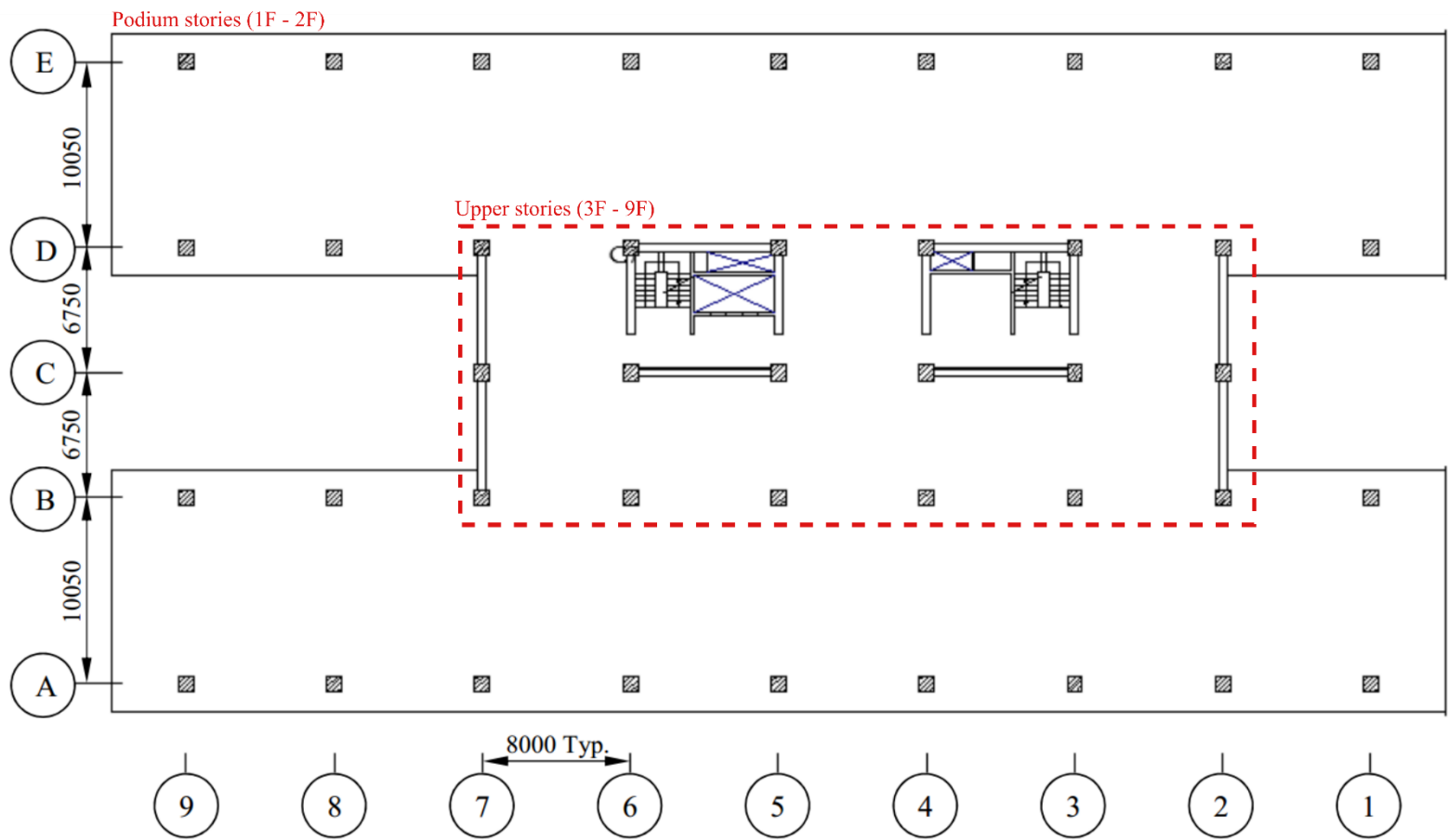


Figure 6-11: Floor plan of the Building of the Department of Civil Engineering (dimensions in mm) [from Wang et al. (2012), Fig. 2].

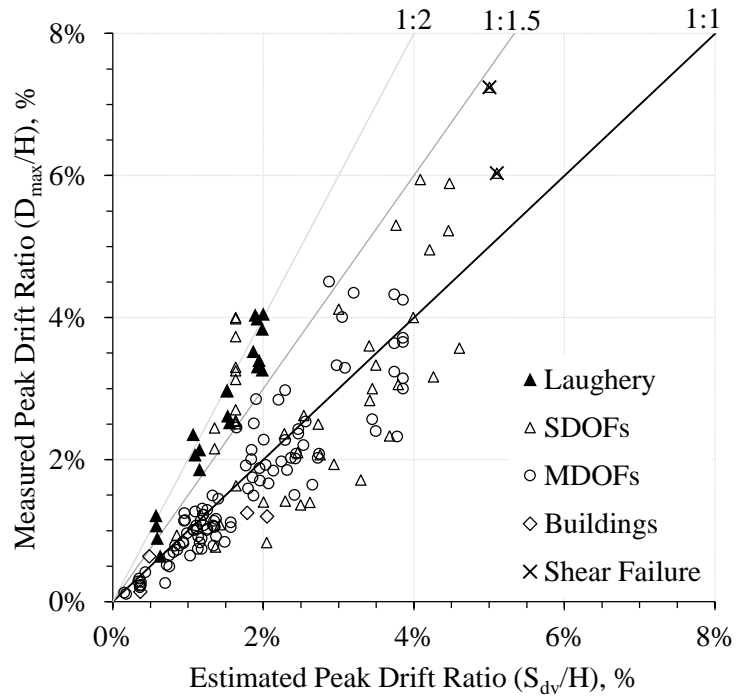


Figure 6-12: Measured versus estimated peak drift (D_{max} = measured peak roof drift, S_{dv} = estimated peak roof drift, H = height of structure).

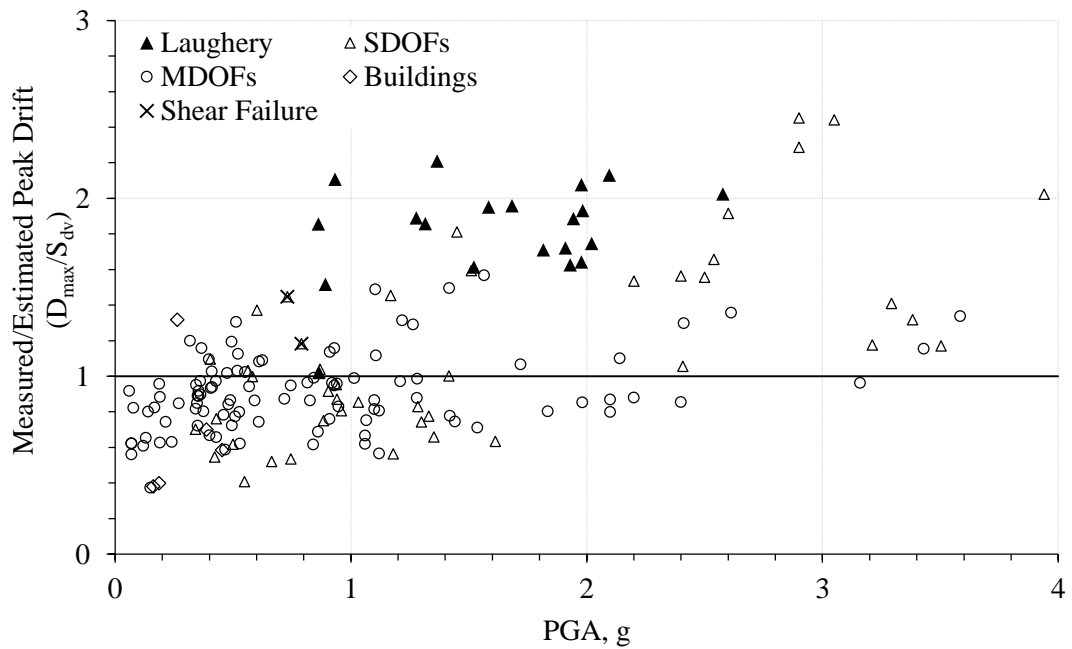


Figure 6-13: Ratio of measured-to-estimated peak drift versus PGA.

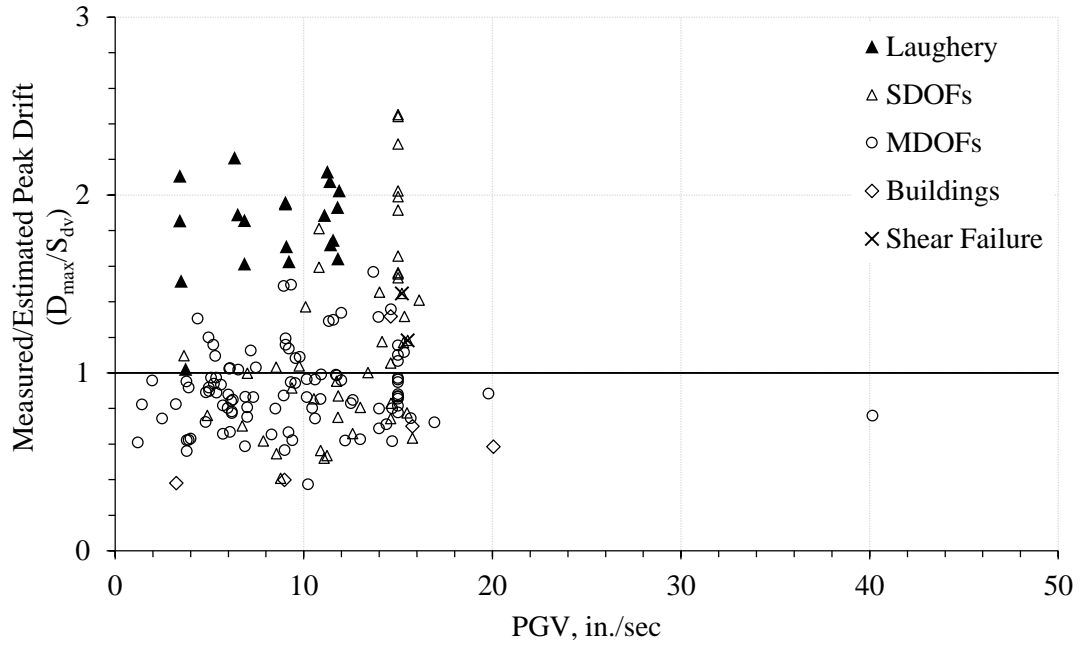


Figure 6-14: Ratio of measured-to-estimated peak drift versus PGV.

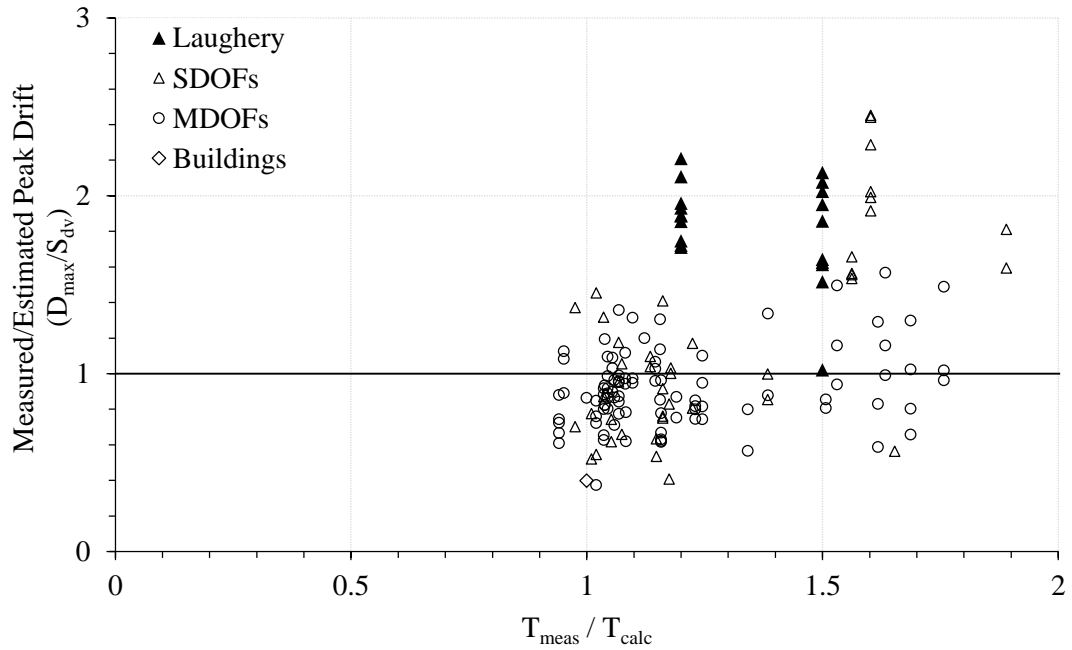


Figure 6-15: Ratio of measured-to-estimated peak drift versus ratio of measured-to-estimated period.

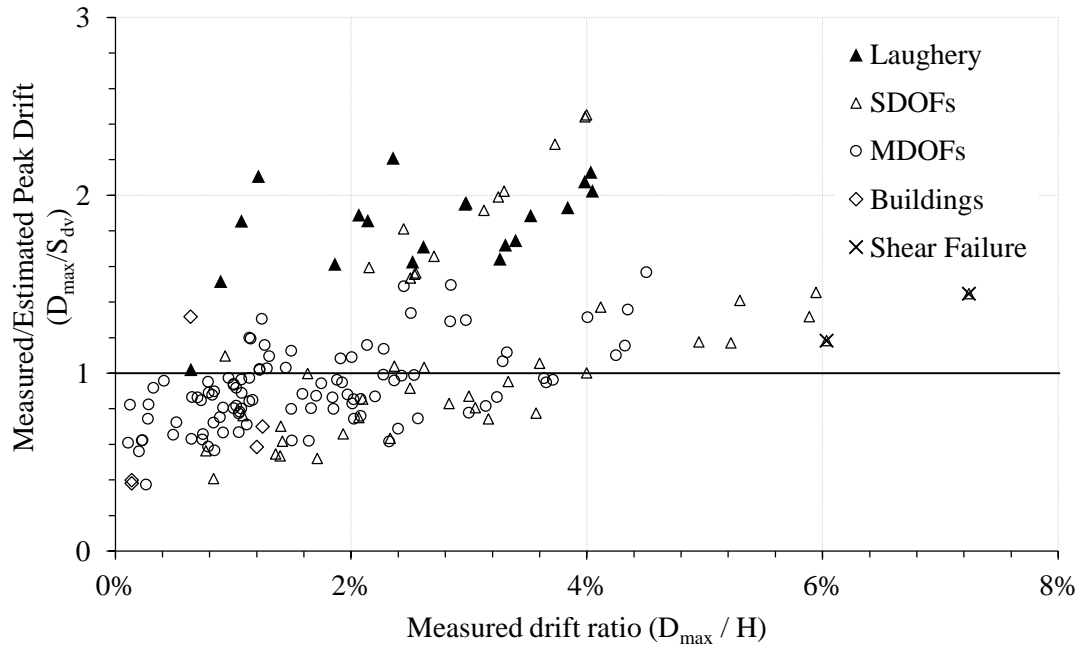


Figure 6-16: Ratio of measured-to-estimated peak drift versus measured peak drift ratio.

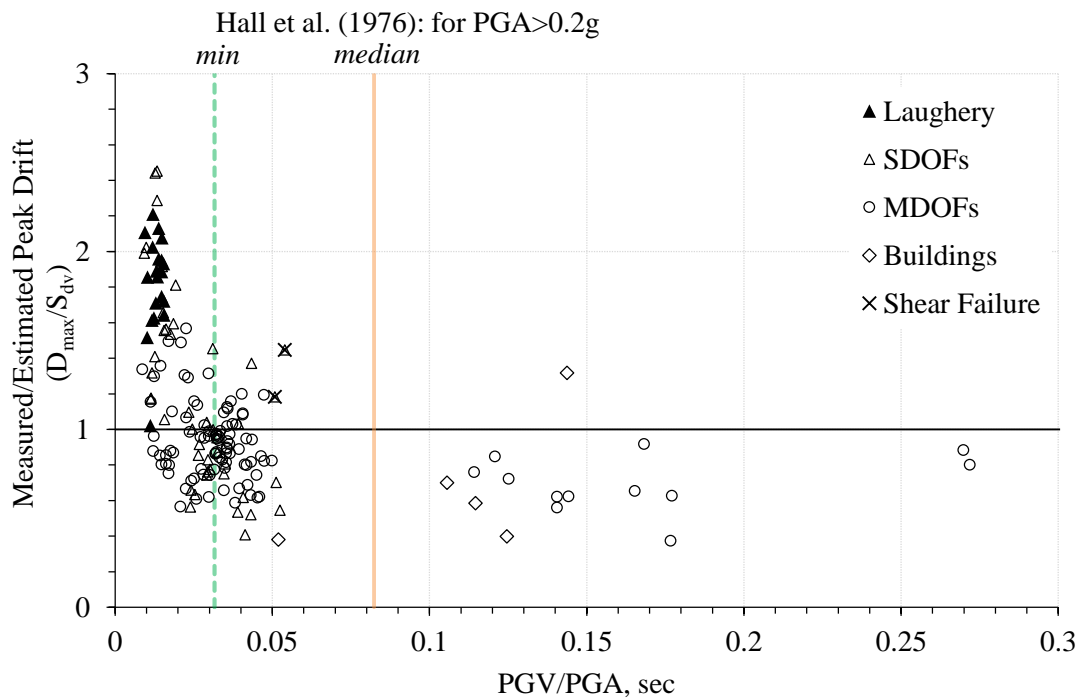


Figure 6-17: Ratio of measured-to-estimated peak drift versus PGV/PGA.

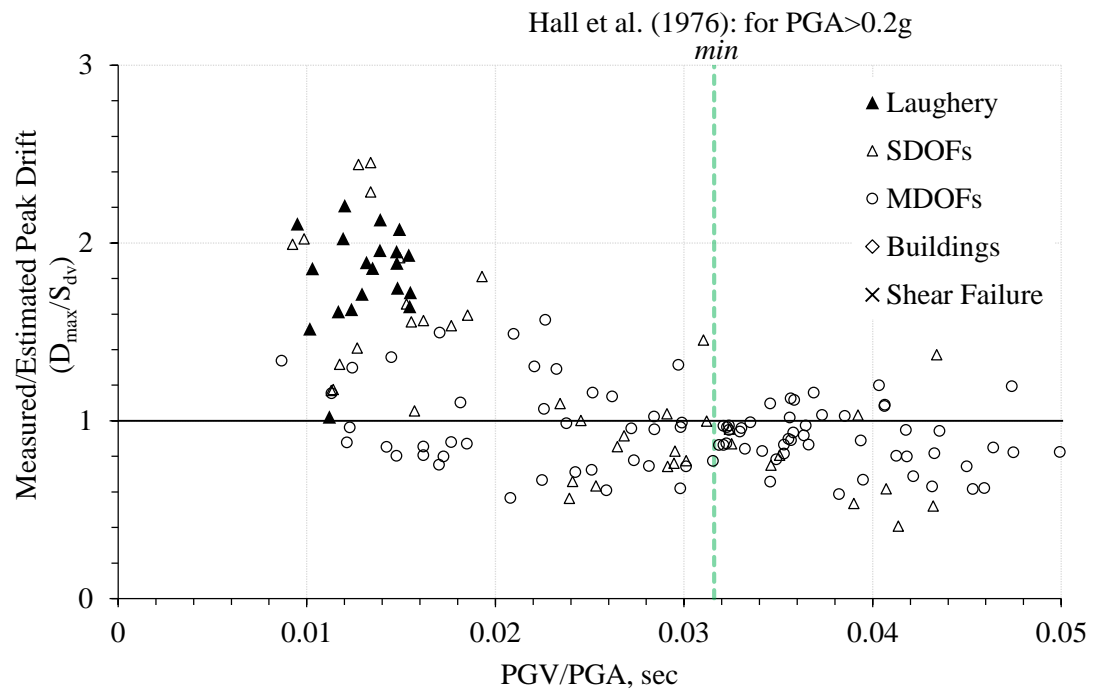


Figure 6-18: Close-up: ratio of measured-to-estimated peak drift versus PGV/PGA.

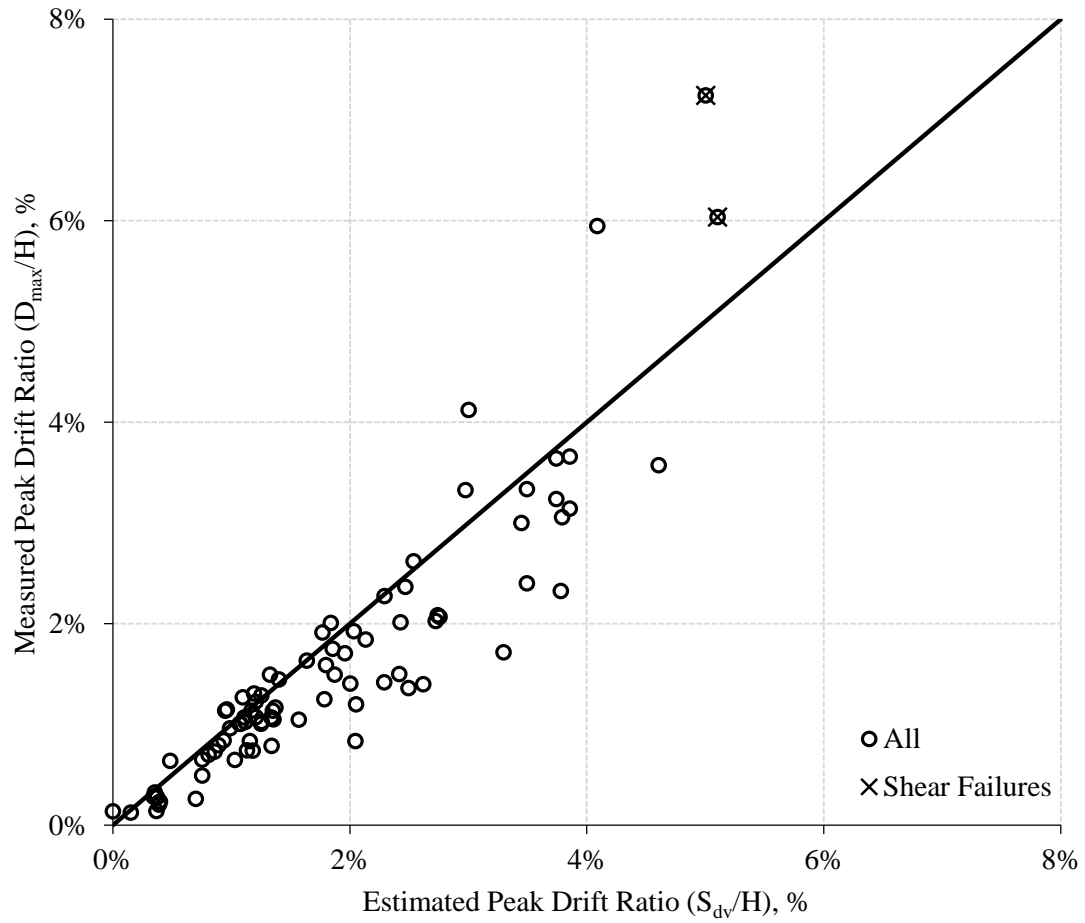


Figure 6-19: Measured versus estimated peak drift ratio for ground motions with PGV/PGA > 0.03 sec.

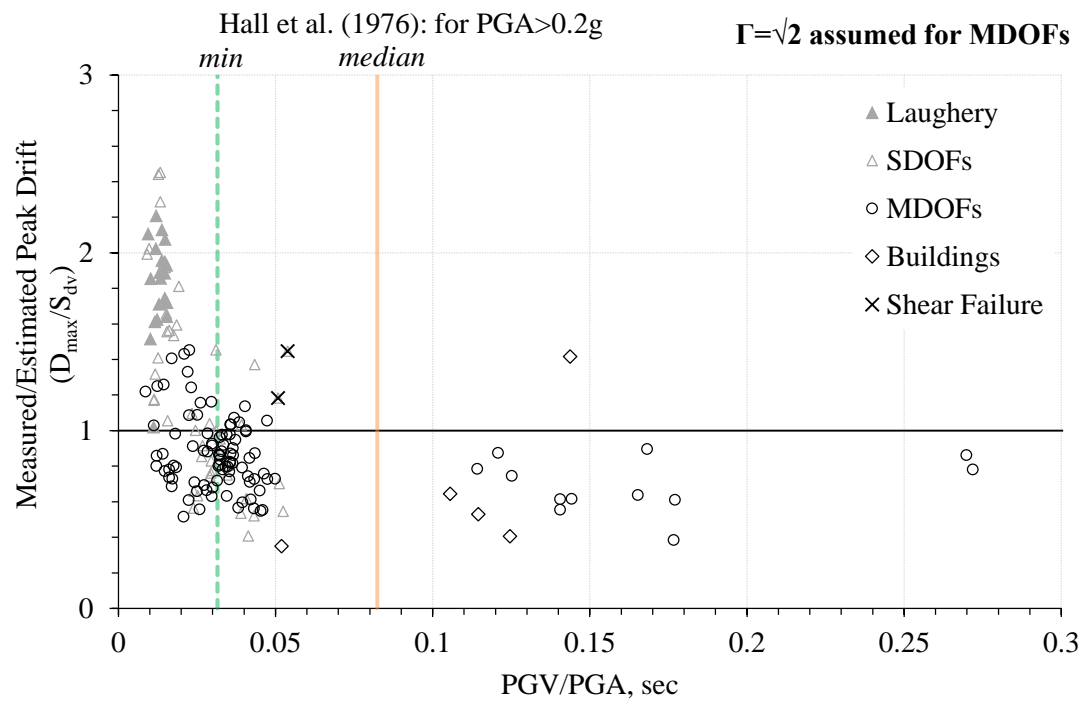


Figure 6-20: Ratio of measured-to-estimated peak drift versus PGV/PGA if $\Gamma = \sqrt{2}$ is assumed for MDOF systems.

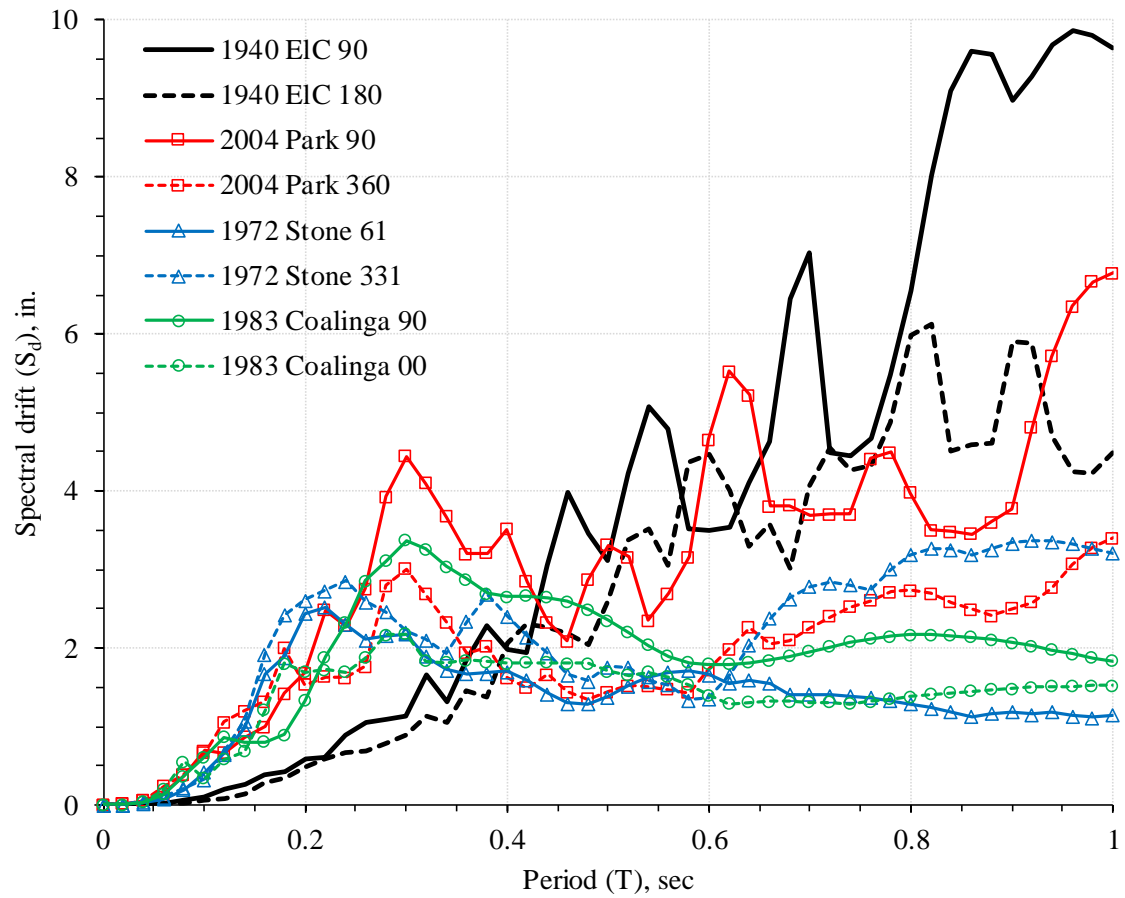


Figure 6-21: Displacement response spectra for records with low PGV/PGA compared with El Centro 1940.

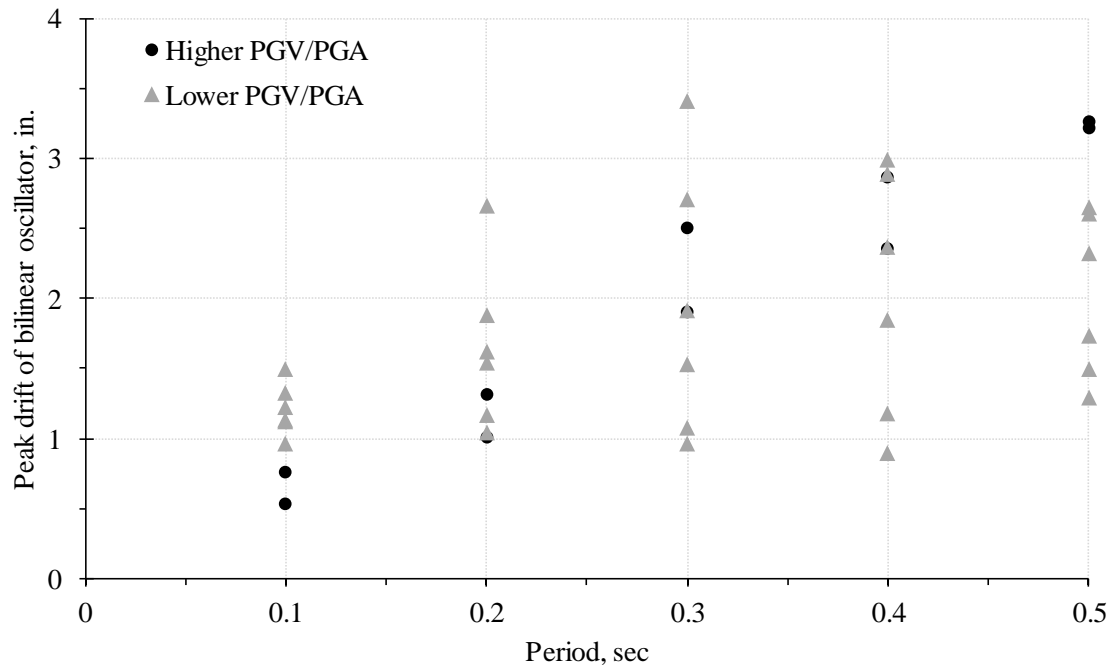


Figure 6-22: Peak drift response of bilinear oscillators with base shear coefficients of 0.2 and initial period indicated on x-axis.

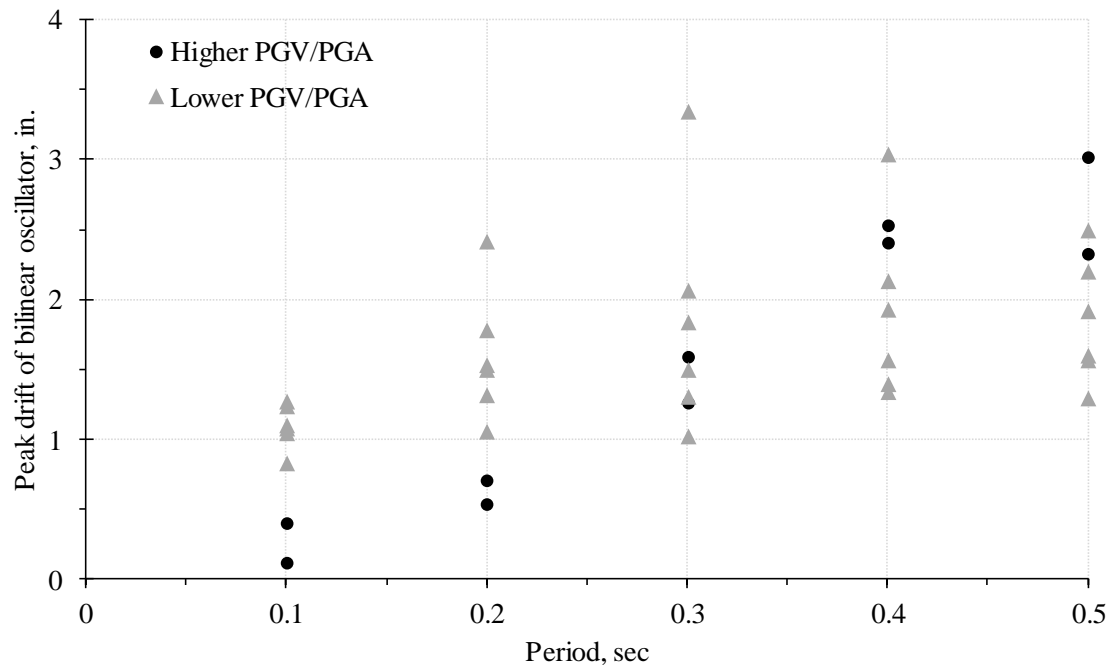


Figure 6-23: Peak drift response of bilinear oscillators with base shear coefficients of 0.3 and initial period indicated on x-axis.

REFERENCES

REFERENCES

1. Abrams, D.A. (1913), "Tests of Bond Between Concrete and Steel." *University of Illinois Bulletin*, Vol. 11, No. 15, 238 pp.
2. Abrams, D.P., and Sozen, M. (1979), "Experimental Study of Frame-Wall Interaction in Reinforced Concrete Structures Subjected to Strong Earthquake Motions." *Civil Engineering Studies, Structural Research Series, University of Illinois, Urbana, IL*, Vol. 460. Urbana, Illinois. 386 pp.
3. ACI Committee 318 (2014), "Building Code Requirements for Reinforced Concrete." *American Concrete Institute*, Farmington Hills, MI.
4. Ansley, M. H. (2002), "Investigation into the Structural Performance of MMFX Reinforcing." *Florida Department of Transportation*. 12 pp.
5. Aristizabal, J.D., and Sozen, M. (1976), "Behavior of Ten-Story Reinforced Concrete Walls Subjected to Earthquake Motions." *Civil Engineering Studies, Structural Research Series, University of Illinois, Urbana, IL*, Vol. 431. Urbana, Illinois. 378 pp.
6. ASCE/SEI 7 (2010), "Minimum Design Loads for Buildings and Other Structures." *American Society of Civil Engineers / Structural Engineering Institute*, Reston, VA.
7. Bah, T., et al. (2016). Inkscape v0.91. Computer Software. <<https://inkscape.org>>
8. Biggs, J. (1964), "Introduction to Structural Dynamics." Mc-Graw Hill. 341 pp.
9. Blume, J.A., and Associates, Engineers. (1973), "Holiday Inn, 8244 Orion Avenue, Van Nuys," In *San Fernando, California Earthquake of February 9, 1971*. U.S. Department of Commerce, Washington, Vol. 1, Pt. A, pp. 359-394.
10. Bonacci, J. F. (1989), "Experiments to Study Seismic Drift of Reinforced Concrete Structures." *Ph.D. Thesis*, University of Illinois at Urbana-Champaign. 395 pp.
11. Cecen, H. (1979), "Response of Ten Story, Reinforced Concrete Model Frames to Simulated Earthquakes." *Ph.D. Thesis*, University of Illinois at Urbana-Champaign. 352 pp.
12. Chiou et al. (2008), "NGA project strong-motion database." *Earthquake Spectra*, Vol. 24, No. 1. pp. 23-44.
13. Computers and Structures, Inc. (2015). SAP2000 Ultimate v17.1.1, build 1099. Computer Software. <<http://www.csiamerica.com>>

14. Dodd, L.L., and Cooke, N. (2000), "Capacity of Circular Bridge Columns Subjected to Base Excitation." *ACI Structural Journal*, Vol. 97, No. 2, pp. 297-308.
15. Eberhard, M., and Sozen, M. (1989), "Experiments and Analyses to Study the Seismic Response of Reinforced Concrete Frame-Wall Structures with Yielding Columns." *Civil Engineering Studies, Structural Research Series, University of Illinois, Urbana, IL*, Vol. 548. Urbana, Illinois. 424 pp.
16. Elwood, K., and Moehle, J. (2003), "Shake Table Tests and Analytical Studies on the Gravity Load Collapse of Reinforced Concrete Frames." *Pacific Earthquake Engineering Research Center Report No. 2003/01*. 364 pp.
17. Ghannoum, W. M., and Moehle, J. P. (2012), "Shake-Table Tests of a Concrete Frame Sustaining Column Axial Failures." *ACI Structural Journal*, Vol. 109, No. 3, pp. 393-402.
18. Gulkan, P., and Sozen, M. (1971), "Response and Energy Dissipation of Reinforced Concrete Frames Subjected to Strong Base Motions." *Civil Engineering Studies, Structural Research Series, University of Illinois, Urbana, IL*, Vol. 377. Urbana, Illinois. 288 pp.
19. Gulkan, P., and Sozen, M. (1974), "Inelastic Responses of Reinforced Concrete Structures to Earthquake Motions." *ACI Journal*, Vol. 71, No. 12, pp. 604-610.
20. Hall, W.J., Mohraz, B., and Newmark, N.M. (1976), "Statistical Studies of Vertical and Horizontal Earthquake Spectra." Report Prepared for the U.S. Nuclear Regulatory Commission. 128 pp.
21. Healey, T.J., and Sozen, M. (1978), "Experimental Study of the Dynamic Response of a Ten-Story Reinforced Concrete Frame with a Tall First Story." *Civil Engineering Studies, Structural Research Series, University of Illinois, Urbana, IL*, Vol. 450. Urbana, Illinois. 120 pp.288
22. Hognestad, E. (1951), "A Study of Combined Bending and Axial Load in Reinforced Concrete Members." *University of Illinois Engineering Experiment Station Bulletin*. No. 399. 128 pp.
23. Hognestad, E. (1962), "High Strength Bars as Concrete Reinforcement, Part 2. Control of Flexural Cracking." *Portland Cement Association Research and Development Laboratories*, Vol. 4, No.1, pp. 46-63.
24. Iemura, H., and Jennings, P.C. (1973), "Hysteretic Response of a Nine-Story Reinforced Concrete Building During the San Fernando Earthquake." *Earthquake Engineering Research Laboratory*. Report No. EERL 73-07. 55 pp.
25. Jeong, S-H., Lee, K-H., Jang, W-S. (2016), "PRISM for Earthquake Engineering." Computer Software. Department of Architectural Engineering, INHA University.
26. Kenai, S., and Bahar, R. (2003), "Evaluation and repair of Algiers new airport building." *Cement and Concrete Composites*, Vol. 25, No. 6, pp.633-641.

27. Kuroiwa, J.H. (1967), "Vibration Tests of a Multistory Building." *Thesis*, California Institute of Technology. 113 pp.
28. Lepage, A. (1997), "A Method for Drift-Control in Earthquake-Resistant Design of RC Building Structures." *Ph.D. Thesis*, University of Illinois at Urbana-Champaign. 251 pp.
29. Lopez, R.R., and Sozen, M. (1988), "A Guide to Data Preparation for LARZWD-1.0 and LARZWS-1.0 Computer Programs for Nonlinear Analysis of Planar Reinforced Concrete Structures Incorporating Frame and Walls." University of Illinois at Urbana-Champaign. 40 pp.
30. Lybas, J.M., and Sozen, M. (1977), "Effect of Beam Strength and Stiffness on Dynamic Behavior of Reinforced Concrete Coupled Walls." *Civil Engineering Studies, Structural Research Series, University of Illinois, Urbana, IL*, Vol. 444. Urbana, Illinois. 569 pp.
31. Matamoros, A.B. (1999), "Study of Drift Limits for High-strength Concrete Columns." *Ph.D. Thesis*. University of Illinois at Urbana-Champaign. 435 pp.
32. Menegotto, M., and Pinto P.E. (1973), "Method of Analysis for Cyclically Loaded Reinforced Concrete Plane Frames Including Changes in Geometry and Non-elastic Behavior of Elements under Combined Normal Force and Bending." *Preliminary Report, International Association for Bridge and Structural Engineering Symposium, Lisbon, Portugal, IABSE Reports, Vol. 13*, pp. 15-22.
33. Mayes, R. (1995), "Interstory Drift Design and Damage Control Issues." *The Structural Design of Tall Buildings*, Vol. 4, pp.15-25.
34. Moehle, J.P., and Sozen, M. (1978), "Earthquake-Simulation Tests of a Ten-Story Reinforced Concrete Frame with a Discontinued First-Level Beam." *Civil Engineering Studies, Structural Research Series, University of Illinois, Urbana, IL*, Vol. 451. 162 pp.
35. Moehle, J.P., and Sozen, M. (1980), "Experiments to Study Earthquake Response of R/C Structures with Stiffness Interruptions." *Civil Engineering Studies, Structural Research Series, University of Illinois, Urbana, IL*, Vol. 482. 421 pp.
36. Morrison, D., and Sozen, M. (1987), "Response of Reinforced Concrete Plate-Column Connections to Dynamic and Static Horizontal Loads." *Civil Engineering Studies, Structural Research Series, University of Illinois, Urbana, IL*, Vol. 490. 249 pp.
37. Newmark, N. (1973), "A Study of Vertical and Horizontal Earthquake Spectra." Report Prepared for the U.S. Atomic Energy Commission. 151 pp.
38. Newmark, N., and Hall, W. (1982), "Earthquake Spectra and Design." Earthquake Engineering Research Institute Monograph. 103 pp.
39. NIED (2016). ASEBI: Archives of Shaking Table Experimentation Database and Information. National Research Institute for Earthquake Science and Disaster Resilience. < http://www.bosai.go.jp/hyogo/asebi/dataopen_1.html>

40. Northern Digital, Inc. (2011), "OPTOTRAK PROseries System User Guide." *User Manual*, Revision 9.
41. Okamoto, M., Sato, T., Tanimura, Y., and Kuroiwa, T. (2003), "Deformation Performance of RC Columns using High-Strength Materials." *Quarterly Report of RTRI*, Vol. 44, No. 4, pp.136–141.
42. Otani, S., and Sozen, M. (1972), "Behavior of Multistory Reinforced Concrete Frames During Earthquakes." *Civil Engineering Studies, Structural Research Series, University of Illinois, Urbana, IL*, Vol. 392. Urbana, Illinois. 551 pp.
43. Ou, Y., and Kurniawan, D.P. (2015), "Shear Behavior of Reinforced Concrete Columns with High-Strength Steel and Concrete." *ACI Structural Journal*, Vol. 112, No. 1, pp. 35–46.
44. Ousalem, H., Takatsu, H., Ishikawa, Y., and Kimura, H. (2009), "Use of High-Strength Bars for the Seismic Performance of High-Strength Concrete Columns." *Journal of Advanced Concrete Technology*, Vol. 7, No. 1, pp. 123-134.
45. Panagiotou, M., Restrepo, J., and Conte, J. (2007), "Shake Table Test of a 7-Story Full Scale Reinforced Concrete Structural Wall Building Slice. Phase I: Rectangular Wall Section." *Structural Systems Research Project Report*. No. SSRP-07-07. 49 pp.
46. Pfund, S.J. (2012), "Cyclic Response of Concrete Beams Reinforced with ASTM A1035 Grade-120 Steel Bars." *M.S. Thesis*. The Pennsylvania State University. 202 pp.
47. Pujol, S. (2001). FLECHA. Macro-enabled spreadsheet for developing moment-curvature diagrams. <<https://nees.org/resources/flecha>>
48. Rautenberg, J. (2011), "Drift Capacity of Concrete Columns Reinforced with High-Strength Steel." *Ph.D. Thesis*, Purdue University. 289 pp.
49. Restrepo, J. I., Seible, F., Stephan, B., and Schoettler, M. J. (2006), "Seismic Testing of Bridge Columns Incorporating High-Performance Materials." *ACI Structural Journal*, Vol. 103, No. 4, pp. 496–504.
50. Risser, R., and Hoffman, M. (2011), "Reinforcing Congestion," <<http://www.concreteconstruction.net/reinforced-concrete/reinforcing-congestion.aspx>>, *Concrete Construction Magazine*, January 2011.
51. Saiidi, M. and Sozen, M. (1979), "User's Manual for the LARZ Family: Computer Programs for Nonlinear Seismic Analysis of Reinforced Concrete Planar Structures." *Civil Engineering Studies, Structural Research Series, University of Illinois, Urbana, IL*, Vol. 466. Urbana, Illinois. 56 pp.
52. Schultz, A.E. (1985), "An Experimental and Analytical Study of the Earthquake Response of R/C Frames with Yielding Columns." *Ph.D. Thesis*, University of Illinois at Urbana-Champaign. 574 pp.

53. Schultz, A.E. (1992), "Approximating Lateral Stiffness of Stories in Elastic Frames." *ASCE Journal of Structural Engineering*, Vol. 118, No. 1. pp. 243-263.
54. Seismosoft (2016). Seismosignal v5.1.2. Computer Software.
< <http://www.seismosoft.com/seismosignal>>
55. Shahrooz, B.M., and Moehle, J.P. (1987), "Experimental Study of Seismic Response of RC Setback Buildings." *Earthquake Engineering Research Center Report*. No. EERC-87/16. 347 pp.
56. Shahrooz, B.M., and Moehle, J.P. (2015), "Experimental Study of Seismic Response of Reinforced Concrete Setback Buildings" DataHub dataset.
<<https://datacenterhub.org/resources/276>>
57. Shibata, A., and Sozen, M. (1974), "The Substitute-Structure Method for Earthquake-Resistant Design of Reinforced Concrete Frames." *Civil Engineering Studies, Structural Research Series, University of Illinois, Urbana, IL*, Vol. 412. Urbana, Illinois. 34 pp.
58. Shiga, T., Shibata, A., Shibuya, J., and Takahashi, J. (1981), "Observations of Strong Earthquake Motions and Nonlinear Response Analysis of the Building of Architectural and Civil Engineering Department, Tohoku University." *Transactions of the Architectural Institute of Japan*. No. 301. pp. 119-129. (in Japanese).
59. Shimazaki, K. and Sozen, M. (1984) "Seismic Drift of Reinforced Concrete Structures." *Special Research Paper, Technical Report, Hazama-Gumi, Tokyo*, pp.145–165.
60. Sozen, M., Otani, S., Gulkan, P., Nielsen, N. (1969). "The University of Illinois Earthquake Simulator." *Proceedings, Fourth World Conference on Earthquake Engineering, Santiago, Chile*, Vol. 3, pp.139–150.
61. Sozen, M. (1980), "Review of Earthquake Response of R.C. Buildings with a View to Drift Control." State-of-the-art in earthquake engineering. *State-of-the-Art Panel Reports Prepared for the Occasion of the Seventh World Conference on Earthquake Engineering, September 8-13, 1980, Istanbul, Turkey*.
62. Sozen, M. (2003), "The Velocity of Displacement." *Seismic Assessment and Rehabilitation of Existing Buildings*, NATO Science Series Vol. 29, pp.11–28.
63. Sozen, M., Schultz, A., Bonacci, J., Eberhard, M., Marquez, A.L.R., Cecen, H., Healey, T., Moehle, J.P., Wolfgram, C.E., Aristizabal, J.D., Abrams, D.P., and Wood, S. (2015), "Earthquake Simulation Tests." DataHub dataset.
<<https://datacenterhub.org/resources/378>>
64. Sugimoto, K., Yonezawa, K., Katsumata, H., and Fukuyama, H. (2016), "Shaking Table Test of Quarter Scale 20 Story RC Moment Frame Building Subjected to Long Period Ground Motions." *Journal of Disaster Research*, Vol. 11, No. 1. pp. 97-105.
65. Takeda, T., Sozen, M. A., and Nielsen, N. N. (1970), "Reinforced Concrete Response to Simulated Earthquakes." *Journal of the Structural Division: Proceedings of the American Society of Civil Engineers*, December, pp.2557–2573.

66. Tavallali, H. (2011), "Cyclic Response of Concrete Beams Reinforced with Ultrahigh Strength Steel." *Ph.D. Thesis*, The Pennsylvania State University. 329 pp.
67. Tretiakova, K. (2012), "Cyclic Response of Concrete Columns Reinforced with SAS 670 Grade-97 Steel Bars." *M.S. Thesis*, The Pennsylvania State University. 165 pp.
68. Van der Laan, J. and Huyser, K. (2015). DataThief III, v1.7. Computer Software. <<http://www.datathief.org>>
69. Wang, Y., Pujol, S., Al-Washali, H., Suzuki, K., Maeda, M., Takahashi, S., and Ichinose, T. (2012), "On the Seismic Response of the Building of the Department of Civil Engineering and Architecture at Tohoku University." *Network for Earthquake Engineering Simulation*, Project No. 1122 Summary Report. 40 pp. <<https://nees.org/warehouse/project/1122>>
70. Wang, Y., and Pujol, S. (2014), "The Capacity Spectrum Method: Evaluation Against the Measured Response of a Nine-Story Structure." *Proceedings, Tenth U.S. National Conference on Earthquake Engineering, Anchorage, Alaska*. 11 pp.
71. Wolfgram, C.E. (1984), "Experimental Modelling and Analysis of Three One-Tenth Scale Reinforced Concrete Frame-Wall Structures." *Civil Engineering Studies, Structural Research Series, University of Illinois, Urbana, IL*, Vol. 513. Urbana, Illinois. 337 pp.
72. Wood, S. (1985), "Experiments to Study the Earthquake Response of Reinforced Concrete Frames with Setbacks." *Civil Engineering Studies, Structural Research Series, University of Illinois, Urbana, IL*, Vol. 544. Urbana, Illinois. 390 pp.
73. Yotakhong, P. (2003), "Flexural Performance of MMFX Reinforcing Rebars in Concrete Structures." *Ph.D. Thesis*, North Carolina State University, 162 pp.

APPENDICES

APPENDICES

These appendices contain additional details of the experimental investigation and dataset. It comprises the following sections:

A1: Materials

A2: Pullout Tests

A3: Test Structures

A4: Test Setup

A5: Control and Instrumentation

A6: Ground Motion Selection and Modification

A7: Test Notes

A8: Dataset Details

A9: Suggestions for Future Tests

The data from this work were uploaded to DataHub and are available at the following link:

<https://datacenterhub.org/resources/14094>

A1. MATERIALS

This section describes the properties of the materials used in the test specimens and the test methods used to obtain these properties.

A1.1. Grout Mix

The specimens were cast using grout with a maximum aggregate size of 3/8 in. All specimens were cast from the same batch on 2014-August-19. The mix proportions of the as-delivered grout are listed in Table A1-1. The sand was INDOT #23 (INDOT, 2014), with gradation requirements shown in Table A1-2.

Specimens, cylinders, and rupture beams were cured for 60 days under moist burlap covered by plastic. During this time period, cylinders were tested periodically to monitor concrete compressive strength. These tests were conducted in accordance with ASTM C39 (2012). Results from these tests are listed in Table A1-3 and are plotted in Figure A1-1. After 60 days, the plastic was removed and the burlap was allowed to dry gradually before being removed.

The specimens were tested between July and December 2015. Material properties were measured throughout the test program. Specimens were tested in the following order: H1, C1, H2, C2. On the first day of testing for each frame, concrete compressive strength and tensile strength were measured in accordance with ASTM C39 (2012) and ASTM C496 (2012). On the first and last testing days in the program (i.e. for frames H1 and C2), rupture modulus and modulus of elasticity were measured also (in accordance with ASTM C78 (2010) and ASTM C469 (2010)). All measured properties of the grout from test days are summarized in Table A1-4.

A1.2. Longitudinal Reinforcement

Three 36-in. long samples were selected at random from among the Grade 60, 3/8-in. deformed reinforcing bars used in the specimens. Four samples were selected from among the 1/4-in. high-strength steel bars. These samples were marked at 6 in., 14 in., 22 in., and 30 in. from one end and tested to failure in a tension testing machine. Over the middle 8-in. length of each sample, an extensometer with a gage length of 8 in. was used to measure strain (Epsilon Technology, model 3543-0800-200T-ST). The samples were tested in a Baldwin 120-kip universal testing machine with an Instron data acquisition system (Figure A1-2). After each test ended, the segment in which fracture occurred was measured to determine ultimate strain. These results are summarized in Table A1-5. Stress-strain diagrams for each sample are provided in Figure 3-3 (conventional steel) and Figure 3-4 (high-strength steel).

Data from the tension tests was used to generate representative steel profiles for the reinforcement. Representative steel models were created using the Menegotto-Pinto model (1973), as described in Chapter 3. This relationship is:

$$\varepsilon_s^* = \left| \frac{\varepsilon_s}{\varepsilon_{s0}} \right| \quad \text{Equation A1-1}$$

$$\sigma_s = \left(k_s \varepsilon_s^* + \frac{(1 - k_s) \varepsilon_s^*}{(1 + \varepsilon_s^{*R})^{1/R}} \right) \sigma_{s0} \quad \text{Equation A1-2}$$

where ε_s = steel strain

σ_s = steel stress

ε_s^* = normalized steel strain

ε_{s0} = steel strain at intersection of initial modulus line and tangent modulus at ultimate

σ_{s0} = steel stress at intersection of initial modulus line and tangent modulus at ultimate

$k_s = E_{s\infty} / E_s$, ratio of tangent modulus at ultimate to initial modulus

R = parameter defining the shape of the curve

The values of ϵ_{s0} , σ_{s0} , k_s , and R were adjusted until visual agreement was reached with the measured curves. The values used for each type of steel are specified in Table A1-6.

A1.3. Transverse Reinforcement

Transverse reinforcement in the specimens consisted of 3/16-in. 12L14 steel wire. Because of its small size, this wire could not be tested in the same machine as the longitudinal reinforcement. This was because (1) no grips were available for the Baldwin testing machine at that size, and (2) the expected strength of the bars was less than 2% of the capacity of the Baldwin. Instead, the wire was tested using a Sintech 30/D Tensile Tester (30-kip capacity). Three 20-in. pieces were selected at random from among the 3/16-in. wires. Over the middle 2-in. length of each coupon, an extensometer with a gage length of 2 in. was used to record strain (MTS model 634.25E-54). Slip of the extensometer on the smooth surfaces of the wire after the steel reached a yield plateau made it impossible to determine the 0.2% offset yield stress of the first two samples. But it was still possible to determine modulus of elasticity and strength from these tests.

A summary of the test results is presented in Table A1-7. The stress-strain curve from the third sample is presented in Figure A1-3. The yield stress from the third sample was 74 ksi. The average strength of all three samples was 82 ksi, and the average modulus of elasticity was 25,400 ksi. All samples fractured near the one of the grips. Based on measurements of this segment before and after testing, the average elongation at fracture was 8.4%. But because the wires were gripped at their ends over a length of approximately 2 in., it is possible that the percent elongation at failure could have been higher.

The wire was bent into rectangular hoops with 135 degree hooks at both ends. Figure A1-4 shows a photograph of the hoops in the lower beam. The hoops were corroded to improve bond with the concrete using the process described in Section A1.4.

A1.4. Corrosion of Reinforcement to Improve Bond

To provide surface roughness and improve bond with concrete, a corrosion process was used on both the high-strength steel bars and 12L14 steel wire. Reinforcement was first bent into the desired shape and cleaned using paint thinner. A 10% solution of hydrochloric acid (HCl) was then sprayed onto the reinforcement. The reinforcing bars were then wrapped in moist burlap and stored in a moist curing room. The acid and humid environment caused the surfaces of the bars to corrode. After 72 hours elapsed, the bars were removed and loose rust was removed using a sponge. The resulting bar surface had small indentations as a result of corrosion. A visual comparison of non-corroded and corroded 12L14 steel wire is shown in Figure A1-4. A visual comparison of non-corroded and corroded high-strength reinforcement is shown in Figure A1-5.

A2. PULLOUT TESTS

As discussed in the main body of this document, the longitudinal steel used in type H columns was expected to experience high bond stresses because of its high strength and small diameter. Combined with the lack of surface deformations, there were concerns that the bars might pull out of the beams before reaching their yield stress. For this reason, “pullout” specimens were built to test different anchorage configurations. Three types were tested. Two types were modeled after a portion of the top beam of the test frames:

- (1) Hook: with the bars terminating in 135-degree hooks with a total length of 22 in. as shown in Figure A2-1(a)³
- (2) Plate: with the ends of the bars threaded and anchored into plates [Figure A2-1(b)]

These specimens were cast with concrete similar to what was used in the test frames. They were 3 in. thick, 10 in. deep, and 19 in. wide. Single-leg transverse reinforcement was included in the hooked specimen to represent the transverse reinforcement in the beams of the frames. A hook with a 135 degree bend was selected over a 90 degree hook because a 135 degree hook was expected to perform better. Whereas the first two types were cast with concrete, the third type was not. The third specimen type comprised a single high-strength bar terminating in an assembly consisting of plates and prestressing anchor chucks [Figure A2-1(c) and Figure A2-2]. This was referred to as

³ Specimens with hooks at 90 degrees were also built, with tie-wire wrapping around the entire length of the hook to the adjacent longitudinal steel in the beam. But the labor involved in constructing specimens with this detail was deemed prohibitive, so this detail was not considered.

the “anchor” specimen. All specimens were tested in the Instron-Baldwin testing machine described in Section A1.2. Details of the test setups and results are described in the following sections.

A2.1. Hook Specimen

This specimen is illustrated in Figure A2-1(a). The specimen was positioned in the Instron-Baldwin universal testing machine as shown in Figure A2-3(a) and Figure A2-4. Angles were fastened to both sides of the concrete block portion of the specimen. These angles were then clamped to the lower crosshead of the testing machine. A steel plate was placed between the concrete block and the bottom surface of the lower crosshead to provide a larger bearing area. The high-strength steel rod extending from the specimens ran vertically through this plate, through the opening in the lower crosshead, and into grips in the upper crosshead. As the upper crosshead moved up during the test, it pulled the steel rod and the concrete block bore against the bottom surface of the lower crosshead.

Applied force and extension of the upper crosshead were recorded. Bar stress was calculated by dividing applied force by the area of the bar. In Figure A2-5, bar stress is plotted against crosshead extension. Superimposed on this figure are stress-extension curves measured from the coupon tests described in Section A1.2. In this figure, the initial extension without an increase in stress is the crosshead moving before the specimens are fully seated. More critical in this plot is stress. The hook specimen reached a peak stress of approximately 92 ksi, when the bar slipped and resistance dropped to just 5 ksi. As the test progressed, stress increased to approximately 50 ksi before dropping again to nearly 40 ksi. From this point onward, the stress increased gradually to a peak of nearly 65 ksi before decreasing gradually again. The test was ended at an extension of 1 in. These test results show that a 135 degree hook with a length of 22 in. was insufficient for the high-strength bars to develop their yield stress without slipping, let alone to develop their strength. It follows that a 90 degree hook would also have been insufficient.

A2.2. Plate Specimen

The setup and testing procedure of this specimen was the same as the hook specimen (described in the previous section). Bar stress from this test is plotted against elongation Figure A2-6 alongside stress-elongation curves from high-strength coupon tests. In contrast to the hook specimen, the bar in the plate specimen developed its yield stress (approximately 160 ksi). But before the bar could develop its strength, it fractured (at approximately 170 ksi). This fracture can be attributed to the reduction in cross-sectional area of the bars where threads were cut. This suggested that any method involving threading of the bars would introduce the risk of premature bar fracture at the threads as a result of reduced cross-section.

A2.3. Anchor Specimens

Neither of the previous configurations successfully anchored the bars. An anchorage system was needed that did not rely on a hook alone and that did not require the bars to be threaded. Because of similarities between the bars and prestressing steel (high strength, small diameter, and smooth surfaces), prestressing anchor chucks were considered next for anchoring the bars.

Instead of constructing forms and casting concrete, a simpler specimen was built. This system comprised steel plates, prestressing anchor chucks, and threaded rods with nuts [Figure A2-2]. An anchor chuck was placed on the bar in reversed direction (i.e. pulling on the bar would not engage the chuck), followed by an assembly consisting of two plates separated by a gap with threaded rods and nuts in between. After this, an anchor chuck was placed in the typical direction (i.e. pulling on the bar would engage the chuck). Turning the nuts on the threaded rods pushed the plates apart and seated the anchor chucks. After seating the anchor chucks, the gap between the plates was filled with Hydrostone® gypsum cement. The first two anchor specimens were built with reusable 1/4-in. anchor chucks donated by Prestress Supply, Inc. The third anchor specimen was built with

anchor chucks that were designed to be left in place after casting concrete. These anchor chucks – and the anchor chucks that were used in the specimens – were donated by Precision-Hayes International.

Because anchor specimens were different in shape than both hook and plate specimens, they were setup differently in the testing machine. Figure A2-3(b) shows a schematic of how the specimens were setup in the testing machine. Stress-elongation curves for the anchor specimens are shown in Figure A2-7. In all tests of this specimen type, the bars were able to develop their strength. For this reason, this method was selected for use in type H frames. Details showing the anchorage assemblies used in type H frames are shown in Figure 3-6.

A3. TEST STRUCTURES

A3.1. Overall Dimensions

Nominal dimensions of the structures are shown in Figure A3-1, and an isometric is shown in Figure A3-2. To connect the specimens to the other components of the test setup, the specimens were cast with holes in the top and bottom beams. These holes were created by casting PVC pipe into the sections. After the concrete hardened, the PVC pipes were removed.

To lift the specimens after cast and place them on the simulator platform, anchors were cast into the top beam. The anchors were HILTI HCI-WF cast-in anchors with a nominal internal diameter of 1/2 in. (13 thread).

After the concrete was cast, the specimens were measured. As-built dimensions are reported in Table A3-1. The accompanying schematic for these as-built dimensions is Figure A3-3.

A3.2. Reinforcing Details

Reinforcing details of the frames are shown in Figure A3-4 and are listed in Table A3-2. The top and bottom beams in both specimen types were longitudinally reinforced using conventional (Grade 60) 3/8 in. deformed bars. Column longitudinal reinforcement consisted of either conventional conventional 3/8 in. deformed bars (type C specimens), or 1/4 in. high-strength steel pencil rod (type H specimens), as discussed in the main body of this document.

In type C frames, column longitudinal reinforcement terminated in 90-degree hooks extending a total of 22 in. into the top and bottom beams (including hook). In type H frames, these hooks were

bent to approximately 105 degrees to accommodate the anchorage assemblies at the ends of the reinforcing bars. These anchorage assemblies were installed to preclude slip of column longitudinal bars out of the beams. Details of the anchorage assemblies are discussed in the next section.

The reinforcing cages were held in place using plastic rebar spacer wheels. Formwork and reinforcing cages were photographed alongside a tape measure before casting concrete to document spacing. Measurements also were taken of the hoop spacing in the columns before casting concrete and are reported in Table A3-3.

A3.3. Anchorage of High-Strength Steel

The anchorage assemblies comprised cast-in prestressing steel anchor chucks separated by plates (Figure 3-6). Two anchors were placed near the end of each rod in the beam opposite one another. The anchors were separated by two 3/4-in. thick steel plates, with threaded rods and nuts placed in between. The threaded rods and nuts were adjusted to provide an initial gap between the plates of 3/4 in. After making the assembly snug by pressing the anchors towards one another, the nuts were turned to push the plates apart (and towards the anchor chucks). Pushing the plates apart seated the anchor chucks. Had this seating process not been done, there could have been some slip of the bars as the anchor chucks were seated.

A4. TEST SETUP COMPONENTS

An isometric of the setup is shown in Figure A4-1. A west elevation with components called out is shown in Figure A4-2. The following is a list of major test components and the sections in which they are discussed:

- Reusable concrete mass: Section A4.1
- Specimen base connection components: Section A4.2
- Out-of-plane bracing: Section A4.3
- Instrumentation truss: Section A4.4

Before testing, drag tests were conducted to estimate the coefficient of friction between the simulator platform and concrete. These tests are described in Section A4.5.

A4.1. Reusable Concrete Mass

A reusable reinforced concrete mass was used in all tests. It was sized so that the effective mass of the system would be approximately 5,000 lb including connection components and the contribution of two-thirds of the weight of the columns. The mass was shaped like an extruded “n” as shown in Figure A4-3. It was cast with vertical holes in it to facilitate post-tensioning to each frame. These vertical holes were created by casting the mass with PVC pipes in it.

Reinforcing details of the mass are shown in Figure A4-3. Longitudinal reinforcement consisted of twelve 3/8-in. Grade-60 reinforcing bars. Twelve 3/8-in. Grade-60 transverse hoops were provided at uniform spacing on either side of the straddle point along its length connected by additional

transverse bars. Around each pipe opening, 3/16-in., 12L14 steel wire spirals were provided to improve concrete confinement.

The mass was placed atop each frame so that it straddled the top beam (Figure A4-2). Before lowering the mass into place, a thin layer of Hydrostone® gypsum cement was spread atop the beam. Two rods passed through the mass and the ends of the top beam. Both rods were tightened to a force of approximately 32 kips. At the center, four threaded rods passed through the mass and a steel plate (PL16x16x2.5), which straddled the underside of the top beam. Each of these rods was tightened to 12 kips. In total, the clamping force connecting the mass to each specimen was approximately 112 kips.

A4.2. Specimen Base Connection Components

The base connection of the specimen is described in Section 3.3.1. Twenty-one 1/2-in., high-strength steel threaded rods were used to fasten each specimen to the simulator platform (Figure 3-12). These rods threaded into helicoil inserts on the simulator platform. They reacted against steel angles (L5x5x3/4) that laid across the top surface of the bottom beam, transverse to the direction of motion. Each threaded rod was tightened to a force of approximately 10 kips using turn-of-the-nut method (calibrated beforehand using a load cell). After making them snug by hand, the nuts were tightened in 1/6-turn increments, starting with the center nut, then the west nut, then the east nut on a given angle. The order in which angles were tightened is illustrated in Figure A4-2. For additional lateral support, steel L8x8x7/8 angles were fastened to the sides of the lower beam as described in Section 3.3.1.

A4.3. Out-of-plane Bracing

A bracing system was constructed to limit out-of-plane movement of the system during testing. This system comprised steel W14x99 posts on the east and west sides of the setup, each with two steel channels “arms” extending towards the mass (Figure A4-4). At the ends of these extension arms, steel angles with PTFE bearing pads were installed. Each bearing pad bore against a stainless steel contact plate attached to the side of the reusable mass. The PTFE bearing pads and stainless steel contact plates were donated by Voss Engineering, Inc. out of Lincolnwood, Illinois.

Connections between the posts and extension arms, and between the extension arms and angles were bolted. The bolt holes were slotted to allow the extension-arm-and-bearing-pad assemblies to be adjusted). Before each test, the assembly was adjusted to provide a 1/8-in. gap between the PTFE bearing pads and the stainless steel plates. In the event of out-of-plane motion during testing, the PTFE pads bore against the stainless steel plates, limiting out-of-plane movement with little in-plane pullback force.

A4.4. Instrumentation Truss

An instrumentation truss was constructed to hold LVDTs. It was critical that the truss have a low period to minimize in-plane displacement response during testing. To achieve this objective, the truss was designed to have high stiffness and low mass.

An annotated photograph of the truss is shown in Figure A4-5. The main portion comprised three steel angles connected at their ends using A490 bolts in slip-critical connections. Transverse to the direction of motion, a channel was attached at the base to add out-of-plane resistance. Approximately 40 in. above the simulator platform, transverse to the direction of motion, a L3x3x3/8 angle was bolted to the truss. This angle had four assemblies installed along its length for connecting to an outrigger system comprised of 5/8 in. threaded rods. These assemblies

connected to the ends of four 5/8-in. diameter steel threaded rods. The threaded rods were connected at their other ends to four points on the simulator platform. This created a system of threaded rod outriggers for the instrumentation truss that added stiffness (both in- and out-of-plane) with little added mass. Before testing, outrigger threaded rods were tightened to increase the stiffness of the system.

As an extra precaution, optical targets were affixed to the instrumentation truss near its top and bottom to monitor movement of the truss during testing (Figure 3-16). This was to enable readings from LVDTs to be adjusted for movement of the truss during testing, if such movement were to occur. At times, these optical targets went outside the visible range of the Optotrak. Nevertheless, for all tests in which both targets were visible, the maximum relative movement of the targets never exceeded 0.01 in. Because of this, it was not necessary to adjust LVDT readings to account for movement of the truss.

The bodies of the LVDTs were held in place using rectangular HDPE (high-density polyethylene) mounts (Figure A4-6). These mounts were tightened around the LVDT body using 1/4-in. threaded rods with nuts. The cores of the LVDTs were threaded onto 4-40 brass threaded rods. These brass threaded rods threaded into metal clips that were epoxied to the concrete surfaces of the test frames.

A4.5. Friction Tests

Before the first test on an earthquake simulator, drag tests were conducted to estimate the static coefficient of friction between the simulator platform and concrete. A dynamometer (Chatillon Model 719-10, 10 lb range) and a concrete cylinder were used for these tests. The cylinder had a diameter of 6 in. and a height of 12 in., and was cast from the same mix as the specimens. A rope was tied around the cylinder at mid-height, and it was placed on the simulator platform. The dynamometer was hooked to the rope and pulled until the cylinder began to slide. At this point, the

force in the dynamometer was read. This process was repeated at various locations on the simulator platform. The cylinder was then weighed and the static coefficient of friction between the concrete and platform was calculated as the ratio of the pulling force in the dynamometer to the weight of the cylinder. Values obtained from this process are summarized in Table A4-1. For all tests, the dynamometer reached its maximum force (10 lb) before sliding initiated, meaning the static coefficient of friction between the platform and concrete was more than 0.25.

A5. CONTROL AND INSTRUMENTATION

A5.1. Control

The hydraulic actuator driving the simulator platform is displacement controlled. This actuator was controlled using a MTS FlexTest™ 60 controller (Series 793) with Station Manager v5.9A 6026 installed on the computer. MultiPurpose TestWare® was used to define a procedure to control the actuator. This procedure had two main parts: (1) a ramp to bring the table to zero displacement, (2) the ground motion displacement profile. The latter was formatted as a BLK file (ASCII text) with the following information in the header:

- “FileType= Block-Arbitrary” – tells MTS system the input format
- “Date= 21-Mar-2015” – the date when the file was created
- “Description= RoscoeE, 3x @ 100p, SpecMod” – user-assigned description
- “Channels= 1” – number of channels to be controlled
- “Channel(1)= Displacement” – channel number and type (i.e. force or displacement)
- “Max=1.2965 in” – maximum displacement command
- “Min=-1.2194 in” – minimum displacement command
- time=0.0033 Sec – time step
- Level1 – channel to be controlled
- in – units of command signal

After these header rows was the command displacement profile, with one value per row. This file has been uploaded to the dataset at DataHub.

A5.2. Instrumentation

Test structures were instrumented with linear variable differential transformers (LVDTs), accelerometers, an optical motion tracking system, and two or more cameras. A detailed instrumentation plan is shown in Figure A5-1. This plan shows the names and channel assignments for all sensors on the test setup. The prefix “Ch” signifies that the sensor was sampled by the main data acquisition system. The prefix “OT” signifies that the sensor was sampled by the optical tracking system. An overhead view of the setup is shown in Figure A5-2. This figure shows the positions of the accelerometers in more detail.

In addition to these digital sensors, dial gauges were installed on the laboratory floor between the simulator platform pedestal and the pedestal on which the actuator was mounted (Figure A5-3).⁴ This was to measure relative movement of the pedestals in the north-south direction. A camera recorded both dial gauges during testing. Review of the videos recorded by this camera showed that there was no movement of the base pedestals during testing.

A5.2.1. Primary Data Acquisition System

The main data acquisition system (DAQ) recorded signals from LVDTs, accelerometers, command displacement to the actuator, and feedback displacement from the actuator. It also sent signals to illuminate an LED that faced towards the northwest of the test setup. This LED was installed to facilitate syncing of data with videos. A breakdown of the sensors handled by the main DAQ, channel assignments, and locations is presented in Table A5-1.

⁴ These gauges were installed only after tests H1-25, H1-50, and H1-75 had been conducted.

National Instruments hardware was used for the main DAQ system. Hardware connectivity is summarized in Table A5-2. LVDT and accelerometers were not powered by National Instruments hardware. Instead, external systems were used to provide power to these sensors.

Labview 2010 was used to interface with the main DAQ hardware. Data were sampled at a rate of 1,000 Hz. Data were recorded as raw voltages and saved as TDMS files. This filetype was selected because it allowed the data to be sampled at a high rate with minimal demand on the DAQ PC. After testing, the files were converted to ASCII (text) for processing.

A5.2.1.1. LVDTs

Ten LVDTs were used on the test setup (Figure A5-1). At the base of each specimen, an LVDT was positioned to measure slip of the specimen. This LVDT had a range of 1 in. ($\pm 1/2$ in.). Along the height of the south face of the south column, seven LVDTs were placed. These LVDTs had ranges of 4 in. (± 2 in.). They were spaced starting at a height of 3 in. above the top of the bottom beam (15 in. above the simulator platform surface), and 6-in. thereafter. Two LVDTs measured the top displacement of the frames. The first had a range of 4 in. (± 2 in.). This LVDT was connected to the centerline of the south face of the top beam. Another LVDT with a range of 6 in. (± 3 in.) was connected to the mass adjacent to the first LVDT. This was to ensure drifts larger than 3 in. could be measured. All LVDTs were manufactured by Schaevitz Sensors, with serial numbers listed in Table A5-3. All LVDTs were powered externally using a custom-built power supply unit.

A5.2.1.2. Accelerometers

Four accelerometers were used on the test setup: two on the platform, one on top of the lower beam, and one on top of the mass above the north column (Figure A5-2). These accelerometers were held in place by mounts that were attached to the respective components using super glue.

All accelerometers were Piezotronics model 333B52, with model numbers listed in Table A5-3 [PCB Piezotronics (2013a)]. These accelerometers have a range of ± 5 g and a minimum measurable frequency of 0.5 Hz. The accelerometers were all powered by a PCB482A22 signal conditioner [PCB Piezotronics (2013b)].

A5.2.2. Optical Tracking System

An Optotrak PROseries optical tracking system was used for all tests [Northern Digital (2011)]. This system allowed the motion of the test setup and specimens to be tracked in three dimensions using targets affixed to the setup. The Optotrak system was positioned west of the test setup. The targets were sampled at a rate of 50 Hz.

An instrumentation plan showing target locations, channel numbers, and names is shown in Figure A5-1. Each column had 28 targets attached: two columns of fourteen rows. The naming convention for these targets was as follows: the first letter (capital N or S) indicated to which column the target was attached, the second letter (lower case n or s) indicated the column (there were two columns of targets per specimen column), the number indicated the row (from 1 to 14). For example, Ns14 was the the southmost target attached to the north column on row 14 (bottom row).

A5.2.3. Cameras

Each experiment was recorded using two or more cameras. Cameras to the northwest and west of the test setup recorded all tests (Figure 3-17). For all tests except H1-25, H1-50, and H1-75, a camera was situated between the actuator and simulator platform pedestals. This camera monitored the dial gauges that measured relative movement of the pedestals.

A6. GROUND MOTION SELECTION AND MODIFICATION

Before the test series, the simulator was run repeatedly to determine its behavior with different payloads and different ground motion profiles. It was run with no added weight, and with 2 kips, 4 kips, and 6 kips added. Different ground motion profiles also were run to find the ground motion that could be reproduced most consistently. These ground motions were downloaded from the PEER NGA Ground Motion Database [Chiou et al. (2008)] and the CESMD Strong-Motion Virtual Data Center [CESMD (2016)]. Dozens of records were considered, including “classic” records obtained from the 1940 El Centro earthquake, the 1952 Kern County (Taft) earthquake, and the 1971 San Fernando earthquake (all of which have been used in previous earthquake simulation tests). Before running a record on the earthquake simulator, the record was processed to determine:

- (1) To what extent the record could be compressed without exceeding the limits of the simulator (i.e. without exceeding the 2 g, 12 in./sec, and ± 2 in. ranges of the actuator)
- (2) The zero crossing rate (ZCR) of the record, defined as the average number of times the acceleration sign changes during the record (i.e. the number of reversals per second)
- (3) The “smoothness” and average slope of the displacement response spectrum in the period range of interest ($T = 0.1 - 0.4$ sec, from 1 to 4 times expected initial period based on gross cross-sectional properties)

The first item was to ensure that the motion could be reproduced without damaging the hydraulic actuator driving the simulator. The second item was observed to have an effect on the repeatability of the tests. As more ground motions were run on the simulator, records with lower ZCRs were found to have: (a) less high-frequency noise, (b) lower amplification of the linear displacement

response spectrum calculated from measured accelerations when compared to the target spectrum, and (c) improved repeatability. Repeatability was measured using the coefficient of variation of the displacement response spectra measured from repetitions of the same motion, as discussed in Section 4.2.2. The third item related to the shape of the displacement response spectrum. It was desirable to use a ground motion that would produce a response spectrum similar in appearance to an idealized spectrum [Newmark (1973)], with assumed regions of nearly constant acceleration, velocity, and displacement (Figure A6-1). As discussed in Section 3.4, spectra without prominent “peaks” and “valleys” were desirable.

The final record chosen for this investigation was the east-west component of the recording obtained at Sun Valley – Roscoe Boulevard during the 1994 Northridge earthquake. This record was chosen because (1) it fit within the limits of the simulator, (2) it had good repeatability compared to other ground motions considered, and (3) based on its displacement response spectrum, it was expected to produce peak drift ratios of up to 2% in the test specimens.⁵ Details of the selected record (its source, site characteristics, etc.) are presented in the next section.

A6.1. Details of Selected Record

The acceleration profile used in this study was based on the east-west component of the recording obtained at Sun Valley – Roscoe Boulevard during the 1994 Northridge earthquake. The record was downloaded from the PEER NGA Database [Chiou et al. (2008)], along with characteristics about the site and station. This station was located at the ground level of a 2-story building at 34.221°N, 118.421°W. The subsurface comprised Holocene medium alluvium with a coarse grain size. The shear wave velocity in the top 30 m of the subsurface (V_{s30}) was approximately 300 m/sec.

⁵ Before the test series, peak drift ratio in the specimens was estimated using Sozen’s (2003) expression, as given in Equation 6-1. The initial period was estimated to be 0.1 sec and a PGV of 11 in./sec was used.

A6.2. Modification of Selected Record

The record obtained from the PEER NGA Database had been pre-processed by the Pacific Earthquake Engineering Research Center (PEER) using a bandpass filter with a lowpass frequency of 30 Hz and a highpass frequency of 0.1 Hz. The original time step of the record was 0.01 sec. The original PGA, PGV, and PGD were 0.30 g, 8.7 in./sec, and 3.09 in. This corresponds to a PGV/PGA ratio of 0.074 sec. The record was compressed in time by a factor of three by reducing the time step to 0.0033 sec, and was then scaled by multiplying by a factor 3.9. The resulting record had a PGA, PGV, and PGD of 1.18 g, 11.2 in./sec, and 1.31 in. Compressing and scaling the record reduced the PGV/PGA ratio to 0.025 sec.

Displacement response spectra for the original and scaled records are shown in Figure A6-2 (up to a period of 6 sec). This figure shows how scaling and compressing a record shifted the shape of the displacement response spectrum to a lower period range. In Figure A6-3, a close-up of this spectra is shown (up to $T = 1$ sec). In the period range of interest ($T = 0.1 - 0.4$ sec), a peak can be seen at $T = 0.22$ sec. As discussed in the main body of this document, it was desirable to use a record that produced a displacement response spectrum without prominent peaks (or valleys).

To reduce the prominence of peaks and valleys in the period range of interest, the acceleration record was modified by adjusting amplitudes in the Fourier domain (Figure 3-18). The frequency ranges and amplitudes used to adjust amplitudes in the Fourier domain are shown in Table A6-1. After making these adjustments, a final highpass filter of 0.5 Hz was applied to the record and it was baseline corrected using Seismosignal [Seismosoft (2016)]. The reason for this final filter was to remove frequency content that could not be measured by the accelerometers (which have a frequency range of 0.5 to 3000 Hz). The resulting acceleration profile was integrated twice to obtain a displacement profile with which to operate the simulator.

A7. TEST NOTES

Text files accompany the data from each shake table test. These files contain notes about the procedure of each test, conditions in the laboratory, whether sensors malfunctioned, and so forth.

This section contains additional notes from the test program.

A7.1. Frames C1 and H1: Initial Period

Frames C1 was subjected to hammer tests before the mass was connected to the top beam. This was to estimate its initial period (and stiffness) without added mass. The frame was placed upright on the strong floor of Bowen Laboratory. A layer of Hydrostone® gypsum cement was spread between the floor and bottom beam of the frame. Steel threaded rods were used to fasten the base of the specimen to the strong floor. Two accelerometers were installed on top of the top beam: one above each column. Like the hammer tests described in Section 3.6, the top beam of the specimen was struck in-plane repeatedly using a 4 lb dead-blow hammer. Period was estimated from the zero crossing rate of the measured acceleration response. The period estimated from these hammer tests was 0.034 sec. Using Equation 3-11 with a reduced effective mass (only the top girder and 2/3 of the columns), the estimated initial period based on gross cross-sections is 0.036 sec. This is within 6% of the period estimated from the hammer tests.

Like frame C1, hammer tests were conducted on frame H1 before the mass was installed. But whereas frame C1 was fastened to the strong floor of the laboratory for these tests, frame H1 was fastened to the earthquake simulator platform. Otherwise, hammer tests were conducted in the same manner as for frame C1. The period estimated from these hammer tests was 0.033 sec. This is

comparable to the period obtained from similar hammer tests of frame H1 (0.034 sec), and to the estimated initial period for the system with reduced mass (0.036 sec).

A7.2. Videos

In addition to videos recorded from the west and northwest of the setup, in several cases additional videos were captured during testing. A detailed listing of videos captured is presented in Table A7-1. In the sections below, the additional videos are described.

A7.2.1. Dial Gauge

Frame H1 was the first frame tested in this investigation. Some additions were made to the testing protocol based on experience from this test. One addition was the dial gauge and camera setup to measure whether there was relative movement of the actuator and simulator platform pedestals. For tests H1-25, H1-50, and H1-75, these dial gauges were not installed and there is no corresponding video. This setup was installed after test H1-75, and dial gauge videos are available from that test onward.

A7.2.2. GoPro

Video was captured of the bottom of the north column (east face) using a GoPro during tests H1-100 and H1-100(2). Before these tests, a speckled pattern was drawn in this region using permanent marker. This was to facilitate using the video later to measure strain. The GoPro was mounted to a steel angle immediately east of the bottom of the north column and recorded deformation of the joint during these tests. It was not necessary to process the videos for the current investigation, but they are uploaded along with the rest of the data.

A7.2.3. Drone

Towards the end of the investigation, an unmanned aerial drone became available for recording the tests. This drone was a DJI Phantom 3 Professional. It recorded the west side of the test setup. Like the GoPro videos, it was not necessary to process these videos for the current investigation. Nevertheless, they are uploaded along with the rest of the data.

A7.3. Sensor Malfunctions

During tests C1-25 and C1-50, the accelerometer on the bottom beam of frame C1 malfunctioned. As a result, measurements from this accelerometer were not included in analysis of tests C1-25 and C1-50. The accelerometer was replaced for subsequent tests, including the remaining three tests of frame C1 and all tests of frames C2 and H2.

A8. DATASET DETAILS

This section provides additional details about how T_i and Γ were calculated for structures for which these values were unavailable in reports.

A8.1. Rayleigh's Method

Rayleigh's method is a simple iterative method of analysis that can be used to estimate the period, modeshape, and modal participation factors of a structure [Biggs (1964), Ch. 3]. To estimate these values, the following parameters must be defined:

- Initial assumed modeshape of the structure: This is used as a starting point for other calculations. Iterations are performed until the modeshape converges.
- Mass of each story: This is needed along with modeshape to estimate story shear.
- Stiffness of each story: This is needed to estimate the deflection of each story given the calculated story shear.

The initial modeshape was assumed to be triangular, from 0 to 1 in $1/N$ increments, where N is the number of stories of the structure. The mass of each story was taken from corresponding documentation. Story stiffnesses were estimated using expressions from Schultz (1992). These expressions include flexibility of all the columns on a given story and the girders above and below that story. Gross cross sections were used for all calculations of moment of inertia. Column heights were taken as clear heights. Similarly, girder lengths were taken as clear lengths. In some experiments, specimens were cast in multiple parts. As a result, concrete in some parts of a structure had a lower modulus of elasticity than in other parts. In these cases, the reduced modulus of elasticity was incorporated into the estimated story stiffnesses.

A8.2. SAP2000 Model of 20-Story Structure

When Rayleigh's method was used to estimate the initial first-mode period of the 20-story structure tested in Japan [Sugimoto et al. (2016)], the estimated period was much smaller than both the estimated period from the literature and the measured period. This is thought to be because Rayleigh's method considers only shear deformations at each story, but in tall buildings axial deformations in the exterior columns can lead to longer periods of vibration than would be expected based on shear deformations alone. For this reason, a model was built in SAP2000 to estimate the initial period of this structure.

Model geometry and materials were defined from drawings and tables in Sugimoto et al. (2016). Instead of modeling the entire building, a single interior frame was modeled in each direction (Figure A8-1 and Figure A8-2). Floor-to-floor heights were 750 mm. Columns were all 225 x 225 mm. The same T-beam cross-section was used in both directions. These T-beams were defined using the SAP2000 section designer. The effective width of the top of beams was established by projecting up at 45 degrees from the bottom face of the beam (Figure A8-3). This led to an effective width of 390 mm. Center-to-center spans were 1625 mm in both directions.

The test specimen was cast in four parts: (1) floors 1 through 8, (2) floors 9 through 13, (3) floors 14 through 17, and (4) floors 18 through 20. Different concrete was used in each part, with the strongest concrete at the lowest levels. To account for this, four different concrete material models were defined, with material properties summarized in Table A8-1. According to Sugimoto et al. (2016), the total weight of each floor of the structure was 177 kN. Three parallel frames resisted demands in the X-direction (longitudinal). Because only one frame was modeled in this direction, a mass of $177 \text{ kN}/3 = 59 \text{ kN}$ was assigned to each floor level in the model. Four parallel frames resisted lateral demands in the Y-direction (transverse). Because only one frame was modeled in this direction, a mass of $177 \text{ kN}/4 = 44.3 \text{ kN}$ was assigned to each floor level in the model.

Fixed end conditions were assigned to the bases of the columns on the first floor. The following degrees of freedom were unlocked: lateral displacement, vertical displacement, and in-plane rotation. Modal analyses were conducted including modes 1 through 10. From these modal analyses, the first-mode initial period was found to be 0.55 sec in the X-direction, and 0.61 sec in the Y-direction. These showed fair agreement with the measured initial first-mode period from Sugimoto (2016), which was approximately 0.6 sec.

A9. SUGGESTIONS FOR FUTURE TESTS

A9.1. Anchorage of High-strength Steel

The high-strength steel in type H frames slipped along the height of the column, reducing the post-cracking stiffness of type H frames. Although this was not detrimental to the present investigation – it actually made for a more demanding test of the hypothesis – it could be detrimental to other investigations of HSSRC. For this reason, the author recommends paying close consideration not only to anchorage of high-strength longitudinal steel within beams, but also along the length of members.

A9.2. Reusable Mass

The reusable mass used in this investigation covered the full depth of the top beam. This prevented Optotrak targets from being installed, and prevented strains from being measured at the top beam-column joint. Had the reusable mass been constructed with a chamfered inner edge or had it been made less deep, an Optotrak target could have been installed on the upper beam. This would have allowed strains to be measured at the top beam-column joint.

Table A1-1: Grout mix proportions (as-delivered, per cubic yard).

Material	Weight, lb	Specification
#23 Sand	2,760	ASTM C33 (2013) and INDOT 2014 Standard Specification §904.02h
Cement	620	ASTM C150 (2012), Type I
Water	410	n/a

Table A1-2: Gradation of INDOT #23 sand [from INDOT (2014) Standard Specification §904.02h)].

Sieve Size	Percent Passing
3/8 in.	100
No. 4	95-100
No. 6	--
No. 8	80-100
No. 16	50-85
No. 30	25-60
No. 50	5-30
No. 80	--
No. 100	0-10
No. 200	0-3

Table A1-3: Concrete compressive strength progression through end of curing.

Cylinder test date	Age, days	Compressive strength, psi		
		Each	Average	Coefficient of variation
2014-Aug-22	3	1,850	1,830	5.4%
		1,920		
		1,720		
2014-Aug-26	7	2,490	2,430	3.8%
		2,470		
		2,324		
2014-Sep-02	14	3,010	2,880	4.5%
		2,870		
		2,750		
2014-Sep-16	28	3,090	3,040	2.7%
		2,940		
		3,080		
2014-Sep-30	42	3,340	3,340	1.8%
		3,400		
		3,280		
2014-Oct-28	70	3,520	3,500	0.6%
		3,480		

Table A1-4: Summary of concrete material properties established on test days.

Property		Specimen				Overall Average
		C1	C2	H1	H2	
Compressive strength, psi	Each	4,040	3,940	3,740	3,720	--
		3,840	3,810	3,550	3,940	
		3,900	3,830	3,680	3,860	
	Avg.	3,930	3,860	3,660	3,840	3,800
Tensile strength, psi	Each	370	420	470	420	--
		450	450	370	370	
	Avg.	410	430	420	400	410
Modulus of rupture, psi	Each	--	780	890	--	--
			910	800		
			890	880		
	Avg.	--	860	850	--	860
Modulus of elasticity, ksi	Each	--	2,470	2,840	--	--
			2,770	2,680		
			--	3,320		
	Avg.	--	2,620	2,760	--	2,700
Date established (2015-)		Sep-12	Dec-23	Jul-15	Dec-06	--

Table A1-5: Longitudinal reinforcing steel sample test results.

Bar ID	Elastic modulus, ksi	0.2% offset yield stress, ksi	Ultimate stress, ksi	Elongation in 8 inches, %
CA	26,300	65	100	15
CB	29,100	65	104	12
CC	30,800	66	101	11
Average	28,700	65	102	12
HS1	30,700	168	184	5
HS2	31,000	162	185	6
HS3	29,300	159	189	7
HS4	28,900	159	190	7
Average	30,000	162	187	6

Table A1-6: Values of parameters used in ideal Menegotto-Pinto (1973) relationship.

Type of Steel	ϵ_{s0}	σ_{s0}	k_s	R
Conventional	0.003	90	0.006	1.5
High-strength	0.006	182	0.004	3.3

Table A1-7: Transverse reinforcing steel sample test results.

Wire ID	Elastic modulus, ksi	0.2% offset yield stress, ksi	Ultimate stress, ksi	Elongation at fracture**, %
W1	25,600	*	81	8.4%
W2	25,500	*	84	8.9%
W3	25,200	74	80	7.9%
Average	25,400	74	82	8.4%
*could not be determined because of slip of extensometer				
**All samples fractured near the grips. These strains are computed over the full 6 in. gauge at the ends, but because the grips would have supported a portion of this length, the percent elongation at fracture may have been higher.				

Table A3-1: As-built measurements of frame dimensions (see Figure A3-3 for key). All measurements are in inches.

Beam Depths	C1	C2	H1	H2	Nom.
D1	10	10	10	10	10
D2	10	10	10	9 15/16	10
D3	10	10	10	9 15/16	10
D4	12	12 1/16	12 1/8	12	12
D5	12	12	12 1/16	12	12
D6	12	12	12	12	12
Lengths	C1	C2	H1	H2	Nom.
LT	76 1/8	76 1/16	76 1/8	76 1/8	76
T1	17 1/16	16 15/16	17 1/16	17 1/16	17
T2	5	4 31/32	4 31/32	5	5
T3	32 1/16	32 1/8	32	32 1/8	32
T4	5	4 15/16	5	5	5
T5	17	17	17 1/16	17 1/16	17
LB	84 1/16	84	84	83 15/16	84
B1	21 1/16	21 1/8	21	21	21
B2	4 31/32	4 15/16	4 15/16	5	5
B3	32	32 1/8	32 1/16	32 1/8	32
B4	5	5	4 15/16	5	5
B5	21	21	21 1/8	21	21
Heights	C1	C2	H1	H2	Nom.
H1	42 1/16	42 1/16	42	42 1/16	42
H2	42 1/16	42 1/16	42	42 1/16	42
H3	42 1/16	42 1/16	42	42 1/16	42
H4	42 1/16	42 1/16	42	42	42
Thicknesses (in out)	C1	C2	H1	H2	Nom.
O1	5 1/8 5 1/8	5 3/32 5	5 1/16 5	5 3/32 5 1/8	5
O2	5 1/8 5 3/32	5 3/32 5 1/16	5 3/32 5 1/8	5 3/32 5 1/16	5
O3	5 1/8 5 1/16	5 3/32 5 1/16	5 1/16 5 1/16	5 3/32 5 3/32	5
O4	5 3/32 5 3/32	5 1/16 5 1/16	5 1/16 5 3/32	5 1/8 5 1/8	5

Table A3-2: Specimen reinforcement summary.

Component	Longitudinal Reinforcement		Transverse Reinforcement
	Type C	Type H	
Columns	4 x 3/8-in. Gr.-60 deformed	4 x 1/4-in. (6.5 mm meas.) high-strength smooth	35 x 3/16-in. 12L14 smooth hoops
Bottom beam	4 x 3/8-in., Gr.-60		30 x 3/16-in. 12L14 smooth hoops
Top beam	4 x 3/8-in., Gr.-60		31 x 3/16-in. 12L14 smooth hoops
<p><u>Note:</u> In all beam column joints, 3/16-in. 12L14 spirals were provided. These spirals had an inside diameter of approximately 3-3/8 in. and a spacing of approximately 1-1/4 in. In addition, two rectangular hoops were provided in all joints. See figures for details.</p>			

Table A3-3: As-built measurements of column hoop spacing.

Row Number	C1				C2			
	A	B	C	D	A	B	C	D
(1)	1	1	1 1/16	1	15/16	1	1 1/16	1
(2)	2	2	2 1/16	2	2	2 1/16	2	2
(3)	3	3	3	3	3	3 1/16	3	3
(4)	4	4	4	4	4 1/16	4	4	4 1/16
(5)	5	5	5	5	5	5	5 1/16	5 1/16
(6)	6	6	6	6	6 1/16	6	6	6 1/16
(7)	7	7	7	7 1/16	7 1/16	7	7	7
(8)	8	8	8	8 1/8	8 1/16	8	8	8
(9)	9	9	9	9 1/16	9	9	9 1/16	9
(10)	10	10	10	10 1/16	10 1/16	10	10 1/16	10
(11)	11	11	11	11 1/16	11	11	11	10 15/16
(12)	12	12	12	12 1/16	12 1/16	12 1/16	12 1/16	12
(13)	13	13	13	12 7/8	13	13 1/16	13 1/16	13
(14)	14 3/4	14 7/8	14 7/8	14 7/8	14 13/16	14 13/16	14 7/8	14 13/16
(15)	16 11/16	16 3/4	16 13/16	16 1/2	16 5/8	16 3/4	16 3/4	16 9/16
(16)	18 9/16	18 7/16	18 11/16	18 7/16	18 1/2	18 5/8	18 1/2	18 1/2
(17)	20 1/2	20 3/8	20 7/16	20 3/16	20 5/16	20 1/2	20 1/2	20 5/16
(18)	22 3/8	22 3/16	22 5/16	22 5/16	22 1/4	22 1/2	22 3/8	22 3/8

A: North column, from top of bottom layer of beam longitudinal steel down to top of hoops in column
 B: North column, from bottom of top layer of beam longitudinal steel up to bottom of hoops in column
 C: South column, from top of bottom layer of beam longitudinal steel down to top of hoops in column
 D: South column, from bottom of top layer of beam longitudinal steel up to bottom of hoops in column

Table A3-3 (continued): As-built measurements of column hoop spacing.

Row Number	H1				H2			
	A	B	C	D	A	B	C	D
(1)	1	1	1	1	1	1	1	1
(2)	2	2	2	2	2 1/16	2	2	2
(3)	3	3	3	3	3	3	3	3
(4)	4	4	4	4	4	4	4	4
(5)	5	5	5	5	5	5	5	5
(6)	6	6	6	6	6	6 1/16	6	6
(7)	7	7	7	7	7	7 1/16	7	7
(8)	8	8	8	8	8	8 1/16	8	8
(9)	9	9	9	9	9 1/16	9 1/8	9	9
(10)	10	10	10	10	10	10 1/16	10	10
(11)	11	11	11	11	11 1/16	11	11	11
(12)	12	12	12	12	12	12 1/16	12	12
(13)	13	13	13	13	13	13 1/16	13	13
(14)	14 13/16	14 13/16	14 13/16	14 13/16	14 13/16	14 13/16	14 13/16	14 13/16
(15)	16 11/16	16 3/4	16 3/4	16 3/4	16 3/4	16 3/4	16 3/4	16 11/16
(16)	18 3/4	18 11/16	18 5/8	18 11/16	18 1/2	18 5/8	18 5/8	18 1/2
(17)	20 1/2	20 5/8	20 3/8	20 5/8	20 5/16	20 1/2	20 1/2	20 7/16
(18)	22 3/8	22 1/2	22 3/8	22 1/2	22 1/4	22 1/4	22 7/8	22 3/8

A: North column, from top of bottom layer of beam longitudinal steel down to top of hoops in column
 B: North column, from bottom of top layer of beam longitudinal steel up to bottom of hoops in column
 C: South column, from top of bottom layer of beam longitudinal steel down to top of hoops in column
 D: South column, from bottom of top layer of beam longitudinal steel up to bottom of hoops in column

Table A4-1: Summary of drag tests (conducted on 2015-July-13).

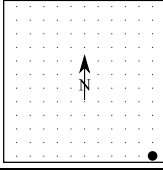
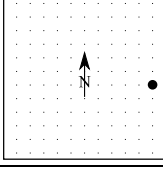
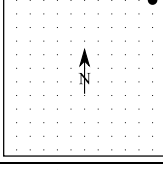
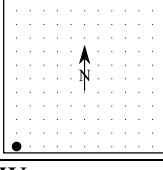
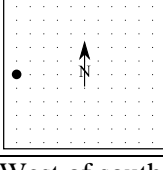
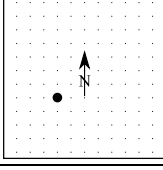
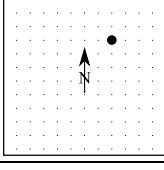
Object	Object weight, lb	Location on platform	Dynamometer force at sliding, lb	Estimated Friction Coefficient
Concrete cylinder	24.9	Southeast corner 	10+ (no sliding)	> 0.25
Concrete cylinder	24.9	East-center 	10+ (no sliding)	> 0.25
Concrete cylinder	24.9	Northeast corner 	10+ (no sliding)	> 0.25
Concrete cylinder	24.9	Southwest corner 	10+ (no sliding)	> 0.25
Concrete cylinder	24.9	West-center 	10+ (no sliding)	> 0.25
Concrete cylinder	24.9	West of south column 	10+ (no sliding)	> 0.25
Concrete cylinder	24.9	East of north column 	10+ (no sliding)	> 0.25

Table A5-1: Channels assignments on main DAQ system. All sensors are connected parallel to the axis of excitation and sample at 1000 Hz.

Channel Nr.	Channel Name	Units	Description
1	D0_3in	in.	LVDT connected to south face of mass near top beam.
2	D1Slip	in.	LVDT connected to north face of bottom beam.
3	D15	in.	LVDT connected to south face of south column at 15 in. above platform surface (3 in. above bottom beam).
4	D21	in.	LVDT connected to south face of south column at 21 in. above platform surface (9 in. above bottom beam).
5	D27	in.	LVDT connected to south face of south column at 27 in. above platform surface (15 in. above bottom beam).
6	D33	in.	LVDT connected to south face of south column at 33 in. above platform surface (21 in. above bottom beam).
7	D39	in.	LVDT connected to south face of south column at 39 in. above platform surface (27 in. above bottom beam).
8	D45	in.	LVDT connected to south face of south column at 45 in. above platform surface (33 in. above bottom beam).
9	D51	in.	LVDT connected to south face of south column at 51 in. above platform surface (39 in. above bottom beam).
10	D57top	in.	LVDT connected to south face of top beam.
11	MTS_disp	in.	Feedback signal from earthquake simulator actuator.
12	MTS_cmd	in.	Command signal to earthquake simulator actuator.
13	Acc1west	g	Accelerometer on simulator platform, northwest corner.
14	Acc2base	g	Accelerometer on top surface of frame lower beam.
15	Acc3south	g	Accelerometer on simulator platform, south center.
16	Acc4top	g	Accelerometer on top of mass above frame north column.
17	Time*10	sec	Time multiplied by 10. Used as part of process that sent signal to LED.
18	LED_Square	V	Signal that indicate whether LED on northwest of simulator platform was ON/OFF (>1, 0).

Table A5-2: Overview of main data acquisition system.

PCI Card	Chassis	Module	Accessory	Power Supply	Ch. Nr	Channel Name
6033E	SCXI-1000	SCXI-1520	SCXI 1314	External non-National Instruments (“Tango”)	1	D0_3in
					2	D1Slip
					3	D15
					4	D21
					5	D27
					6	D33
		7	D39			
		8	D45			
		9	D51			
		10	D57top			
		11	MTS_disp			
		12	MTS_cmd			
6259	n/a	n/a	SCB 68	PCB 482A22 signal conditioner	13	Acc1west
					14	Acc2base
					15	Acc3south
					16	Acc4top
				n/a	17	Time*10
				SCB 68	18	LED_Square

Table A5-3: Model and serial numbers of instrumentation used.

Sensor type	Manufacturer	Model number	Serial number	Range	Channel ID
LVDT	Schaevitz Sensors	DC-E 500	23618	$\pm 1/2$ in.	D1Slip
		DC-EC 2000	J7578	± 2 in.	D15
		2000 DC-E	8860	± 2 in.	D21
		2000 DC-E	8862	± 2 in.	D27
		DC-EC 2000	J7491	± 2 in.	D33
		DC-EC 2000	J7579	± 2 in.	D39
		2000 DC-E	7324	± 2 in.	D45
		DC-E 2000	J7250	± 2 in.	D51
		DC-E 2000	8859	± 2 in.	D57top
		3000 DC-E	1684	± 3 in.	D0_3in
Accelerometer	PCB Piezotronics	333B52	34452	± 5 g	Acc1west
			34453 (replaced with 34415)	± 5 g	Acc2base
			34411	± 5 g	Acc3south
			34454	± 5 g	Acc4top

Table A6-1: Ranges and factors used to modify Fourier amplitudes of acceleration record.

Frequency range (Period range)	Sine Cycle	Amp.	Shape of A_F	Reason
4 – 6 Hz (0.17 – 0.25 sec)	Full	-0.8		Reduce peak and valley in spectral displacement
2 – 6 Hz (0.17 – 0.5 sec)	Half	0.2		Increase spectral displacement in range of interest
2 – 7 Hz (0.14 – 0.5 sec)	Half	0.4		Increase spectral displacement in range of interest

Table A7-1: List of videos recorded during test program.

Test	Video				
	West	Northwest	Dial Gauges	GoPro	Drone
<u>Frame H1</u>					
H1-25	✓	✓			
H1-50	✓	✓			
H1-75	✓	✓			
H1-100	✓	✓	✓	✓	
H1-100(2)	✓	✓	✓	✓	
<u>Frame C1</u>					
C1-25	✓	✓	✓		
C1-50	✓	✓	✓		
C1-75	✓	✓	✓		
C1-100	✓	✓	✓		
C1-100(2)	✓	✓	✓		
<u>Frame H2</u>					
H2-25	✓	✓	✓		
H2-50	✓	✓	✓		
H2-75	✓	✓	✓		
H2-100	✓	✓	✓		
H2-100(2)	✓	✓	✓		
<u>Frame C2</u>					
C2-25	✓	✓	✓		
C2-50	✓	✓	✓		
C2-75	✓	✓	*		✓
C2-100	✓	✓	✓		✓
C2-100(2)	✓	✓	✓		
*Camera battery died during test.					

Table A8-1: Summary of concrete material properties used in SAP2000 model.

SAP2000 Concrete Model Name	Modulus of Elasticity (E_c), MPa	Compressive strength (f'_c), MPa	SAP2000 Sections to which material assigned
Conc01-08	39,200	85.1	Col01-08 TBm01-08
Conc09-13	31,500	60.8	Col09-13 TBm09-13
Conc14-17	26,700	50.3	Col14-17 TBm14-17
Conc18-20	25,800	43.5	Col18-20 TBm18-20

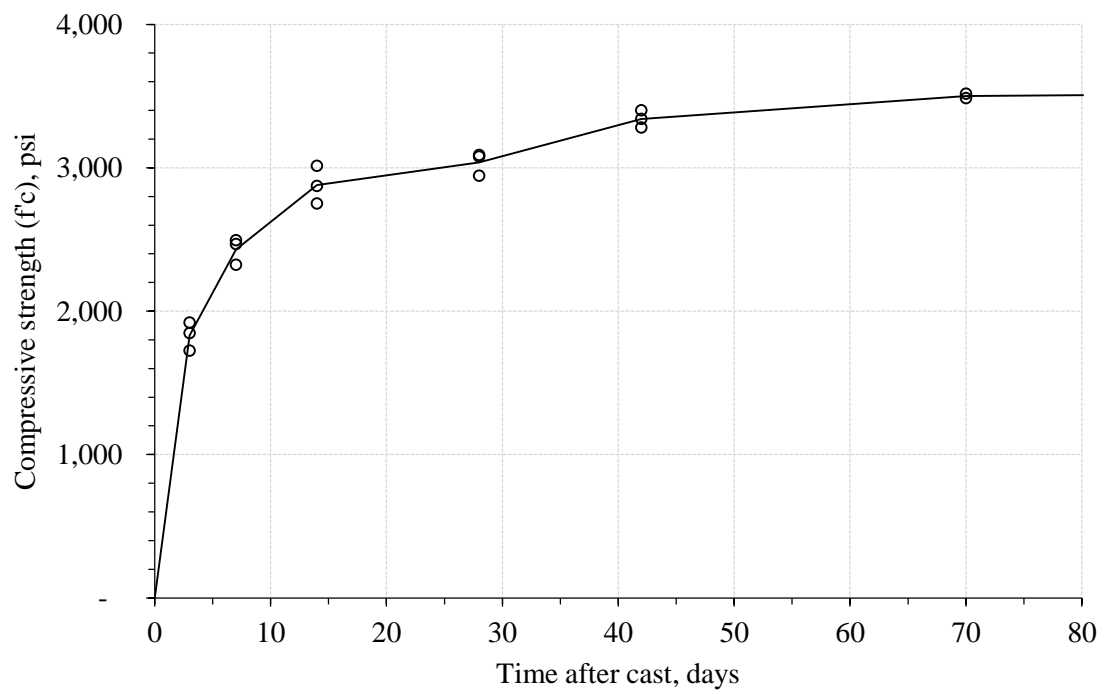


Figure A1-1: Development of concrete strength during and after curing process.

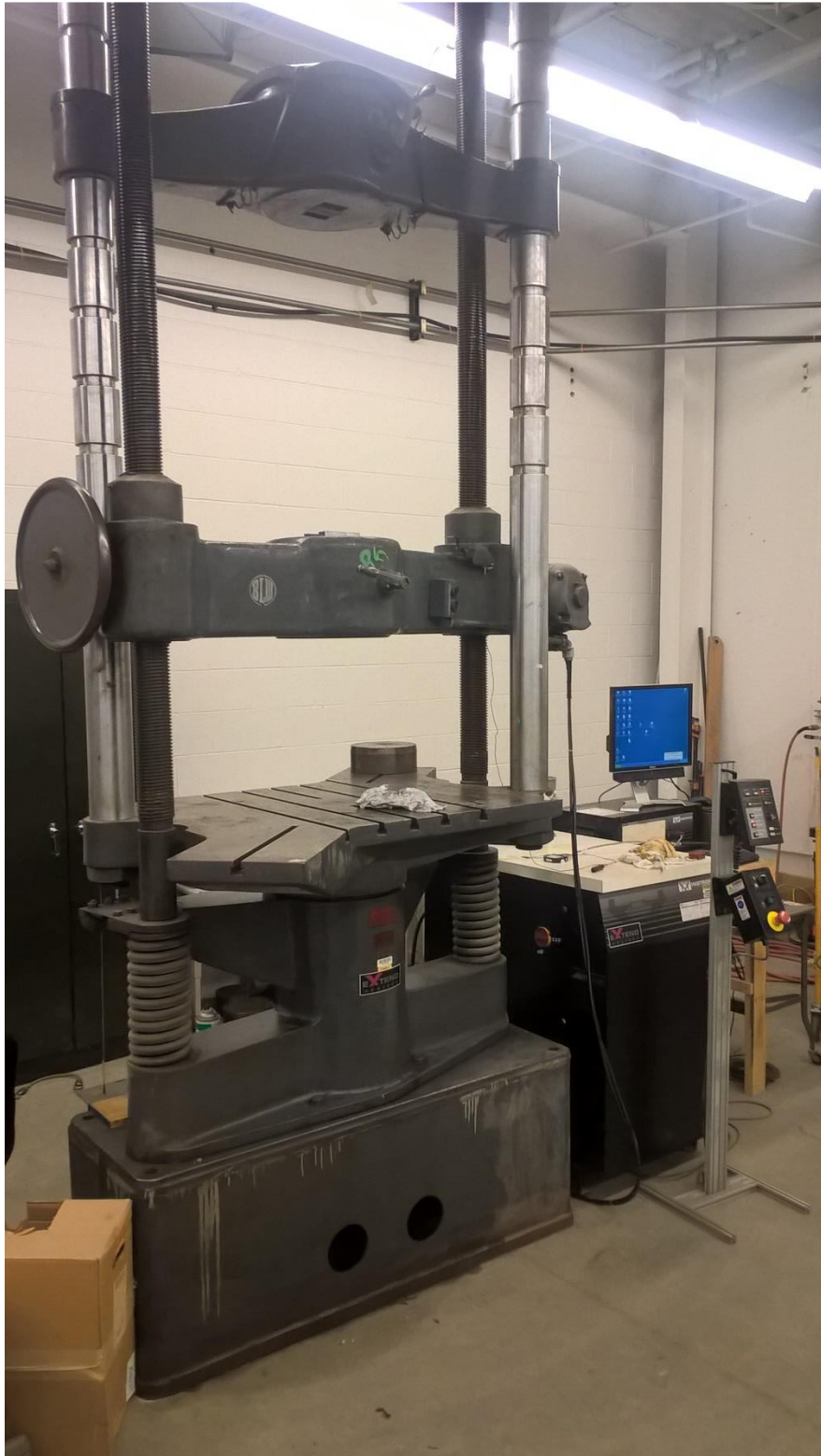


Figure A1-2: Baldwin 120-kip universal testing machine used to test reinforcing bars.

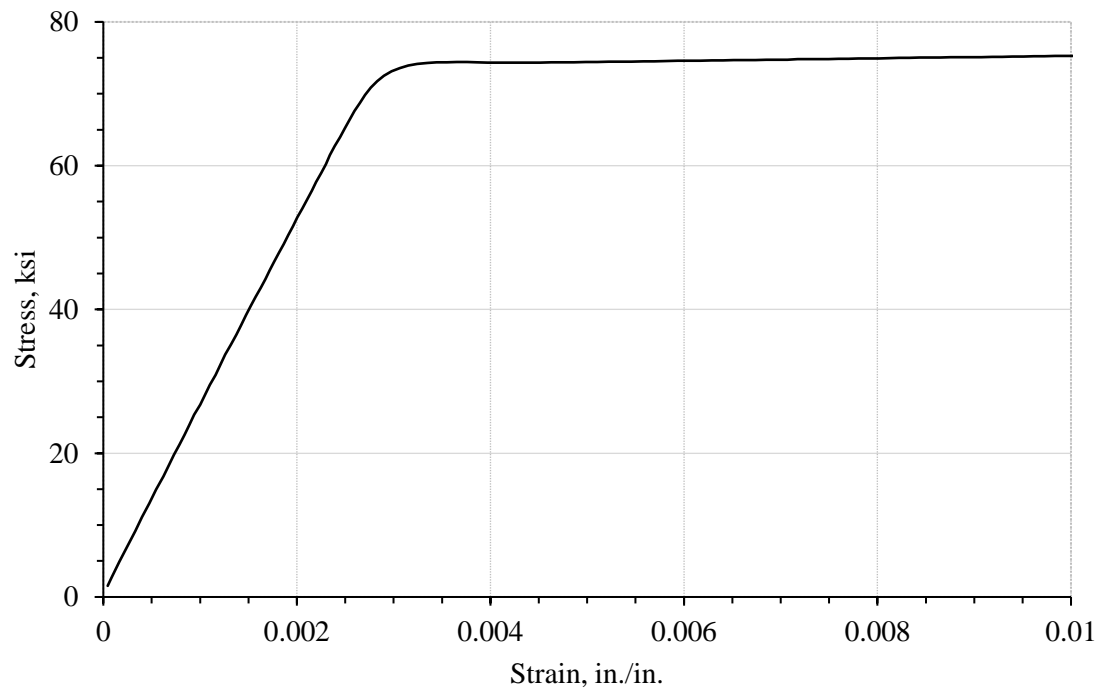


Figure A1-3: Measured stress-strain relationship of 12L14 steel wire used as specimen transverse reinforcement (extensometer was removed at 1% elongation to prevent damage to it).

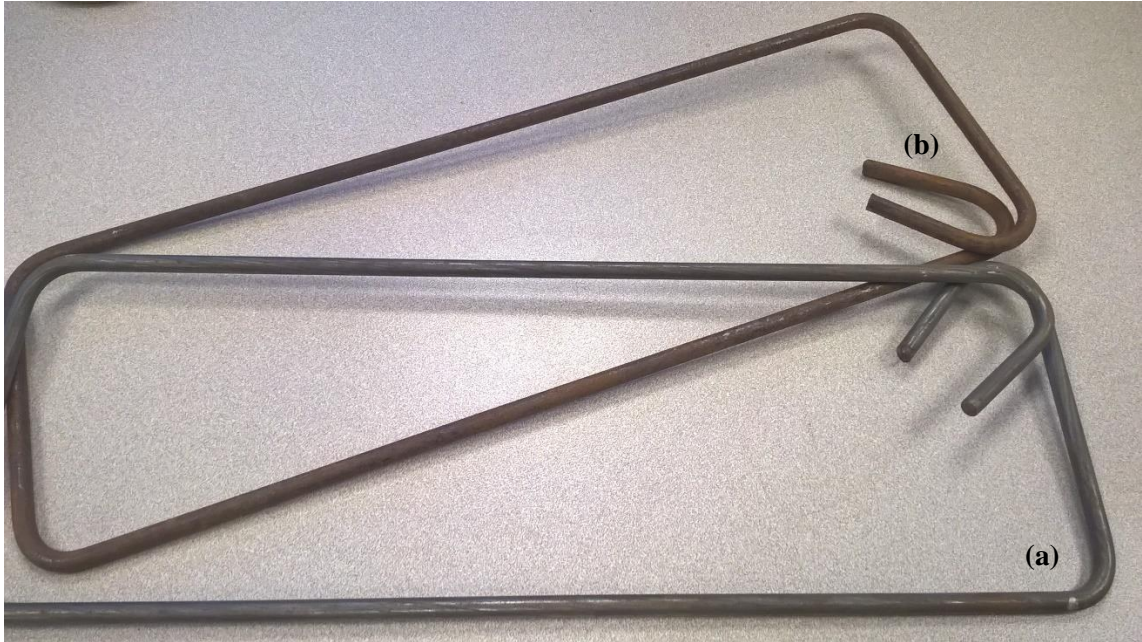


Figure A1-4: Comparison of (a) non-corroded, and (b) corroded transverse reinforcement.

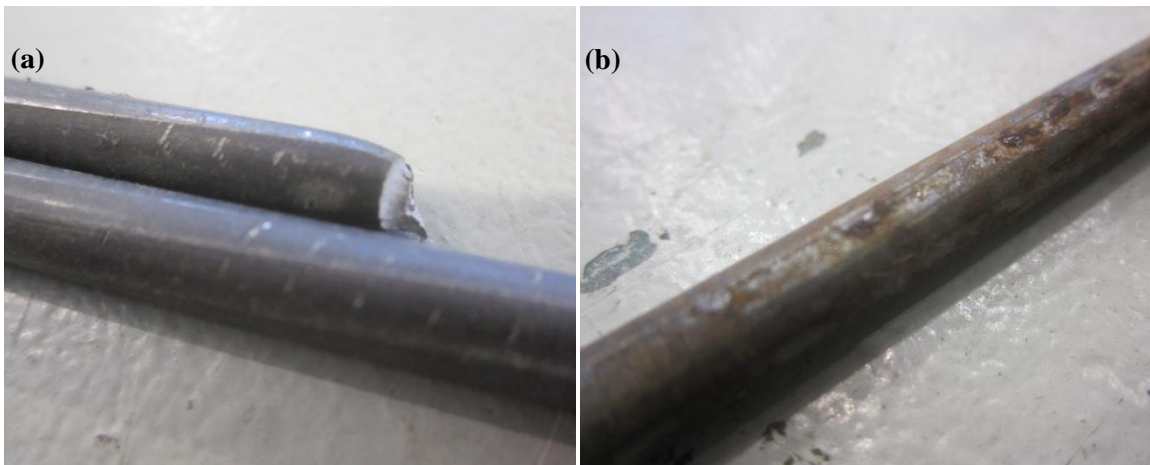


Figure A1-5: Comparison of (a) non-corroded, and (b) corroded high-strength steel.

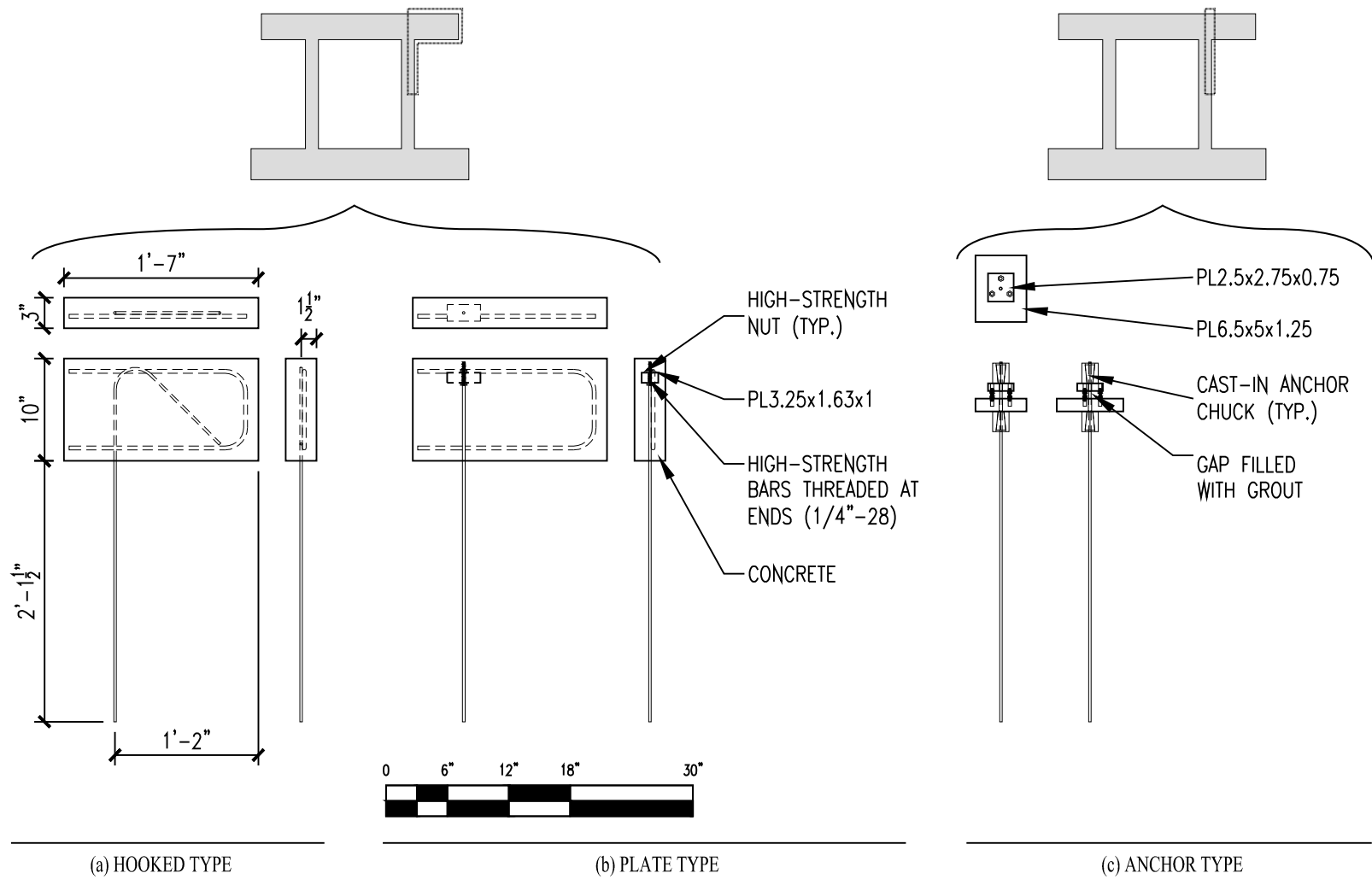


Figure A2-1: Pullout test specimen types.

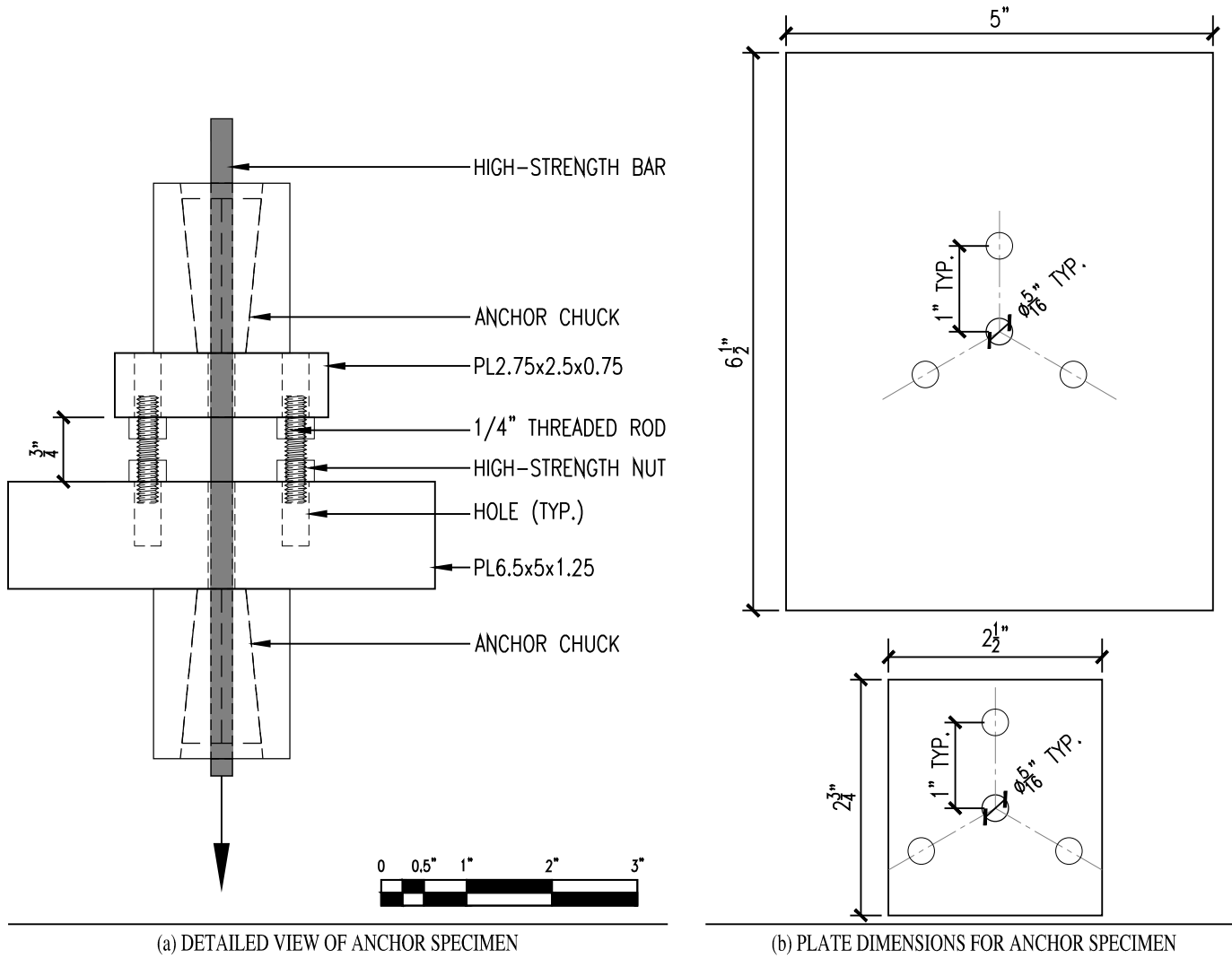
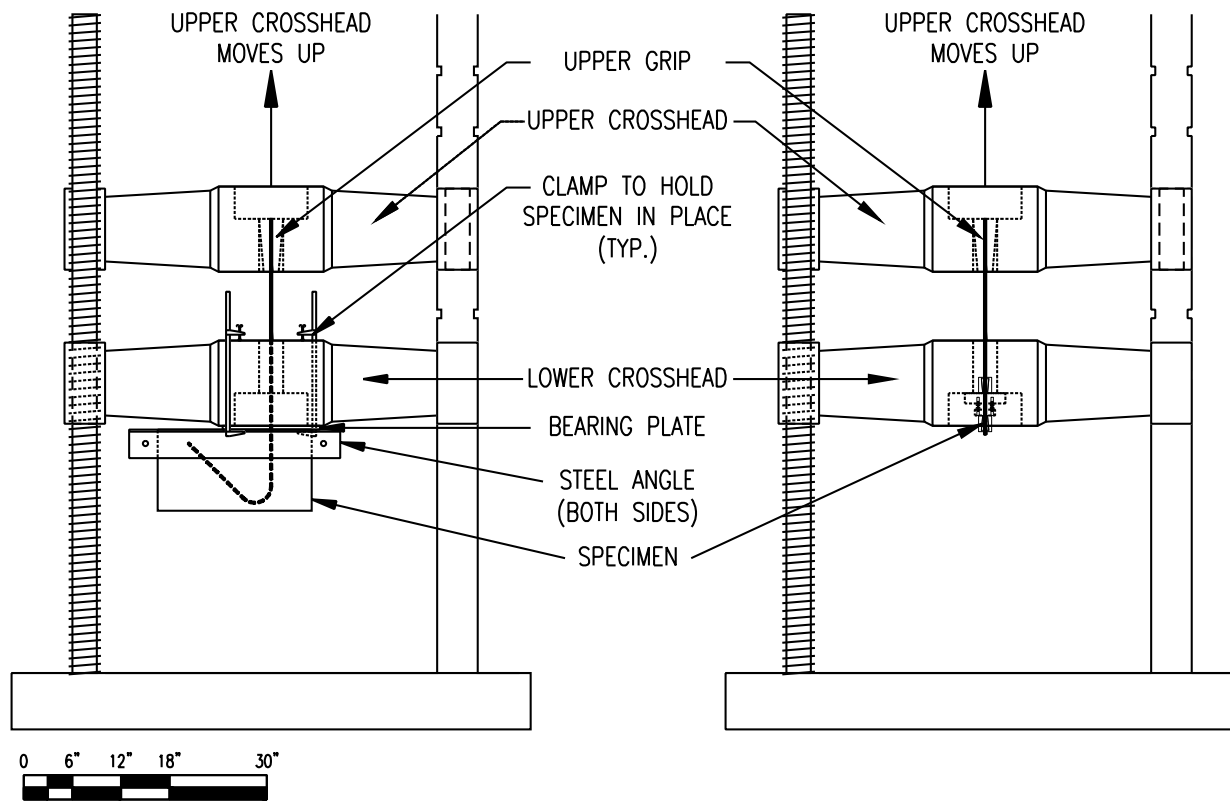


Figure A2-2: Anchor specimen details.



(a) SETUP FOR HOOKED AND PLATE TYPE SPECIMENS

(b) SETUP FOR ANCHOR TYPE SPECIMENS

Figure A2-3: Schematic of pullout test setup.

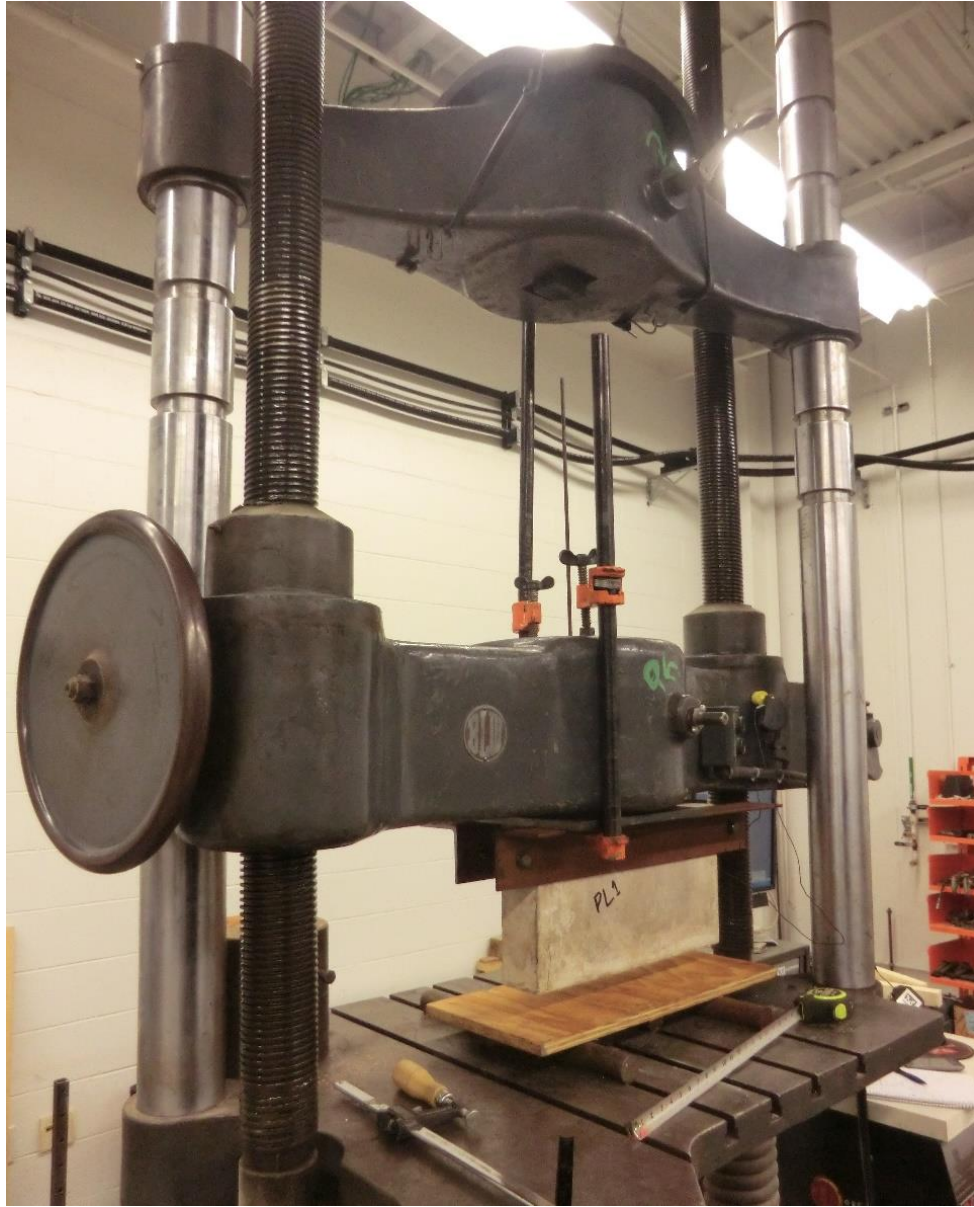


Figure A2-4: Photograph of pullout test setup (plate specimen).

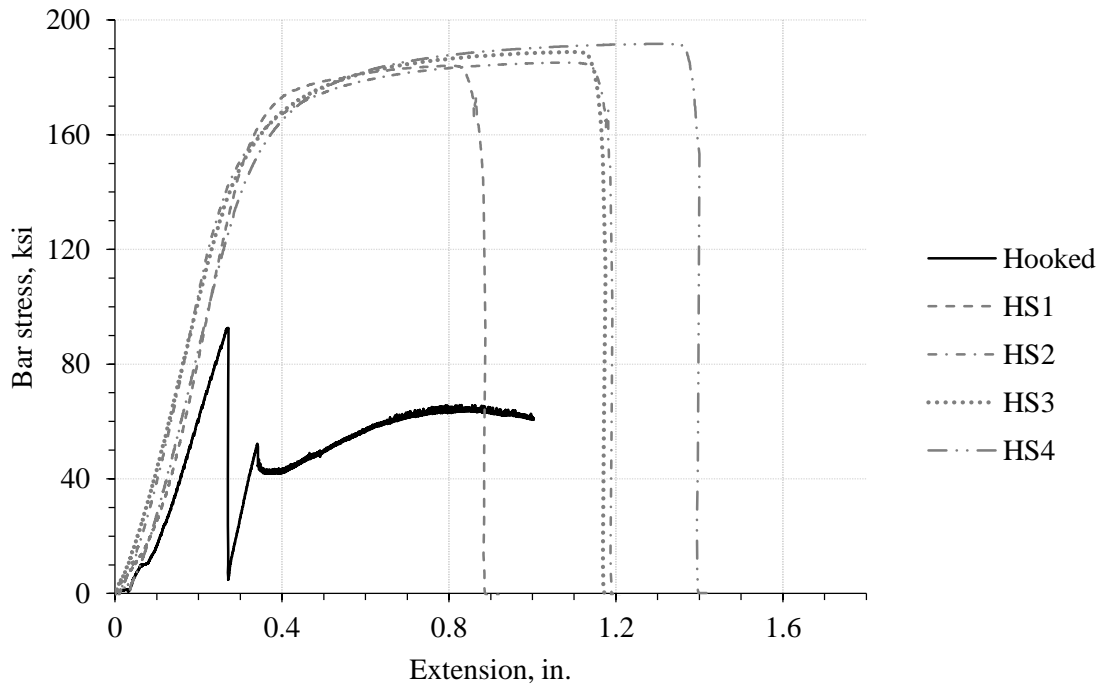


Figure A2-5: Stress-extension curve for hook pullout specimen.

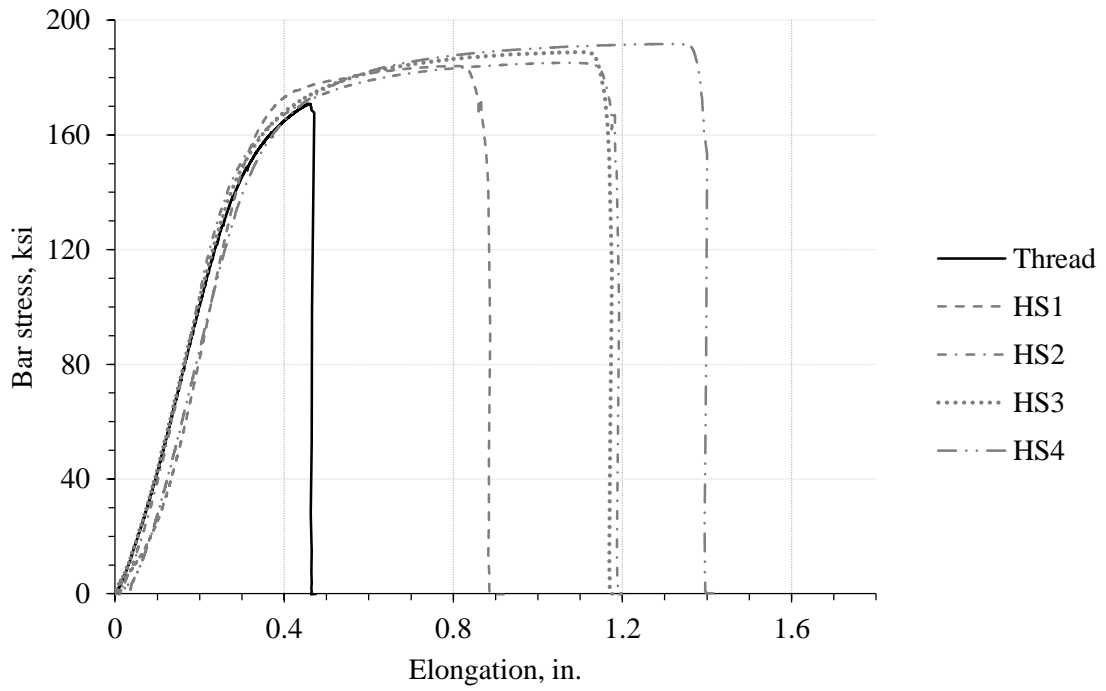


Figure A2-6: Stress-extension curve for plate pullout specimen.

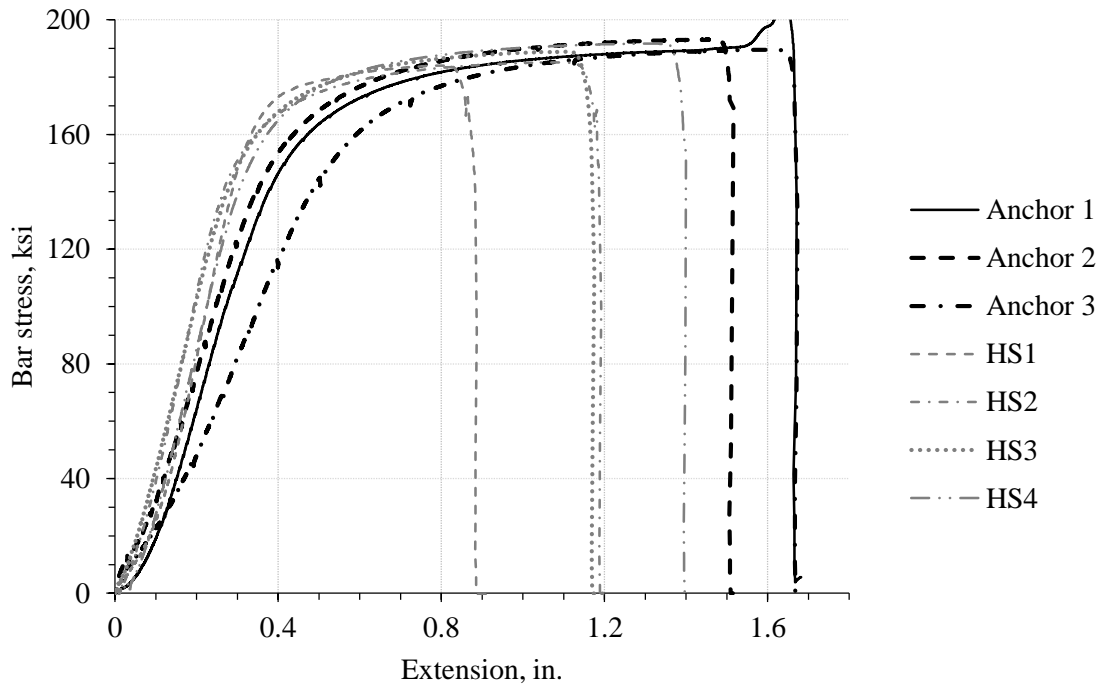


Figure A2-7: Stress-extension curve for anchor pullout specimens.

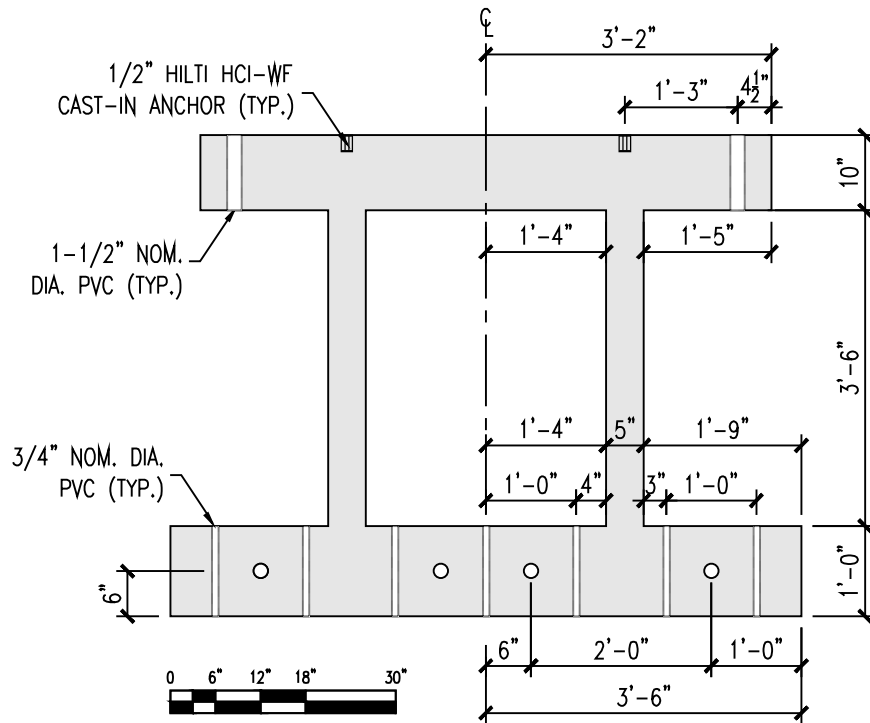


Figure A3-1: Overall dimensions of frames.

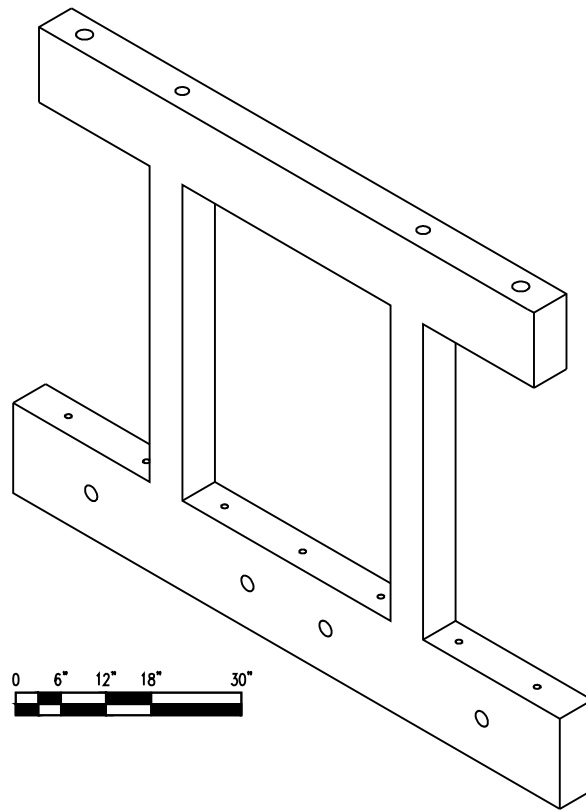


Figure A3-2: Isometric of frames.

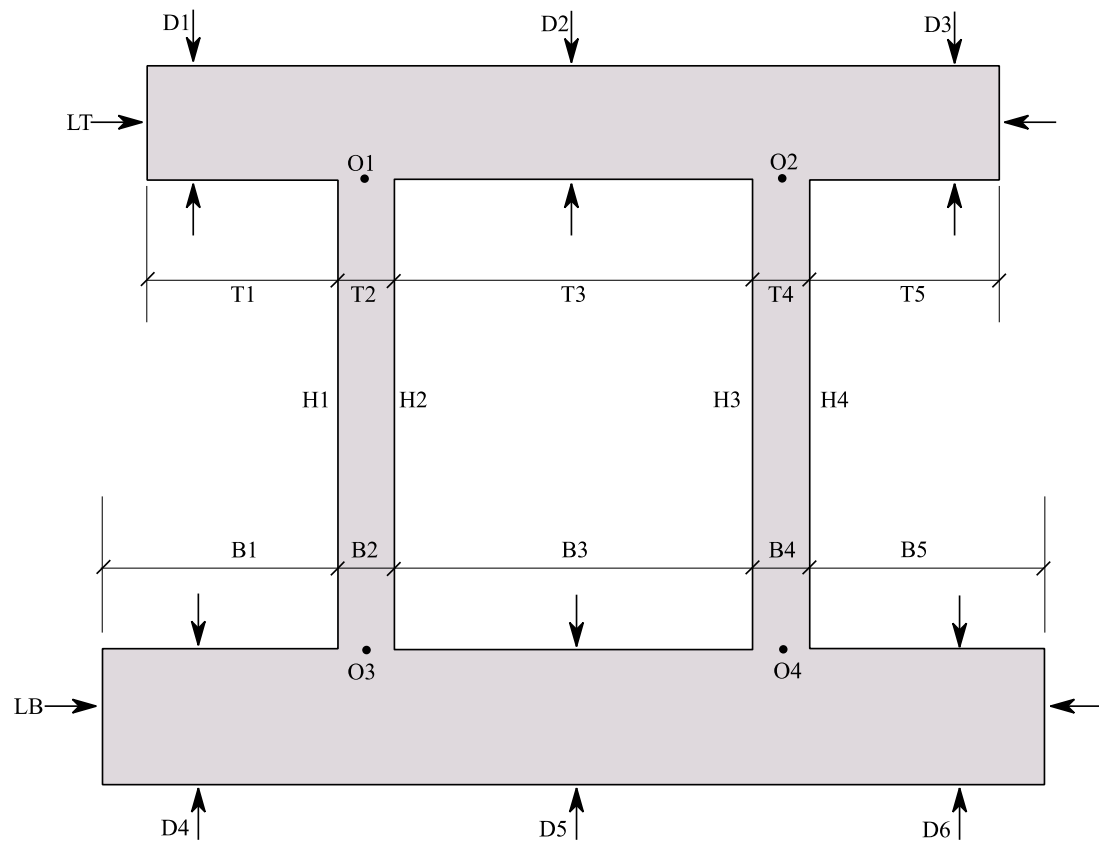


Figure A3-3: Schematic for as-built dimensions.

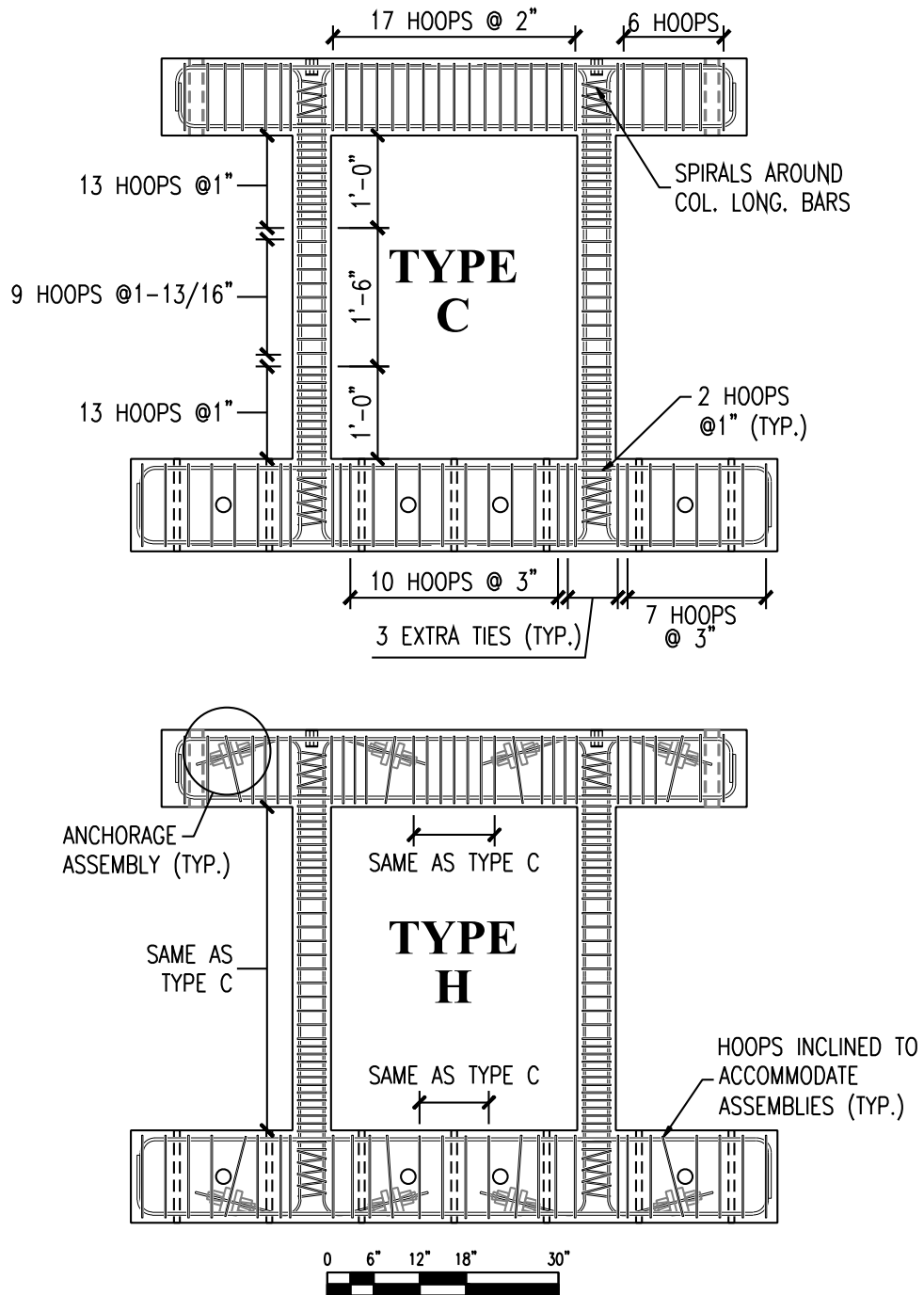


Figure A3-4: Comparison of specimen reinforcement details.

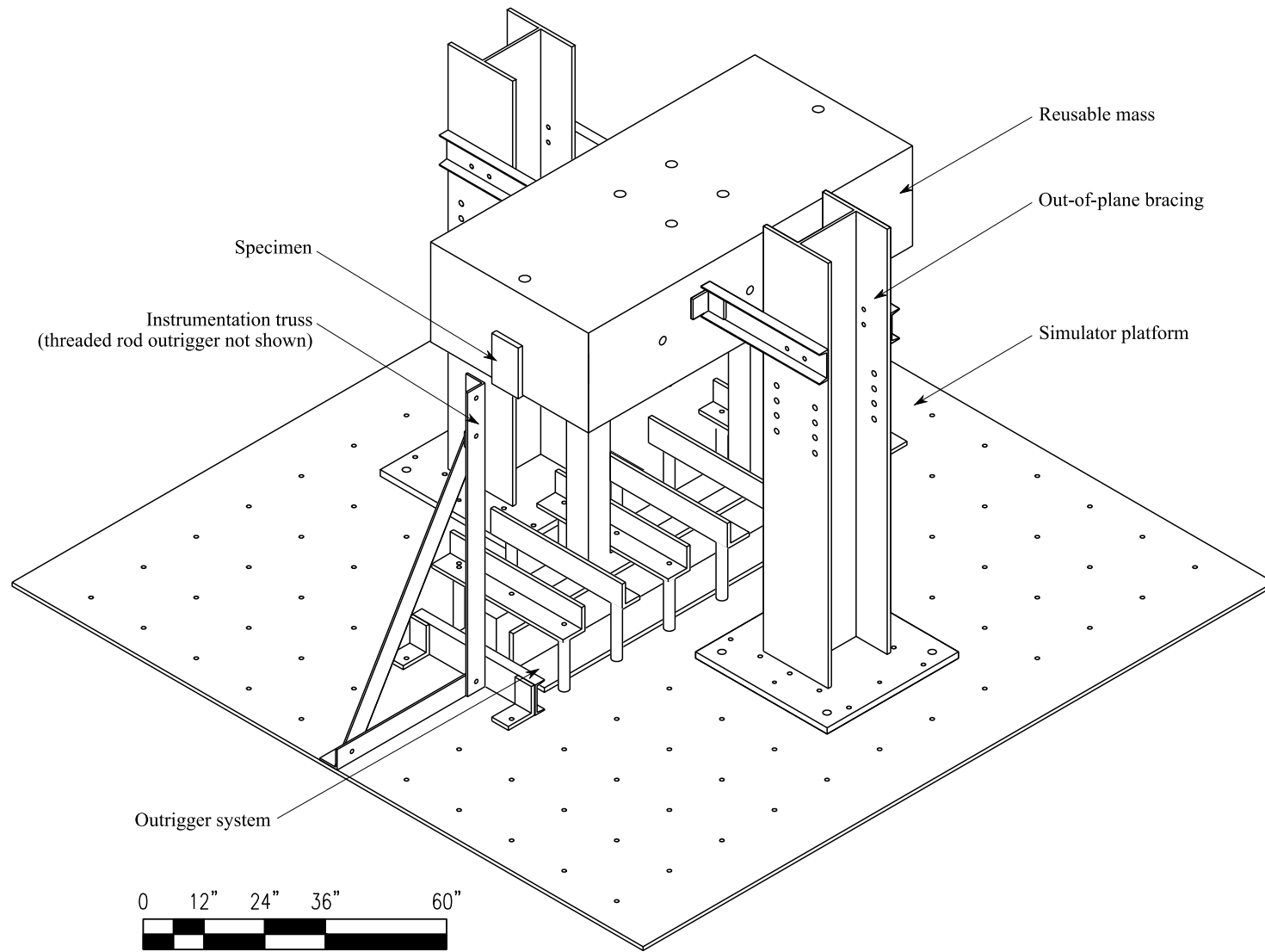
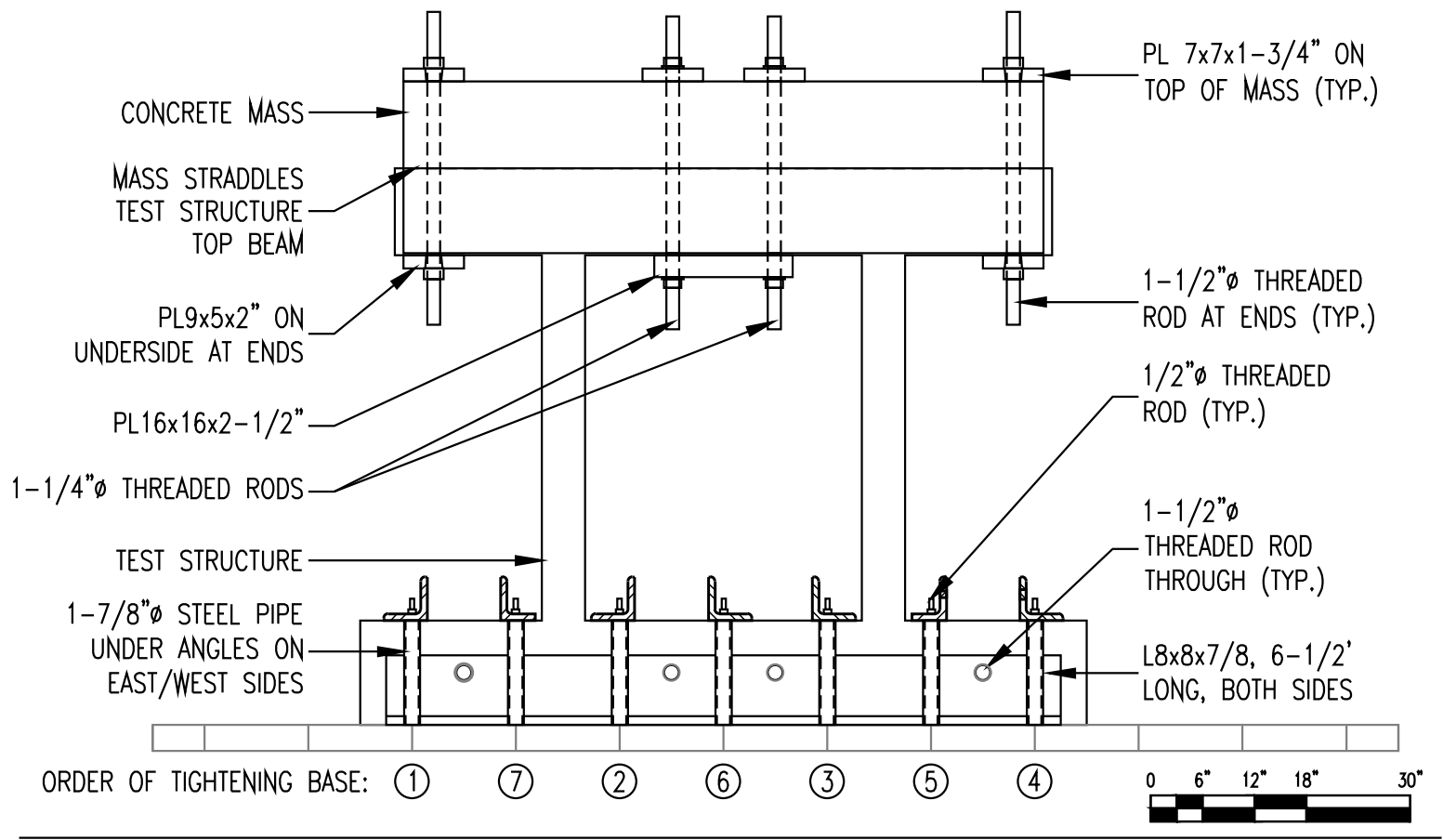


Figure A4-1: Isometric of test setup (for clarity, threaded rods, nuts, and plates are not shown).



WEST ELEVATION OF TEST SETUP

Figure A4-2: Test component details.

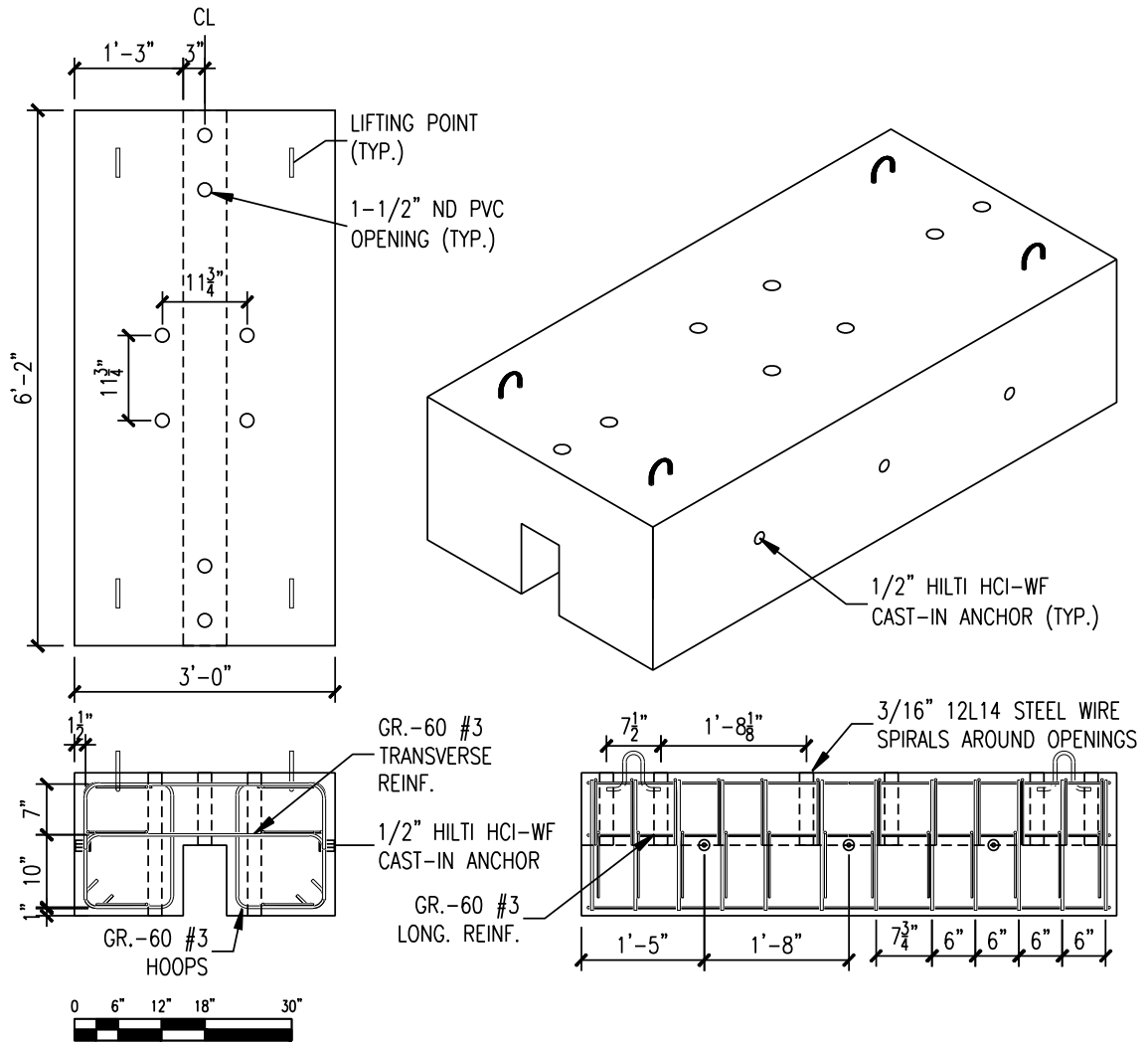


Figure A4-3: Mass reinforcement details.

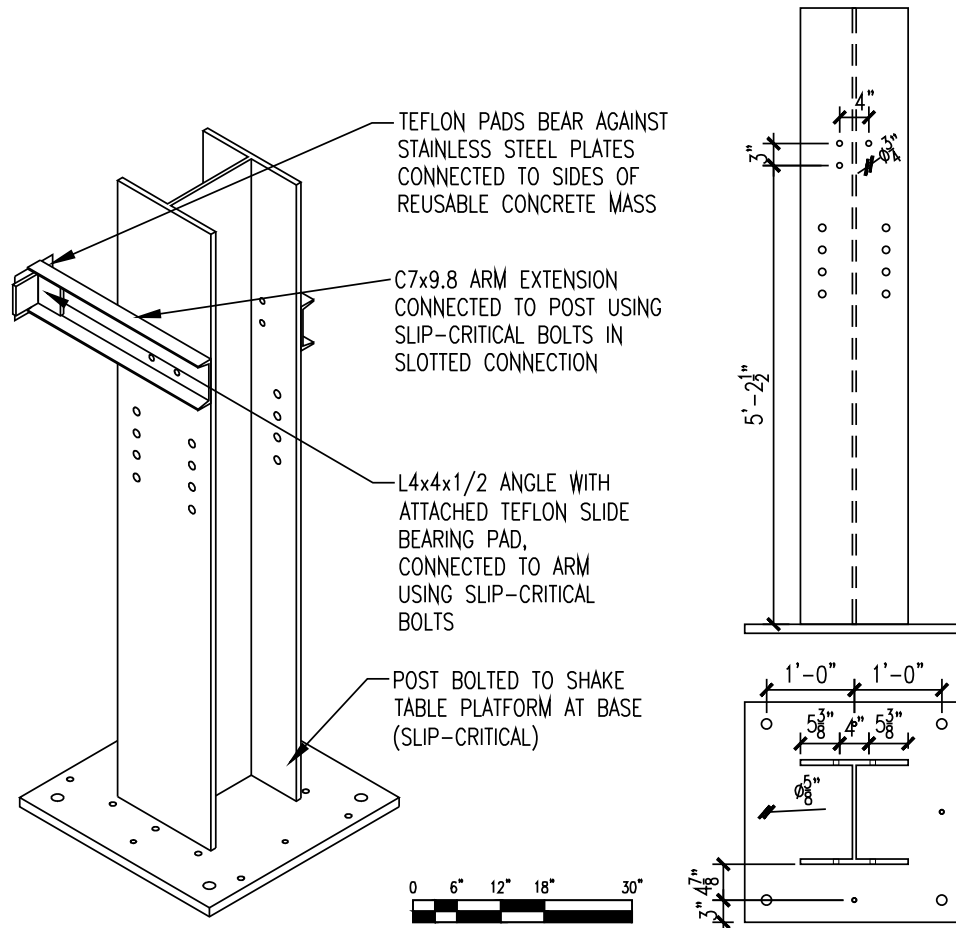


Figure A4-4: Out-of-plane bracing system.

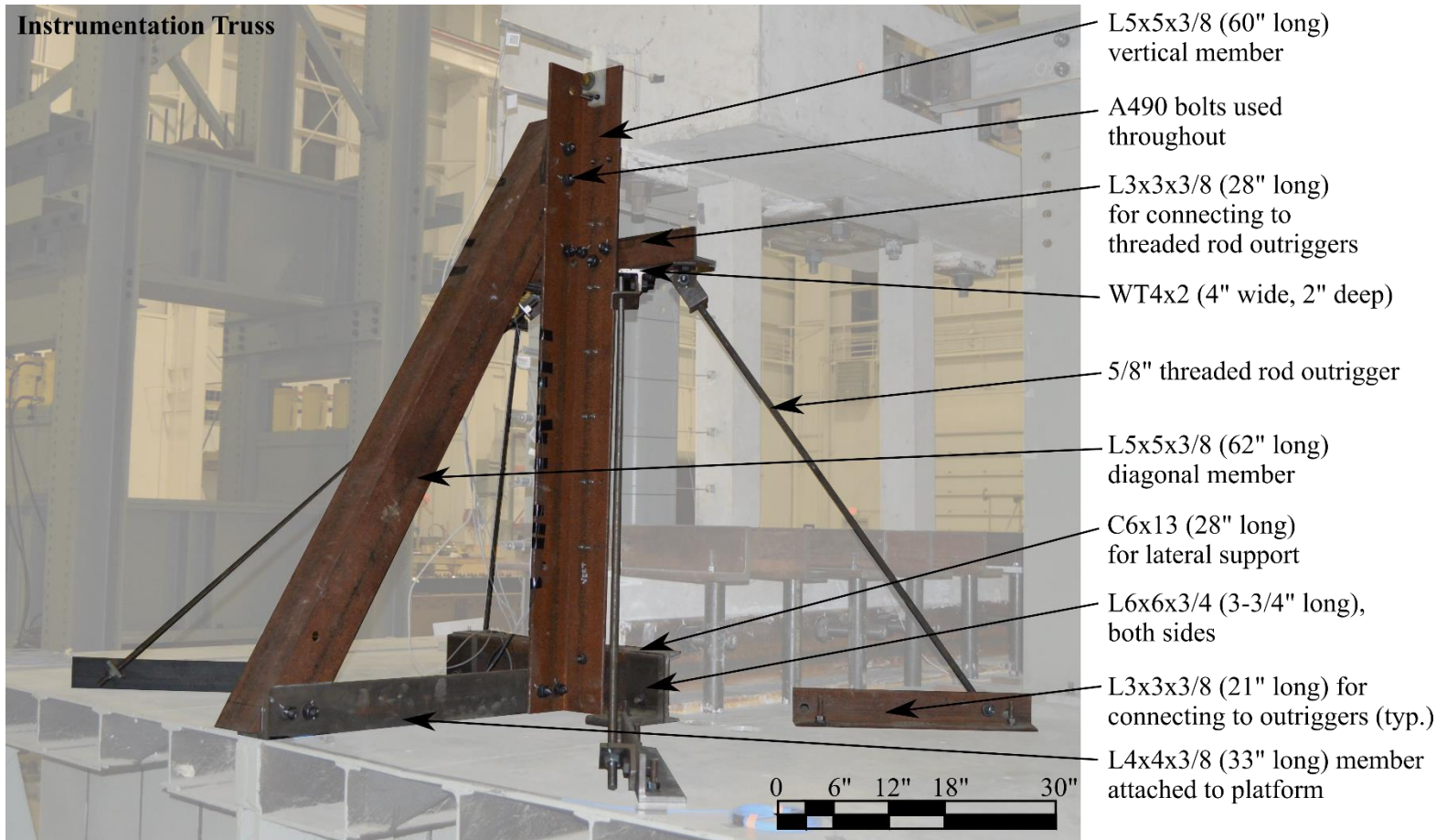


Figure A4-5: Annotated photograph of instrumentation truss.

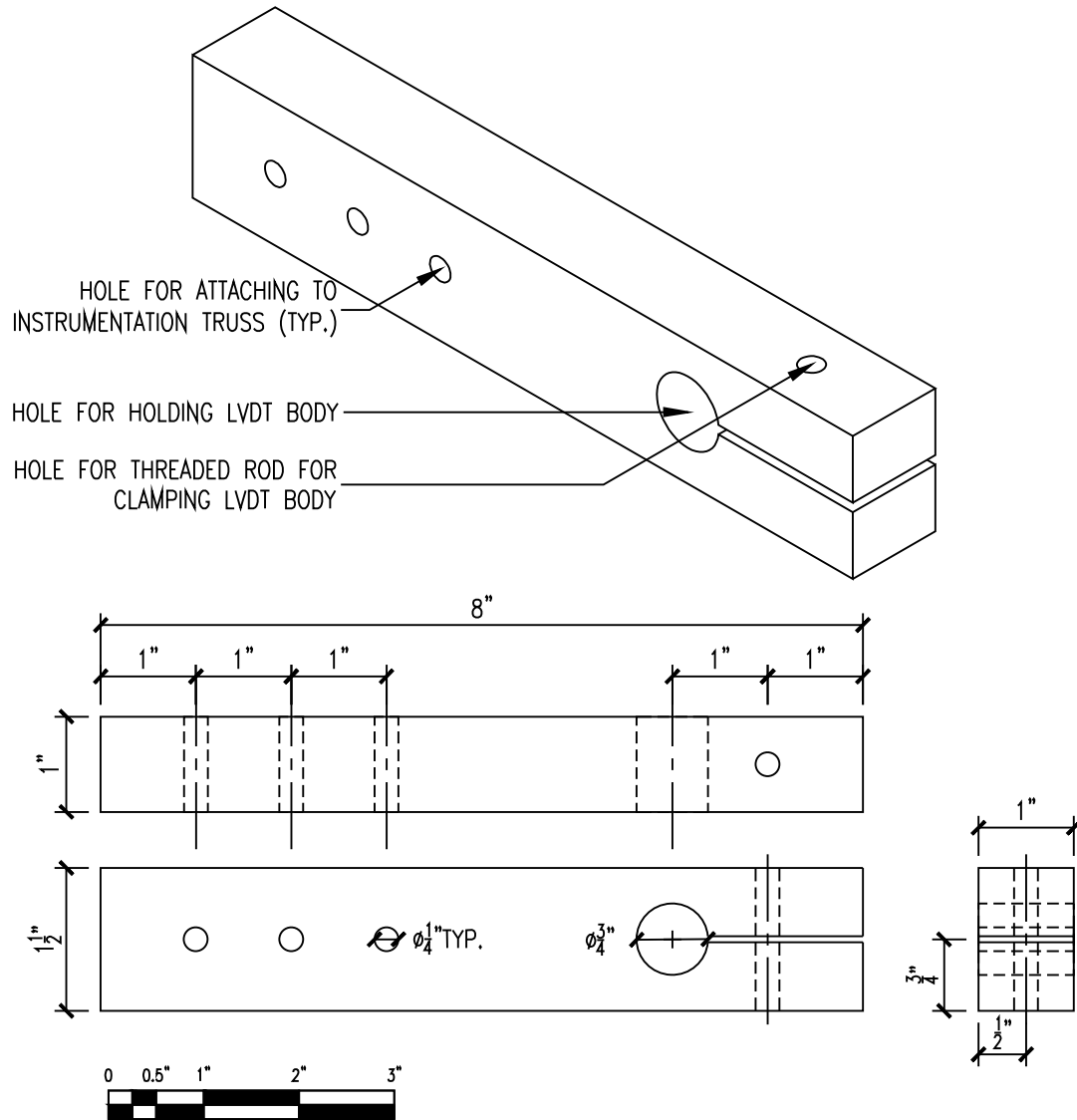


Figure A4-6: Schematic of LVDT mount.

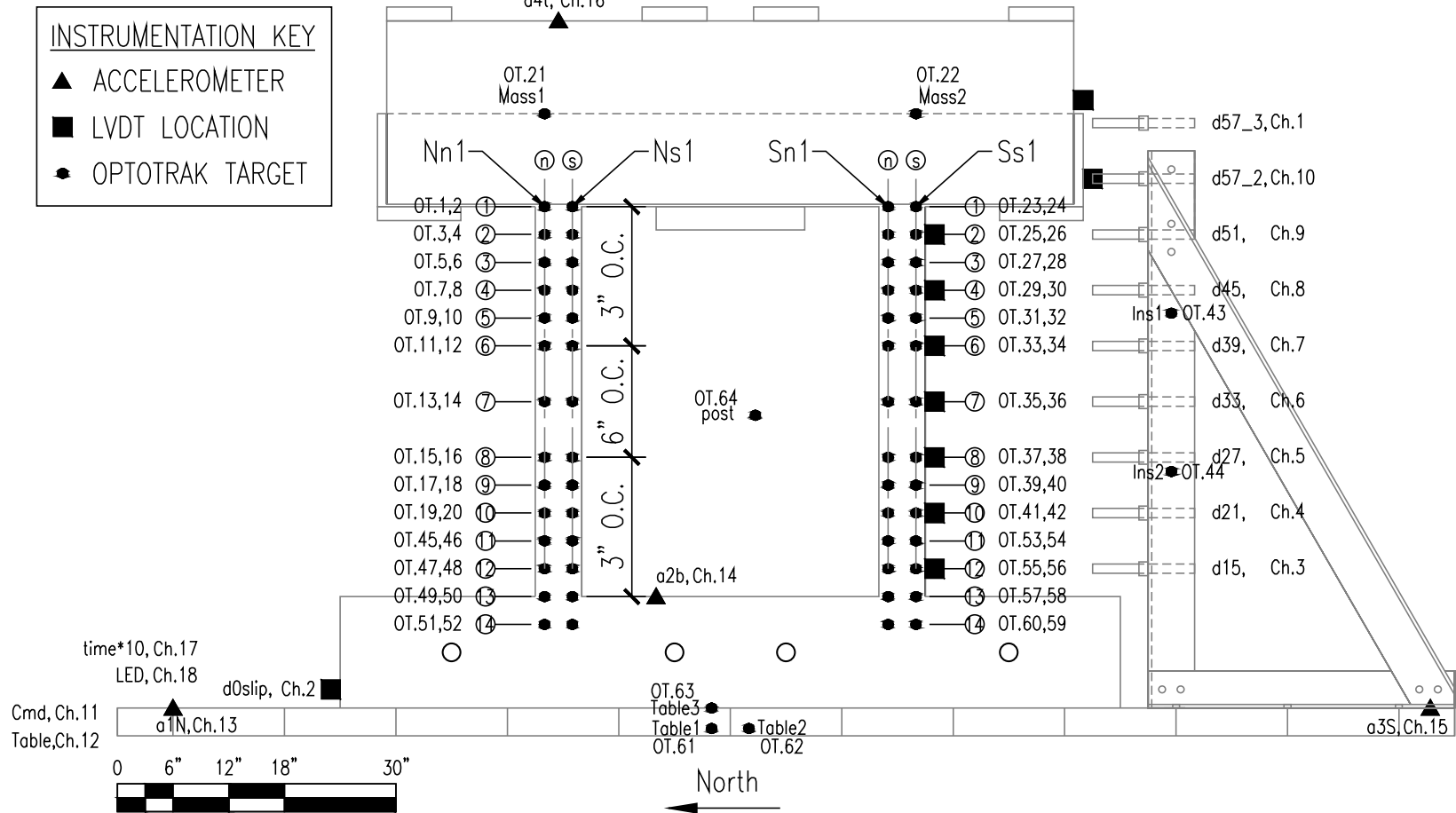


Figure A5-1: Master instrumentation plan (west face of test setup).

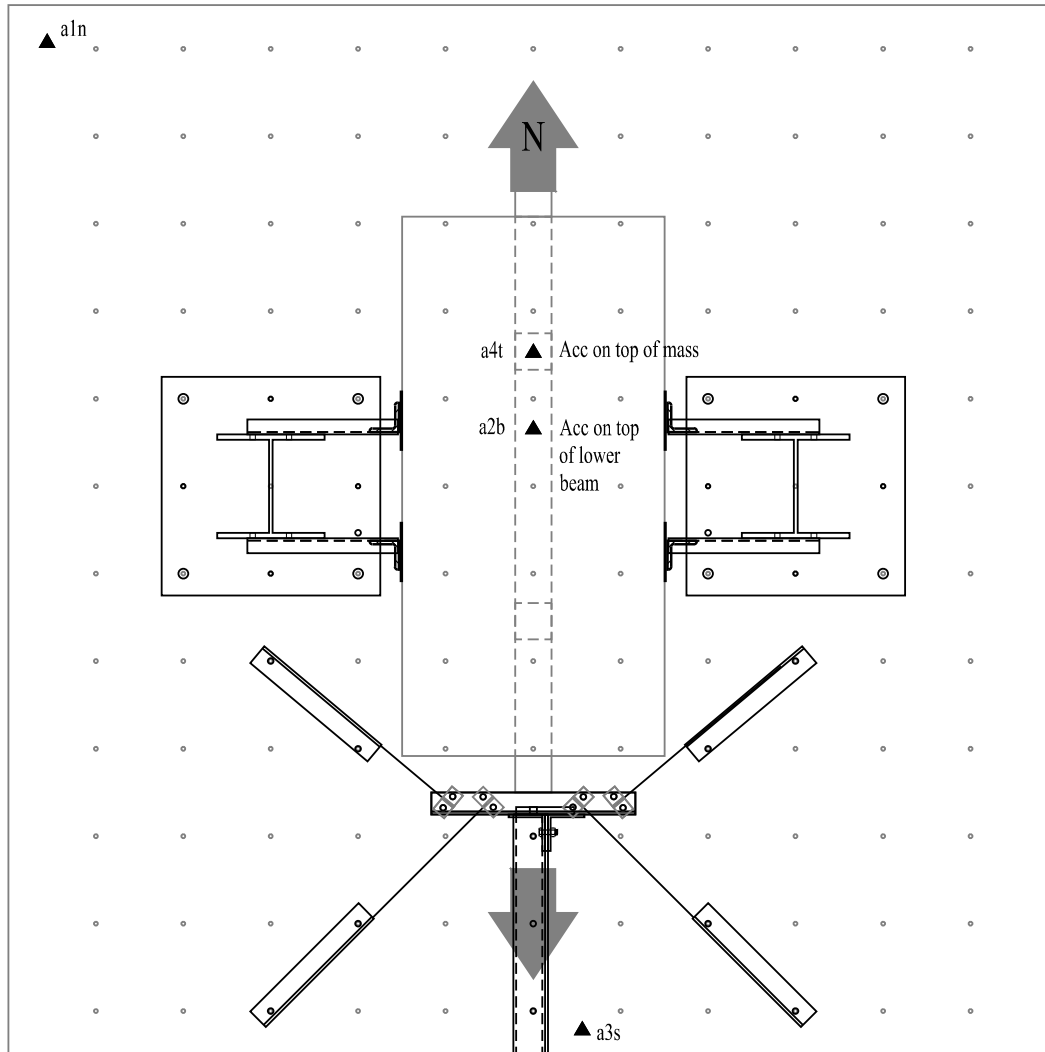


Figure A5-2: Overhead view of instrumentation plan.

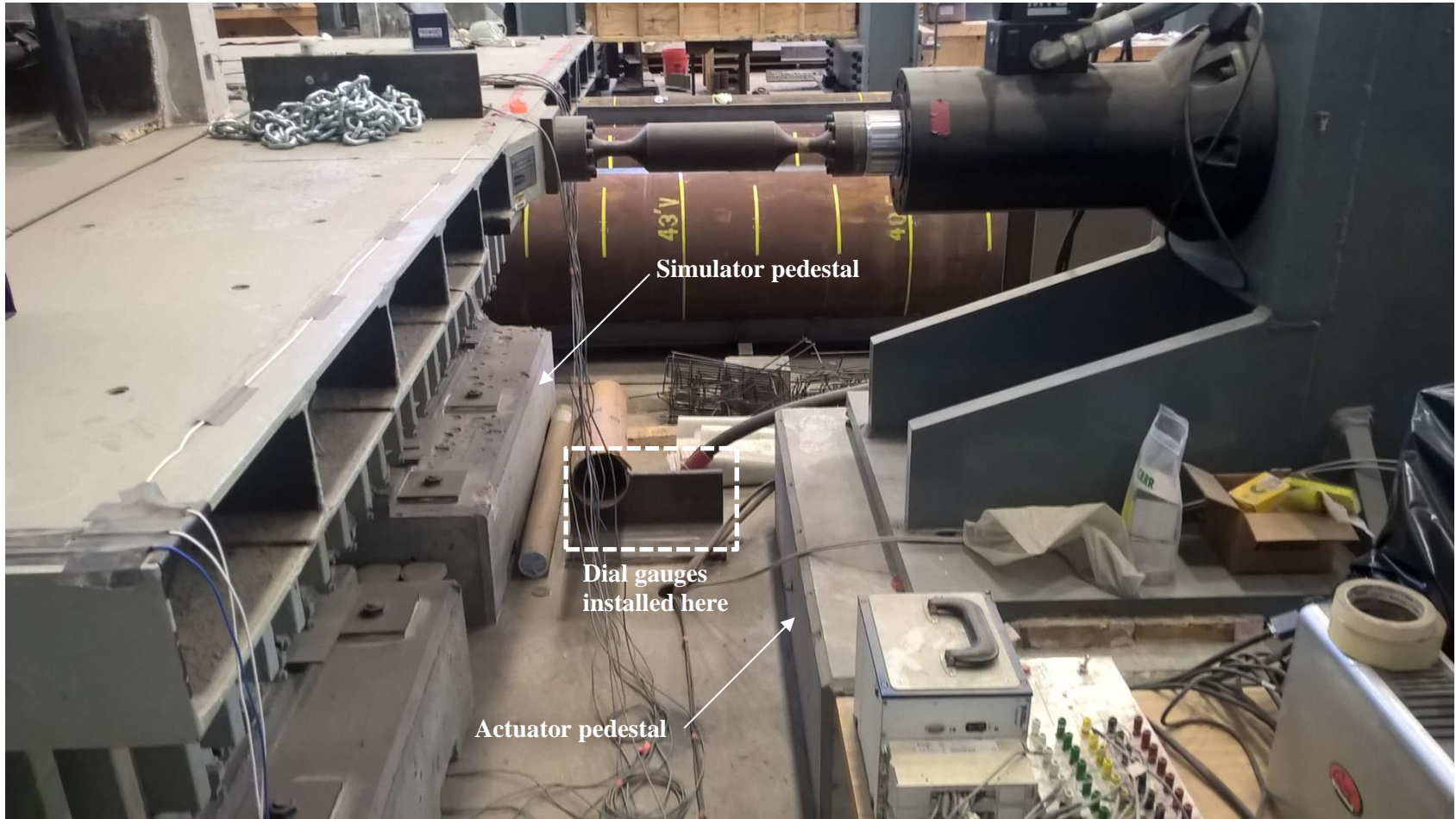


Figure A5-3: Photograph showing location where dial gauges were installed.

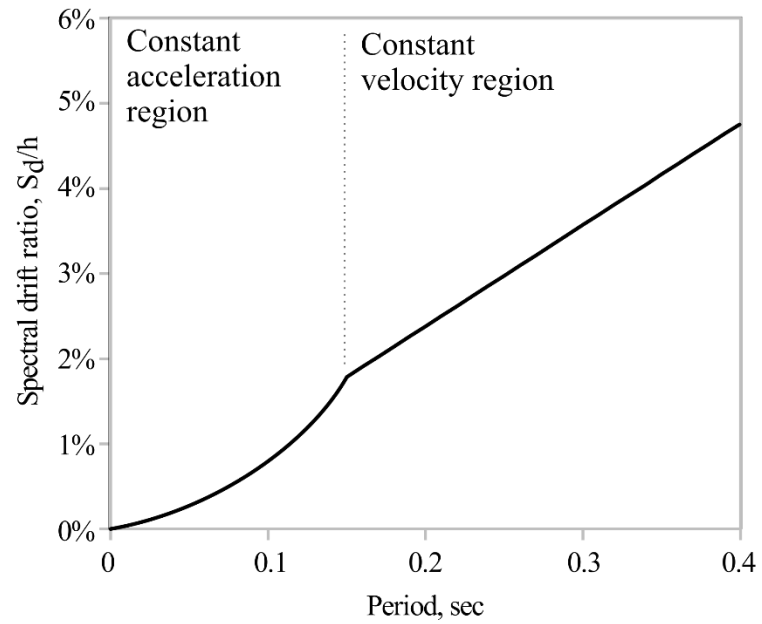


Figure A6-1: Idealized displacement response spectrum.

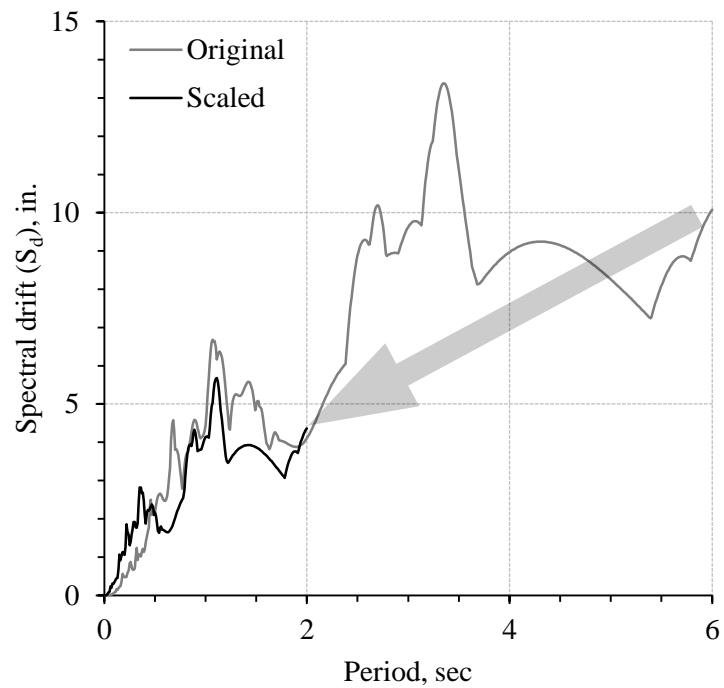


Figure A6-2: Displacement response spectra of original and compressed/scaled record.

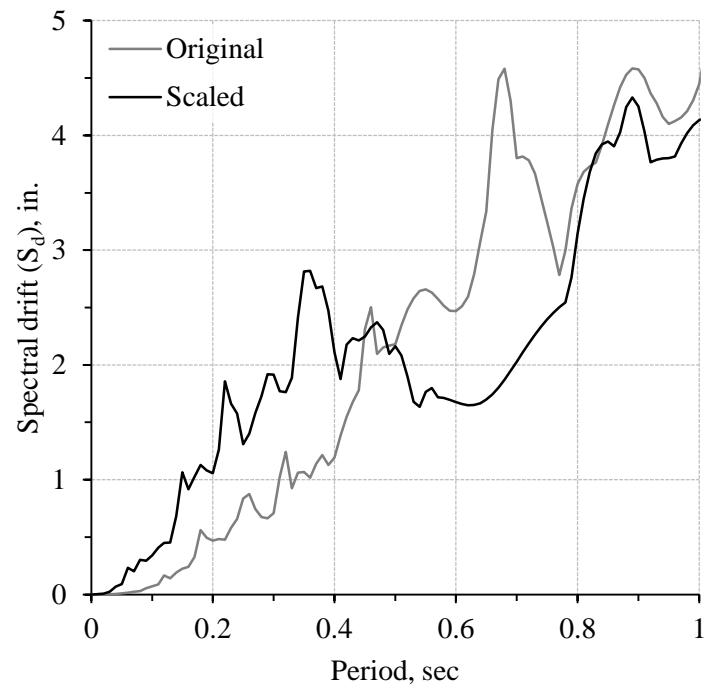


Figure A6-3: Close-up of displacement response spectra of original and compressed/scaled record.

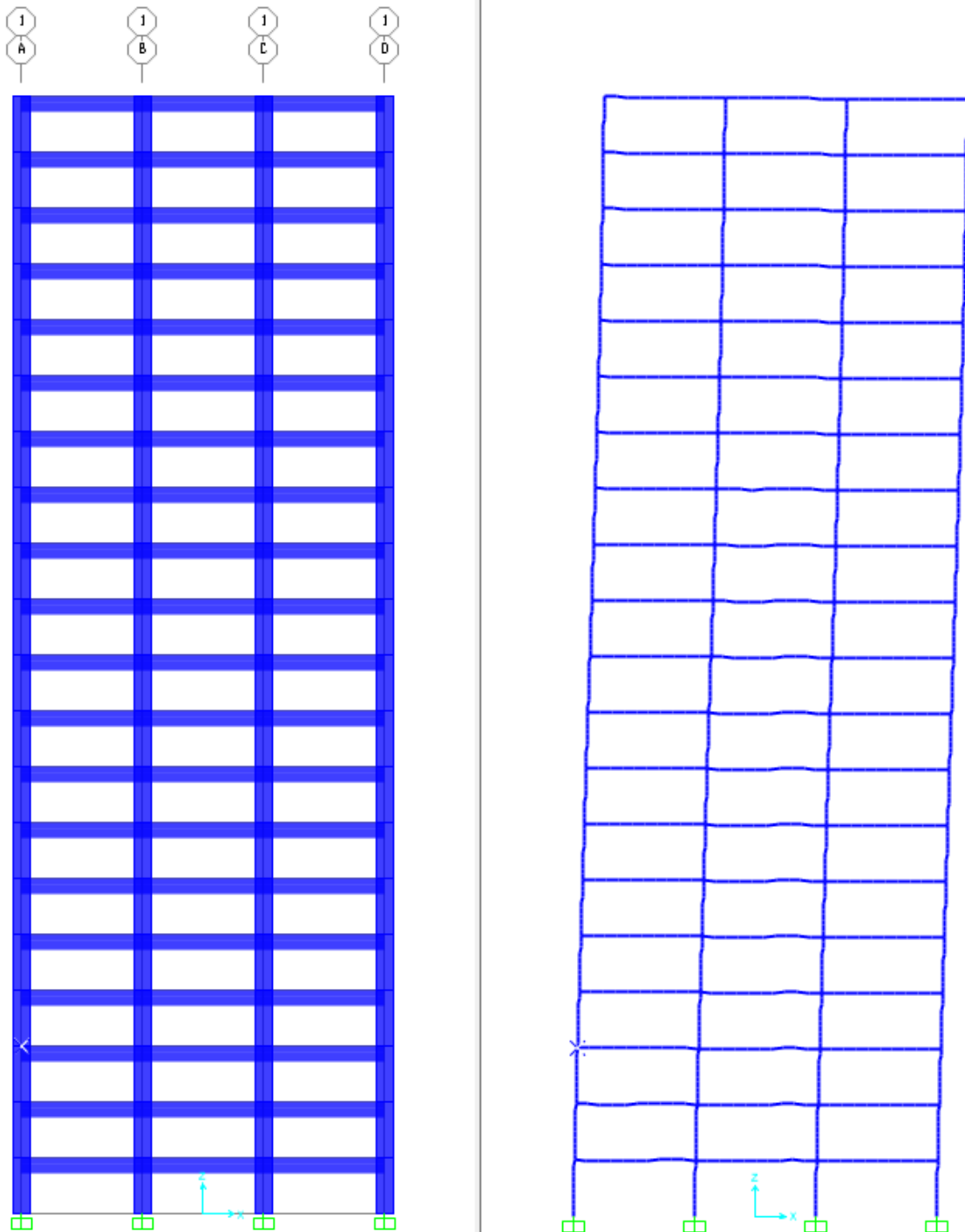


Figure A8-1: SAP2000 models of 20-story frames tested in Japan, X-direction.

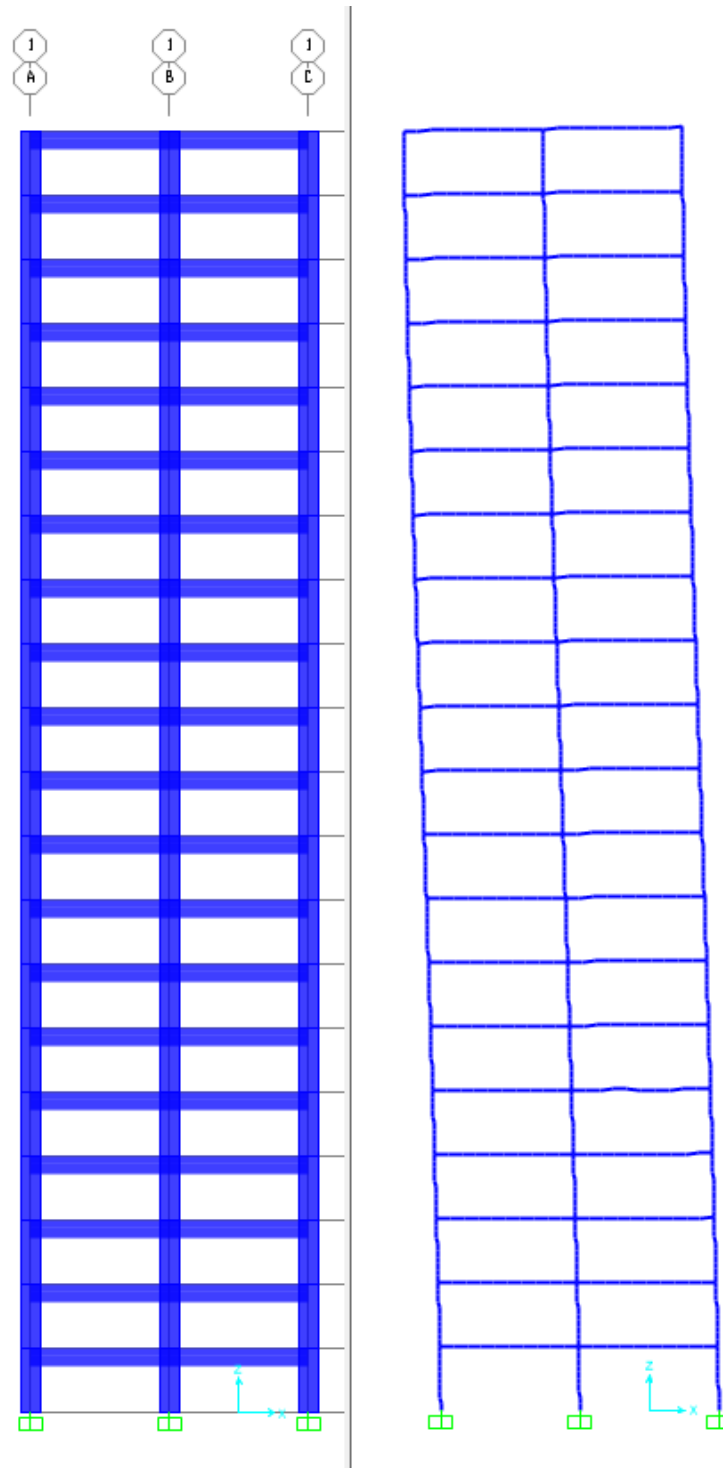
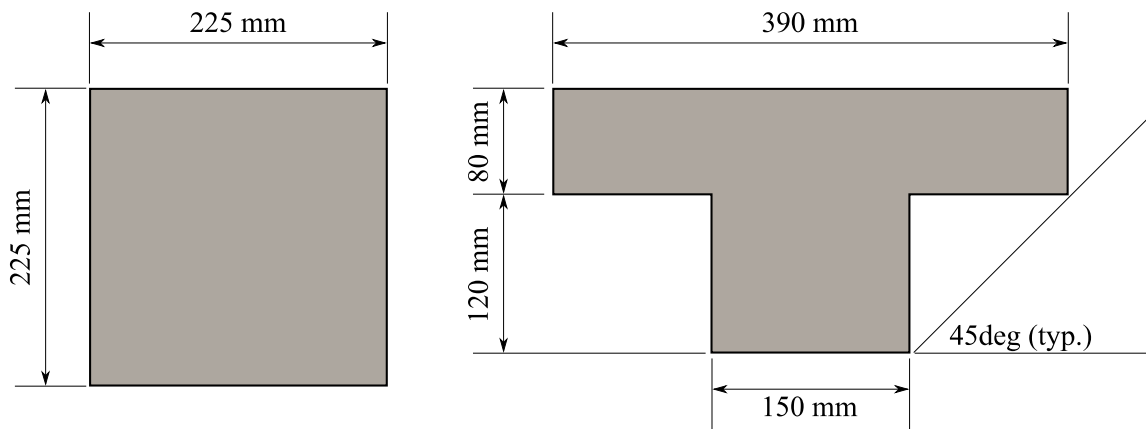


Figure A8-2: SAP2000 models of 20-story frames tested in Japan, Y-direction.



(a) Column Gross Cross Section

(b) Beam Gross Cross Section

Figure A8-3: Gross dimensions of members in SAP2000 models.

APPENDIX REFERENCES

1. ASTM C33 (2013), *Standard Specification for Concrete Aggregates*. American Society for Testing and Materials, West Conshohocken, PA. 11 pp.
2. ASTM C39 (2012), *Standard Test Method for Compressive Strength of Cylindrical Concrete Specimens*. American Society for Testing and Materials, West Conshohocken, PA. 7 pp.
3. ASTM C78 (2010), *Standard Test Method for Flexural Strength of Concrete (Using Simple Beam with Third-Point Loading)*. American Society for Testing and Materials, West Conshohocken, PA. 4 pp.
4. ASTM C150 (2012), *Standard Specification for Portland Cement*. American Society for Testing and Materials, West Conshohocken, PA. 9 pp.
5. ASTM C469 (2010), *Standard Test Method for Static Modulus of Elasticity and Poisson's Ratio of Concrete in Compression*. American Society for Testing and Materials, West Conshohocken, PA. 7 pp.
6. ASTM C496 (2012), *Standard Test Method for Splitting Tensile Strength of Cylindrical Concrete Specimens*. American Society for Testing and Materials, West Conshohocken, PA. 5 pp.
7. CESMD (2016), *Strong-Motion Virtual Data Center*. Center for Engineering Strong Motion Data. Website. < <http://strongmotioncenter.org/>>
8. INDOT (2014), *Standard Specifications*. Indiana Department of Transportation, Indianapolis, IN. 1074 pp.
9. PCB Piezotronics (2013a), "Model 333B52. Modal array, ceramic shear ICP® accel, 1000mV/g, 0.5 to 3k Hz, 10-32 side. Installation and Operating Manual." *User Manual*. Downloaded 2013. < <http://www.pcb.com/products.aspx?m=333B52> >
10. PCB Piezotronics (2013b), "Model 482A22. 4-channel, line-powered, ICP® sensor signal cond., unity gain, BNC. Installation and Operating Manual." *User Manual*. Downloaded 2013. < http://www.pcb.com/products/model/482a22/item_id/11643>

VITA

VITA

Lucas Alan Laughery was born in Sedalia, Missouri. He received bachelor's degrees in Civil Engineering and Architectural Engineering from Missouri University of Science and Technology in May 2012. He went on to pursue a coursework-only master's degree in Civil Engineering with an emphasis on Structural Engineering at Purdue University, which he received in December 2013. During his coursework-only master's degree, the author began the work for his Ph.D. dissertation, which he completed in August 2016.